MECHANISTIC MODELING OF STATION BLACKOUT ACCIDENTS FOR CANDU REACTORS

MECHANISTIC MODELING OF STATION BLACKOUT ACCIDENTS FOR CANDU REACTORS

By

FENG ZHOU, B.Eng., M.A.Sc.

A Thesis

Submitted to the School of Graduate Studies

in Partial Fulfilment of the Requirements

for the Degree

Doctor of Philosophy

McMaster University

Doctor of Philosophy (2018) McMaster University
(Department of Engineering Physics) Hamilton, Ontario, Canada

TITLE: Mechanistic Modeling of Station Blackout Accidents for CANDU Reactors

AUTHOR: Feng Zhou
B.Eng. (2012) USTC, China
M.A.Sc. (2014) McMaster University

SUPERVISOR: Dr. David Novog

NUMBER OF PAGES: xiii, 189

Abstract

Since the Fukushima Daiichi nuclear accident, there have been ongoing efforts to enhance the modelling capabilities for severe accidents in nuclear power plants. The primary severe accident analysis code used in Canada for its CANDU reactors is MAAP-CANDU (adapted from MAAP-LWR). In order to meet the new requirements that have evolved since Fukushima, upgrades to MAAP-CANDU have been made most recently by the Canadian nuclear industry. While the newest version (i.e. MAAP5-CANDU) offers several important improvements primarily in core nodalization and core collapse modelling, it still lacks mechanistic models for many key thermo-mechanical deformation phenomena that may significantly impact accident progression and event timings. It is also a general consensus that having alternative analysis tools is beneficial in improving our confidence in the simulation results, especially given the complex nature of severe accident phenomena in CANDU and the limited experimental support. This thesis seeks a novel approach to CANDU severe accident modelling by combining the best-estimate thermal-hydraulic code RELAP5, the severe accident models in SCDAP, and several CANDU-specific mechanistic deformation models developed by the author.

This work mainly consists of two parts. The first part is focused on the assessment of natural circulation heat sinks following crash-cooldown in the early-phase of a Station Blackout (SBO) accident where fuel channel deformation can be precluded. The effectiveness of steam generator heat removal after crash-cooldown and that of the several water make-up options were demonstrated through the simulation of several SBO scenarios with/without crash-cooldown, sensitivity studies, as well as benchmarking against station and experimental measurements.

In the second part, several mechanistic severe accident models were developed to enhance the simulation fidelity beyond the initial steam generator heat sink phase to the moderator boil-off and core disassembly phases. This includes models for predicting the pressure tube ballooning and sagging phenomena during the fuel channel heat-up phase and models for the sagging and disassembly of fuel channel assemblies during the core disassembly phase. After benchmarking against relevant channel deformation experiments, the models were successfully integrated into the RELAP/SCDAPSIM/MOD3.6 code as part of the SCDAP subroutines. The advantage of utilizing a code such as SCDAP is that generic models for fission product release and hydrogen generations, which are well benchmarked, can be directly applied to CANDU simulations. With the modified MOD3.6 code the early-phase SBO simulations were extended to include the later stages of SBO until the calandria vessel dryout. The current modelling approach replaced the

simple threshold-type models commonly seen in the integrated severe accident codes such as MAAP-CANDU with more mechanistic models thereby providing a more robust treatment of the core degradation process during severe accident in CANDU.

Acknowledgements

The work is financially supported by the Canadian Nuclear Safety Commission (CNSC), the Natural Sciences and Engineering Research Council of Canada (NSERC) and the University Network of Excellence in Nuclear Engineering (UNENE), which are greatly acknowledged.
In addition, I would like to take this opportunity to express my sincere gratitude to those who have offered me their invaluable help without which it is impossible for me to finish this thesis.

First, I must thank my supervisor Professor David Novog. He has been guiding me all the way through my master's and PhD's. His extensive work/research experience and profound knowledge in nuclear engineering have truly benefited me. This thesis could never have reached its present form without his enlightening guide and illuminating instructions. Second, I would like to express heartfelt appreciation to the committee of my thesis, Professor John Luxat, and Professor David Jackson, for all the valuable comments on my work. The time and effort spent on reviewing my thesis/papers are greatly appreciated.

Many thanks go to the people at Innovative System Software, Dr. Chris Allison for generously providing me the source code, training, and his valuable comments on my work, and Larry Siefken who walked me step-by-step through the first stage of code development within SCDAP, and to other lovely people Dick, Judy, and Jenny. My gratitude also goes to the people at Stern Labs (SL), especially Gordon for offering me the opportunities to work for SL over the summer, and Farzin for kindly providing me technical support, comments, and suggestions on my CFD work at SL. I also want to thank the people at McMaster Nuclear Reactor (MNR), especially Dr. Simon Day. The experience as a MNR tour guide and data analyst is very rewarding to me.

Also, I would like to thank all the faculty members of Engineering Physics Department at McMaster University, for their precious instructions in various courses, especially Dr. Ben Rouben who made me determined in pursuing the Ph.D. degree. Thanks also go to Morgan Brown at Canadian Nuclear Laboratories for answering my questions and providing valuable and enlightening comments on my work. Thanks go to my friends and colleagues at McMaster University, Chris, Fred, Amen, James, Hummel, Junfeng, Changrui, Mengmeng, Xiaopan, Yang, Shaun, Eddy ... It is their company that makes my graduate studies colourful.

Most importantly, I would like to express my deepest love and thanks to my dearest wife Jing for her love, support, trust, and patience in every day of my life. I cannot imagine my life without her. Special thanks to my parents for their eternal love, and consistent support. I wish them good health and happiness forever.

Table of Contents

List of Figures

List of Tables

Nomenclature

1-D	One-Dimensional
AC	Alternating Current
ASDV	Atmospheric Steam Discharge Valve
BDBA	Beyond Design Basis Accident
BWR	Boiling Water Reactor
CANDU	CANada Deuterium Uranium reactor
CATHENA	Canadian Algorithm for THErmalhydraulic Network Analysis
CNL	Canadian Nuclear Laboratories
CNSC	Canadian Nuclear Safety Commission
COG	CANDU Owners Group
COMPASS	Core Meltdown Progression Accident Simulation Software
CSDV	Condenser Steam Discharge Valve
CT	Calandria Tube
CV	Calandria Vessel
CWIT	Cold Water Injection Test
DC	Direct Current
ECCS	Emergency Core Cooling System
EME	Emergency Mitigating Equipment
EPS	Emergency Power Supply
EWS	Emergency Water System
FAI	Fauske and Associates Inc.
FES	Fuel Element Simulator
IBIF	Intermittent Buoyancy Induced Flow
ISAAC	Integrated Severe Accident Analysis code for CANDU plants
ISS	Innovative Systems Software (Owner of RELAP/SCDAPSIM code)
IST	Industry Standard Toolset
KAERI	Korea Atomic Energy Research Institute
LCDA	Limited Core Damage Accidents
LOCA	Loss of Coolant Accident
LRV	Liquid Relief Valve
MAAP	Modular Accident Analysis Program
MSSV	Main Steam Safety Valve
NGS	Nuclear Generation Station

NPD	Nuclear Power Demonstration
NPP	Nuclear Power Plant
NRC	Nuclear Regulatory Commission
OPG	Ontario Power Generation
PHTS	Primary Heat Transport System
PHWR	Pressurized Heavy Water Reactor
PSA	Probabilistic Safety Assessments
PT	Pressure Tube
PWR	Pressurized Water Reactor
RELAP5	Reactor Excursion and Leak Analysis Program
RIH	Reactor Inlet Header
ROH	Reactor Outlet Header
SBO	Station Blackout
SCDA	Severe Core Damage Accidents
SDTP	SCDAP Development and Training Program
SG	Steam Generator (also referred to as boiler)
SGECS	SG Emergency Cooling System
TH	Thermal-hydraulics

1. Introduction

1.1 Background

On March 11th 2011, a magnitude of 9.0 earthquake shook the Fukushima Daiichi nuclear power plant (NPP) causing the loss of grid power and the automatic shutdown of all active units. The situation worsened after the station was flooded by the subsequent 15-metre high Tsunami wave, damaging the emergency power generators and emergency batteries. A Station Blackout (SBO) was officially declared shortly after flooding. The active and passive cooling systems of units 1, 2 and 3 progressively failed or came to a stop. The resultant loss of core cooling led to the gradual boil-off of water in the reactor pressure vessel until the uncovery of fuel assemblies which initiated the fuel meltdown process. Molten fuel mixed with structural materials (often referred to as corium) slumped down to bottom of the reactor pressure vessel. Volatile fission products along with explosive hydrogen gas were released into the containment through venting via the reactor pressure vessel safety valves and/or other leak pathways. The steam and hydrogen gas being produced caused the pressurization of the containment. The operators initiated the venting process to avoid containment failure by releasing gas which carried radioactive materials into the atmosphere. The function and/or timing of venting was not successful in some units and hydrogen accumulated in the service floor of the reactor building. The subsequent hydrogen explosions led to site-wide contamination and significantly impeded recovery operations.

The Fukushima accident has caused immeasurable and long-lasting impact on the local residents, the environment, and the nuclear industry in Japan and other countries. Nearly every country using or planning to use nuclear power undertook immediate actions after the accident, with Germany deciding to phase out nuclear by 2022 [1], China suspending approval of new stations and pausing work on those under construction[1] [2], and many others including Canada initiating programs to undertake comprehensive safety checks and upgrades for their NPPs [3].

All of the power reactors in Canada are of the Pressurized Heavy Water Reactor (PHWR) type, i.e. CANDU® reactors (CANDU is an acronym of CANada Deuterium Uranium). At the time of writing, a total of 19 nuclear power reactors are operating across Canada with only one located outside of Province of Ontario, i.e. a single unit CANDU 6 at Point Lepreau Nuclear Generation

[1] Construction suspension in China was lifted by the end of 2011 after additional safety checks and features were added; approval for new projects reopened in October 2012 [87].

® CANDU is a registered trademark of Atomic Energy of Canada Limited (AECL)

Station (NGS) in New Brunswick. The rest of them are concentrated in three sites, i.e. Pickering (six units), Bruce (eight units) and Darlington (four units) [4].

Pickering NGS (strictly speaking, Pickering A) was constructed as the first multi-unit CANDU plant following the successes at Nuclear Power Demonstration plant (NPD) and Douglas Point [5]. The six operating units in Pickering (two in Pickering A, four in Pickering B) each have an electrical output of 500MW. The 500MWe Pickering design later became the design basis of the 600MWe CANDU (i.e. CANDU 6) [6], which is the major CANDU systems exported to foreign countries. Only two CANDU 6 units were installed in Canada both of which are located outside Ontario, i.e. Gentilly-2 (permanently shut down) and Point Lepreau (operating). The Bruce and Darlington sites both employed a larger-scale design. Bruce site has eight units each having an electrical output of about 800MW, while Darlington consists of four 900MWe units.

The Canadian Nuclear Safety Commission (CNSC) which is the regulatory body of the Canadian nuclear industry lunched an extensive review of all nuclear facilities in Canada shortly after the Fukushima accident [3], and later established a four-year action plan to further enhance the safety of NPPs and other main nuclear facilities [7]. As lessons learned from Fukushima, Nuclear operators performed extensive reviews, analyses and upgrades, including the increase of the number of emergency power generators, and the addition of emergency mitigating equipment (EME) such as portable pumps, power generators, and fire trucks [8], all of which ensure a sufficient and timely supply of water to various components of the reactor system.

The Fukushima accident also calls for the enhancement in the current modeling capabilities for severe accidents to help develop a better understanding of the severe accident progression and to assist the establishment of a more robust Severe Accident Management Guidelines (SAMGs). Much effort has been made by other researchers to upgrade their severe accident analysis tools in order to meet the new requirement. In an attempt to reduce the modeling uncertainties, this thesis work provides an alternative and more mechanistic approach to the severe accident analysis for CANDU reactors as will be discussed below.

1.2 CANDU Design

1.2.1 Primary Heat Transport System (PHTS)

The CANDU reactor is a pressure-tube type reactor using natural uranium as fuel, and separate coolant and moderator systems utilizing heavy water. The reactor is divided into two identical primary heat transport loops each in a figure of eight arrangement with each loop having two alternating-direction core passes. The two loops are connected via small diameter piping to the pressurizer, and can be isolated by the closing of loop isolation valves.

A prototypical 900MWe CANDU unit has a total of 480 horizontal fuel channels with 120 fuel channels per core pass. Each fuel channel consists of a Zr-2.5%-Nb pressure tube (PT) surrounded by annulus insulating gas and a Zr-2 calandria tube (CT). The reactor has four Class-IV-powered primary heat transport pumps (one per core pass). Coolant from each primary heat transport pump is distributed to the fuel channels via inlet feeder pipes. The fuel channels span horizontally the calandria vessel containing heavy-water moderator. Outlet feeder pipes connect the channel outlets to the reactor outlet headers which are connected to the steam generators (SGs) via large diameter pipes. Four large steam generators (one per core pass) transfer heat to the secondary side system. The primary side of the SG consists of U-tubes and an inlet/outlet plenum. Coolant enters the semi-spherical inlet plenum of the SG where it is distributed amongst the 4663 inverted U-tubes, and exits to the outlet plenum after passing through the U-tubes.

The pressurizer is the main component controlling the pressure and inventory of the primary heat transport system. The heating of the heavy water in the pressurizer creates a vapor space at its top which can be used to control the pressure in both loops and to cushion pressure variations. In Darlington NGS the pressurizer is located below the headers (Figure 1). Pressurizer pressure is controlled by heat addition through six heaters located at the bottom of the pressurizer, sprays which add subcooled liquid and condense some of the vapour in the steam space, or by bleeding heavy water vapor from the pressurizer to the bleed condenser (also referred to as degasser condenser) through the steam bleed valve.

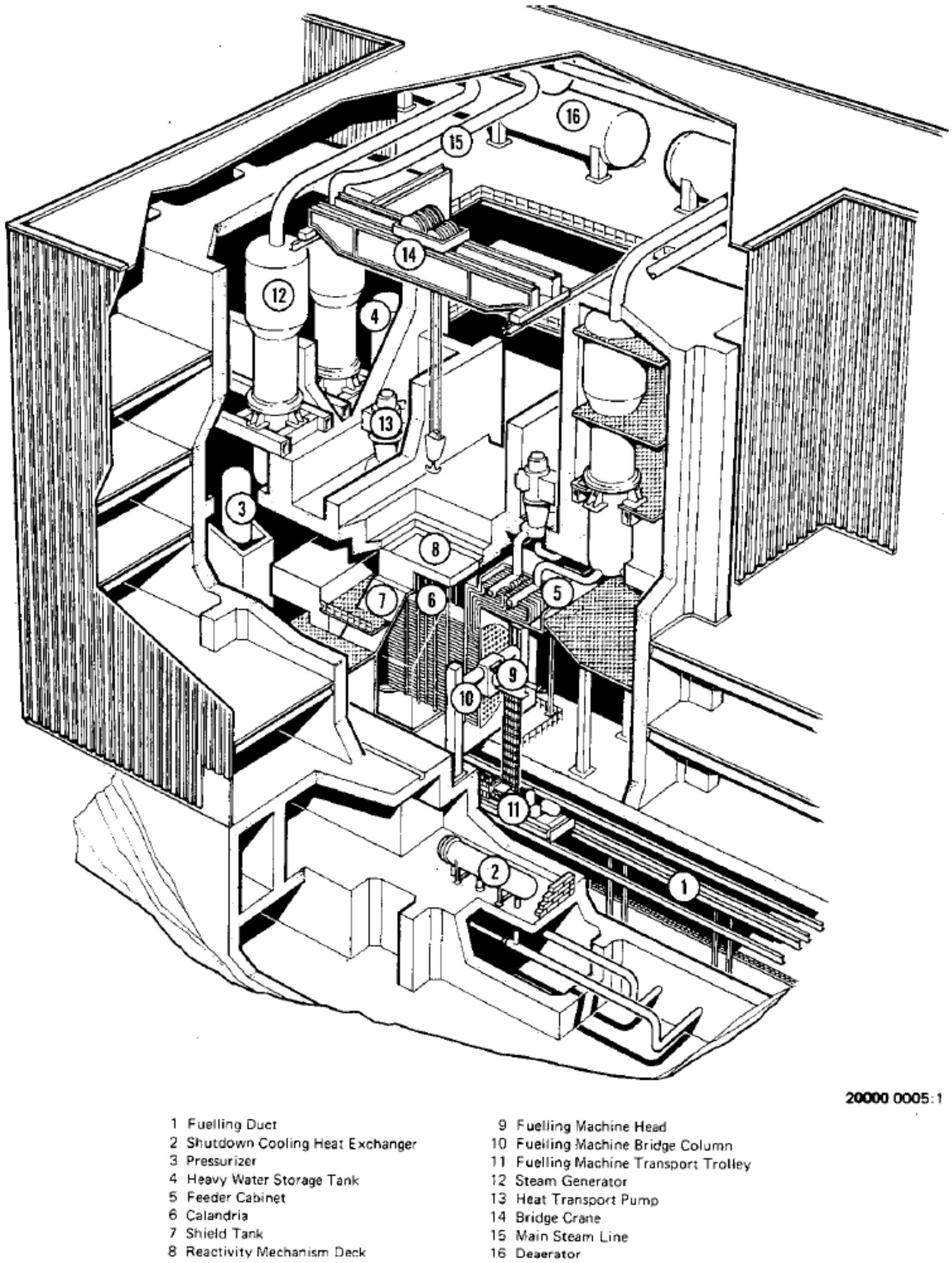

Figure 1 Darlington NGS Reactor Building [9]

1.2.2 Feedwater and Main Steam Supply System

The feedwater system consists of three 50% feedwater pumps relying on Class IV power and one 3-4% auxiliary feedwater pump relying on Class III power (refer to Section 1.2.4 for more information on classes of power). Water is pumped from the condenser, the deaerator tank, to the SGs. Before entering the SGs the feedwater is heated up to approximately 170^{o}C [10] by a series of feedwater heaters (high-pressure and low-pressure) which receive heat from the steam extracted from the turbines. The feedwater control valves are the key components controlling the SG level/inventory. Each SG has a set of three parallel control valves with different capacities (one small 18% and two large 100% [10]) to handle a wide range of operating conditions.

The majority of the feedwater enters the preheater section of the SG where it is heated up to near saturation point. A small fraction of the feedwater "leaks" through the leakage plate to the lower boiler section [11] where it meets the water from the downcomer annulus. The flow from the lower boiler section and the preheater section eventually merge together in the upper boiler section where the majority of the steam is generated. The two-phase flow leaving the upper boiler passes through the riser and enters the centrifugal separators where the vapor and liquid are separated. The liquid phase returns to the lower boiler through the downcomer. The dry steam is delivered to the two-stage turbines via the main steam piping to drive the generator and produce electricity.

Pressure relief and over-pressure protection of the secondary side are provided by the Condenser Steam Discharge Valves (CSDVs), the Atmospheric Steam Discharge Valves (ASDVs), and the Main Steam Safety Valves (MSSVs), with relief capacities of 86%, 10%, and 115% respectively [12]. Upstream of the high-pressure turbine, Governor Valves are used to regulate steam flow to the turbines, and Emergency Stop Valves are designed to quickly shut off the steam flow in the case of a sudden removal of load from the generator.

1.2.3 Moderator and Shield Water Cooling System

The calandria tubes of the 480 fuel channels are contained in a large horizontal Calandria Vessel which is filled with heavy water acting as moderator (Figure 2). Under normal operating conditions, about 5% of the total power is deposited into the moderator, the majority of which is by direct deposition (neutron moderation, and absorption of gamma ray). The moderator cooling system transports this heat to the main moderator heat exchangers which in turns transfers the energy to the recirculated cooling water system which is a closed loop service water system utilizing demineralized water for cooling [12]. The average moderator temperature is normally kept at around 65^{o}C [13]. The significant liquid swell/shrink during reactor start-up or shutdown due to moderator temperature change is accommodated by the moderator head tank connected to the top of the calandria vessel. Four large discharge ducts are also connected to the vessel at the top, while at the top end of each discharge duct there is a rupture disk designed to prevent calandria vessel from significant overpressure. The moderator system pressure is normally regulated via the cover-gas system and associated relief valves.

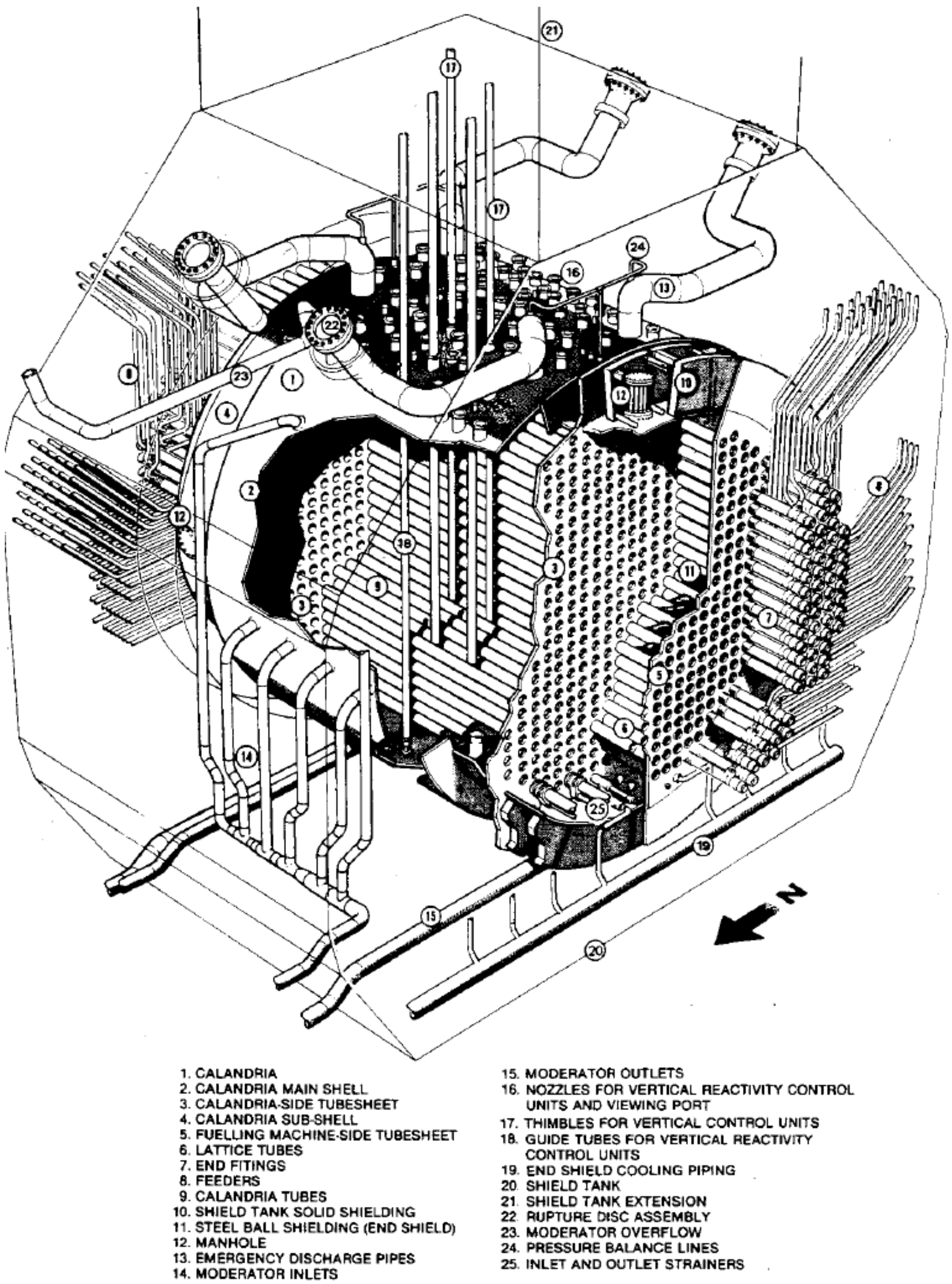

Figure 2 Darlington NGS Reactor Assembly [9]

The calandria vessel is contained within the shield tank (Figure 2) (calandria vault for CANDU 6) in which large volume of light water is used to provide biological shielding in the radial direction. Axial biological protections on both reactor faces are provided by the end shields which are filled with steel-balls and light water. The end shield and the shield tank are interconnected and share the same cooling circuit, relief valve, expansion tank and rupture disks. Water enters the bottom of end shields and exits at the top to flow into the shield tank. Both the moderator cooling pumps and shield cooling pumps are powered by Class III power to ensure rapid restoration of circulation following a loss of Class IV power (Power classes will be defined in the next section.)

1.2.4 Electrical Power Sources

The electrical power sources in a typical CANDU NPP are classified into four classes, i.e. Class I, Class II, Class III, and Class IV, in the order from highest to lowest level of reliabilities. Each class has a normal power source and emergency power source [14].

The Class IV power is primarily supplied by a unit service transformer and by a station service transformer connected to the grid for Group A and Group B electrical systems, respectively. Class IV power is considered interruptible and is used to supply large electrical loads directly, e.g. the primary heat transport pumps and the SG main feedwater pumps.

Class III power is normally supplied from Class IV systems. In the event where the Class IV power is lost, the standby power generators will be started up as back-up power sources. Class III power is used to supply loads that can tolerate a short period of interruption, such as the SG auxiliary feedwater pumps, the moderator and shield water cooling pumps. Other important systems powered by Class III include the heat transport feed pumps, the shutdown cooling pumps and the emergency core cooling pumps. The duration of interruption is typically within 5 to 15 minutes including the time to start up the standby power generator and the time to reload the Class-III-powered systems [15].

Both Class I and Class II powers are uninterruptible. Class I power supplies direct-current (DC) loads. It is connected to Class III power via rectifiers which converts alternating current (AC) to DC. Batteries are used in parallel to ensure uninterruptible power supply to critical loads. The batteries are always fully charged. If both Class IV and Class III power are lost, the batteries can supply DC loads for about an hour [15] (this number may vary depending on the specific site design). Class-II power supplies AC loads. Its power is normally supplied from Class I power via invertors.

The Emergency Power Supply (EPS) acts as an alternative back-up power sources and is independent from all other power supplies. But unlike the standby generators the EPS is both seismically and environmentally qualified, which means the equipment is protected from earthquakes, water flooding, fires, and other hazardous conditions [14]. The EPS is used to power certain safety-related systems on a priority basis, e.g. pumps of the emergency water system, in the event of a loss of both Class IV and III power.

1.3 Heat Sink Provisions

The CANDU reactors have multiple heat sink provisions depending on the availability of systems, components and electrical power [16]. Those heat sinks can be categorized into several groups according to their dependencies on the SG steam discharge, electrical power and service water.

1.3.1 Steam Generator as Heat Sink

In accidents where the PHTS remains intact but electrical systems are compromised the water inventory in the SGs is the primary heat sink during the first stage of an accident. Continuous and/or intermittent natural circulation within the primary system allows heat from the relatively low elevation core components to circulate to the cooler SGs providing an effective heat removal pathway provided that there is sufficient water in the SG shell side. Steam from the shell side can be condensed or vented to the environment, depending on the availability of systems.

Under normal operating conditions, the SG water level is maintained at its set-point by the boiler level control system. Thus the four SGs in the very beginning of an SBO accident will contain a significant amount of water which is able to maintain natural circulation in the PHTS after the loss the primary heat transport pumps for a few hours (the duration varies depending on the specific site design). The addition of water to the SGs can extend this natural circulation thus providing additional time for operators to take mitigating actions. Table 1 summarizes the available water sources for SG water make-up for a typical CANDU NPP.

Table 1 Potential Water Sources for Steam Generator in a CANDU Plant

System	Power	Water Sources	Depress. of SG
Feedwater	Class IV	Deaerator/Storage Tank, Condenser Hot Well	No
Auxiliary Feedwater	Class III	Deaerator/Storage Tank, Condenser Hot Well	No
Deaerator	No[1]	Deaerator/Storage Tank	Yes
Emergency Water System (EWS)	EPS	Emergency Service Water reservoir	Yes
	No[1]	Dousing Tank (Bruce B, CANDU6)	Yes
SG Emergency Cooling	No[2]	SGECS tank (Darlington A)	Yes
EME	Yes	External water source via portable pumps	Yes

1: Passive as it relies on gravity
2: Passive as it relies on air accumulator pressurized by instrument air

The normal water inventory of the four SGs in Darlington NGS is more than 300Mg, which can provide 4-6 hours of post-shutdown cooling [13]. This inventory is maintained by supplying water from the deaerator tank with the three main feedwater pumps (powered by Class IV power). In the event where the Class IV power is lost, the auxiliary feedwater pumps powered by Class III power can maintain SG inventory indefinitely for decay heat levels.

The emergency water system (EWS) provides one or two additional low-pressure water sources to the SGs dependent on the design. All reactors have capability to use water from the EWS reservoir via the EWS pumps which are powered by the EPS [17] (Table 1). For some other reactors with single-unit containment structures (e.g. CANDU 6) [14][17] the gravity-feed system can supply steam generator makeup from the dousing tank. In addition to the above Darlington has a SG emergency cooling system (SGECS), designed to provide short-duration interim water supply to the SGs following the steam line rupture and/or the loss of feedwater supply until the emergency water system becomes available. The SGECS system consists of two air accumulators pressurized by instrument air and two water tanks, with each tank and an accumulator suppling two steam generators [3]. Both the EWS and the SGECS require the depressurization of secondary side: SGECS valves will open when the steam drum pressure drops below 963kPa, and the EWS valves are automatically opened when the pressure drops below 345kPa [18].

However, in the case of an SBO where Class IV, Class III, and EPS may be lost, all feedwater systems become unavailable. Several options for water make-up to the SGs are available including internal water sources such as the mass in the deaerator tank, or external water source makeup. The deaerator tank which has normal inventory of about 320Mg is one of the highest elevation vessels in a CANDU reactor system (Figure 1). If crash-cooling of the steam generators is credited, the associated depressurization of the secondary side will allow water in the deaerator tank to flow by gravity into the SGs and provide an interim supply of water to the heat sink [2].

After the Fukushima Daiichi accident additional provisions have been implemented in the Canadian NPPs including the EMEs such as portable pumps and power generators. With these emergency measures external make-up water can be supplied to the steam generators and other key reactor components such as the calandria vessel and calandria vault/shield tank.

1.3.2 Primary Heat Transport System

The second group of heat sinks is related to the PHTS and also relies on the availability of service water and electrical power. This includes the Shutdown Cooling System, the Emergency Core Cooling system (ECCS), and the Feed and Bleed system.

The shutdown cooling is an alternative to the SG for decay heat removal. It is designed to provide cooling when the temperature of PHTS drops below 177^{o}C, but is also capable of cooling the system at full HT pressure and temperature [16]. For Darlington, the coolant is drawn from the reactor outlet headers (ROHs) by three 50% shutdown cooling pumps, and returns to the reactor inlet headers (RIHs) after rejecting heat to the recirculated cooling water in the heat exchanger [17]. Both the shutdown cooling pumps and the recirculated cooling water pumps are supplied from Class III power bus.

The purpose of ECCS is to replenish the reactor coolant and to assure cooling of the reactor fuel in a loss-of coolant accident. Light water is injected (or pumped) to headers in each loop regardless of the location of break. There are three stages in ECC operation: high, medium and low pressure stages. The high-pressure injection is triggered by the low PHTS pressure (5.5MPa) plus a conditioned signal [19]. Some stations use high-pressure tanks to inject water from ECCS tank into the headers (e.g., Bruce), while some (e.g. Darlington) uses high-pressure pumps for water injection. For medium and low pressure stages, the ECCS pumps are used to pump water from the dousing water tank (medium-pressure stage) or the reactor sump (low-pressure stage) into the headers. These pumps are powered by the Class III power and backed up by EPS [10].

The feed and bleed system is designed to control the PHTS pressure and inventory by regulating the feed and bleed flows and can remove a limited amount of heat via the bleed coolers and condensers. The bleed flow is taken from the primary heat transport pump discharge. Coolant passes through the bleed condenser, the bleed cooler, and the purification system, and then is pumped back to the primary heat transport pump suction. To avoid damage to the ion exchange resin in the purification system by the high-temperature coolant, the bleed cooler uses recirculated cooling water to cool its outflow to around 60^{o}C. Thus, the feed and bleed system is a potential heat sink during some accidents. For a 900MWe CANDU, the bleed cooler has the ability to remove up to 28.5MW (~1%FP) of heat from the PHTS [20]. The power to the heat transport feed pump of this system is supplied from Class III power.

1.3.3 Moderator and Shield Water as Heat Sinks

The third group of heat sinks includes the moderator and shield water (i.e. water in the end shield and shield tank). As discussed in Section 1.2.3, the heat loss to moderator under normal operating conditions is significant (about 5% of its total power). This heat is removed by the heat exchanger of the moderator cooling system. If the moderator heat removal becomes unavailable while the reactor continues operating at full power (very unlikely as the reactor trips on high moderator temperature), the moderator will start boiling (in just a few minutes [14]).

In accidents where the heat removal capabilities of the primary coolant and its associated systems are lost, e.g. a Loss of Coolant Accident (LOCA) with loss of ECCS, the moderator system is a potential heat sink. The fuel channels are submerged in the moderator at the time of fuel channel heat-up. The deformations of PTs (via ballooning and/or sagging) and the contact between PTs and CTs establish an effective heat conduction pathway so that energy from the fuel can be transported to the moderator. The presence of moderator prevents widespread fuel channel failure and significant core degradation, and allows the core geometry to be preserved [21]. If the moderator cooling remains available, the accident progression may be terminated. If the moderator cooling is also lost, the calandria vessel still contains a significant amount of moderator (about 260Mg for Darlington [13]) which is a passive heat sink and provides time for the operator to take mitigating actions (e.g., emergency make-up to the calandria vessel). Again, the establishment of water make-up to the calandria vessel will halt the accident progression.

Though very unlikely, if no water make-up is available the remaining moderator will eventually be boiled away exposing the fuel channels. With no moderator fluid to receive the heat the channels quickly heat up and disassemble. The end state of the core disassembly process is a terminal debris bed sitting at the bottom of the calandria vessel externally cooled by the water in the end shield and shield tank. The shield water thus becomes the heat sink (which is also passive) for the next-stage of accident. The shield tank for a 900MWe CANDU contains about 800Mg [13] of light water. The calandria vessel wall will remain intact until the water level in the shield tank is boiled down to approximately the level of corium pool top surface [21].

1.4 Station Blackout Accidents in CANDU Reactors

1.4.1 System Availabilities

The main focus of this thesis is on the Station Blackout accident (often referred to as SBO). SBO is defined by the US Nuclear Regulatory Commission (NRC) as the complete loss of AC power to the essential and non-essential switchgear buses in a nuclear power plant (i.e. the loss the off-site power, concurrent with turbine trip and failure of onsite standby and emergency AC power sources) [22]. The Canadian nuclear power plants are equipped with multiple back-up power sources if the grid power is lost, including onsite power (i.e. power produced by the plant itself), standby power generators, and emergency power generators. SBO in CANDU is thus referred to as the total loss of off-site power, on-site power, standby power generator, and emergency power generators (or in short, the loss of Class IV, Class III, and EPS). In addition, analyses must also consider Class I battery power depletion for equipment and instrumentation that are dependent on battery supplies.

In the event of an SBO, safety systems that do not rely on AC power are critical. Table 2 summarizes the availabilities of key cooling systems in CANDU during SBO (using information gathered from various resources [5][12][14][18][23]). Many safety systems relying on electrical power or service water becomes unavailable in an SBO, e.g. shutdown cooling system, ECCS, and feedwater systems.

The SG Emergency Cooling System (for Darlington), and the water in the deaerator tank are available as both of them provide passive water sources to the SGs (replying on pressurized air tank and gravity respectively). Besides, the normal inventories in the four SGs, the PHTS, the calandria vessel and the shield water are all passive heat sinks that can delay the accident progression for an appreciable time.

Table 2 System Availabilities in a 900MWe CANDU Plant during Station Blackout

		Class IV Power	Class III Power	Emergency Power Supply	Passive
HTS	Heat Transport Pump	✓			
	Heat Transport Feed Pump (feed & bleed system)		✓		
	Shutdown Cooling Pump		✓		
	ECCS [1] (high pressure stage)		✓	✓	
	ECCS (medium/low pressure stage)		✓	✓	
SG	Main Feedwater Pumps (feedwater system)	✓			
	Auxiliary Feedwater Pumps (feedwater system)		✓		
	SG Emergency Cooling System				✓
	Water Inventory in SG, and Deaerator Tank				✓
-	Moderator Cooling Pumps		✓		
	Shield Water Cooling Pumps		✓		
	Water Inventory in Calandria Vessel				✓
	Water Inventory in End Shield and Shield Tank				✓
Service Water Systems	Raw Service Water [2] Pumps		✓		
	Recirculated Cooling Water [3] Pumps		✓		
	Emergency Water System Pumps			✓	

1: Pickering and Darlington adopt a pumped system for the high-pressure stage, while Bruce and CANDU 6 use the gas-pressurized storage tank system.
2: open loop system utilizing fresh/sea water for cooling.
3: closed loop system utilizing demineralized water for cooling.

Table 3 Different Phases of the SBO Accident

Phase	**Heat Sinks**	**Prerequisite**	**Phenomena**
1	SG Inventory	HTS remains intact	Natural Circulation
2	HTS Inventory (Coolant)	HTS remains intact	Boil-off of HTS Coolant
3	Moderator	Calandria Vessel remains intact	PT deforms into contact with CT
4	Shield Water	Shield Tank remains intact	In-Vessel Retention

1.4.2 Early Phase – Natural Circulation

The total loss of electrical power disables the PHTS pumps, the feedwater pumps, the auxiliary feedwater pumps and the D_2O feed pumps (Table 2). The moderator and shield water cooling pumps are also lost. The subsequent event progression falls into several phases according to their dependence on the available heat sinks (Table 3). The primary heat sink in an SBO accident would initially be the SGs with heat removal occurring via natural circulation (after pump run-down). Due to the high elevation of the SGs continuous natural circulation is established shortly after the coast-down of the PHTS pumps and will continue until the secondary-side of the steam generators is depleted.

The current safety practice in CANDU is to initiate SG depressurization (or crash-cooling) once the loss of all electrical power has been declared. This is done through operator actions to manually open the MSSVs on the secondary side. The rapid reduction in secondary-side pressure and temperature will temporarily enhance heat removal from the primary side thereby further cooling the PHTS. Crash-cooling thus has the effect of:

a) Lowering the PHTS, fuel and sheath temperatures since the heat sink temperature is reduced.
b) Lowering the secondary side pressure which allows reverse flow from the deaerator tanks.
c) Lowering the secondary side pressure to allow for alternative inventory sources (e.g. SGECS and EME)

However, it is likely that soon after crash-cooling is initiated continuous natural circulation in the PHTS would be replaced with intermittent buoyancy induced flow (IBIF). This happens because the rapid cooldown of the PHTS results in coolant shrinkage causing the primary side to depressurize. As the pressure of the primary side approaches that of the secondary side (if ECCS is not available), the combination of the higher PHTS void fraction, the lower PHTS pressures and the lower buoyant force available (due to lower primary to secondary side temperature differences) leads to the breakdown of continuous natural circulation and the transition into IBIF. The flow in the channel is driven by the static head when giant bubbles formed in the stagnant channel reach one of the two feeders and rise (i.e. the venting of an IBIF cycle). The superheated steam after rising to the SG U-tubes is condensed and falls back to the core to replenish the vented fuel channel. Provided that this intermittent natural circulation is sufficient to remove the decay heat from the core, heat removal will persist as long as there is secondary-side inventory. If any of the aforementioned SG passive make-up water options is successful, the SG secondary side dryout would be delayed as compared to cases where the system is left at high pressure.

When the steam generators are depleted the heat removal capacity is impaired, the PHTS system would begin to heat up and re-pressurize. During this repressurization IBIF ceases and interchannel flow is initiated. Interchannel flow phenomenon is unique to the CANDU design in that complete flow stagnation is unlikely if the headers remain full. In this instance any liquid in the headers is drawn into channels by vapour exiting from the opposite end of the channel. Therefore in a core-pass while the net flow between the headers may be near zero, appreciable channel flows may exist albeit in opposite directions from channel to channel. When the PHTS pressure increases to the Liquid Relief Valve (LRV) set-point, coolant is discharged through the LRV to the bleed condenser which has been isolated early during the transient. The bleed condenser is equipped with two spring-loaded relief valves for over-pressure protection. With the continuous addition of hot coolant from the PHTS, the bleed condenser pressure quickly rises to its relief valve set-point. The PHTS pressure is then governed by the set-point and capacity of the bleed condenser relief valves.

When the PHTS inventory is boiled down to uncover the feeder connections on the headers, inter-channel flows cease and coolant in the corresponding channels will completely stagnate. The feeder inventories then provide liquid to the channel until the available volume is depleted. When the channel inventories drop below the highest elevation fuel pins the fuel will begin to heat-up. At this time, the fuel channel is still submerged in the moderator, and the likely scenario under high pressure will be for the PT to balloon into contact with CT establishing the moderator as the next available heat sink (Table 3).

1.4.3 Later Phase – Severe Accidents

Based on the above evolution, the focus of the operator actions after fuel channel heat-up is thus to supply water to the calandria vessel and keep the fuel channels submerged (if the operators fail to restore electrical power and the relevant core cooling systems). The presence of moderator, as mentioned earlier in Section 1.3.3, prevents widespread fuel and channel failures and allows the core geometry to be preserved. Accidents as such are called the Limited Core Damage Accidents (LCDAs) which are considered as design-basis accident for CANDU reactors [21].

Severe accidents are defined in CANDU as “beyond-design-basis accidents involving significant core degradation”. Thus for the accidents to progress into “severe accidents”, the moderator heat sink must be lost. In the case of an SBO, there are several possible progression pathways leading to the loss of moderator inventory:

1) Provided that all the fuel channels survive the aforementioned fuel channel heat-up phase with their PTs deform into contact with the CTs, and that the calandria vessel steam relief valves are sufficient in releasing steam generated in the calandria vessel, the moderator inventory will be gradually lost through continuous boiling and evaporation.
2) Fuel channels survive the fuel channel heat-up phase and successfully establish the moderator as heat sink. However, as the heat removed by the moderator increases, moderator steaming rate eventually exceeds the relief valve capacity causing the calandria vessel to pressurize and the rupture disks to burst. This leads to a sudden loss of moderator (a significant amount) by expulsion surges through the discharge ducts.
3) Depending on the liquid stratification and circumferential temperature gradients on the pressure tube the fuel channel integrity may be lost early before the PT-to-CT contact due to non-uniform stresses. The failure of the fuel channel at high pressure causes the high temperature steam to be ejected into the calandria vessel. The rupture disks burst upon channel failure, which again leads to the rapid moderator expulsion uncovering a number of fuel channel rows at the highest elevations.

In any of the three cases, the fuel channels, starting at the highest elevation, will be uncovered. After uncovery the fuel channels heat up quickly and will soon begin to sag as their CTs lose strength at high temperatures. The sagged fuel channel may come into contact with the lower channel or it may disassemble (i.e. channel separated at the bundle junctions into a number of segments). The disassembled channel segments may relocate directly to the calandria vessel bottom or it may temporarily come to rest on lower elevation channels. These disassembled core parts together with the sagged channels form a suspended debris bed which is supported by the first fuel channel row that are still submerged thus sufficiently cooled.

The suspended debris bed gradually relocates downward one channel elevation at a time, as the moderator level drops (thus more channels are uncovered) with its mass increasing each time it relocates to a lower elevation. This continues until it exceeds the maximum load the supporting channels can tolerate. At this point in the transient the channels supporting the suspended debris bed are pulled out from their rolled joints at the two ends resulting in core collapse to the bottom of the calandria vessel. Some moderator is immediately expelled out through the discharge duct following core collapse, while the remainder will quench the terminal debris bed. When the moderator is boiled away, the dry terminal debris bed will begin to heat up. The decay heat is then externally removed by the water in the shield tank and end shield. Analysis of terminal debris bed cooling is beyond the scope of this work.

1.5 About This Study

1.5.1 Gaps in Modeling of Early-phase SBO with Crash-Cool

It has been discussed that crash-cooling during an SBO has several potential benefits, one of which is that it allows several low-pressure passive water sources (including the new EMEs implemented after Fukushima accident) to be supplied to the SGs. However, the credit of crash-cooling without water injection from ECCS into the PHTS is expected to cause an early breakdown of continuous natural circulation, and the transition into IBIF. Provided that the IBIF mode of circulation in the PHTS is successful removing heat from the fuel and transferring heat to the secondary side, the available time for the operators to restore the power and/or to take other mitigating actions can be significantly extended. Thus there is a need to demonstrate the effectiveness of SG heat removal by reflux condensation under the IBIF mode following crash-cooldown. While the SBO scenarios in a CANDU reactor without any operator intervention have been studied and simulated extensively by other researchers and are thus well understood, the ones with operator initiated crash-cooling are less frequently studied or simulated (especially with system thermal-hydraulic code).

1.5.2 Gaps in CANDU Severe Accident Modelling

CANDU reactors possess several unique design features, e.g. horizontal fuel channels, and coolant separated from the moderator, some of which prevent the straightforward application of many existing severe accident codes that were originally developed for LWRs, e.g. MAAP, MELCOR, SCDAP/RELAP5.

MAAP-CANDU (Modular Accident Analysis Program-CANDU) is the CANDU Owner Group (COG) Industry Standard Toolset (IST) code for CANDU severe accident analysis. The code is primarily used in Canada for severe accident analysis, and has been successful in supporting the development of Level 2 Probabilistic Safety Assessments (PSA). MAAP-CANDU is one of the parallel versions of the MAAP code. The code is adapted from its LWR version by Fauske and Associates Inc. (FAI) through the addition of a large number of CANDU specific models (some of the models were developed by Ontario Hydro, now Ontario Power Generation) [24]. While the original intent was to facilitate the parametric analyses of a CANDU severe accident, which purpose the MAAP-CANDU code serves well, it still has many areas that can be improved (Table 4).

First, the thermal-hydraulic model is relatively simple. The heat transport system employs a two-phase homogeneous model prior to phase separation, and a lumped multi-component, non-equilibrium model after phase separation [25]. For example, a simple user-input threshold value of coolant void fraction is used to determine the occurrence of phase separation. Therefore, the code does not benefit from the large amount of existing thermal-hydraulic modelling and expertise available in codes such as RELAP5. This limits the accuracy and application of the code to distinct phases in the transient.

Second, many accident phenomena after fuel channel dryout, e.g. the failure, the deformation and the relocation of fuel channels, are not mechanistically modeled in MAAP-CANDU IST. The code largely relies on threshold models, e.g. at high PHTS pressure the PT is assumed to fail when its temperature exceeds a value above which the PT starts to balloon; and similarly for the failure at low pressures. Furthermore, during the core disassembly phase the fuel channels remain in their original position until the average temperature exceeds the melting temperature, after which they are directly relocated to some artificial holding bins where they will be treated as the “suspended debris bed”. The use of such threshold models does not allow one to examine the mechanistic models, their uncertainty, and the contribution to event trajectory. This assessment of severe accident sensitivity and uncertainty has become increasingly important.

Third, core nodalization is relatively coarse in MAAP-CANDU which directly impacts the core deformation and collapse phases. Specifically, the reactor core is divided into six vertical nodes. The channels in each vertical core nodes are then grouped into six characteristic channels mainly by their channel powers (three per HTS loop per vertical node). Axially, the channels are divided into five horizontal nodes. Such coarse nodalization induces large uncertainties and makes it unlikely to capture the details of the core disassembly phase (refer to Chapter 2 for more details).

In the light of the CNSC action plan, the CANDU Owners Group (COG) initiated a development programs for MAAP5-CANDU, i.e. the newest version of the MAAP-CANDU tool suite [26]. MAAP5-CANDU possesses two major improvements over its previous version MAAP4-CANDU, e.g. reactor core and channel nodalization, and core collapse modeling. However, some of the issues that require further improvements remain (Table 4).

Table 4 Comparison of Existing Severe Accident Codes for CANDU [21] [26][27]

	MAAP4-CANDU	MAAP5-CANDU	RELAP/SCDAPSIM/MOD3.4
Failure at High Pressure	$T > T_{PT\text{-}balloon}$		$T > T_{PT\text{-}balloon}$ (900K)
Failure at Low Pressure	Melt-through T>2033K / Sagging T>1473K		Average CT >1200K
Core Disassembly	T_{ave} > Melting T of Oxygenated Zr; Relocate to "holding bins"		Average CT >1500K
Core Collapse	25,000kg/loop	Elastic beam theory	25,000kg/loop
Core Nodalization	18 per HTS loop (Axial=5, Vert.=6)	24*24 (up to 480) All Channels	4 per HTS loop
TH	Two-phase homogeneous (prior to phase separation) / separated lumped non-equilibrium (after phase separation)		Two-fluid, non-equilibrium, TH model (six equations)

The SCDAP/RELAP5 code is a US-NRC code originally designed for LWRs. This code is an integration of the RELAP5 code for thermal-hydraulics, the SCDAP code for the severe accident related phenomena and the COUPLE code for the lower vessel head problem. While RELAP5 code has been used in many CANDU applications, the SCDAP part of the code has not been utilized at the same level due to difficulties in the modelling of horizontal fuel channels degradation, failure and core disassembly.

The RELAP/SCDAPSIM code originates from the US-NRC SCDAP/RELAP5 code, and is being developed as part of the international SCDAP Development and Training Program (SDTP) [28]. SDTP involves nearly 60 organizations in 28 countries all over the world (the numbers were published in 2010 [28], thus may be outdated). The code is being used by members and licensed users to support various activities including the safety analysis for CANDU reactors in Romania and Argentina [27][29]. Researchers in Romania have also done some pioneer work to adapt the RELAP/SCDAPSIM code to CANDU with focuses on the early phase degradation modeling within a fuel channel by modifying SCDAP [30][31], and the in-vessel retention studies by modifying COUPLE [32][33], (refer to Chapter 2 for a more thorough review/discussion of these works).

However, as seen in Table 4, the detailed modeling of many severe accident phenomena such as PT ballooning/sagging and channel sagging and disassembly is still lacking. Instead, simple threshold models are often utilized to determine whether the channel has ballooned/failed/

disassembled. Those threshold models often require the use of certain conservative assumptions thus precluding the best-estimate analyses. Lacking the actual physics behind these models also leads to the difficulties in quantifying the uncertainties in severe accidents event modelling.

1.5.3 Objectives of the Study

The ultimate goals of this thesis are to use (and develop if necessary) the best-estimate tools to simulate as mechanistically as possible the postulated prolonged SBO transients for a 900MWe CANDU reactor, and to contribute to the understanding of the reactor behaviors during such accidents through sensitivity analyses. To make the plan reasonable and executable while not overlapping with other researchers' work, the scope of this study is defined as the modeling of SBO from the initiating event to the end of core disassembly phase until the calandria vessel dryout (i.e. the first three phases in Table 3). The subsequent shield water system response or the in-vessel retention phase is outside the scope of this study.

Part 1 - Simulation of Early Phase SBO

The first part[2] of this research involves the use of a best estimate tool (RELAP5) for the simulation of early phase SBO while focusing on the natural circulation behavior and the assessment of water make-up to SGs for scenarios where operators initiate crash-cooling. The early phase is defined here as from the initiating event until the start of fuel channel heat-up, thus does not involve any significant thermo-mechanical deformations.

The RELAP5 (version MOD3.3) [34] is a non-equilibrium, six-equation, two-fluid system thermal-hydraulic code, and has been successfully used by other researchers on the thermal-hydraulic analysis of CANDU reactors. Validation of the code against CANDU-related experimental data (e.g. the RD-14M tests) is available in literature. There are also code-to-code comparisons with CATHENA (Canadian Algorithm for THErmalhydraulic Network Analysis) [35] which was developed specifically for modeling the thermal-hydraulic response of CANDU reactors under accident conditions. However, the accidents that have been simulated using RELAP5 are typically for design basis events and at higher HTS pressure conditions. RELAP5 is considered superior to the thermal-hydraulic model in most of the severe accident codes such as MAAP-CANDU and MELCOR, and is therefore used for the analysis of the early phase of SBO.

This part of the work is subdivided into a number of tasks:

[2] This part of the work is financially supported by the Canadian Nuclear Safety Commission (CNSC) under contract 87055-15-0226-2.

1) Create a RELAP5 model for a 900MWe CANDU including the PHTS, the SG secondary side, the feed and bleed system, the calandria vessel, the end shield and shield tank. The secondary side should also include the SGECS, the deaerator flow path, and simplified EME flow path so that the operator initiated crash-cool and different water make-up options can be assessed.
2) Benchmark the RELAP5 model against station measurements from 1993 Loss of Flow event at Darlington NGS. This event was initiated by a switchyard transformer explosion, resulting in the loss of Class IV power to Unit 4 and a consequential turbine trip [36]. Class III power was restored on standby power generator shortly after the loss of Class IV power. Data from this event is ideal for validation purpose as the reactor response to such event in first few tens of seconds is expected to be the same as that in an SBO.
3) Simulate several extended SBO scenarios with/without crash-cool and with different water make-up options. The effectiveness of SGs heat removal after crash-cooling and that of several external water make-up options will be examined. The capabilities of RELAP5 in predicting the thermal-hydraulic behavior after crash-cooling will be assessed.
4) Investigate the sensitivity of results to various modeling parameters including but not limited to:
    a) Sensitivity to system nodalization, in particular, the fuel channel grouping schemes and the use of multiple flow paths in representing the boiler tubes,
    b) Sensitivity to certain parameters related to the injection of make-up water, e.g. the timing and location of water injection,
    c) Sensitivity to the CCFL model and its related input parameters,
    d) Sensitivity to the potential loss of PHTS inventory through leakage, i.e. via pump seal.

The results of this work are documented in the journal publication presented in Chapter 3.

<u>Part 2 - Simulation of Later Phase SBO</u>

The second part[3] of this thesis is focused on the simulation of the later-stage SBO including the fuel channel heat-up phase, the fuel channel uncovery and the core disassembly phases. The goals are to improve the modeling of CANDU severe accident and to fill some of the gaps as recognized

[3] This part of the work is financially supported by the Natural Sciences and Engineering Research Council of Canada (NSERC) and the University Network of Excellence in Nuclear Engineering (UNENE).

and discussed in Section 1.5.2. This requires the use and/or development of a severe accident code that is able to model several key CANDU severe accident phenomena mentioned above.

The RELAP/SCDAPSIM (version MOD3.6) (hereinafter referred to as MOD3.6) is selected for this work. MOD3.6 is a new version of the RELAP/SCDAPSIM tool suite being developed to support the severe accident analysis for PHWRs. MOD3.6 uses the publically available RELAP5/MOD3.3 for thermal-hydraulics. This allows a smooth and direct extension of our early-phase SBO simulation to include the later severe accident stages. SCDAP in MOD3.6 is responsible for modeling all severe accident related phenomena, e.g. material oxidation, fission product releases, fuel rod cladding deformation, fuel rod liquefaction and relocation. While the details of these models are well documented in the code manual [37], the SCDAP code is originally developed for LWRs with vertical core geometries. Although, there are some ongoing activities at the Innovative Systems Software (ISS)[4] in association with users in Romania and Argentina to adapt RELAP/SCDAPSIM/MOD3.6 to CANDU, the SCDAP code still lacks the mechanistic models for many CANDU specific severe accident phenomena as discussed earlier in Section 1.5.2.

Thus, within the objectives of the second part of this thesis, the aim is not just to use the as-received MOD3.6 to simply extend our early-phase SBO simulation, but rather to create, test and deploy mechanistic thermo-mechanical models under the framework of MOD3.6 for predicting the later phases of SBO evolution. This part of the thesis work can also be divided into several tasks:

1) Replacement of the outdated threshold models in MOD3.6 with more mechanistic and physics-based deformation models including
    a) PT ballooning and PT sagging during the fuel channel heat-up phase,
    b) Fuel channel sagging and failure in the core disassembly phase,
    c) Suspended debris bed failure (end-fitting pullout or channel collapse).
2) Validation / benchmarking of the developed mechanistic models against the available PT deformation experiments in literature.
3) Extension of the early-phase SBO simulations using the modified MOD3.6 to include the fuel channel heat-up phase and the core disassembly phase, and to investigate the impacts of the early-phase operator actions (i.e. crash-cooling, and water make-up to SGs) on the later-phase accident progression.
4) Perform more physics-based uncertainty/sensitivity analysis for the later phases.

[4] Innovative Systems Software (ISS) is the owner of the RELAP/SCDAPSIM codes, and the administrator for the SDTP program.

The results of the mechanistic model development and validation are provided in the journal publication in Chapter 4, while the SBO event predictions and their sensitivities are provided in the Journal publication in Chapter 5.

1.5.4 Thesis Structure

Chapter 2 presents a literature review of the relevant studies in CANDU severe accident modeling, followed by the main body of this thesis which consists of three chapters (i.e. Chapter 3, 4, and 5).

Each of the three chapters consists of a published (or submitted) journal article and a proceeding introduction page. The first paper in Chapter 3 is aligned to the objectives of the first part of this thesis (i.e. Part I – Section 1.5.3), and focuses on the prediction of CANDU system response during the early-phase SBO with and without operator action credits. The second and third paper in Chapter 4 and 5 are in alignment with the objectives of the other part of the thesis (i.e. Part II – Section 1.5.3). While Chapter 4 focuses on the development and benchmarking of mechanistic deformation models and their integration or coupling with the existing models in MOD3.6, Chapter 5 is on the use of this modified MOD3.6 code in simulating the later-phase SBO.

Additional studies and model descriptions that were not detailed in the papers are included in the appendices as a supplement. This includes:

A) A detailed description of RELAP5 model for the early phase SBO simulation in Appendix A
B) A description of the mechanistic models in Appendix B
C) The simulation of Cold Water Injection Test in Appendix C
D) The validation of MOD3.6 against CANCHAN test in Appendix D
E) A summary of potential future improvement in Appendix E

2. Literature Review

While Section 1.5.2 is an overview of the gaps in modeling of CANDU severe accidents, this chapter presents, in a more detailed and systematic manner, a review of the existing CANDU severe accident codes and the relevant studies. Some of the studies have already been reviewed in the three published papers, thus the main purpose of this chapter is to further discuss their limitations and/or potential improvements.

2.1 MAAP-CANDU Code & Related Activities

2.1.1 MAAP-CANDU

The MAAP-CANDU code has evolved from its first version developed at the end of 1980s [25] progressively to the current version MAAP4-CANDU [38], and finally to MAAP5-CANDU [26] that has yet to be released at the time of writing.

Like many other integrated severe accident codes, the nodalization of primary heat transport systems in MAAP-CANDU (even its newest version) is relatively coarse. Using MAAP4-CANDU as an example, each loop of the PHTS is modeled with only 14 nodes, including two SGs, two pumps, two RIHs and two ROHs with feeders connecting the inlet/outlet end of fuel channel to the RIHs/ROHs (Figure 3) [21]. While such models capture the gross response of the PHTS it was originally developed for LOCA-LOECC scenarios where primary-circuit phenomena are confided to a relatively short duration and where system responses (e.g., control system or operator action) are limited. While such idealizations may provide adequate accuracy for some events they preclude detailed evaluation of individual phenomena (e.g., groups of channels are assumed to deform together rather than a channel at a time).

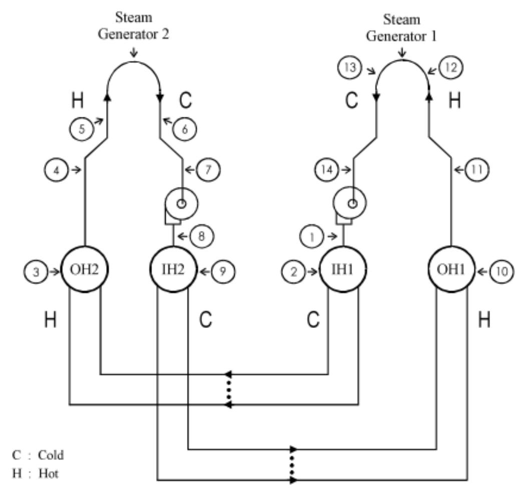

Figure 3 Nodalization Scheme of CANDU Primary Heat Transport System in MAAP4-CANDU [21]

The modeling of any accident scenarios in MAAP-CANDU is carried out in multiple stages:

1) Before phase separation, a two-phase homogenous thermal-hydraulic model is used for the PHTS which interacts with the other systems such as the calandria vessel, the shield tank and the containment via energy and/or mass transfer. The core at this stage is represented as a lumped parameter model.
2) When phase separation occurs, i.e. when the void fraction of the PHTS exceeds a user-input threshold, MAAP-CANDU activates a lumped non-equilibrium model with multi-component (including water, steam, and non-condensable gases) for the PHTS thermal-hydraulic calculation [25]. The fuel channels at this stage are grouped into a number of characteristic channels according to their channel power and elevation. In MAAP4-CANDU and its previous versions, the reactor core is vertically divided into six nodes, and axially into five nodes (Figure 4). The fuel channels at each of the six elevations are grouped into three characteristic channels (per loop) with high, medium, and low powers respectively, resulting in a total of 36 characteristic fuel channels (18 in each loop). Each average fuel channel is represented by a lumped heat source until the remaining coolant in the corresponding channel and feeders is boiled off.

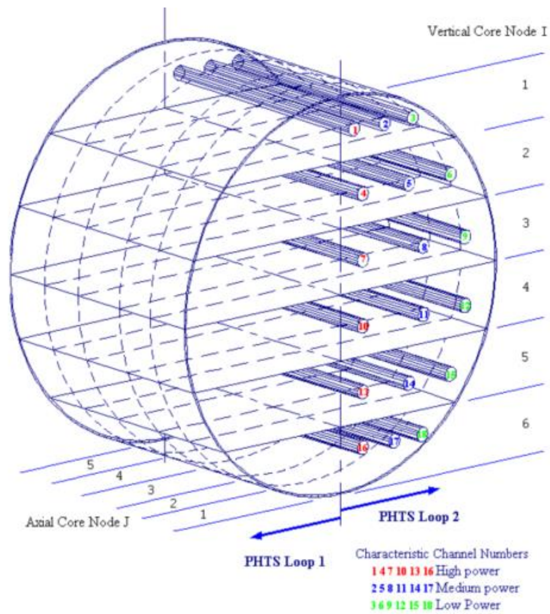

Figure 4 Nodalization Schemes of CANDU Core in MAAP4-CANDU [26]

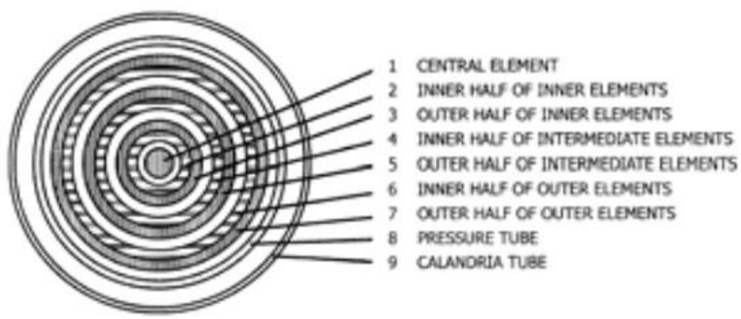

Figure 5 Nodalization Schemes of CANDU Fuel Channel in MAAP4-CANDU [21]

3) After the complete dryout of fuel channels, a number of thermo-mechanical and thermo-chemical models are activated to predict core degradation phenomena, e.g. zircaloy-steam reaction inside/outside the fuel channel, deformation and relocation of the fuel channel, the formation, heat-up and motion of the suspended debris bed, and fission product releases. Inside the fuel channel, the steam and hydrogen flow is determined by the channel resistance, the chemical environment of the PHTS, and a user-input header-to-header pressure differential when the fuel channel is intact (after channel failure, the difference in fluid conditions between the PHTS and the calandria vessel) [25]. The fuel channel is represented with 9 concentric rings with the inner, intermediate, and outer elements each modeled as two rings (Figure 5) instead of individual fuel pins. Steam flow

outside the calandria tube is determined from the steaming rate of the calandria vessel pool taking into account the obstruction formed by the suspended debris bed [25].

One area that has attracted most of the attention when upgrading the MAAP4-CANDU to MAAP5-CANDU is in the core disassembly and collapse modeling. The suspended debris in MAAP-CANDU is represented by a number of artificial holding bins. When the temperature of a fuel channel segment exceeds the user-input threshold (i.e. the melting temperature of oxygenated Zr, Table 4), it is relocated to the corresponding "holding bin" whose mass is tracked dynamically to assess it against core collapse criteria. The disassembly and suspended debris behaviors are modeled on a core node basis. In MAAP4-CANDU the resolution of the core is relatively coarse which can cause large uncertainty in the modeling of core disassembly and collapse. In developing MAAP5-CANDU, significant effort has been devoted to refining the core nodalization. In MAAP5-CANDU, the number of axial nodes has been increased from 5 to 13, the vertical nodes from 6 to 26, and lateral nodes from 1 to 24 (originally no lateral dimension was considered) [26]. The threshold-type core collapse criterion has also been replaced by a mechanistic model based on elastic beam theory (Table 4). However, at the time of writing no changes have been made to the physical models as described above.

2.1.2 Studies Using MAAP-CANDU

A large number of studies have been carried out in literature by researchers in Canada using MAAP-CANDU code covering a wide range of accident scenarios, such as SBO, Small/Large LOCA, Stagnation Feeder Break, Steam Generator Tube Rupture etc. Since the focus of this study is on the simulation SBO for a 900MWe CANDU, only a few of the relevant studies are reviewed in this section (ranked in the order from most to least relevant).

Darlington NGS – 900MWe CANDU

Blahnik, et al. (1993) [13] carried out some pioneering work on the use of MAAP-CANDU (a very early version) to simulate a postulated total loss of heat sinks event for Darlington NGS. It was assumed that all AC power supplied to one of the four units was lost including grid power, local power supplies, and emergency power generators, and that the operators failed to take any mitigating actions (such as crash-cooling). Their simulation predicted that the four SGs with a normal inventory of 340Mg $\pm$ 10% were depleted between 5 and 6 hours. This is significantly longer than the reported SG dryout time in literature for a CANDU 6 under the same accident scenario (see below), and is attributed to the oversized SG at Darlington NGS. Relief of coolant from the PHTS via relief valves was predicted to start at about 6 hours. Reactor headers became voided at around 6.5h, at which point the PHTS phase separation was assumed to occur. After the remaining coolant was boiled off, the fuel channel ruptured at 8.4 $\pm$1h by non-uniform strain. The uncertainty in fuel channel failure timing stems from the uncertainty in timing of phase separation. The rupture disks opened when the discharge from the ruptured channel exceeded the capacity of the calandria vessel relief valves causing significant moderator expulsion, and between 6 and 10 rows of channels became uncovered. The core disassembly was then modeled according to the logic described above. In their simulation, the suspended debris bed built up quite rapidly to the collapse threshold and core collapsed at around 11 hours. After core collapse a terminal-debris was formed at the bottom of the calandria vessel which dried out at about 14 hours.

The work carried out by Blahnik et al. [13] has a major improvement in core disassembly modeling over earlier works, i.e. the work conducted by Rogers (1984) [39] for the Atomic Energy Control Board [5], and the early CANDU 6 Level 2 PSA studies by Howieson et al. (1988) [40], Allen et al. (1990) [41]. Blahnik et al. assumed that the fuel channel after disassembly will be supported by the lower intact channel (represented by an artificial holding bin in the MAAP-CANDU methodology) to form a suspended debris bed which will relocate downward as the moderator level decreases and thus more channel rows are uncovered. Whereas, Rogers, Howieson and Allen in their early studies all assumed that the fuel channel after meeting the disassemble criteria (i.e. PT/CT temperature exceeded a predefined temperature threshold) would fall directly to the bottom of the calandria vessel (the detailed review of these early studies has already been carried out by Meneley et al. [42] thus will not be repeated here). This simple core disassembly model precluded the possibility of forming a suspended debris bed, and it was claimed to be more conservative as it would cause higher hydrogen and fission product releases at the later stage of accident sequence when the containment failure might occur. Although, the model in MAAP-CANDU used by Blahnik et al. [24] also relies on the temperature threshold to predict fuel channel failure/disassembly, it is considered more mechanistic than the simple disassembly model by Rogers et al. [39], and may be more appropriate for accident scenarios where channel uncovering begins several hours after the initiating event [42] (thus, the heat-up rate is lower due to the relatively lower decay power level).

More recently, the CNSC (2015) [43] has released a review of Darlington's Level 2 PSA performed by Ontario Power Generation (OPG). In the PSA, the MAAP4-CANDU code was used to simulate various highly unlikely accident scenarios including a similar SBO scenario where the external power sources, standby and emergency power generators were unavailable and no

[5] now Canadian Nuclear Safety Commission (CNSC)

operator intervention cases. The accident progression in their SBO analysis followed the same pathway as that described in Blahnik et al. [13] with slightly different event timings [6]. The SG dryout occurred at 5.0 hours, and fuel channel dryout began at 6.4 hours. Almost immediately after fuel channel dryout, the fuel channel ruptured causing the pressurization of calandria vessel and the burst of calandria vessel rupture disks (i.e. at 6.4 h as opposed to 8.4 ± 1h in Blahnik et al. [13]). Core disassembly started at about 8.8 hours, and core collapsed at 10.7 hours (as opposed to 11 h in Blahnik et al. [13]). Water in the calandria vessel was boiled off completely at about 16 hours (14 h in Blahnik et al. [13]). The shield tank failed at the bottom of seam weld due to inadequate pressure relief at about 22.8 hours (27 h in Blahnik et al. [13] due to the same reason) causing the rapid decreasing of shield tank water level, and the subsequent calandria vessel failure at 24.5 hours.

The results of OPG's MAAP4-CANDU simulation also indicated that there is readily available water for SG water make-up which only requires simple operator actions and can provide approximately 8 to 10 hours of additional passive core cooling [43]. Moreover, if additional field operators are successful in connecting EME to the SGs and securing a continuous water supply, the accident progression will be terminated. However, these actions require the depressurization of the SGs (or crash-cooling). Their report does not provide the simulation results for such a scenario or a discussion on the code reliability in predicting the post-crash-cool natural circulation behaviors. Given the simple thermal-hydraulic models in MAAP4-CANDU, evaluation of complex two-fluid phenomena such as IBIF would have large uncertainties. It is desirable therefore to use a more robust and detailed treatment of the PHTS to evaluate the effectiveness of crash-cooling scenarios.

CANDU 6 – 600MW CANDU

While only limited severe accident studies conducted for a 900MWe CANDU are available in the open literature, many more can be found on CANDU 6 which has an electrical output of approximately 600MW. While the event progressions may be similar, the timings are significantly different owing to different component sizes and capabilities.

Nitheanandan, et al. (2013) [44] analyzed a prolonged SBO scenario without operator intervention for a CANDU 6 using the MAAP4-CANDU code. Their analysis showed that the SGs could remove decay heat for about 1.9 hours without any water make-up. Beyond this point the remaining liquid in HTS boiled off. The first channel ruptured at about 3.9 hours followed by

[6] A more detailed comparison on the predicted event timings are presented in the third paper in Chapter 5.

opening of the calandria vessel rupture disks for overpressure protection. Without ECCS, core disassembly started at about 5.5 hours. Water in the calandria vessel was depleted at around 11 hours. The timings of these key events are approximately 3 hours earlier than those predicted for a 900MWe CANDU [13] [43] due primarily to the difference in SG volumes. Nevertheless, water in the calandria vault delayed the calandria vessel failure until 46 hours (significantly later if compared to the work by Blahnik et al. [13] and OPG [43]). The deviation in calandria vessel failure timings is attributed to the difference in modeling assumptions. While both Blahnik et al. [13] and OPG [43] considered the worst scenario, i.e. the shield tank failed at the bottom of seam weld due to overpressure, Nitheanandan, et al. [44] assumed that the calandria vault rupture disk was available and had sufficient capacity for pressure relief.

Petoukhov (2014) [45] assessed the effectiveness of SG secondary side water make-up from the containment dousing tank in a CANDU 6 unit during SBO scenarios using MAAP4-CANDU. Two SBO cases with and without water make-up were simulated. The reference case was similar to that in Nitheanandan et al. [44], i.e. both the secondary and primary-side pressures stayed high with no water make-up to the SGs. In the other case, MSSVs were locked-open at about 1.13h when the SG water level dropped below 7.5m to initiate crash-cooldown and water in the dousing tank was allowed to flow by gravity into the SGs. To avoid liquid overflow the valves connecting the dousing tank and the SGs were manually opened by operator actions when the SG level was less than 8.0m and closed when greater than 10.0m. In the reference case without water make-up, the SGs emptied at 2.65h, and the PHTS pressure started to rise before SG dryout with first coolant relief via LRVs at 2.44h. In the crash-cool case, make-up water from the dousing tank commenced at about 1.3h (i.e. 10 mins after crash-cooling). The on-off cycles of water make-up from dousing tank kept the SG U-tubes covered in water throughout the simulation for over 500,000 seconds (138.9h) due to the large water inventory in the dousing tank. Not surprisingly, the LRVs remained closed for the duration of the accident.

Petoukhov's study [45] thus demonstrated that crediting water make-up to the SGs was effective in delaying accident progression. Although, this action will remove or partially impair the containment dousing spray system at the later stage of accident, the estimated decay power level at the end of the simulation (i.e. 500,000s) was 0.30%FP as opposed to 1.1%FP when the SG dried out in the reference case. The remaining water in the SGs, PHTS, the calandria vessel, and the calandria vault are the heat sinks of the next stages and would further delay the accident progression should his simulation proceed further. However, his paper, again, did not examine the primary-side thermal-hydraulic behavior predicted by MAAP4-CANDU following crash-cooldown, and did not conclusively show whether the IBIF mode of natural circulation is sufficient in removing heat from the core and preventing fuel channel failure.

2.2 ISAAC Code & Related Activities

2.2.1 ISAAC Code

Korea has four operating CANDU 6 units in Wolsong NPP. ISAAC (Integrated Severe Accident Analysis code for CANDU plants) is currently the most used severe accident code for CANDU reactors in Korea. ISAAC was developed in the middle 1990s by KAERI (Korea Atomic Energy Research Institute) and FAI [46], originally to support the Level 2 PSA for the CANDU 6 reactors in Wolsong NPP.

Similar to MAAP-CANDU code, ISAAC used MAAP4-LWR (i.e. the newest MAAP version at that time) as its reference code. Most of the severe accident models in ISAAC were inherited from MAAP4-LWR meaning that it has most of the merits and demerits of the MAAP4 code. The additional Wolsong-specific models for the horizontal core, PHTS, calandria vessel, and various safety systems [21] enabled it to analyze severe accidents at Wolsong NPP.

The fuel channel modeling adopted an approach slightly different from MAAP-CANDU. Instead of using 9 concentric rings to represent the fuel channel, the 37 fuel elements are lumped into a single rod (Figure 6). The pressure tube and the calandria tube are each represented by a concentric ring. Axially, the fuel channel can be nodalized into a maximum of 12 axial horizontal nodes. Accident phenomena, such as cladding failure, oxidation, channel sagging, and relocation of debris to the bottom of calandria vessel are modeled by its "core module".

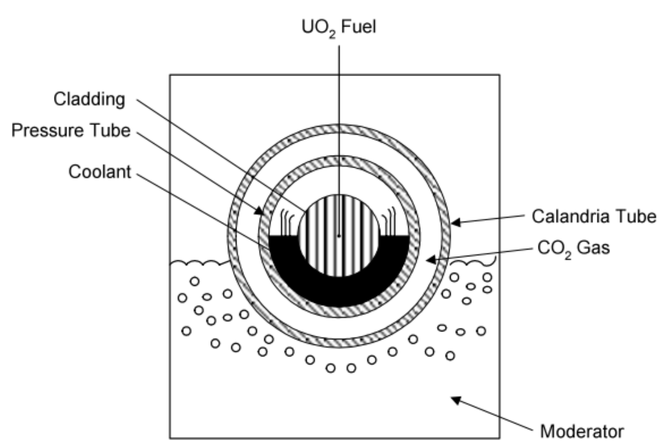

Figure 6 Fuel Channel Configuration Model in ISAAC [21]

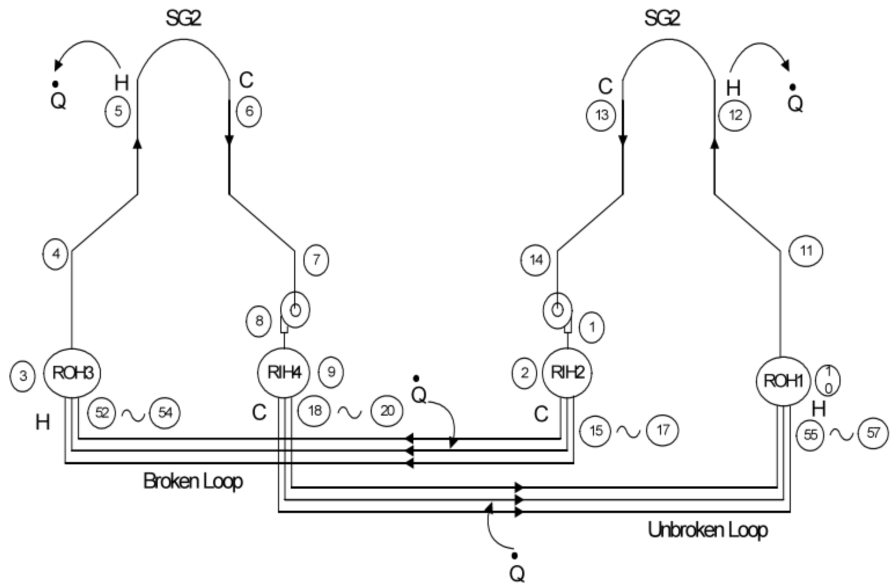

ROH: reactor outlet header; RIH: reactor inlet header; SG: steam generator;
H: hot; C: cold, O: heat flux, and 1 ~ 57: node number

Figure 7 PHTS Nodalization in ISAAC for a 3×3 Core Passes per Loop [21]

Heat losses from the PHTS to the moderator system via the CO_2 annulus and to the containment atmosphere via the PHTS wall are modeled. The 380 fuel channels can be grouped into a maximum of 74 average fuel channels (as opposed to 36 groups in MAAP4-CANDU) according to their elevations, power levels, core passes and loops [21].

Overall, MAAP-CANDU and ISAAC are very similar to each other. Nodalization of the PHTS in ISAAC is also very coarse (Figure 7), and both codes use relatively simple thermal-hydraulic models. Steam flow through the fuel channel during the fuel channel heat-up phase is also determined by the user-input header-to-header pressure difference from external analyses. The core disassembly model is also similar to MAAP-CANDU, i.e. when reaching the disassembly criteria the fuel channel fragments are relocated to the “holding bins” where they are treated as “suspended debris bed” until core collapses.

2.2.2 Studies Using ISAAC

This section reviews a few studies performed with the standard ISAAC code.

Kim et al. (2008) [47] in KAERI released a detailed report on the validation of ISAAC computer code. The validation was carried out in three steps. In the first step, seven typical scenarios including SBO, In-core Tube Rupture, Small/Large LOCA, SG Tube Rupture etc. were simulated for their CANDU 6 reactors. The results predicted by the ISAAC code were found reasonable in general. In the second step, the ISAAC code was compared against CATHENA for several LOCA scenarios and against MAAP4-CANDU for an SBO and a Large LOCA sequences. The thermal-hydraulic models in ISAAC were much simpler than system codes like CATHENA. It was thus expected that the plant response predicted by ISAAC would deviate from the CATHENA calculations. However, the overall trends predicted by the two codes were similar. For severe accident modeling, the ISAAC code showed similar accident progression sequences when compared to MAAP4-CANDU. The accident, however, was found to progress faster than that predicted by MAAP4-CANDU. Finally, the ISAAC results were compared with the experimental data, but limited to steam explosion, and steam generator behaviors [47].

Park et al. (2011) [48] carried out a comparative analysis of an SBO accident for a typical PWR [7], BWR [8] and PHWR [9] in the same year after the Fukushima Daiichi accident. The study was performed using the PWR and BWR version of MAAP code for the selected PWR and BWR plants, respectively, and the ISAAC code for the CANDU 6 plant. For the CANDU 6 SBO sequence, all the ECC systems, the moderator cooling, the end-shield cooling, and the local air coolers were assumed to be inoperable (refer to [48] for the modeling assumptions for PWR and BWR). A comparison of the predicted key event timings for the three selected reactor types is shown in Table 5. It is seen that the accident progression of the CANDU 6 reactor until corium relocation was considerably earlier than those for the PWR or BWR plants [48]: in the CANDU 6 plant the SG dryout occurred at 2.5 hours, the first failure of fuel channel occurred at about 4.1 hours, and corium relocation from the “suspended debris bed” to the calandria vessel bottom started at 6.4 hours. However, it is important to note that the turbine driven pump of the auxiliary feedwater system for the PWR, and the high pressure cooing injection (HPCI) and reactor core isolation cooling (RCIC) for the BWR were available in their analysis until the batteries were depleted (batteries lasted for 4 hours in PWR, and 6 hours in BWR). Nevertheless, the calandria vessel dryout in CANDU 6 occurred at almost the same time as PWR and BWR (Table 5), and the failure of the calandria vessel was delayed significantly due to the large water volume in the calandria vault.

[7] OPR-1000-like PWR, OPR-1000 is a two-loop 1000 MWe PWR designed by South Korean (KHNP and KEPCO).
[8] Peach Bottom-like BWR, i.e. BWR/4 with Mark I Containment.
[9] Wolsong-like, i.e. CANDU 6.

Table 5 Comparison of the Accident Progression of the 1000MW PWR, CANDU6, and BWR4/MARK1 for a Station Blackout Accident (unit: hours) [48]

EVENT	1000MW PWR	CANDU6	BWR4/MARK1
Battery power depleted	4.0	N/A	6.0
PSV (or LRV) open	7.3	2.6	< 0.1
SG dryout	7.5	2.5	N/A
Core uncovery start	8.5	3.7	7.7
Core melt start(PWR, BWR4) or fuel channel rupture (CANDU6)	10.2	4.1	8.9
Corium relocation start	11.7	6.4	11.8
RV (or Calandria vessel) dryout	11.9	12.8	12.0
RV (or Calandria vessel) failure	12.0	47.0	12.3
Containment (or R/B) failure	113.1	28.2	17.9

Kim et al. (2013) [49] investigated the effectiveness and/or the grace time of several mitigating actions (including SG water make-up from Dousing tank, moderator water make-up, and local air cooler) during SBO for unit 1 of Wolsong NPP using the ISAAC code. In their study, a series of sensitivity cases were simulated assuming certain mitigating system availability, and were compared to a reference case where no mitigating action was credited. The reference case was similar to the CANDU 6 case in Park et al. [48] as discussed above except with slightly different predicted event timings: the SG dryout occurred at about 2.8 hours, first channel failure occurred at about 4.0 hours, and the calandria vessel inventory was depleted at 12.2 hours. The four sensitivity cases simulated include

1) Case 1 assumed that make-up water was supplied to the SGs and the calandria vessel at 5.0 hours, and the local air cooler was inoperable. Because, the rupture of the fuel channel occurred before water make-up, the water supplied to the SGs had no effect on the accident progression. While the water supplied to the calandria vessel effectively prevented the formation of molten corium.
2) Case 2 credited SG water make-up from dousing tank at 2.0 hours (before SG dryout), while both moderator make-up and local air cooler were not credited. The large water inventory in the dousing tank delayed channel failure from 4.0 hours to 2.9 days. However, without moderator make-up core melting was not prevented (occurred at about 3 days).
3) Case 3 was identical to Case 2 except that the local air cooler was assumed available. The results confirmed that when the local air cooler was used, venting of the reactor containment was not required.
4) Case 4 established a mitigating strategy based on the results of Case 1, 2, and 3, i.e. the water make-up from dousing tank was credited within 2.0 hours, the water make-up to the

calandria vessel was established within 24 hours, and the local air cooler was credited within 48 hours. The results showed that fuel channel failure was delayed to 3.6 days, and no core melting occurred. Venting of the reactor containment was not needed, and the predicted peak containment pressure was approximately 50kPa.

2.3 RELAP/SCDAPSIM Code & Related Activities

Romania currently has two operating nuclear reactors generating about 20% of its electricity[10]. Both reactors are CANDU 6 type, located in Cernavoda NPP. Argentina has three nuclear reactors one CANDU 6 reactor in Embalse NPP, and two Siemens-designed PHWRs (Atucha 1 and Atucha 2) located in the town of Lima, Buenos Aires [11]. The Siemens design also employs the pressure tube concept and separates coolant from moderator both utilizing heavy water. The major difference between CANDU 6 and Atucha-PHWR is that the latter has vertical-oriented core (Figure 8). The three operating reactors in Argentina produce about 10% of its electricity. Argentina also has a plan to build two more nuclear power reactors, one 700MWe CANDU 6 reactor (construction is expected to begin in 2018), and one 1000MWe Hualong One PWR [50].

Researchers in both Romania and Argentina have made significant efforts to apply and/or adapt the RELAP/SCDAPSIM code (as introduced in Section 1.5.2) to severe accident analysis of their PHWRs. These studies can often be categorized into three groups, i.e. 1) full-plant simulation of the entire scenario, 2) early phase degradation/hydrogen modeling within a single fuel channel, and 3) in-vessel retention studies. Some of these studies in first two groups are reviewed below with a highlight on the modeling methodology. The in-vessel retention phase is beyond the scope of this thesis, thus will not be discussed here. The reader may refer to the work conducted by Dupleac et al. (2008) [51], Mladin et al. (2010) [32], Dupleac et al. [52], and Nicolici et al. [33] for CANDU in-vessel retention studies using the COUPLE module in RELAP/SCDAPSIM.

[10] The numbers are from the article "Nuclear Power in Romania" published by World Nuclear Association (updated October 2017).
[11] The numbers are from the article "Nuclear Power in Argentina" published by World Nuclear Association (updated May 2017).

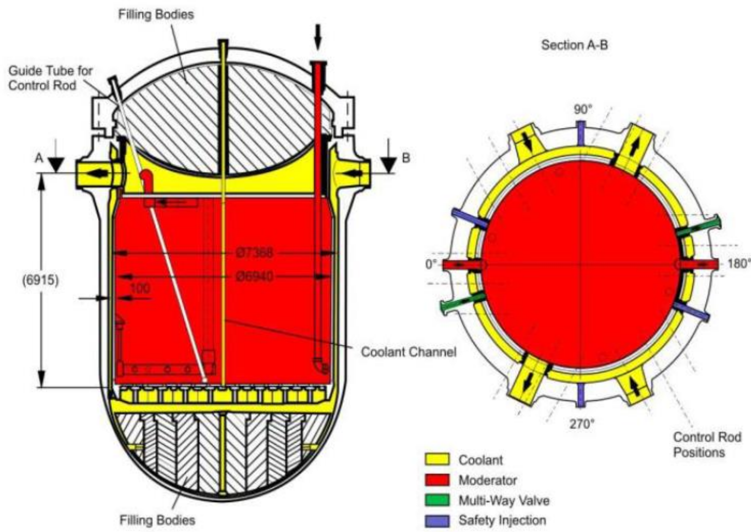

Figure 8 Atucha II Reactor Pressure Vessel (only 1 fuel channel and 1 control rod are shown) [29]

Full-Plant SBO Transient Simulations

Dupleac et al. (2009) [27] simulated an SBO scenario and a LOCA + LOECCS scenario for a CANDU 6 reactor using RELAP/SCDAPSIM (version MOD3.4). The main purpose of their study was to assess the capabilities of the RELAP/SCDAPSIM code in severe accident analysis for CANDU. The simulation was carried out in two steps covering the entire scenarios from initiating event until the failure of calandria vessel.

In the first step, a full-plant model including the PHTS, the SG secondary side and the calandria vessel was used to simulate the first stage of accident until core collapse occurred. A total of eight characteristic channels were used to represent the 380 fuel channels, i.e. two per core pass representing channels in the top and bottom half of the calandria vessel respectively. The calandria vessel was modeled as two vertical parallel pipe components each representing half of the calandria vessel volume (Figure 9). The model relied on simple threshold-type failure criteria to determine fuel channel failure and disassembly as have been discussed in Section 1.5.2 (Table 4). The core disassembly modeling adopted an approach similar to MAAP4-CANDU. However, lacking the proper models for the suspended debris bed in RELAP/SCDAPSIM the disassembled channel remained in their original position (only the mass of the suspended debris bed was tracked to determine core collapse). The second step continued the first-step simulation up to the point of calandria vessel failure using a different model developed specifically for late-phase in-vessel retention study (Figure 10). The debris and the calandria vessel wall were modeled using the

COUPLE module (i.e. 2D finite element model originally developed for PWR lower vessel problem) that was embedded in RELAP/SCDAPSIM.

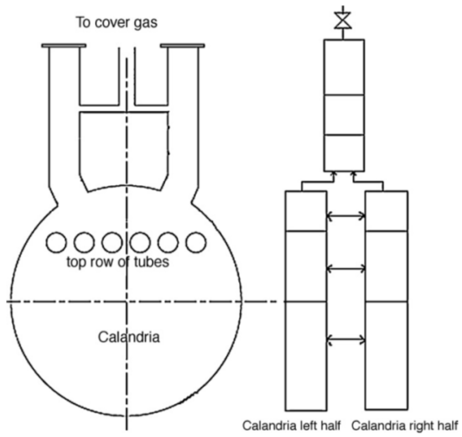

Figure 9 Calandria Vessel Nodalization in RELAP/SCDAPSIM [27]

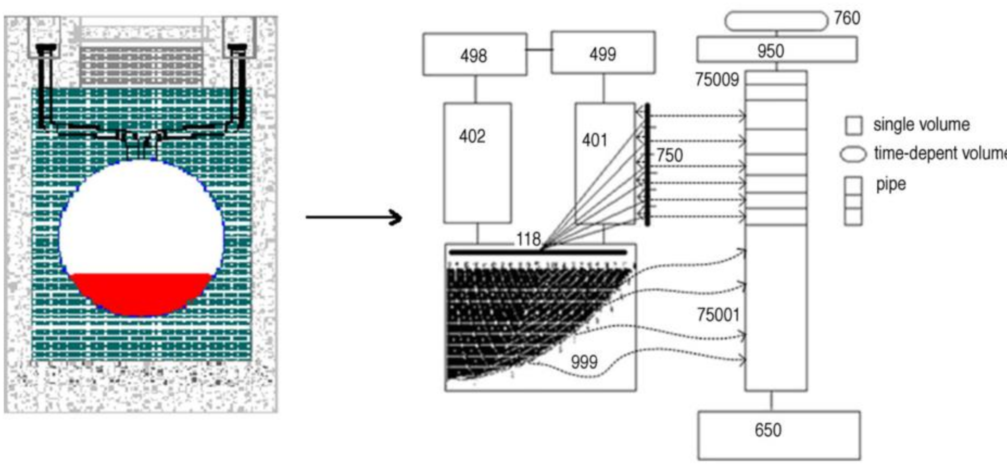

Figure 10 Later Phase Severe Accident Model in RELAP/SCDAPSIM [27]

Their RELAP/SCDAPSIM simulation results were compared to the reported results obtained with MAAP4-CANDU by Petoukhov and Mathew [38] for similar accident scenarios. In the SBO case, the agreement was very good between RELAP and MAAP4-CANDU in the predicted event timings until the SG dryout and the start of coolant relief. The first fuel channel dryout/failure occurred in RELAP at about 3.52/3.63 hours, significantly earlier than in MAAP4-CANDU (i.e. 4.34/4.41 hours), while the start of core disassembly occurred much later at 5.86 hours than MAAP-CANDU prediction (i.e. 4.81 hours). The longer duration from the first fuel channel failure to the start of core disassembly is attributed to the coarse core nodalization in RELAP.

Nevertheless, the core collapse and the failure of calandria vessel occurred at almost the same times as in MAAP4-CANDU.

The studies performed by Dupleac et al. also pointed out the areas in RELAP/ SCDAPSIM that require future improvements [27]:

1) Detailed fuel channel degradation modeling, to account for phenomena such as bundle distortion, fuel liquefaction, metallic melt relocation and re-solidification within the fuel channel.
2) Modification of the COUPLE code for a more robust treatment of the behaviors of terminal debris at the bottom of the calandria vessel.
3) Modification on shroud component (which is used to model the PT and CT) to take into account the oxidation of the outer surface (corresponding to the CT external surface);
4) Modeling of the mechanical and thermal interaction between rows of fuel channels, i.e. a more robust core disassembly model.

Improvements have already been made in the first two areas mainly by researchers in Romania (these studies are reviewed later in this section), while the rest of the problems remained. One of the objectives of this thesis is to improve the modeling of core disassembly which is addressed in Chapter 4 of this thesis.

In-Channel Fuel Degradation Modeling

Due to the differences between LWR and CANDU in fuel channel design, the fuel bundle degradation during temperature escalation has different phenomenology. For the vertical fuel assembly in LWR, the molten cladding/fuel after breaching the oxide shell will slump downward on the surface of the fuel rod, i.e. a phenomenon often referred to as “candling”. For the CANDU fuel bundle, the fuel elements will first sag into contact and fuse with each other to form a close-packed pile, i.e. bundle slumping, before significant melt relocation takes place [53]. Metallic melt on a horizontal CANDU fuel bundle will first move along the element circumference, and when encountering an inter-element contact point will be relocated from one element to another (i.e. inter-element relocation).

The fuel degradation model in SCDAP, i.e. LIQSOL (Liquefaction-flow-Solidification) model [37], was originally developed for LWR with vertical fuel assemblies, thus cannot be applied to CANDU directly. Mladin et al. (2008) [30] made the first attempt to modify the RELAP/SCDAPSIM/MOD3.4 code for the detailed modelling of fuel degradation within a fuel channel. The original LIQSOL model was modified based on experimental evidence from the high temperature bundle heat-up test conducted by Kohn et al. [53], and Akalin et al. [54]. Their model did not change the modeling methodology in LIQSOL for the initial degradation stages, including the liquefaction and the dissolution of UO_2 by molten Zircaloy, the breach of oxide shell and the formation of molten metallic drops. The modified LIQSOL, however, introduced new possibilities and allowed metallic drops to relocate from one component to another (element-to-element or element-to-PT). When a drop encountered a contact point, it split according to an input matrix which specified the component-to-component relocation fractions. This input matrix was composed according to the arrangement of components and the number of rods in each component as seen in Figure 11 (Right).

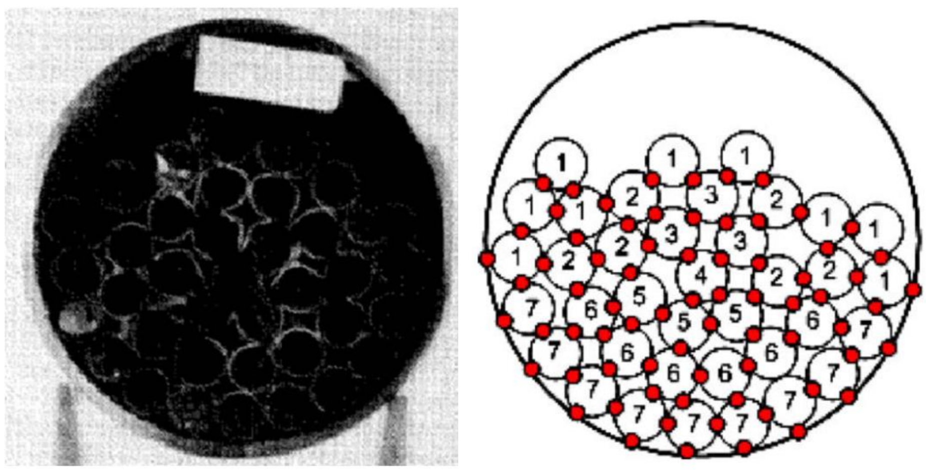

Figure 11 Slumped Bundle in Experiments [53] (Left) and Schematic of Slumped Bundle in RELAP/SCDAPSIM [37] (Right)

Additional modifications were also made to other parts of the code including the resizing of sub-channels during bundle slumping and the contact heat transfer between two contacting components. Bundle slumping was assumed to occur when the average fuel temperature exceeded a user-input threshold (1673K in their study). When the criterion was met, the fuel bundle formed a predefined “close-packed configuration”. The area and the hydraulic diameter of the pipes representing the fuel channel (including a fuel sub-channel and a bypass sub-channel) were modified automatically according to the input values. Testing of the modified code showed that allowing bundle slumping, metallic melt relocation, and contact heat transfer to occur reduced the maximum cladding temperature significantly. The modifications implemented by Mladin et al. have not been made available to other users, and due to the complexity of their models their use in a full-core simulation may not be practical. However, inclusion of these models would lead to higher fidelity predictions of oxidization rates and fuel temperatures prior to the disassembly phase.

2.4 Other Severe Accident Studies

2.4.1 Non-MAAP-CANDU Activities in Canada

Luxat (2008) [16] made a thorough discussion on three general classes of severe accidents including a total loss of all heat sink event where there was a loss of grid power, onsite standby and emergency power generators (i.e. an SBO). The early phase of the SBO sequence before fuel channel failure was divided into three phases, i.e. SG inventory depletion phase, HTS heat-up phase, and HTS inventory depletion phase. The key event timings of these phases were estimated using a number of energy balance equations with input parameters from a generic 900MWe CANDU. Two scenarios with and without crash-cooling were considered (both assumed no water make-up was credited). The calculation was generally performed in a conservative way. In the case without crash-cooldown, the four SGs with an initial inventory of 300Mg were calculated to dry out at about 4 hours. In the case with crash-cooldown, phase 1 lasted for 3.7h before SG dryout, while both phase 2 and 3 existed for longer periods. The time at which the HTS inventory was depleted to 50% of the initial inventory was estimated to be 8.4 hours in the crash-cool case as opposed to 5.76 hours in the non-crash-cool case. The calculations and discussions made by Luxat [16] for the SBO scenario with crash-cooldown were based on the assumption that passive core cooling under IBIF mode was able to continuously remove heat from the fuel channels. There is still a need to demonstrate the accuracy of this assumption by using more advanced thermal-hydraulic codes.

In Luxat's paper [16], in-depth discussions were made covering several different aspects of the accidents including the later stages (such as the moderator system response, reactor heat-up and disassembly, and in-vessel retention). Analysis was also performed to demonstrate that after HTS inventory depletion the first component to fail was a fuel channel, and that the failure of SG tubes and the resultant containment bypass were very unlikely. However, this analysis was performed based on the assumption that both the primary and secondary sides are under high pressure conditions which are more relevant for SBO scenarios without crash-cooldown. After crash-cooldown, the MSSVs stay open and SG secondary pressure will be close to atmosphere pressure. When the PHTS is repressurized the pressure difference across the SG tube will be greater than that in a non-crash-cool case thereby imposing greater risk of SG tube failure and containment bypass. A reanalysis under crash-cooldown conditions is therefore needed.

In response to the Fukushima Daiichi accident, additional provisions for water make-up to various components of the reactor systems have been implemented in the Canadian NPPs. A review of these new provisions and the current strategies in a Canadian NPP for mitigating a Beyond Design

Basis Accident (BDBA) similar to the Fukushima accident can be found in the paper by Marcoux et al. (2016) [55]. In summary, emergency water make-up with EMEs can be supplied to the SGs, the HTS, the calandria vessel, and the shield tank in the order of increasing accident severity.

To determine the effectiveness of external water make-up in accident mitigation, the CNSC has requested that Canadian Nuclear Laboratories (CNL) to model some of the water make options, in particular emergency SG make-up. Harwood and Baschuk (2015) [56] presented in their paper some of the preliminary results on the simulation of prolonged SBO with crash-cooling and SG water make-up for a generic CANDU 6 using system thermal-hydraulic code CATHENA [35]. Three SBO scenarios were examined:

1) Case 1: Prolonged SBO with no mitigation action, i.e. no crash-cool and no ECCS.
2) Case 2: Prolonged SBO with crash-cooling initiated at 15min after SBO; gravity-driven make-up water from the deaerator tank was supplied to the SGs; high pressure ECC injection was available.
3) Case 3: Same as Case 2, but high pressure ECC injection was not available.

In Case 1, the inventory of the SG was depleted at 1.9 hours, and coolant relief via LRVs commenced at 2 hours. The inlet and outlet headers became void at about 2.5 hours, immediately followed by the heat-up of fuel channel. The simulation was terminated when the maximum sheath temperature exceeded 800^{o}C shortly thereafter. In Case 2, the rapid depressurization of the SG secondary side temporarily enhanced the SG heat removal capability thereby cooling down the primary side and causing the PHTS to depressurize. ECC high-pressure injection valves were opened about 4 mins after crash-cooling. The addition of water into the HTS prevented the HTS pressure from falling below 1.8MPa. The coolant therefore remained as single phase liquid, and the system was able to maintain a primary-to-secondary-side pressure difference which was necessary for continuous natural circulation to establish. With water make-up from the deaerator tank SG dryout in Case 2 was delayed to 11.1 hours. In Case 3, high-pressure ECC injection was not available to prevent the HTS pressure from falling. The reduction in HTS pressure lowered the coolant saturation temperature causing the boiling to occur and the HTS void fraction to increase. As a result, thermo-syphoning was disrupted at about 0.7 hours and IBIF began in the fuel channel. The predicted intermittent flow, however, was too small to prevent large temperature oscillation on the fuel sheath. Maximum sheath temperature exceeded 800^{o}C at about 0.9 hours.

Examination of the coolant void distribution in Case 3 showed “liquid-hold-up” in the SG tubes, i.e. a situation where stagnant superheated vapor is in the core region and high density cold fluid is in the higher elevation SG tubes, which is believed to be responsible for the code failure in predicting steam flows and condensation in the SGs. The code behavior appears to be erroneous given the large diameter piping between the headers and the SG as well as the very large number of SG tubes, and is contrary to experimental evidence in the RD-14M and CWIT facility. Therefore, re-examination of the post-crash-cool thermal-hydraulic behavior using alternative system codes is needed.

2.4.2 COMPASS-CANDU Code (Under Development in Korea)

Most recently, KAERI (2017) [57] started a new project to develop a mechanistic severe accident code for CANDU named COMPASS-CANDU (Core Meltdown Progression Accident Simulation Software - CANDU). The COMPASS code which was developed by KAERI for severe accident analysis of Pressurized Water Reactors (PWRs) will be used as its reference code. The goals of their development project are to compete against the existing well-known severe accident codes and to achieve technical self-reliance for export without obligation[12]. The plan is to finish individual core degradation module development by 2019, and complete the construction of integral analysis code structure by 2021 [57]. While the details on COMPASS-CANDU have not been provided at the time of writing, one of the significant improvements over the existing severe accident codes is in the fuel channel modeling. Rather than using the concentric ring structure (MAAP concept) to represent a fuel bundle, a 3-D node system is utilized, and the user will be able to specify the number of fuel rods in each axial node [57]. The pressure tube and calandria tube will also be divided into multiple nodes circumferentially (Figure 12). Such fine nodalization enables COMPASS-CANDU to consider the water level in a fuel channel, and allows the fuel bundle to be uncovered gradually. It also makes the mechanistic modeling of fuel rod melt relocation, fuel rod sagging, and localized fuel channel failure become possible. None of these phenomena are modeled mechanistically in most existing severe accident codes for CANDU. The calandria vessel tank will be modeled in a similar manner in COMPASS-CANDU, i.e. utilizing 3-D node system for the 380 fuel channels in the calandria vessel to enable the modeling fuel channel sagging and melt-relocation.

[12] ISAAC or (MAAP-ISAAC) is owned by Electric Power Institute (EPRI) software program that performs severe accident analysis for nuclear power plants including assessments of core damage and radiological transport. A valid license to MAAP4 and/or MAAP5 from EPRI is required to use MAAP-ISAAC [88].

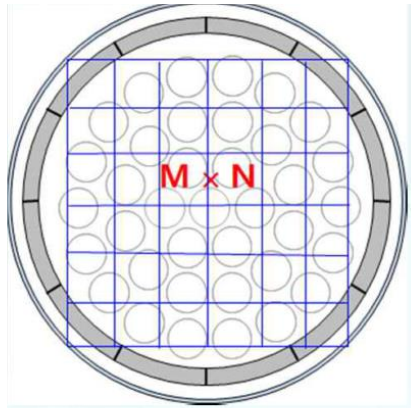

Figure 12 COMPASS-CANDU Fuel Channel Modeling Concept [57]

2.4.3 Multi-Step Approach with RELAP5 & ANSYS (India)

In India, there are a total of 22 operating reactors among which 18 of them are PHWRs [13] (CANDU derivatives). The PHWRs in India are either of 220MWe or 540MWe capacity. Overall, the Indian PHWR design is similar to that of the CANDU reactors developed by Canada. Both of them are natural Uranium fueled, pressure tube type reactors utilizing heavy water as coolant and moderator. However, there are also considerable differences between the two designs which prevent the straightforward comparison between the two on the predicted accident progression and event timings. This section thus will only discuss the methodology adopted by India for the severe accident analysis of their PHWRs.

Using the work conducted by Gupta et al. (2006) [58] as an example, a multi-step approach was used for the analysis of PHWR severe accident in India. In this multi-step approach, RELAP5/MOD3.2 was responsible for all the thermal-hydraulic calculation, and ANSYS was used to do mechanical calculations. The analysis was carried out in four steps:

1) In the first step, the RELAP5/MOD3.2 code was used to perform transient calculation from the initiating event until the moderator in the calandria vessel was depleted. The RELAP5 model includes the PHTS (Figure 13), the secondary side, the moderator system, and the reactor kinetics. The 306 fuel channels are grouped into four channels (two average fuel channels each with 152 channels, and two maximum power channels). From the RELAP5 results, the moderator level as a function of time was plotted, and was used

[13] The numbers are from the article "Nuclear Power in India" published by World Nuclear Association (updated October 2017).

to find out the channel uncovery timing (which will be used in Step 3 to determine channel disassembly).

2) In the second step, the fuel channel assembly was modeled in ANSYS as a simple beam element with two fixed ends (Figure 14). Both the load and the calandria tube temperature were varied to find out the “CT temperature at which the fuel channel failed/disassembled at a particular load” (which will also be used in Step 3).

3) In the third step, the RELAP5 simulation of Step 1 was restarted from the time when a channel was uncovered (the calandria vessel was artificially voided, and filled with steam to allow the heat-up of the uncovered channel). The time at which this uncovered channel failed was determined using the temperature disassembly criteria, i.e. “CT failure temperature vs. load relation” obtained in Step 2. This process was repeated for all the rows of channels (because the timings of channel uncovering were different for channels at different row) until the core was predicted to collapse to the bottom of the calandria vessel.

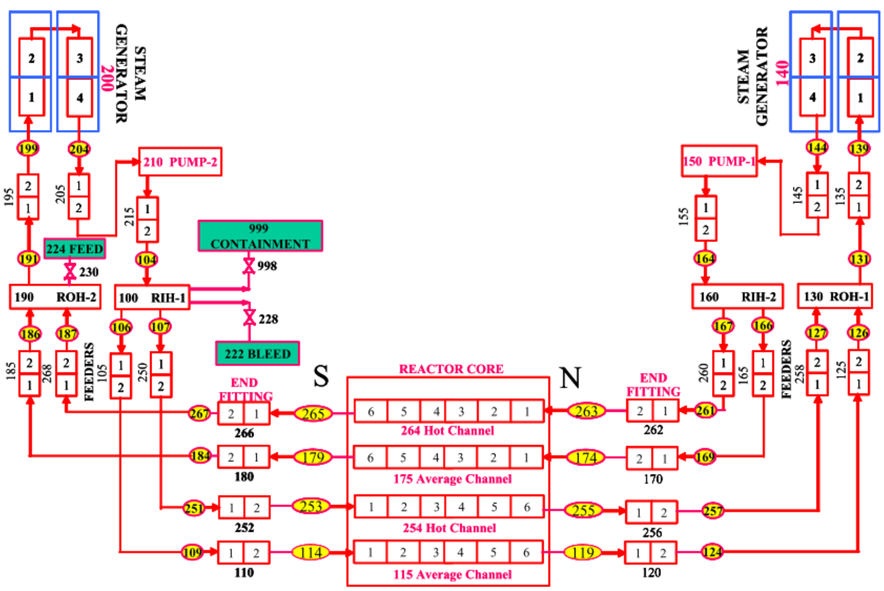

Figure 13 Nodalization of Primary Heat Transport System [58]

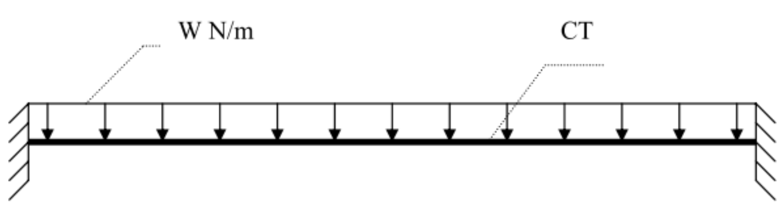

Figure 14 Schematic Diagram of ANSYS Model [58]

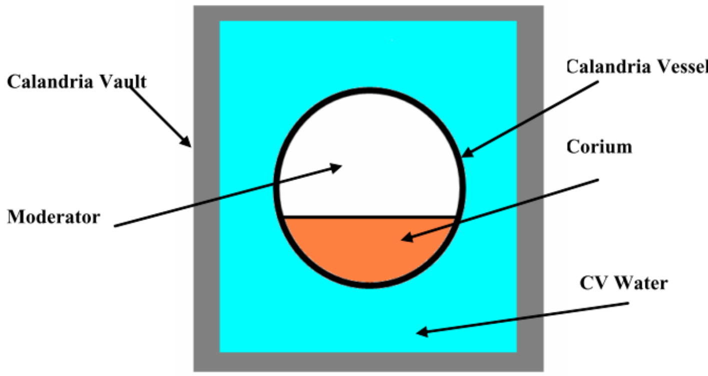

Figure 15 Schematic of Calandria Vault Modeling for Step Four [58]

Figure 16 Schematic of Corium Modeling in RELAP5 [58]

4) In the last step, the corium, the calandria vessel and the calandria vault were modeled using RELAP5/MOD3.2 (Figure 15). The corium and the part of the calandria vessel that is in contact with the corium was modeled one corium heat structure as seen in Figure 16. Heat generated in the corium was removed by the remaining water in the calandria vessel through its top surface and/or by the water in the calandria vault via the bottom surface. The fluid conditions in calandria vessel at the time of core collapse were used as initial condition of this step.

This multi-step approach overcomes the limitation the RELAP5 code in modeling severe accident phenomena. Several key phenomena, i.e. the boil-off of moderator, the disassembly of fuel channels, and in-vessel retention, are addressed in different steps. Such approach is simple and straightforward as it does not require two-way coupling between each step. Rather, the computed data of one step is used directly as boundary/initial conditions of another step without feedback or iteration. This approach, however, neglects the potential interactions amongst these phenomena, and introduces additional modeling uncertainties. For example, the heat-up and disassembly of fuel channels interacts strongly with the moderator level since the relocation of suspended debris into the remaining moderator may cause a sudden moderator loss through expulsion surges. Furthermore, given that only four characteristic channels were modeled, the moderator heat load was likely to be overestimated.

3. Simulation of Early Phase with RELAP5

About This Paper

Citation:

F. Zhou and D. R. Novog, "RELAP5 Simulation of CANDU Station Blackout Accidents with/without Water Make-up to the Steam Generators," *Nucl. Eng. Des.*, vol. 318, pp. 35–53, 2017. DOI: 10.1016/j.nucengdes.2017.04.014

Contribution to Knowledge

The objective of this paper was to use a full system thermal-hydraulic code to model the early stages of an SBO and assess the impact of various operator or emergency equipment actions of station response. During this phase of the transient full system-level simulations are needed including various control systems. As such simulation with RELAP5 of the entire primary, secondary and support systems is superior to the coarse nodalization provided in MAAP-CANDU. Of particular importance is the assessment of low-pressure IBIF phenomena during the majority of this phase of the event, in particular given the results reported using other system codes such as CATHENA.

The RELAP5 model was developed based on the SOPHT input for Darlington NGS [20], as well as the work by P. Sabouri [11]. This paper presented results on the benchmarking of RELAP5 model against the station measurements in a Loss of Flow event of an operating 900MWe CANDU in order to first provide some level of validation for the full plant model. The thermal-hydraulic behaviours during the early stage of the event and post-crash-cooling, the mechanism of the predicted intermittent natural circulation flows, and the sensitivity to various modelling parameters (such as the timing of operator actions) were then thoroughly investigated. The results of the case without crash-cooling agreed well with the reported MAAP4-CANDU predictions although the level of detail provided by RELAP5 was superior (e.g. fuel sheath temperatures and interchannel flows). The results of the cases with crash-cooling showed that the SG heat removal after crash-cooling is sufficient in removing the decay heat from the core and ensuring fuel/fuel channel integrity. The paper thus demonstrated that the current safety practice in the event of an SBO (i.e. credit crash-cool and maintain SG inventory through water make-up) is effective in delaying (or terminating) accident progression.

<u>Author's Contribution to Paper:</u>

The author (F. Zhou) is the primary contributor to this paper. The RELAP5 model was developed primarily by Zhou with guidance from the co-author (D.R. Novog). Model executions were carried out entirely by Zhou. Analysis of the results was performed primarily by Zhou with guidance from the co-author. Writing of the draft paper was done primarily by Zhou. The co-author also contributed significantly to the editing of this paper. The paper was submitted to Nuclear Engineering and Design in middle Nov., 2016, and was accepted in early April, 2017 after one minor revision.

Nuclear Engineering and Design 318 (2017) 35–53

Contents lists available at ScienceDirect

Nuclear Engineering and Design

journal homepage: www.elsevier.com/locate/nucengdes

RELAP5 simulation of CANDU Station Blackout accidents with/without water make-up to the steam generators

Feng Zhou *, David R. Novog

Department of Engineering Physics, McMaster University, 1280 Main Street West, Hamilton, ON L8S 4L7, Canada

HIGHLIGHTS

- Benchmarking RELAP5 against Loss of Flow measurements from an operating 900 MW CANDU reactor.
- Prediction of Station Blackout response with and without operator action credits.
- Assessment of continuous and intermittent natural circulation heat sinks.
- Role of passive water supplies on event timing and emergency response times.

ARTICLE INFO

Article history:
Received 14 November 2016
Received in revised form 6 April 2017
Accepted 7 April 2017

Keywords:
CANDU
Station Blackout
Crash-cooling
RELAP5
Thermal hydraulics
IBIF

ABSTRACT

In the event of a complete Station Blackout (SBO) of a CANDU reactor, the current safety practice is to initiate depressurization early in the transient once a lack of power has been declared. This requires operator actions to manually open the main steam safety valves (MSSVs) on the secondary side initiating a crash-cool procedure. The depressurization of the secondary side allows make-up water to be supplied to the steam generator (SG) secondary-side thereby extending natural-circulation driven heat removal from the fuel in the primary heat transport system. Once depressurized there are several additional water sources available to replenish the secondary-side inventory, and in the event that emergency power cannot be restored emergency mitigating equipment (EME) are available to provide alternative water make-up. The objective of this paper is to examine the processes and phenomena involved during and after crash-cooling and compare these results to cases where operator actions are not credited. Simulations are performed until such time as the secondary-side inventory is stabilized from alternative water sources or until it is depleted.

A detailed RELAP5 model of a 900 MW CANDU plant has been created including the primary heat transport system (PHTS), the feed and bleed system, the steam generator secondary side, the moderator system, and the shield water cooling system. The 480 fuel channels were grouped into 20 channels by elevation and channel power. The models were benchmarked against the 1993 loss-of-flow event at Darlington NGS and agreed with the station data within the reported measurement uncertainty. Then the models were used to simulate the Station Blackout accidents with loss of class IV, class III, and emergency power supplies. Five different scenarios with/without crash-cool and with different water make-up options are modeled and key sensitivities determined. The results show that the depressurization of the secondary side may create a situation where continuous natural circulation breaks down and intermittent buoyancy induced flows (IBIF) takes place. The RELAP5 predicted IBIF phenomena are discussed, as well as the limitations of the current RELAP5 code. The main focus of this paper is on the early stage of the accidents, i.e. when adequate steam generator secondary side inventory exists and where damage to the main heat transport system can be precluded. The results demonstrate that EME actions to maintain SG inventory are effective and ensure fuel and fuel channel integrity.

1. Introduction

The CANDU® reactor (CANada Deuterium Uranium) is a pressure-tube type reactor using natural uranium as fuel and separate coolant and moderator systems utilizing heavy water.

* Corresponding author.
E-mail address: zhouf5@mcmaster.ca (F. Zhou).

http://dx.doi.org/10.1016/j.nucengdes.2017.04.014
0029-5493/

Nomenclature

AECL	Atomic Energy of Canada Limited
ASDV	Atmospheric Steam Discharge Valve
BC	Bleed Condenser
CANDU	CANada Deuterium Uranium
CCFL	Counter Current Flow Limit
CNSC	Canadian Nuclear Safety Commission
CSDV	Condenser Steam Discharge Valve
CT	Calandria Tube
CWIT	Cold Water Injection Tests
DEA	Deaerator
ECCS	Emergency Core Cooling System
EME	Emergency Mitigating Equipment
EPS	Emergency Power Supply
ES	End Shield
ESV	Emergency Stop Valve
EWS	Emergency Water Supply
IBIF	Intermittent Buoyancy Induced Flow
IF	Inlet Feeder
LOF	Loss of Flow
LRV	Liquid Relief Valves
MCA	Mechanical Control Absorbers
MSSV	Main Steam Safety Valve
NGS	Nuclear Generating Station
OF	Outlet Feeder
PHTS	Heat Transport System
PT	Pressure Tube
RIH	Reactor Inlet Header
ROH	Reactor Outlet Header
SBO	Station Blackout
SDS	Shutdown System
SG	Steam Generator
SGECS	SG Emergency Cooling System

The reactor is divided into two identical primary heat transport loops each in a figure of eight arrangement with each loop having two alternating-direction core passes. The two loops are connected via small diameter piping to the pressurizer, and they can be isolated by closing the loop isolation valves. A 900 MW CANDU has a total of 480 horizontal fuel channels with 120 fuel channels per core pass. Each fuel channel consists of a Zr-2.5%-Nb pressure tube (PT) surrounded by annulus insulating gas and a Zr-2 calandria tube (CT). Coolant from each Class IV powered primary circulation pump is distributed to the channels via an inlet feeder and feeder pipes. Outlet feeders connect the channel outlets to the reactor outlet headers which are connected to the steam generators. Four large steam generators (one per core pass) transfer heat to the secondary side system. Power is normally supplied to key cooling systems through Class IV power (supplied by station or grid transformers) or Class III power (via Class IV or from standby generators). In addition the Emergency Power Supply (EPS), Emergency Water Supply (EWS) and Emergency Mitigating Equipment (EME) are available for implementing emergency measures.

The calandria tubes are contained in a large horizontal calandria vessel which is filled with heavy water acting as moderator. Under normal operating conditions about 5% of the fission power produced in the core is deposited into the moderator. The moderator cooling systems circulates the moderator to the main moderator heat exchangers where the heat is transferred to the recirculated cooling water system. The moderator system pressure is regulated via the cover-gas system and associated relief valves, and through rupture disks which prevent significant overpressure. The calandria vessel is contained within the shield tank in which a large volume of light water is used to provide biological shielding in the radial direction. Axial biological protection on both reactor faces is provided by the end shields which are filled with steel-balls and light water. The heat lost to the end shields as well as to shield tank is removed by a separate cooling circuit. Both the moderator cooling pumps and shield cooling pumps are powered by Class III power to ensure rapid restoration of circulation following a loss of Class IV power (Jiang, 2015).

The CANDU reactors have multiple heat sink provisions depending on the availability of systems, components and electrical power. In accidents where the PHTS remains intact but electrical systems are compromised, e.g. a SBO, continuous and/or intermittent natural circulation within the primary system allows heat from the relatively low elevation core components to circulate to the cooler steam generators providing an effective heat removal pathway provided that there is sufficient water in the steam generator shell side. The normal water inventory of the four steam generators in the 900 MW Darlington NGS is 340 Mg ± 10% which can provide 4–6 h of post-shutdown cooling (Blahnik and Luxat, 1993; Luxat, 2008). Several options for water make-up to the SGs are available including internal water sources such as the auxiliary feedwater pumps running under standby or emergency power supplies, stored inventory in the deaerator tank, or external water source makeup. The addition of water to the SGs can extend thermo-syphoning in the PHTS thus providing additional time for operators to take mitigating actions.

In a generic 900 MW CANDU the auxiliary feedwater pumps powered by Class III power can maintain SG inventory. The deaerator tank which has normal inventory of about 320 Mg may also provide makeup as it is one of the highest elevation vessels in a CANDU reactor system. If crash-cool of the steam generators occurs the associated depressurization of the secondary side will allow water in the deaerator tank to flow by gravity into the SGs (Harwood and Baschuk, 2015). Crash-cooling is an emergency procedure in CANDU to rapidly reduce the pressure of the SGs by the opening of main steam safety valves (MSSVs). The EWS powered by EPS may also provide inventory to the SGs after crash-cool. Depending on the specific CANDU design, emergency water may be supplied by gravity via the dousing tank and in others via pumping from the EWS. Furthermore, some stations, e.g. Darlington NGS, have a SG emergency cooling system (SGECS) consisting of two air accumulators pressurized by instrument air and two water tanks with each tank and an accumulator suppling two steam generators (Wu, 1993). Both the SGECS and the gravity-fed reserve water system are designed to provide interim water supply to the SGs following the steam line rupture and/or the loss of feedwater supply. After the Fukushima Daiichi accident additional provisions have been implemented in the Canadian NPPs including the EMEs such as portable pumps and power generators. With EMEs external make-up water can be supplied to the steam generators and/or to the calandria vessel.

In a SBO accident the loss of electrical power and service water will disable all active heat sinks including the feedwater system, the EWS system, the shutdown cooling system, the feed and bleed system, and the Emergency Core Cooling System (ECCS) (if pumps are used for the high-pressure injection). The moderator cooling and shield water cooling systems are also lost. However, the water in the SGs and deaerator tank, the moderator in the calandria vessel and the shield water inventories are temporary passive heat sinks that can delay the accident progression for an appreciable time. The primary heat sink in an SBO accident would initially be the SGs. Due to the high elevation of the SGs continuous natural circulation is established shortly after the coast-down of the PHTS pumps and will continue until the secondary-side SGs dry out. If the operators initiate crash-cooling, the rapid reduction in secondary-side pressure and temperature will temporarily enhance heat removal from the primary side thereby further cooling the PHTS. The rapid cooldown of the PHTS results in coolant shrinkage which causes the primary side to depressurize. If the ECCS is not available to prevent the PHTS pressure from falling, the effectiveness of SG heat removal may become impaired leading to the breakdown of continuous natural circulation (Harwood and Baschuk, 2015). The coolant in the horizontal fuel channels may then enter a mode of natural circulation called Intermittent Buoyancy Induced Flow (IBIF). IBIFs have been observed experimentally, e.g. in the RD-14M tests (Ingham et al., 2000), in the cold water injection tests (CWIT) McCallum and Wedgwood, 1996, and other experiments (Karchev and Kawaji, 2009). The IBIFs in the CWIT experiments have been simulated using thermal-hydraulic code GOTHIC (Spencer, 2010). Analysis has also been performed to assess the fuel fitness-for-service after repeated IBIF cycles during maintenance outages in CANDU (Lei and Gulshani, 1998). Provided this intermittent natural circulation is sufficient to remove the decay heat from the core, heat removal will persist as long as there is secondary-side inventory.

Blahnik and Luxat (1993) carried out a simulation of the loss of all heat sinks (crash-cooling was not credited) for a 900 MW CANDU using an early version of the severe accident code MAAP-CANDU. A key assumption was that the system remained at high pressure and crash-cooling was not initiated. Their results showed that the SGs inventory was depleted between 5 and 6 h after the onset of SBO, and the coolant pressure relief via the relief valves commenced at about 6 h. Reactor headers became voided at around 6.5 h, and fuel channel ruptured at 8.4 ± 1 h.

Luxat (2008) discussed three general classes of severe accidents in CANDU including the loss-of-coolant-accident initiated events, the loss of shutdown events and the loss of all heat sink events. The event timings in the total loss of heat sink accidents were calculated using the energy balance equations for a typical 900 MW CANDU plant. For the case without crash-cooling, the calculated SG dryout time was at 4.0 h, the PHTS inventory depleted at 5.76 h, and the moderator started boiling at about 7.2 h. For the case with crash-cooling, the SG pressure was assumed to be at or below 800 kPa, and the PHTS at slightly higher pressure with a temperature of 170 °C. Because water make-up to the SGs was not credited, the SG was calculated to dryout at 3.7 h. However, the time to PHTS inventory depletion was significantly later (8.4 h) as larger stored heat must be delivered to the coolant and metal mass in the PHTS to replace the heat removed during cooldown.

Petoukhov (2014) simulated two SBO scenarios for CANDU 6 with and without water make-up from the dousing tank using MAAP4-CANDU. In the case with SG water make-up crash-cooling was initiated on low SG level (<7.5 m) by opening the MSSVs. The valves connecting the dousing tank and SGs were opened by operator actions when the SG level was less than 8.0 m and closed when greater than 10.0 m. In the reference case without water make-up, the SGs emptied at 2.65 h; while in the case with water make-up the SG U-tubes remained covered for over 139 h due to the very large inventory in the dousing tank. However, the HTS model in MAAP4-CANDU is relatively simple (Blahnik, 1991) lacking detailed channel and HTS components, and the paper does not show conclusively that the IBIF mode of heat removal after crash-cooling can effectively remove heat from the core.

System code simulations of SBO transients in CANDU with operator initiated crash-cool are less frequently studied. Most recently, Harwood and Baschuk (2015) modeled an extended SBO for CANDU 6 using system code CATHENA (Hanna, 1998). In their paper, three scenarios were examined: in the reference case no mitigation action was taken, i.e. no crash-cool and no ECCS; in the other two cases crash-cooling was initiated at 15 min after SBO (make-up water from the deaerator tank), and in one of them the high pressure ECCS was also credited. In the reference case, the breakdown of thermo-syphoning occurred at 2 h due to U-tube dry-out. In the crash-cool case with ECCS, the ECC injection kept the PHTS pressure high after crash-cool. Single phase thermo-syphoning was maintained until the SG dry-out at 11.1 h. However, in the crash-cool case without ECCS, these simulations show that after the break-down of continuous thermo-syphoning at 0.7 h intermittent flow phenomena were not sufficient to prevent large temperature oscillation on the fuel sheath. The transient was terminated at 0.9 h when the maximum sheath temperature exceeded 800 °C. The code behavior was attributed to the predicted "liquid-hold-up" phenomenon wherein void generated in the core did not provide sufficient buoyancy induced flow to penetrate the steam generators creating a situation with stagnant superheated vapor in the core region and high density cold fluid in the higher elevation SG tubes. Given the large diameter piping between the headers and the SG as well as the very large number of SG tubes, the failure of the code to predict steam flows and condensation in the SG is erroneous and contrary to experimental evidence in the CWIT facility. Hence there is need to examine the behavior using alternative system codes.

The RELAP5 code (Systems Laboratories, 2010) has been used for CANDU reactors in several cases with some validation against CANDU-related experimental data (e.g. the RD-14M tests) and code-to-code comparisons with CATHENA (Kim et al., 1995; Atomic Energy Agency, 2004). The RELAP5/SCDAP code (Allison and Hohorst, 2010) which is an integration of RELAP5, SCDAP (severe accident) and COUPLE code (lower vessel phenomena) are being used by Romania (Dupleac et al., 2009), China (Tong et al., 2014), and Argentina (Bonelli et al., 2015) in the safety analysis for CANDU reactors. However, the use of RELAP5 code to simulate a SBO transient with crash-cooling has not previously been documented, and in particular its capability of modeling IBIF phenomena has not been demonstrated under these conditions. This work provides new results on the application of RELAP5 to such scenarios and examines the features of these predictions during natural circulation phenomena.

The main purposes this study are to simulate a postulated extended SBO accident for a 900 MW CANDU using RELAP5/MOD3.3 code, to examine the effectiveness of SGs heat removal after crash-cooling and that of several water make-up options, and to assess the capability of RELAP5/Mod3.3 code in predicting the low-pressure natural circulation phenomena.

2. RELAP5 model for a 900 MW CANDU plant

A detailed RELAP5 model of a generic 900 MW CANDU plant has been created using RELAP5/MOD3.3. This model includes the PHTS, the feed & bleed system, the secondary side, the moderator system, and the shield water cooling system. In addition it includes models of a SGECS and deaerator flow path so that the effects of operator initiated crash-cooling on SBO performance can be assessed.

The nodalization of PHTS and part of the feed & bleed system are shown in Fig. 1. Various control systems are added into the current model to obtain the steady-state initial conditions of the sys-

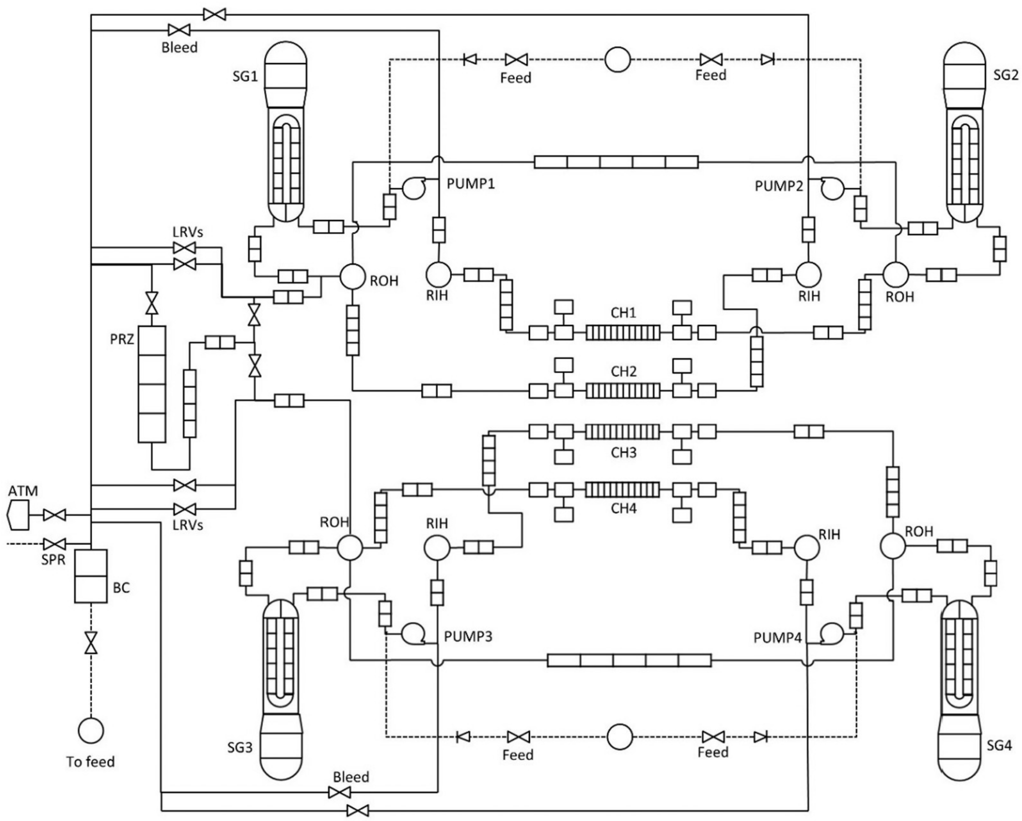

Fig. 1. Nodalization of the Heat Transport System (4-group model).

tems. The pressurizer heaters and steam bleed valve control the reactor outlet header (ROH) pressure at a setpoint of 9921 kPa. When the ROH pressure exceeds 10,551 kPa, the four PHTS liquid relief valves (LRVs) open discharging coolant to the bleed condenser. The pressurizer level is maintained at 6.5 m by controlling the feed and bleed valves. The bleed condenser pressure is controlled at 1720 kPa by varying the feed and bleed flow as well as the reflux flow, and its level is controlled at about 0.9 m via the level control valve. When the temperature downstream of the bleed cooler exceeds the set-point, the bleed condenser level control valve will be forced close. The bleed condenser also has a spray valve and a pressure relief valve with a pressure set-point of 1891 kPa and 10,270 kPa respectively.

The nodalization of steam generator secondary side and the SGECS is shown in Fig. 2. The deaerator tank, the turbine and the condenser are modeled as time-dependent volumes. The feedwater pumps are modeled as pump components with the appropriate affinity curves while the auxiliary feedwater pump is simplified as a time-dependent junction connected to a time-dependent volume. In cases where the Class III power is available the auxiliary feedwater pump is capable of supplying 3% of full-power feedwater flow. Under normal operating conditions the SG level is maintained at 14.4 m using three-element logic control, i.e. the actual level, the steam flow and the feedwater flow are used to determine the gain applied to the feedwater control valves. At full-power steam generator secondary side pressure is controlled at 5050 kPa by adjusting the opening of governor valve. The atmospheric steam discharge valve (ASDV), the condenser steam discharge valve (CSDV), and the MSSVs are designed for pressure relief and over-pressure protection of the secondary side. The SGECS tank and the air accumulator are modeled as a time-dependent volume with constant pressure. When the SG pressure drops below 963 kPa, the SGECS valves open and water is injected into the steam drum. A check valve is used to prevent flow reversal. Each SGECS tank has a volume of approximately 70 m^3. The amount of water leaving SGECS tank is integrated throughout the RELAP5 transient, and the RELAP5 SGECS flow terminates once the total volume of water leaving the tank exceeds 70 m^3. The external water supply by EME is similarly modeled except the water supply can continue indefinitely.

The 480 fuel channels in a 900 MW CANDU are arranged in 24 columns and 24 rows. Channels of the two loops are symmetric with respect to the vertical plane parallel to the calandria axial. To overcome memory constraints in RELAP5 each core pass is simulated using a number of representative channels. The number of these average channels and the grouping scheme used to accurately represent the core are accident dependent. For the early-phase of a SBO transient where natural circulation effectiveness is the main focus, channel elevation and power may be the two most important parameters to consider since static head and decay power levels are likely to be the most sensitive factors contributing to flow. In particular during intermittent buoyancy induced flow channels at higher elevations are more likely to experience flow reversal because they have smaller elevation changes (from channel to header) thus smaller driving forces resulting from the density difference between the hot and cold legs (inlet and outlet feeder pipes).

To examine the sensitivity of the results to channel grouping, three different grouping schemes are used, i.e. the 480 channels are represented by 4, 8 and 20 characteristic channels respectively. In the 4-group model, each core pass is represented by an average channel and no channel elevation effects are modeled. In the 8-group model each core pass has two representative channels and as such the upper and lower half (Fig. 3) elevations are included.

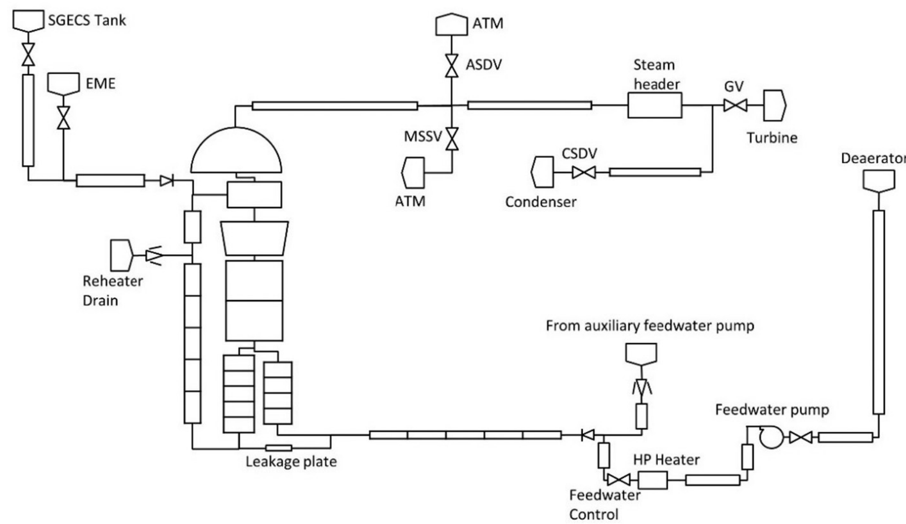

Fig. 2. Nodalization of the SG secondary side.

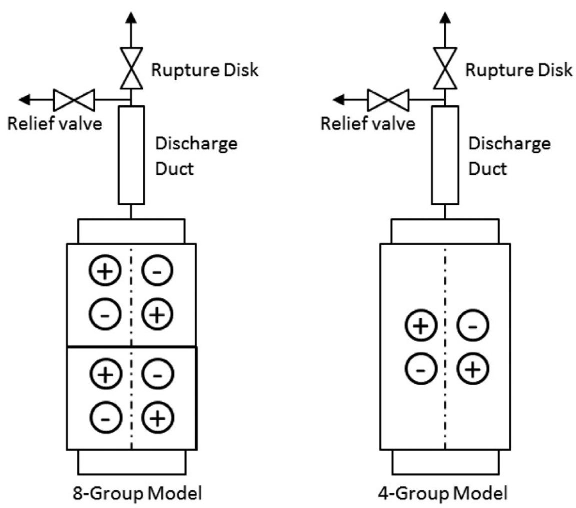

No. of GPs	Loop	Pass	Code	No. of CHs	Power Av. (kW)
8	1	1	1T	61	5514.0
			1B	59	5494.8
		2	2T	59	5581.5
			2B	61	5465.2
	2	3	3T	59	5600.7
			3B	61	5484.0
		4	4T	61	5532.9
			4B	59	5513.6
	Total			480	2651MW
4	1	1	CH1	120	5504.6
		2	CH2	120	5522.4
	2	3	CH3	120	5541.4
		4	CH4	120	5523.4
	Total			480	2651MW

Fig. 3. Nodalization of calandria vessel and channel grouping scheme (8-group and 4-group models).

Fig. 4 shows the current grouping scheme of the 20-group model. In loop 1, there are a total of five vertical elevations considered, three in the upper half of the core and two in the lower half. Each core node in the upper half of the core is subdivided into two power groups for each core pass. Loop 2 requires only minimal resolution due to core symmetry, and thus has four characteristic channels which are the same as those in the 8-group model. Figs. 3 and 4 also include tables summarizing the number of channels and the average channel power of each group. Beyond the natural circulation phenomena discussed in this paper, it is desirable to maintain the nodalization for subsequent analyses where steam generator inventory is depleted and the moderator may become the heat sink. During this later stage of the accident channel elevation, moderator and end-shield water levels, and shield tank phenomena may also be required and the 20-channel grouping scheme considered here may still be used.

The calandria vessel is modeled as a vertical pipe component with 3, 4, 7 hydraulic cells for the 4, 8, 20-group model respectively (Figs. 3 and 4). While the calandria vessel is a horizontal cylinder, the current limitations on tracking liquid level in such a configuration in RELAP5 required the vessel to be simulated as a vertical cylinder with non-uniform diameter. The diameter, volume and flow area of the hydraulic cells in the calandria are carefully calculated so that the volume as a function of elevation is preserved. The four large moderator relief ducts are modeled as an average pipe component linked to the top of the vessel. The duct volume also accounts for the moderator head tank volume. The four rupture disks at the ends of the relief ducts are modeled in RELAP5 as a trip valve with the same total area and a set-point of 239 kPa.

The moderator relief valve is designed to prevent the moderator and cover gas pressure from exceeding 165 kPa while the rupture disks provide additional relief capability at 239 kPa. In the current model, the cover gas system is represented as a pipe component connected to the discharge duct. The remainder of the moderator and cover gas systems is not modeled since moderator and cover gas circulation is lost as a consequence of the SBO. The shield tank and the end shields are both modeled as pipe components in a similar way as the calandria vessel (i.e., as a non-uniform diameter vertical pipe). A heat structure representing the end fitting and the lattice tube is used to model the heat loss from the fuel channel to end shield. In the current model, there are also heat structures representing the inner tube sheet, the calandria shell, and the steel balls inside the end-shields so that the individual contributions to the heat sink can be assessed.

40 F. Zhou, D.R. Novog / Nuclear Engineering and Design 318 (2017) 35–53

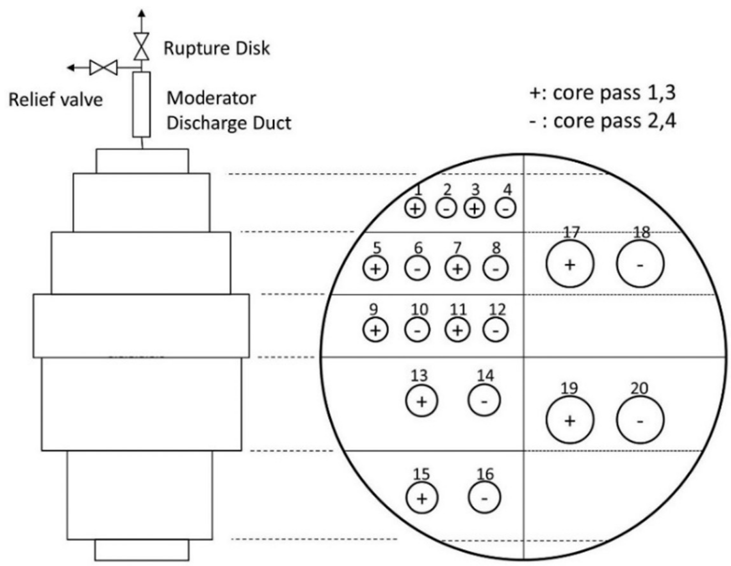

Loop	Pass		Code	No. of CHs	Power Av. (kW)
1	1	1	1T1	10	4218.7
		3	1T2	5	5976.6
		5	1T3	11	6153.1
		7	1T4	11	4971.5
		9	1T5	12	6365.6
		11	1T6	12	5460.4
		13	1B1	35	5853.6
		15	1B2	24	4971.5
	2	2	2T1	9	4281.6
		4	2T2	5	5907.4
		6	2T3	10	5141.2
		8	2T4	11	6171.3
		10	2T5	12	5465.9
		12	2T6	12	6362.6
		14	2B1	35	5916.9
		16	2B2	26	4857.2
2	3	17	3T	59	5600.7
		19	3B	61	5484.0
	4	18	4T	61	5532.9
		20	4B	59	5513.6
Total				480	2651MW

Fig. 4. Nodalization of calandria vessel and channel grouping scheme (20-group model).

Fig. 5 shows the cross-section of a typical CANDU fuel channel. The 37-element fuel bundle is modeled as one RELAP5 heat structure, i.e. all the fuel elements of the same bundle are assumed to have the same average power. The PT-CO_2-CT is modeled as one heat structure with three layers of materials, i.e. Zr-2.5%Nb, CO_2, and Zr-2. In the current version of RELAP5, the radiation heat transfer model only allows radiation to occur among external surfaces of heat structures. To model the radiation across the PT-CT annulus, i.e. between the outer surface of the PT and the inner surface of the CT, the model is input in a way that the inner surface of the PT will artificially irradiate on the outer surface of the CT. This approach is expected to cause acceptable error because of the small difference in surface temperature between the inner and outer walls of the pipes and the small thickness of pipe wall compared to its radius. The radiation heat transfer among the 37 fuel sheaths and the inner surface of PT is also modeled. The individual element view factor matrix is calculated by GEOFAC (Hedley and Chin, 2007), and is then lumped into a view-factor matrix between two surfaces (i.e., the PT and all fuel sheaths). The emissivity of fuel sheath, pressure tube, and calandria tube used in the current model are 0.25, 0.25, and 0.2 respectively which are for unoxidized Zircaloy (Mathew, 1989). Sensitivity studies on emissivity are also performed.

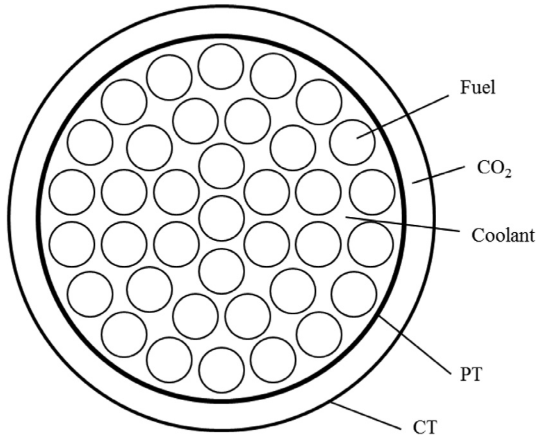

Fig. 5. CANDU fuel channel.

The ANS79-3, i.e. 1979 ANS Standard data for daughter fission products of U-235, U-238 and Pu-239, is used for modeling fission product decay. The relative heat load distributions used in the current model are calculated based on the reported values for CANDU 6 (Aydogdu, 2004) and are summarized in the Table 1. Of importance is the change in the relative power deposition to various systems under decay heat as compared to normal full power loads. For example, all energy from actinide decay is deposited into the coolant because the low-energy gamma photons (e.g. from actinide decay) are more likely to be thermalized within the channels (Whittier et al., 1977). The nature of actinide decay time constants therefore drive an increase in the relative heat load in the channel as compared to other components during the evolution of the event. The changes in relative heat loads from fission products and actinide decay is considered as a function of time in this work.

CANDU reactors have two independent shutdown systems (SDS): SDS1 consists of mechanical shutdown rods; SDS2 injects gadolinium nitrate into the moderator. In the current model, only the SDS1 is modeled. The mechanical control absorbers (MCAs) are also modeled and actuated on a turbine trip signal to initiate a reactor stepback. The relevant control logic and safety system setpoints used in the model are summarized in Table 2 (Wu, 1993).

3. LOF event at Darlington – model benchmarking

3.1. Modeling assumption of the LOF event

The 1993 Loss of Flow event (LOF) at Darlington Unit 4 is simulated using the RELAP5 model. This event was caused by a switchyard transformer failure resulting in the loss of class IV power. Details about the event can be found in the international agreement report by Naundorf et al. (2011). In their report, this event has already been simulated using RELAP5/MOD3.3, and the predic-

Table 1
Heat loads in the 900 MW CANDU model.

	Fission	FP Decay	Actinides Decay
To Moderator	4.202%	8.752%	0%
To Shield Water	0.181%	0.198%	0%
To Coolant	95.617%	91.050%	100%
Total	100%	100%	100%

Table 2
Reactor trips in the 900 MW CANDU model.

Reactor Trips	Trigger Signal	Set Point	Delay
SDS1 Trip 1	Neutron Power	1.14 frac nom	0.1 s
SDS1 Trip 2	Power Log Rate	10%FP/s	0.1 s
SDS1 Trip 3	Inlet Feeder Flow	0.71 frac nom	0.3 s
SDS1 Trip 4	ROH pressure	10,700 kPa	0.3 s
Stepback	Turbine Trip	Power to 60%	0.5 s

tions agreed well with the station measurements. However, the model details and nodalization were not provided in literature. The purpose of reproducing their work is to validate the current 900 MW CANDU model. In addition the event sequences in this LOF event are very similar to those in the early stage of a SBO. Thus the simulation results and the system response in this event are highlighted here.

The following assumptions are made when simulating the LOF event:

1) Loss of Class IV power occurs at time zero and coincident with a turbine trip.
2) The four HTS pumps, the feedwater pumps, and the D_2O feed pump all tripped at time zero.
3) The period of interest is from 0 s to 80 s. In such a short time period, heat removed by the moderator and shield water is negligible therefore their heat removal is not modeled in detail and assumed fixed at their pre transient value.
4) The auxiliary feedwater pump is started on class III power 2 s after the initiating event.
5) Following the turbine trip a reactor power stepback is initiated to 60% by inserting the MCA with a delay of 0.5 s.
6) ASDVs are available and actuate according to their control logic. The CSDVs are available until the condenser vacuum was lost at 13.5 s.
7) Pressurizer steam bleed valve and LRVs are available.
8) The reactor is tripped when any of the trips in Table 2 are triggered.
9) Consistent with Naundorf's work (Naundorf et al., 2011), the temperature override of the bleed condenser level control valve is masked so that the valve stays open.
10) No emergency stop valve (ESV) is present in the current model. The closing of ESV is modeled by closing the governor valve with a closing time of 0.2 s and a delay of 0.08 s.

3.2. Results of LOF event

Results are shown in Fig. 6 through 10 while Table 3 gives the predicted event timings compared to the station measurements. Results are provided for the RELAP5 model (with 9 channel groups) by Naundorf et al. (2011) and for the present 4 and 8-channel group models, while those of the 20-group model are not presented since no observable differences occur in this time frame between the 20 and 8 channel groups for this benchmark. The transient is initiated by the loss of Class IV power. The coolant flow rate gradually decreases as the PHTS pumps rundown (Fig. 6). The reactor continues operating at full power until the insertion of MCA at 0.5 s bringing the power down to about 60%FP. When the inlet feeder flow drops below the SDS1 setpoint, the shutdown rods are inserted into the core rapidly reducing the power to decay heat levels. The ROH pressure is governed by the mismatch between the reactor power and the heat removed by the coolant. Thus the ROH pressure increases initially until the SDS1 trip after which it decreases quickly to approximately 9 MPa and much more slowly thereafter (Fig. 7).

Fig. 8 shows that the SG pressure increases after the close of ESV. Following the turbine trip, if CSDVs are available they are designed to open first, and ASDVs will only open when the pressure error increases to 270 kPa. Station data showed that ASDVs opened at 1 s which is much earlier than that predicted by RELAP5 (Table 3). This implies that the actual SG pressure during the first 13.5 s was higher than the ASDV set-point. After the loss of condenser vacuum at 13.5 s, CSDVs are no longer available and ASDVs are designed to open when the pressure error is greater than 35 kPa (setpoint is lowered from 270 kPa (Wu, 1993). The SG pres-

Table 3
Measured and predicted event timings (8-group).

	Station data (s)	RELAP5 Predictions (s)
Loss of Class IV Power	0	0
Turbine Trip	0	0
ESV Close	No data	0.28
Stepback on Turbine Trip	0.5	0.5
CSDV Open	0.8	0.8
ASDV Open	1.0	13.6
SDS1 Low Flow Trip	2.9	3.3
LRV open	3.5	4.2
SDS2 Low Flow Trip	11.6	N/A

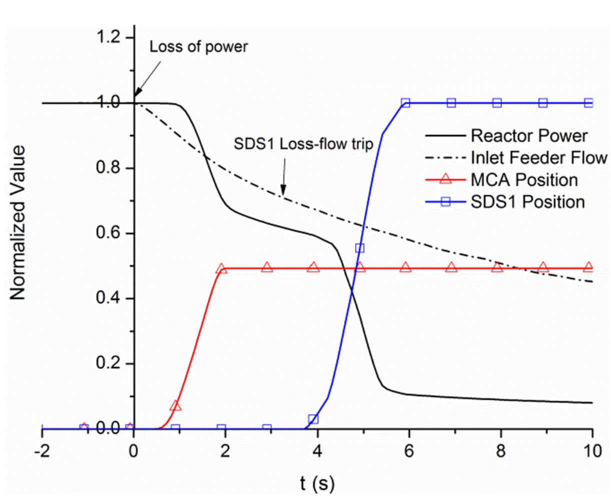

Fig. 6. Normalized power, flow, etc. (8-group).

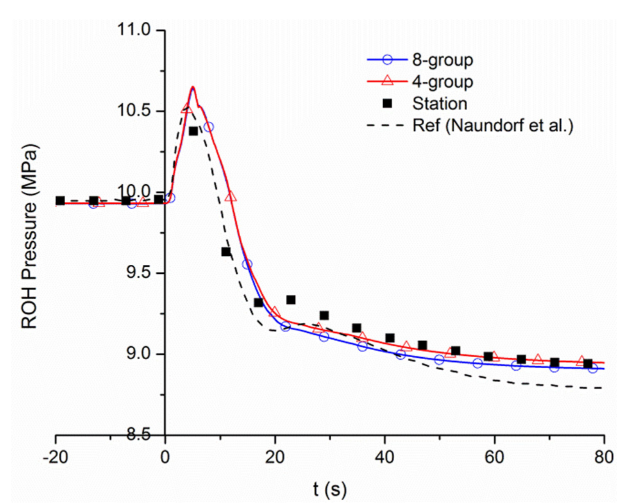

Fig. 7. Measured and predicted ROH pressure.

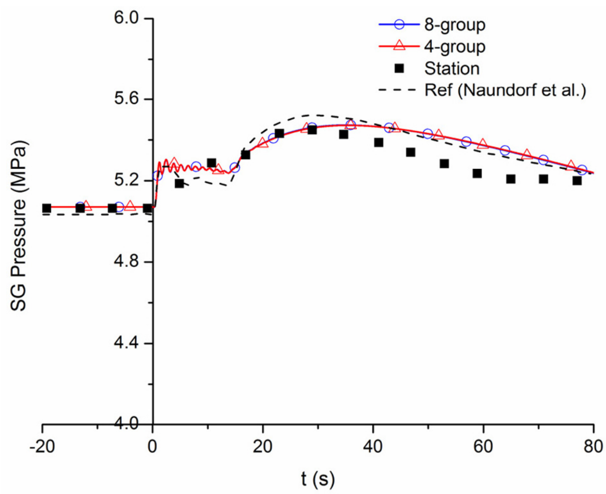

Fig. 8. Measured and predicted shell-side SG pressure.

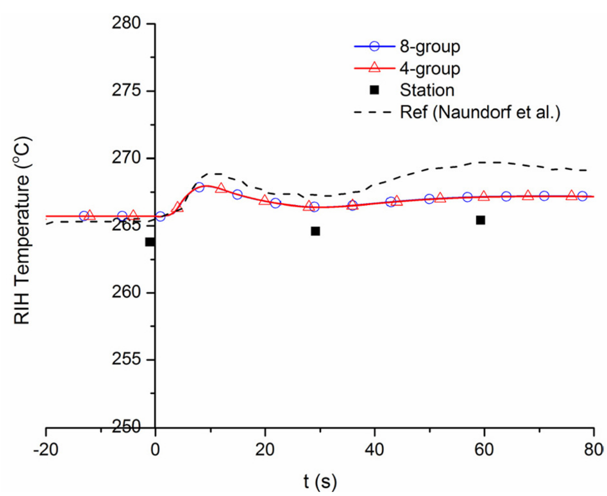

Fig. 9. Measured and predicted RIH temperature.

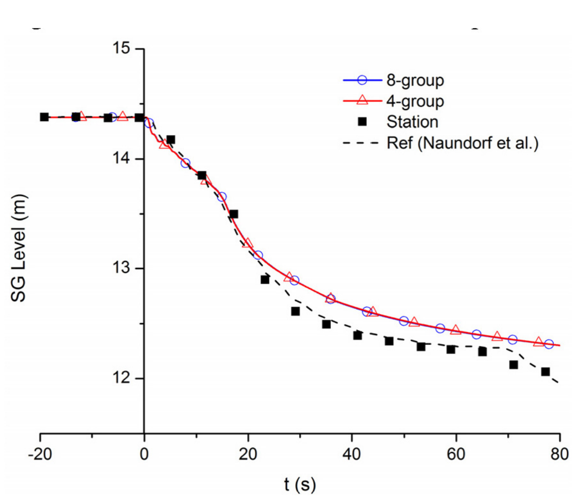

Fig. 10. Measured and predicted SG Level.

sure is now governed by the capacity of ASDVs and the heat deposited into the secondary side (Fig. 8).

Fig. 9 shows that the reactor inlet header (RIH) temperature closely follows the changes in the predicted secondary side pressures and temperatures. The SG level drops quickly in the first 30 s in Fig. 10 and then approaches the asymptotic behavior expected due to the heat deposited from the primary side. This initial drop is mainly due to the collapse of void in the shell-side of SGs after shutdown.

These results show that the RELAP5 predictions by both the 4-group and 8-group models agree well with the station measurements, and the difference between 4-group and 8-group models is negligible over this time frame. The predicted peak ROH pressure is slightly higher than that predicted by Naundorf et al. (2011). This could be due to the different capacities of LRVs used in these models. The decrease in SG level is slightly under-predicted and is attributed to the different initial void in the shell-side SG and/or the different SG geometries and nodalization between these models. In either case, the differences are small and overall the simulations adequately capture the core-wide phenomena in this event.

4. Extended SBO transients

The benchmarked models are then used to simulate an extended SBO accident with the loss of Class IV, Class III power and the emergency power supplies. As shown in Table 4, five different scenarios with and without crash-cool and with different water make-up options are modeled. In all the four crash-cool cases (C0 to C3), the MSSVs were open at 15mins. Case C0 is the reference case where the deaerator (DEA) water, the SGECS and EME are available and the inventory of the external water source is assumed to be infinite (thus SG dryout never occurs). In case C1 both the deaerator water and the SGECS are available, while in C2 only the deaerator water is credited. Case C3 examines the separate effect of crash-cooling, thus no water make-up from any source is credited. C4 is the non-crash-cool case. Various sensitivity studies are also provided to examine the effect of modeling assumptions and operator actions.

4.1. Modeling assumptions

For all the scenarios (with and without crash-cool), the following modeling assumptions are made:

1) Loss of Class IV power occurs at time zero and coincident with a turbine trip.
2) The four HTS pumps, the feedwater pumps, and the D_2O feed pump are all tripped at time zero.
3) The auxiliary feedwater pump is not available due to a loss of Class III power and a failure of EPS.
4) Following the turbine trip a reactor power stepback is initiated to 60% by inserting the MCA with a delay of 0.5 s.
5) ASDVs are available and actuate according to their control logic. The CSDVs are available until the condenser vacuum was lost at 13.5 s.
6) The reactor is tripped when any of the trips in Table 2 are triggered.
7) Pressurizer steam bleed valve and LRVs are available. Loop isolation is not credited and pressurizer is not isolated.

Table 4
Simulated SBO scenarios.[a]

Case	MSSV (timing)	DEA	SG ECS	EME	Note
C0	Y (15 min)	Y	Y	Y	Crash-cool
C1	Y (15 min)	Y	Y	–	Crash-cool
C2	Y (15 min)	Y	–	–	Crash-cool
C3	Y (15 min)	–	–	–	Crash-cool
C4	–	–	–	–	No crash-cool

[a] See text for abbreviations in this table.

8) The moderator is initially subcooled with an inlet temperature of 45 °C and outlet temperature of 66 °C. Water in the end shield and shield tank is also subcooled with an average temperature of 55 °C and 62 °C respectively. Moderator cooling and shield water cooling are not available.
9) The calandria vessel steam relief valve and the rupture disk are available.
10) Bleed condenser level control valve closes on high coolant temperature downstream of the bleed cooler.
11) Bleed valves close fully, feed valve and reflux valves open fully on low pressurizer level (and high bleed condenser pressure) signal.
12) ECCS is not available since EPS power to the ECC pumps is assumed to fail.

In addition to the above, during cases where operator action is credited to crash-cool the SGs (C0-C3) also assume:

13) Crash-cooling is initiated by opening the MSSVs 15mins (900 s) into the accident. The total opening area of MSSVs per SG is assumed to be 0.04 m^2 in all four cases. The depressurization rate is sensitive to this area.
14) During normal operation, the pressure and temperature of the water in the deaerator are 571 kPa and 154.8 °C. After turbine trip, steam supply to the deaerator is lost. Its pressure and temperature are assumed to gradually decrease to 229 kPa, 120 °C within 15mins at which point crash-cool is initiated, and stay constant thereafter (to be consistent with the work by Harwood and Baschuk (2015)).
15) In case C0, C1 and C2, the feedwater control valves fail-safe (i.e., open) during transient. This allows water in the deaerator tank to flow by gravity into the SGs once the secondary side is depressurized. The valve downstream of the deaerator stays open until deaerator tank is depleted. The inventory of deaerator tank is assumed to be 319,244 kg.
16) In case C0 and C1 where the SGECS is available, water properties in the SGECS storage tanks are assumed to be constant at 963 kPa and 37.4 °C. The SGECS valve opens when the SG pressure drops below 963 kPa, and closes when the total volume of water leaving a tank exceeds 70 m^3.
17) In case C0, the external water source is assumed to be at room temperature and 200 kPa. The EME actions are credited after the SGECS and the deaerator tank flow. The valves open when the SG level drops below 4 m and close at 12 m consistent with the expected duty cycle during an emergency response.

4.2. Results and discussion

Case C1 and C4 are simulated using all three channel grouping models (4, 8, and 20 groups) to determine the sensitivity to channel grouping, while the rest of the cases are simulated with the 20-group model only. For the reference case C0, simulations are terminated at 80,000 s as the system has reached a new stable state of cooling with the SG inventory actively managed until such time as power is restored. For case C1 with the 4 and 8 groups, the simulation is run for only 10,000 s, as they are designed mainly to investigate the effect of channel grouping on the predicted IBIFs. For all the other cases, the simulations are terminated when the maximum PT temperature is greater than 600 °C since simulations beyond this point must consider potential fuel channel deformation. The event timings predicted are summarized in Table 5. The system responses during the first 80 s of a SBO accident in these four cases are very similar to those in the LOF event in the previous section. The main focus of the following sections is on the thermal-hydraulic behavior after this very-early phase.

4.2.1. Station Blackout event without crash-cooling

While post-Fukushima measures indicate that early crash-cooling provides a significant benefit (i.e. Case C0, C1, C2 and C3) most studies in literature assume the system remains pressurized and as such the results from case C4 are discussed first for benchmarking to these previous studies.

As the PHTS pumps rundown, coolant flow rate decreases and eventually the pump inertia is exhausted. Post shutdown heat loads to the primary and moderator systems are partitioned as described previously. Continuous natural circulation is established shortly after the initiating event from the low elevation core to the higher elevation SGs. During this time the decay heat deposited into the coolant is continuously removed by SG secondary side. The primary-side pressure is governed by the mismatch between reactor power and coolant heat removal rate. Initially the reactor power after shutdown decreases much faster than the coolant flow rate resulting in the decrease in PHTS pressure (Fig. 11). An equilibrium state is then reached when the heat removal rate matches the reactor power and the pressure in the PHTS stabilizes at approximately 9 MPa until the SG inventory is depleted.

After the trip of the main feedwater pumps, water supply to the SGs is lost and the SG level gradually decreases as shown in Fig. 11. During the period where the SG U-tubes remain covered most of the decay heat deposited into the coolant is removed by the SGs, and only a small portion is removed by the moderator through the fuel channel annulus and by the end-shield water through the gap between the end fitting and lattice tube (Fig. 12).

When the SGs are depleted the heat sink to the SGs is lost. Subsequently, the heat removed from the fuel exceeds the heat sink capabilities and the PHTS is pressurized. The pressurizer steam bleed valves open with subsequent LRV action to relieve PHTS pressure. Coolant is discharged into the bleed condenser which was previously isolated on high coolant temperature downstream of the bleed cooler. The bleed condenser pressure therefore increases rapidly until it equals the ROH pressure (Fig. 11). The PHTS and bleed condenser pressures then continue to increase until reaching the bleed condenser relief valve set-point with the maximum system pressure being governed by the bleed condenser relief valve set point and capacity. The SG boil-off time and the bleed condenser (BC) relief valve timing predicted by the three models are almost identical with little sensitivity to channel grouping (Table 5).

The moderator is initially subcooled but increases in temperature as the heat deposited increases (Fig. 13). The associated liquid swell is accommodated by the head tank. The cover gas system which connects the head tank, the discharge duct, and the piping above the calandria vessel therefore increases in pressure until reaching the relief valve setpoint at 165 kPa (Fig. 14). When the moderator starts boiling, steam together with the inert cover gas (helium) is discharged through the relief valve into the containment and the calandria vessel pressure is maintained at its relief valve set-point (Fig. 14). All three models showed that the moderator starts boiling between 5.0 h and 5.5 h (as opposed to 7.5 h calculated by Blahnik and Luxat (1993)). The difference is attributed to more accurate decay heat load distribution used in the present work.

The end shield is connected to the shield tank at its top. Under normal operating conditions, the water enters the bottom of the end shield and exit at the top to flow into the shield tank which has some 800 Mg of light water. The water temperature in the shield tank increases slowly, and is still at less than 80 °C at the end of the simulation (Fig. 15). The end shield water reaches saturation much earlier than the moderator due to its relatively small inventory, but the end shield water level will not change before the water level in the shield tank is boiled down to uncover its

44 F. Zhou, D.R. Novog / Nuclear Engineering and Design 318 (2017) 35–53

Table 5
RELAP5 predicted event timings for various SBO scenarios (s).

	C0	C1			C2	C3	C4		
No. of channel groups	20	20	8	4	20	20	20	8	4
Loss of Class IV	0	0	0	0	0	0	0	0	0
Turbine trip	0	0	0	0	0	0	0	0	0
ESV close	0.28	0.28	0.28	0.28	0.28	0.28	0.28	0.28	0.28
Reactor stepback	0.5	0.5	0.5	0.5	0.5	0.5	0.5	0.5	0.5
CSDV first open	0.8	0.8	0.8	0.8	0.8	0.8	0.8	0.8	0.8
SDS1 trip	3.8	3.8	3.8	3.8	3.8	3.8	3.8	3.8	3.8
LRV first open	4.6	4.6	4.6	4.6	4.6	4.6	4.6	4.6	4.6
ASDV first open	13.6	13.6	13.6	13.6	13.6	13.6	13.6	13.6	13.6
MSSV Open	900	900	900	900	900	900	–	–	–
SGECS flow begins	1192	1196	1198	1198	–	–	–	–	–
DEA flow begins	1684	1692	1724	1720	1768	–	–	–	–
IBIF begins	2040	2020	2000	2092	2080	2050	–	–	–
EME first begins	36040	–	–	–	–	–	–	–	–
SG dryout	–	57840	–	–	41504	11624	18360	18160	18140
Moderator saturated[1]	42008	41808	–	–	40848	–	19720	18380	18120
BC relief valve first open	–	64104	–	–	46232	16448	19810	19840	19850
Channel Stagnant[2]	–	66880	–	–	48832	17112	21500	21870	21050
RIH/ROH void ($\alpha > 0.999$)	–	67440	–	–	49784	17192	21590	21990	21340
Transient Terminate[3]	80000	70248	10000	10000	52056	18112	22580	23870	22520

[1] Moderator is assumed to be saturated when the average temperature exceeds 110 °C.
[2] Highest channel in core pass one of loop if more than one channel is present.
[3] Transient terminated when the PT starts to balloon (T > 600 °C).

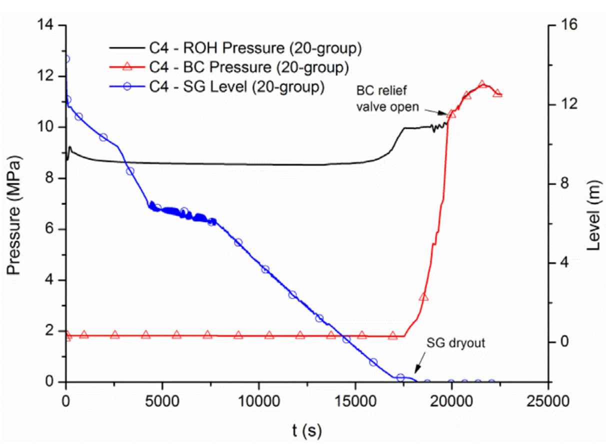

Fig. 11. ROH pressure, bleed condenser (BC) pressure, and SG level (Case C4).

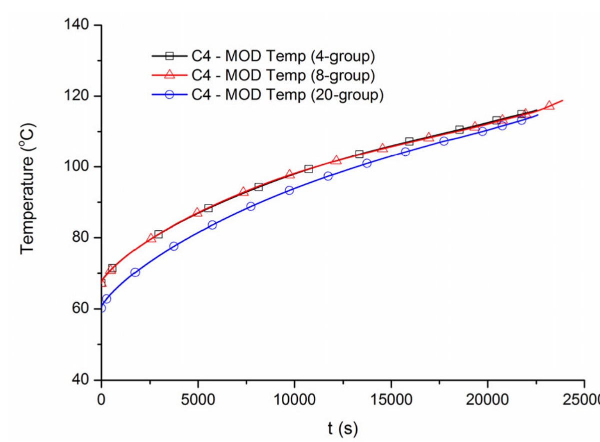

Fig. 13. Moderator temperatures (Case C4).

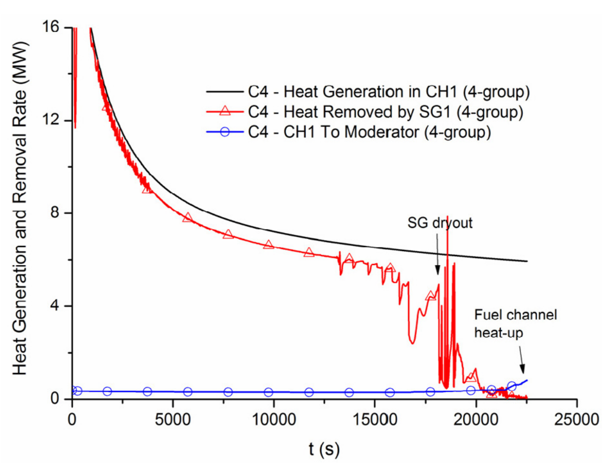

Fig. 12. Heat generation and removal rate (Case C4).

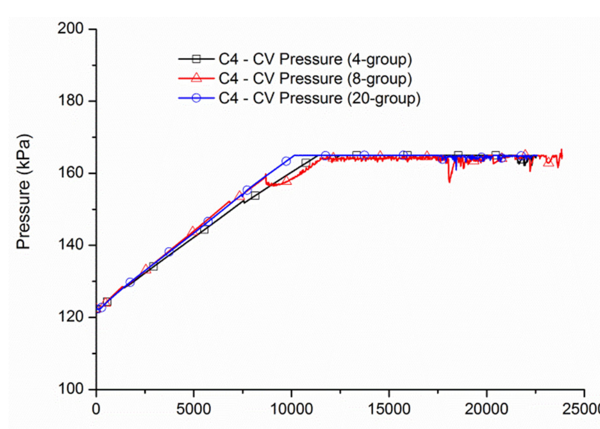

Fig. 14. Calandria vessel cover gas pressure (Case C4).

connections with the end shields. Hence significant end-shield depletion does not occur within the scope of this analysis.

Primary circuit natural circulation does not breakdown immediately at the time of SG dryout because some coolant in the primary side is still subcooled. When the coolant starts boiling,

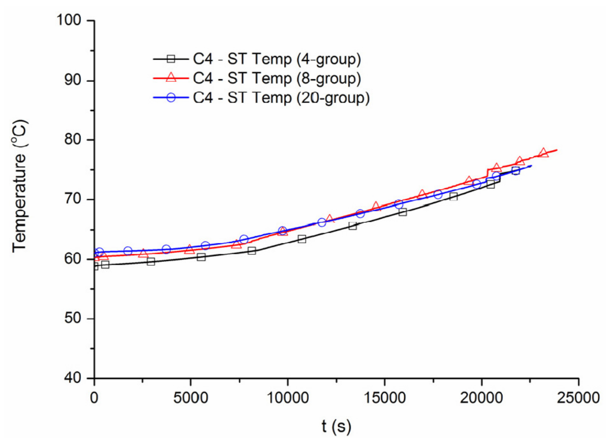

Fig. 15. Shield tank water temperatures (Case C4).

coolant void in the loop increases. Bubbles tend to accumulate at the highest point of the loop, i.e. the U-bends in the SGs. When the number of U-tubes that are vapor-locked increases, the flow resistance in the loop increases significantly resulting in the breakdown of continuous natural circulation. Up to this point, the results predicted by the three models are similar. After this point, both the 8-group and 20-group model predict interchannel flows among channels in the same core pass (Fig. 16), whereas the 4-channel model (with only a single channel per core pass) shows earlier complete stagnation. The RELAP5 simulations therefore show some sensitivity to channel grouping in that at least two channels per core pass must be modeled in order to allow for interchannel natural circulation pathways within the same core pass.

During this period some channels in a core pass may reverse flow direction, allowing local channel flows to persist even though the average flow across the core pass is zero. The flow reversal starts as a result of the negative RIH-to-ROH pressure differential when the flow resistance in the steam generator increases. When this pressure differential becomes large enough (more negative) to overcome the hydrostatic head difference between the inlet and outlet feeder the channel flow becomes reversed in that channel group. Thus the channels at higher elevation are more likely to experience flow reversal due to their smaller elevation difference with the headers. Such phenomenon has been observed experimentally, e.g. in the RD-14M test (Soedijono et al., 2001). This interchannel flow phenomenon persists until the PHTS inventory is depleted to a level below the headers, i.e. once the RIH and/or

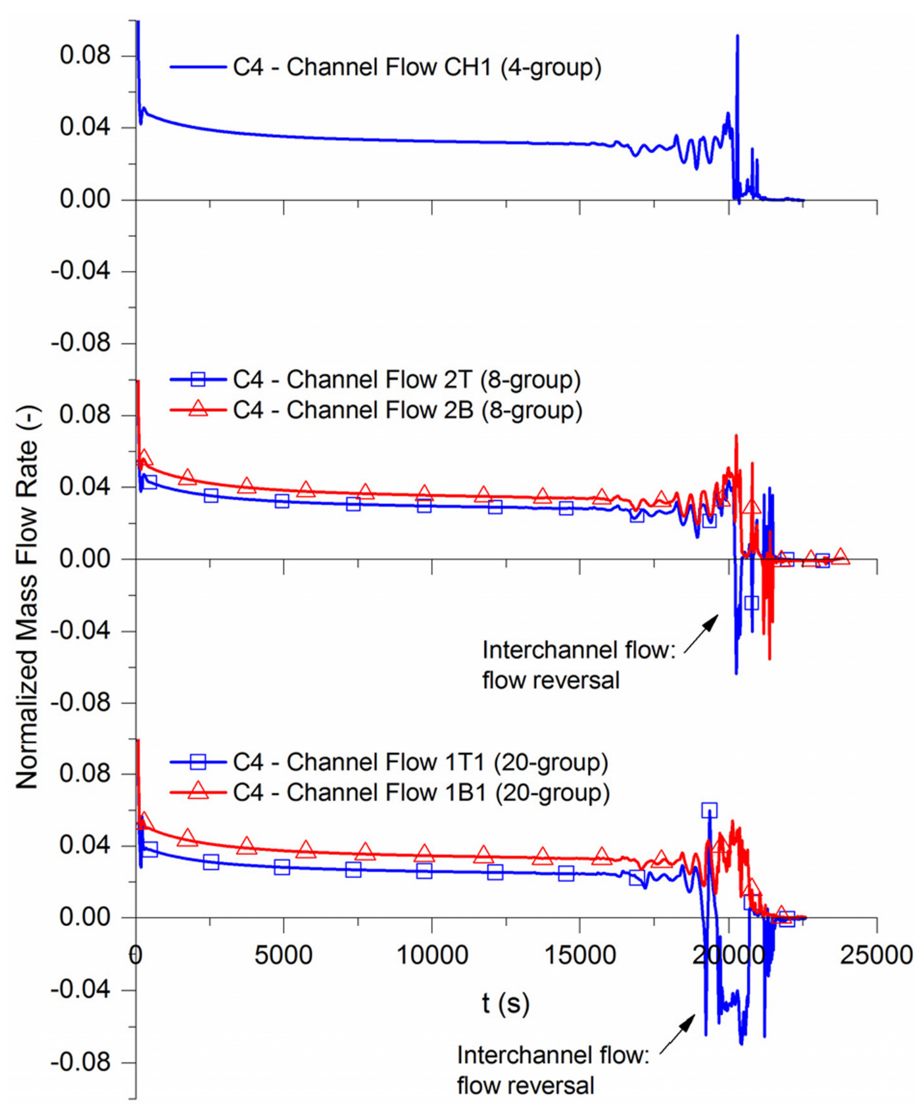

Fig. 16. Fuel channel normalized mass flow (Case C4).

46 F. Zhou, D.R. Novog / Nuclear Engineering and Design 318 (2017) 35–53

ROH are voided interchannel flow phenomena cease and coolant in all channels therefore stagnates (Fig. 16).

After the cessation of interchannel flows, the void in the channel increases and the fuel and PT may experience high and potentially non-uniform temperatures (Fig. 17) and eventual deformation and/or failure. In CANDU the deformation in the fuel channel may lead to PT-CT contact which can allow for a heat removal pathway to the moderator under some conditions. Given the limitations in RELAP5, the simulations of subsequent phases in the event require coupling to Multiphysics codes that can treat the non-uniform heatup and deformation of the fuel channels and also model the moderator boil-off phenomena. For the present study the scope of these RELAP5 simulations is to examine the effect of SG as a heat sink and hence the simulations are terminated shortly after steam generator dryout and prior to significant channel deformation.

4.2.2. SBO with crash-cool

In case C0-C3, crash-cooling was initiated at 900 s (15mins) and different water make-up options are credited (see Table 4). After the opening of MSSVs, the rapid depressurization of the SG secondary side causes water in the SG to vaporize resulting in an initial SG level transient more severe than the non-crash-cool case (Fig. 18). In case C0 and C1 where the SGECS is available, flow from the SGECS tanks starts about 5mins after the opening of MSSV when the SG pressure drops below 963 kPa (Table 5). This injection decreases the rate of the SG level transient (Fig. 19). As the pressure decreases further, at approximately 1700 s (13–14 mins after crash-cool) gravity driven flow from the deaerator is passively initiated. The combined make-up water from SGECS and deaerator tanks causes a temporary increase in the SG level. When the inventory of the SGECS and deaerator tanks are depleted the flows cease and at this point the SG level is about 14 m (Fig. 19). In case C2 without the SGECS, the SG level after deaerator tank flow is about

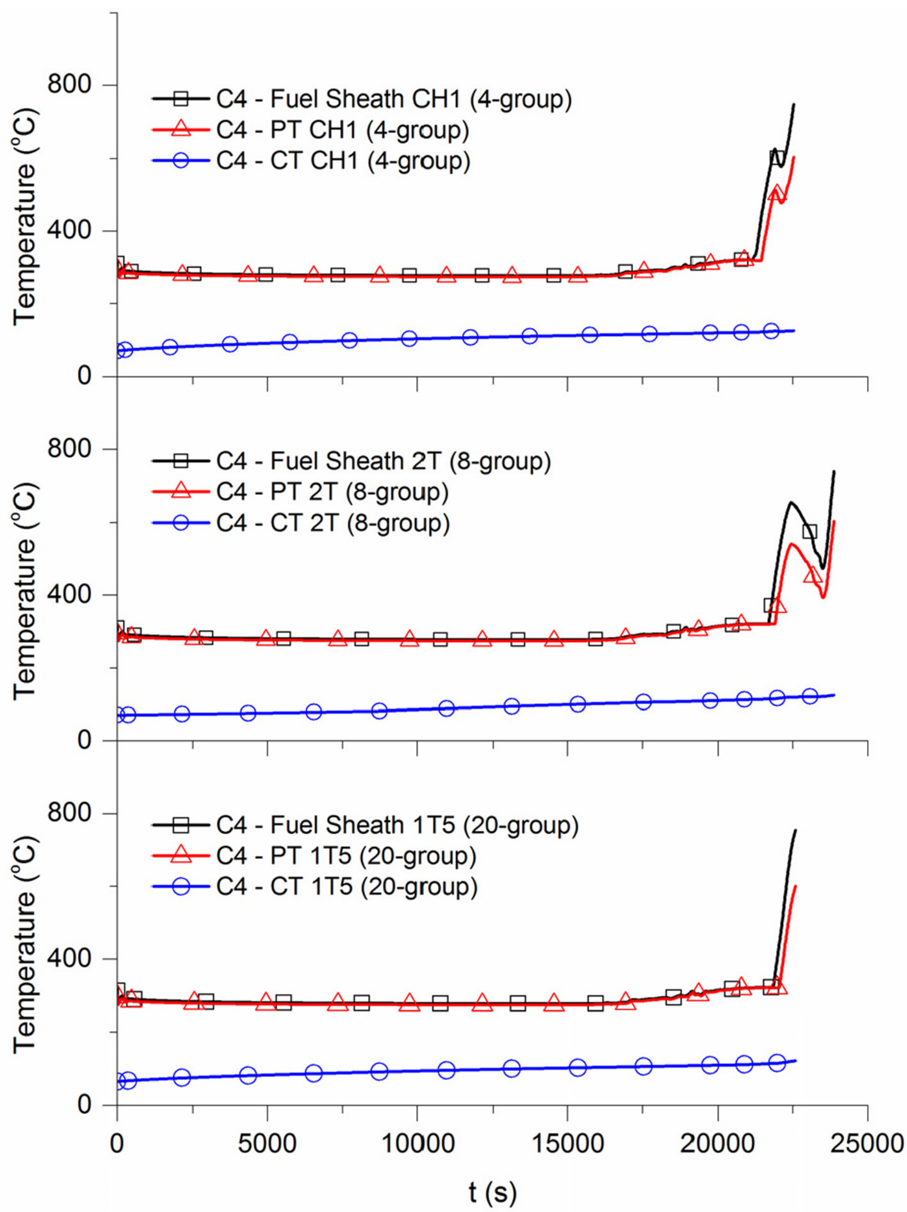

Fig. 17. Fuel sheath, PT and CT temperatures (Case C4).

F. Zhou, D.R. Novog / Nuclear Engineering and Design 318 (2017) 35–53 47

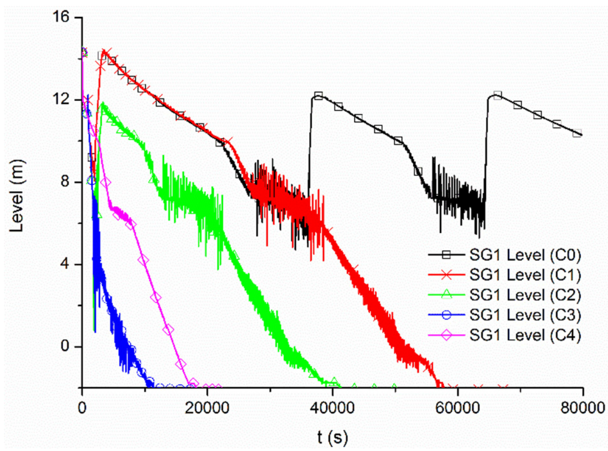

Fig. 18. SG level in Case C0 to C4 (20-group model).

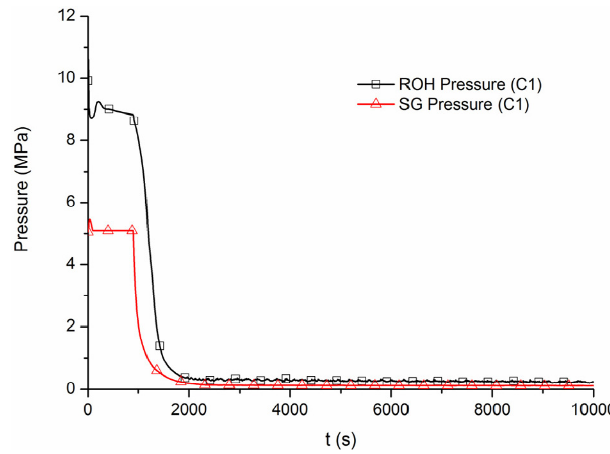

Fig. 20. SG tube-side and shell-side pressures (Case C1).

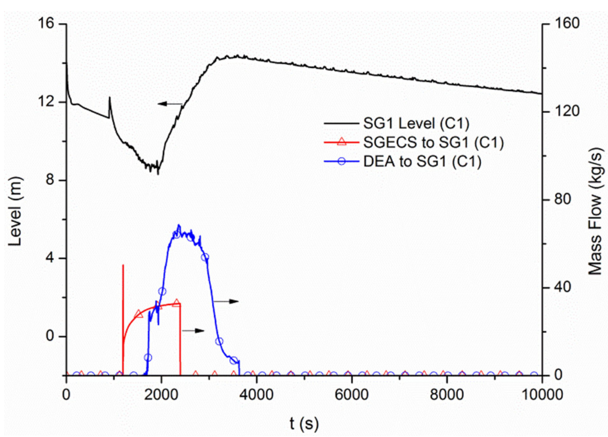

Fig. 19. Mass flow into SG and SG level (Case C1).

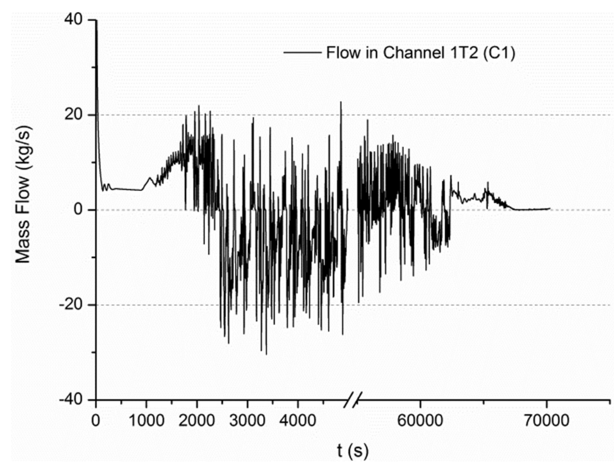

Fig. 21. Channel flow in 1T2 (Case C1).

12 m. In case C3 where no make-up water is supplied to the SG, the SG level initially drops to 4 m during the first 15mins and then continues to decrease until dryout.

The depressurization of the secondary side reduces the shell side temperature to the corresponding saturation temperature. This reduction in the secondary side temperature enhances heat removal from the primary side reducing the primary side temperature. The associated shrinkage in the PHTS coolant reduces the pressure on the primary side to the saturation pressure corresponding to the coolant temperature (Fig. 20). The initial heat transfer enhancement during the secondary-side depressurization temporarily enhances natural circulation flows in the primary side (Fig. 21) while the decrease in the primary-side pressure also introduces void in the hot leg of the loop which further acts to improve natural circulation flows. Void in the ROH thus increases (Fig. 22) and eventually is condensed a short distance into the U-tubes. The cold leg of the loop (e.g. from the SG outlet to the fuel channels) thus remains single-phase (Fig. 22 for RIH void). Since both the secondary and primary sides are under two-phase conditions and the heat transfer coefficients under boiling and condensation are very high, the temperature on the primary side will approach that of the secondary side (Fig. 20).

The partial-equalization of temperatures in the primary and the secondary sides eventually impairs heat removal and leads to a reduction in the driving forces for natural circulation. The reduction in natural circulation also causes an increase in the vapor

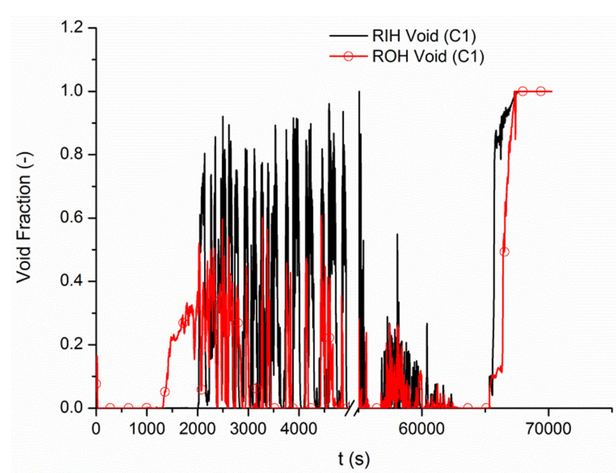

Fig. 22. Void fractions in RIH and ROH (Case C1).

quality in the loop which increases flow resistances in the hot leg. These two factors lead to the breakdown of continuous natural circulation at about 2000 s (Fig. 21).

Immediately following the disruption of continuous natural circulation, IBIF begins in the primary side. All four crash-cool cases (C0-C3) predicted the first occurrence of IBIF at almost the same time (about 19mins after the opening of MSSVs). The detailed behavior and the mechanism of predicted IBIF phenomenon will be discussed in next section, but it is important to note here that the magnitude of flow oscillations (Fig. 21) is much greater than that predicted by Harwood and Baschuk (2015). These large amplitude intermittent flows allow the steam generated in the core to be vented to the SG and condensed (Fig. 22).

IBIF continued to remove the decay heat from the core indefinitely so long as alternative means are established to maintain SG inventory or until the SG inventory is depleted and the heat sink is lost (Fig. 18). In case C0 the SG level is maintained between 4 and 12 m through water make-up from the SGECS, the deaerator tank and external (EME) water sources allowing IBIF continued indefinitely. For events where Class III power or EPS cannot be restored and EME injection to the SG fails (case C1), the SGECS and the deaerator inventory provide 57,840 s (16.1 h) of heat sink capacity. For the case where only passive flow from the deaerator tank are credited (i.e., SGECS is unavailable), the steam generator provides 41,504 s (11.5 h) of heat sink capacity (case C2). In the case where operator-initiated crash-cooling is not credited (case C4), flow from the deaerator cannot be established and hence timing is dictated by the initial inventory in the steam generator providing 18,360 s (5.1 h) of heat sink. Therefore operator actions to depressurize the secondary side may provide a significant benefit in emergency response times. However, in case C3 where crash-cooling was credited but water make-up from any source is unavailable, SGs dried out at 11,624 s (3.2 h) significantly earlier than in case C4. The early SG dryout is as expected since large stored heat in PHTS was taken away by the SGs during crash-cooldown.

The heat-up of the primary side after the complete boil-off the SGs is similar to that in the non-crash-cool case. When the steam generators dry out heat transfer from the primary to secondary sides is lost, and decay heat is deposited into the primary coolant. Without a heat sink the primary side temperatures increase leading to repressurization to a pressure corresponding to the LRV set-point (Fig. 23). Since additional heat needs to be delivered to the coolant to replace the heat removed during crash-cool, it took much longer time in the three crash-cool cases C1–C3 than in case C4 to raise their PHTS pressures to the BC relief valve set-point. Thus the first opening of BC relief valve was further delayed to 64,104 s (17.8 h) in case C1 and to 46,232 s (12.8 h) in C2 as opposed to 19,810 s (5.5 h) in C4 (Table 5). However, in case C3 the BC relief valve first open at 16,448 s (4.6 h) and the RIH/ROH become voided at 17,192 s (4.8 h) which is an hour earlier than in case C4. This implies that if the water make-up from any source is unavailable, crash-cooling has no benefit in delaying the fuel channel heat-up. This conclusion disagrees with that from the work by Luxat (2008) in which the crash-cooling with no water make-up was calculated to delay fuel channel heat-up.

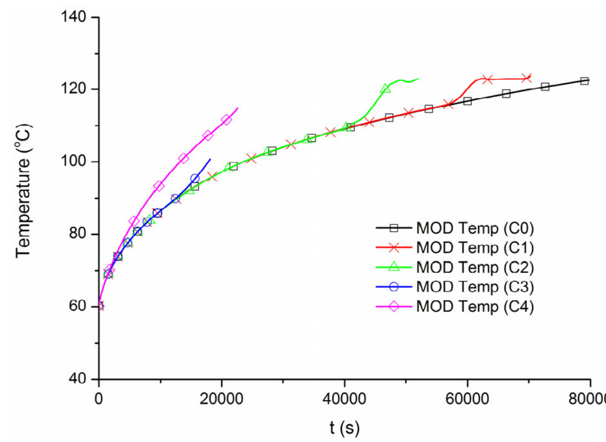

Fig. 24. Moderator temperatures in Case C0 to C4.

During the repressurization of PHTS the IBIFs ceased. However, complete coolant stagnant is still not likely and interchannel flows may occur until the feeder connections on the headers are uncovered (Figs. 21 and 22). When the headers become voided the flow in the channel is again stagnant. The fuel channels then begin to heat up.

Another benefit of crash-cooling is that the PHTS pressure stays low during the IBIFs and the coolant temperature after cooldown was much lower than that in the non-crash-cool case (C4). The lower channel temperatures result in lower temperature differentials with the end-shield and moderator liquid and hence lower heat transferred. The moderator heat-up rates in C0-C3 are thus low until the repressurization of PHTS (Figs. 23 and 24). The moderator saturation times in case C0, C1 and C2 were significantly delayed compared to case C4 (Table 5). The moderator level changes are insignificant throughout the transient in all five scenarios since simulations were terminated prior to channel deformation (Fig. 25).

The end shield water temperature shows similar behavior as the moderator temperature (Fig. 26). The maximum averaged shield tank water temperature is found in case C1 at the end of the run, and is still subcooled at 87 °C. The end-shield water levels

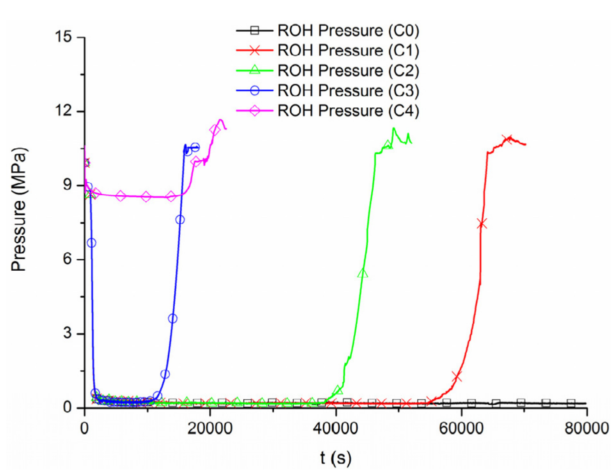

Fig. 23. ROH pressure in Case C0 to C4.

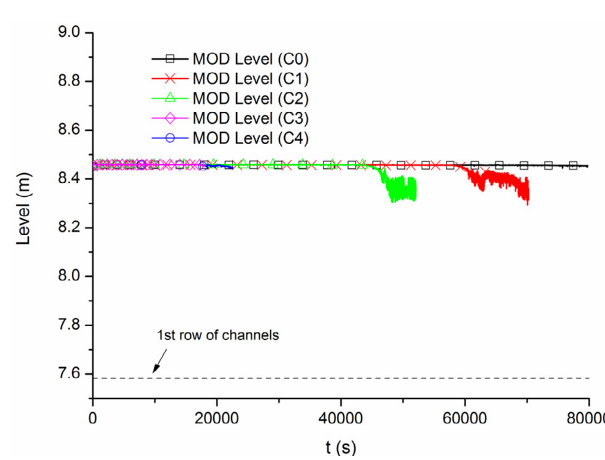

Fig. 25. Collapsed moderator level in calandria in C0-C4.

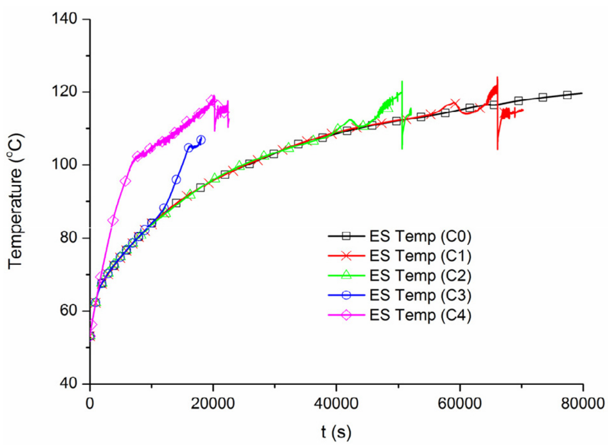

Fig. 26. End shield water temperatures in Case C0 to C4.

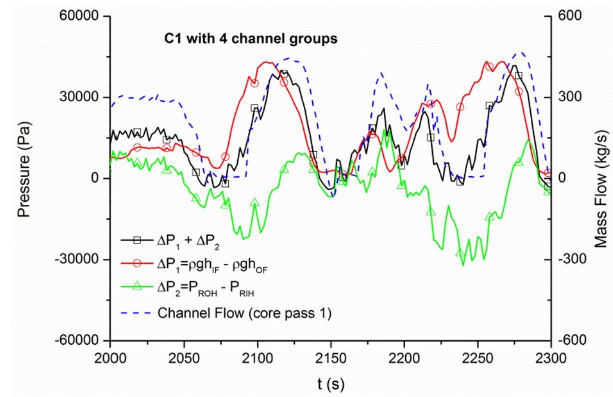

Fig. 27. Driving forces of IBIFs (C1 with 4-group).

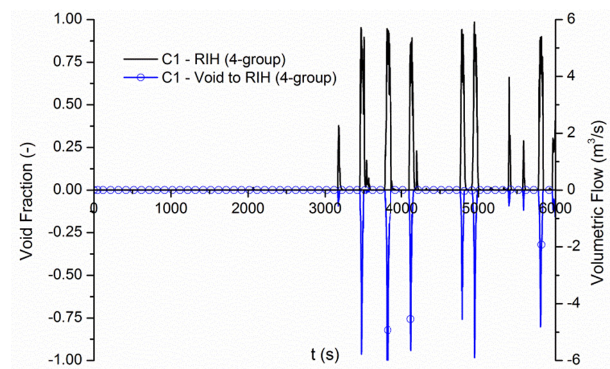

Fig. 28. ROH void fraction and vapor volumetric flow from channel to ROH (C1 with 4-group).

do not show appreciable change during the simulation times reported.

4.2.3. Assessment of RELAP5 IBIF phenomena

Case C1 was simulated using three different nodalizations containing 4, 8, and 20 channel groups. In this section, the IBIF phenomena predicted by RELAP5 are examined in detail.

Table 6 shows the channel void fraction distribution within a typical IBIF cycle in core pass one of the 4-group model. The flow in the fuel channel is initially stagnant with only trace amounts of void (2066 s). Due to the low flow in the channel, a bubble starts to grow beginning at the center of the channel where the decay heat is highest. As the bubble rapidly expands from the channel center it soon enters one or both of the two end fittings (2074 s). Void generation causes the void to continue growing and eventually reach one of the vertically oriented feeders connected to the end fittings. At this point the vertical piping provides a flow path for the low density vapor to rise (2094 s). While this create a hydrostatic pressure difference between the inlet feeder (IF) and the outlet feeder (OF), i.e. $\Delta P_1 = (\rho gh)_{IF} - (\rho gh)_{OF}$, the pressure difference between the RIH and ROH also contributes to the driving force of the flow, i.e. $\Delta P_2 = P_{RIH} - P_{ROH}$, see Fig. 27. The latter (ΔP_2) can be negative depending on the fluid condition above the headers. When $\Delta P_1 + \Delta P_2$ becomes large enough to overcome the flow resistance across the channel, significant flows are generated (Fig. 27). The void along with the entrained hot liquid from the channel rises through the feeder while cold liquid from the opposite feeder enters the channel (i.e., a phenomena referred to as channel venting). For the IBIF in Table 6, the vapor in this one-channel per core pass model reaches the outlet feeder first which is consistent with the direction of the induced channel flow, i.e. from inlet feeder to outlet feeder.

When the vapor is vented to RIH/ROH, a void fraction spike can be observed in the RIH/ROH (Figs. 28 and 29). In the 4-group model all 120 channels of each core pass are lumped into one average channel hence bi-directional flows within a core pass are precluded. In reality, the IBIF frequency may vary from channel to channel depending on a number of parameters such as channel power and channel elevation, and the channels do not necessarily vent at the same time and same direction. Therefore it is expected that the header void transients in the 20-channel group may be different since bi-directional flows may transport some void to the inlet headers.

The IBIFs phenomena predicted by the 20-group model are also examined. Overall, the thermal-hydraulic behaviors during IBIFs predicted by the 20-group model are similar to those predicted by the 4-group model:

1) The breakdown of continuous natural circulation or the first occurrence of IBIF predicted by the 20-group model is close to those predicted by the 4-group model (Table 5).
2) The driving forces of the IBIFs appear to be the same, i.e. venting is caused by the hydrostatic head difference between the feeders and the RIH-to-ROH pressure difference.

Table 6
Void along channel of core pass 1 and channel flow during a typical IBIF cycle (C1 with 4-group).

Time (s)	IEF1	IEF2	CH1	CH3	CH5	CH7	CH9	CH11	OEF1	OEF2	Flow (kg/s)
2066	0.00	0.01	0.00	0.00	0.00	0.02	0.17	0.00	0.00	0.00	−18.6
2070	0.00	0.01	0.03	0.34	0.67	0.69	0.69	0.73	0.49	0.10	14.6
2074	0.02	0.29	0.85	0.81	0.82	0.77	0.79	0.81	0.76	0.42	2.5
2086	0.00	0.32	0.82	0.91	0.92	0.91	0.92	0.93	0.69	0.62	6.9
2094	0.00	0.00	0.00	0.00	0.01	0.44	0.63	0.64	0.63	0.63	178.3
2102	0.00	0.00	0.00	0.00	0.00	0.00	0.41	0.58	0.57	0.55	249.4

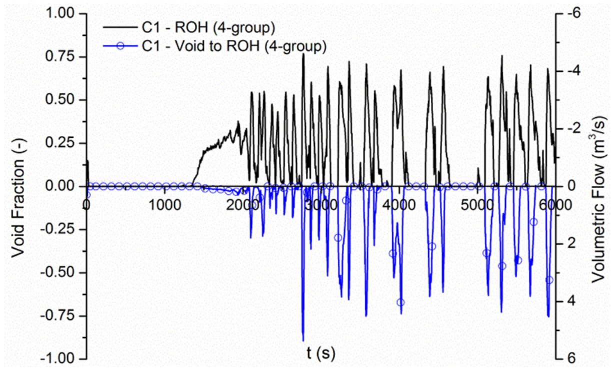

Fig. 29. RIH void fraction and vapor volumetric flow from channel to RIH (C1 with 4-group).

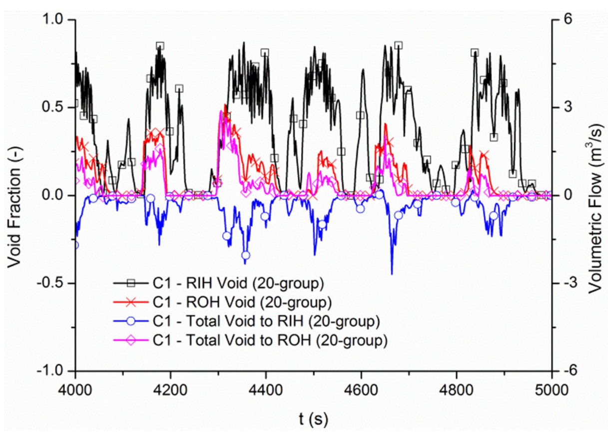

Fig. 30. RIH/ROH void fraction and vapor volumetric flow from channels of core pass one to RIH/ROH (C1 with 20-group).

3) In the 20-group model a majority of simulations show that within a core pass, the first venting occurrence in a channel cause a sufficient perturbation such that venting in the rest of the channels is initiated. At such times large amounts of vapor are transported to the headers and large scale void variations occur in the headers (Fig. 30).

   Significant differences between the results predicted by the 4-group and the 20-group models can also be observed:
4) In the 20-group model bi-directional venting occurs in each core pass with the venting times largely dictated by the perturbation caused by the first predicted venting event. The void fractions in the RIH and ROH thus peak at the similar times (Fig. 30). Since the 20-group model has multiple channels per core pass it simulates the bidirectional flow phenomena, whereas the 4-group model cannot predict bi-directional phenomena in the same core pass.
5) In the 20-group model the core passes of the same loop do not necessary vent together, possibly resulting from the smaller overall perturbation during bi-directional events (as opposed to unidirectional voiding which causes a larger perturbation to the outlet header).
6) While channel venting is often initiated by a single channel venting there is some variability in the venting frequency (i.e. the venting frequency at a given decay power level is not constant amongst channel groups). It is found that the higher the channel elevation or channel power, the higher the IBIF frequency (Table 7). This is consistent with the experimental findings that show the venting time increases with the increase in water level inside the feeder pipes and the decrease in power level (Karchev and Kawaji, 2009).
7) The channel void fraction oscillates during IBIF cycles (Figs. 31 and 32). The predicted flow regime transitions into horizontal-stratified when the channel is stagnant and void fraction is high, then into bubbly or slug regime after venting is initiated. The time of flow stagnation and stratification appears to be shorter in the 20-group model than in the 4-group model and the venting frequency increases with the number of channels considered in a core pass (Table 7).
8) Small magnitude of temperature oscillations are observed on fuel cladding during IBIF cycles. The peak cladding temperatures are typically reached prior to venting when the channel void fractions are high (Figs. 31 and 32). The maximum cladding surface temperatures predicted by the 4-group and 20-group models are both well below the safety limit. The lowest temperatures and smallest oscillations occur in the 20-group model.
9) In the 20-group model both countercurrent and co-current flows were observed at the U-tube inlet/outlet. When the vapor velocity at the inlet/outlet junction is low, the liquid film flows downwards with the vapor flowing upward. As

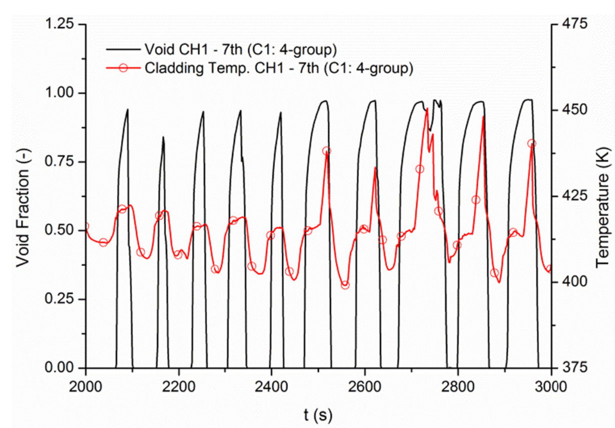

Fig. 31. Void fraction and cladding temperature in CH1 of the 4-group model (Case C1).

Table 7
IBIF[1] cycles per 1000 s in channels of core pass 1.

Group	Top						Bottom	
	1T1	1T2	1T3	1T4	1T5	1T6	1B1	1B2
20	15	23	17	16	16	19	18	12
8	18						9	
4	13							

[1] An IBIF cycle is recorded when the flow regime in the channel changes from "bubbly/slug" to "horizontal stratified" and back; the numbers in the table are the average between 4000 s and 10,000 s.

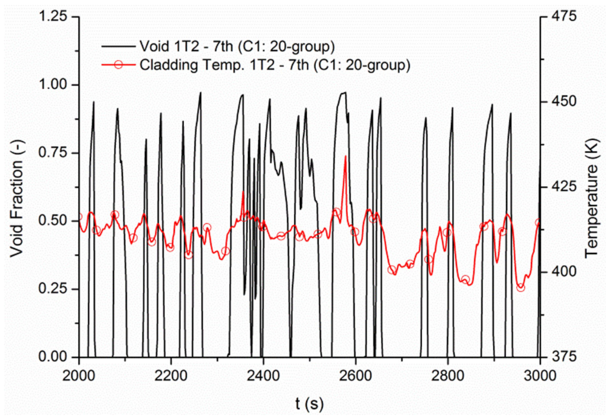

Fig. 32. Void fraction and cladding temperature in 1T2 of the 20-group model (Case C1).

the relative velocity increases the interface friction begins to reverse the flow of liquid. Any steam reaching the other side of the U-tube will be condensed and falls together with the liquid carried over to the other core pass. Sensitivity studies to Counter Current Flow Limit (CCFL) model parameters did not show any significant changes in U-tube flow behaviors.

Robust IBIF cycles are observed until the SG inventories are depleted with sensitivity studies on channel grouping, interfacial parameters, heat transfer coefficients and loss factors not significantly impacting the peak sheath temperatures. However, it is important to note that the current RELAP5 code has several limitations in accurately predicting the IBIFs. First, in the current study all the U-tubes of one SG are lumped into one average pathway. In reality, the behaviors of the U-tubes under the IBIF mode of natural circulation are expected to vary with some U-tubes in forward flow, some in stalled conditions and some in flooding or CCFL conditions (D'Auria and Galassi, 1990). These variations, which may have some influence on the system thermal-hydraulic behavior, could be due to the difference in U-tube length/elevation, or the variation of local fluid conditions in the SG inlet/outlet plenum. Sensitivity studies examining several U-tube models in parallel arrangements showed that the former has negligible effect on the predicted IBIFs. The latter requires a two-dimensional solution in the SG plenum thus cannot be captured by RELAP5 which is a one-dimensional code.

Second, as discussed earlier, RELAP5 has limitations on horizontal heat structures, i.e., water level tracking and its impact on phenomena in the horizontal fuel channels are lacking. In reality, when the flow in the channel is stratified, the top fuel pins are exposed to superheated steam while the bottom pins are submerged in liquid. Thus pins in a fuel assembly will gradually be exposed to steam as the vapor grows and hence the void generation will be lower than an equivalent case in RELAP5 which will utilize nucleate boiling relationships for all pins until the bundle is almost completely uncovered.

Third, during the stagnant phase of each IBIF cycle, the steam in reality will flow in the top portion of the channel towards the end fittings while liquid near the bottom of the channel will flow in the opposite direction. RELAP5 as a one-dimensional code has difficulties predicting this liquid replenishment accurately which may result in liquid starvation and the overestimation of IBIF period. However, since the length of an IBIF cycle in this paper is on the order of 10 s, such errors are mitigated by the large liquid flow caused by the venting at the end of the IBIF cycle, and the sheath temperature deviations are expected to be small.

4.2.4. Sensitivity studies

In all the above discussed crash-cool cases, the MSSVs are opened shortly (15 min) after the initiating event. However, in some situations the opening of MSSV may be delayed such that the effectiveness of crash-cooling might be impaired. In order to investigate the sensitivity to the timing of crash-cooling and to confirm the acceptability of operator actions for crash-cool, additional cases were simulated:

Case D1: MSSV are opened at 3600 s (1 h);
Case D2: MSSV are opened at 18,000 s (5 h) with very low SG water level;
Case D3: MSSV are opened at 21,600 s (6 h) after SG dryout and some coolant is lost through LRVs.

Since the focus of the sensitivity study is to investigate whether IBIFs can be established with delayed operator actions, only the gravity-driven deaerator flow is credited in these three cases and all the other modeling assumptions remain the same as those in case C2. The predicted event timings are shown in Table 8. In all the three cases IBIFs are established shortly after crash-cooldown and continue to remove heat from the core until the SG dryout.

Loop isolation is not credited in D1, D2 and D3, and at the time of MSSV opening there is still some liquid left in the pressurizer. During the depressurization of the PHTS the remaining liquid in the pressurizer was found to have transferred into the PHTS via the ROHs. In case D3 the PHTS inventory is about half-depleted at the time of crash-cooling while the pressurizer still contains significant amount of liquid. All the water in the pressurizer transfers into the PHTS during crash-cooldown providing sufficient inventory for intermittent natural circulation establish (Fig. 33).

To further demonstrate the role of the pressurizer inventory in establishing IBIF, the three cases (D1, D2 and D3) are repeated but with their pressurizers isolated prior to crash-cool (i.e. D1B, D2B and D3B). Only the results of D3B are presented (Table 8). Without the pressurizer the primary side pressure decreases more quickly after crash-cooling (Fig. 34). In case D1B and D2B where MSSVs are opened before SG dryout the faster decrease in primary side pressure leads to an earlier breakdown of continuous natural circulation, nevertheless the first occurrence of IBIF is also advanced. However, in case D3B with the pressurizer isolated the PHTS inventory insufficient for IBIF to occur and the predicted channel flows are small (Fig. 34) resulting in large cladding temperature oscillations. Hence the inventory in the pressurizer may have some importance for cases where crash-cooling is implemented much later than envisioned.

The sensitivity to additional damage or PHTS leakage was also examined. In sensitivity Case E PHTS leakage is superimposed on case C0 to observe at which inventory level the PHTS loses natural circulation cooling. The break is modeled using a trip valve with an area of 3E-4 m^2 on the ROH which opens at 2900 s (i.e. leakage starts 2000 s after the opening of MSSVs). In this case the pressure difference between the PHTS and the containment is small after crash-cooldown and thus the PHTS inventory decreases slowly after the opening of break valve. It is found that IBIF is able to continue until the PHTS inventory (excluding the pressurizer) drops to approximately 40% of its normal inventory (i.e. when headers are completely voided), and immediately following the cessation of IBIFs the fuel channels begin to heat-up.

As discussed earlier, the behaviors of the U-tubes during reflux condensation may be affected by the local fluid conditions in the SG inlet/outlet plenum resulting in some U-tubes in stalled/flooding conditions and some with forward or reversed flows. Sensitivity studies are carried out to investigate the potential effect of such phenomena by dividing each average U-tube pathway into four

Table 8
Key event timings of D1, D2, D3 and D3B (s).

	D1	D2	D3	D3B
Loss of Class IV	0	0	0	0
Reactor stepback	0.5	0.5	0.5	0.5
SDS1 trip	3.8	3.8	3.8	3.8
SG dry	–	–	18360	18360
BC relief valve open	–	–	19810	19810
Pressurizer isolated	–	–	–	21600
MSSV Open	3600	18000	21600	21600
Deaerator flow begins	4178	18128	21676	21676
IBIF begins	4572	18684	21928	–

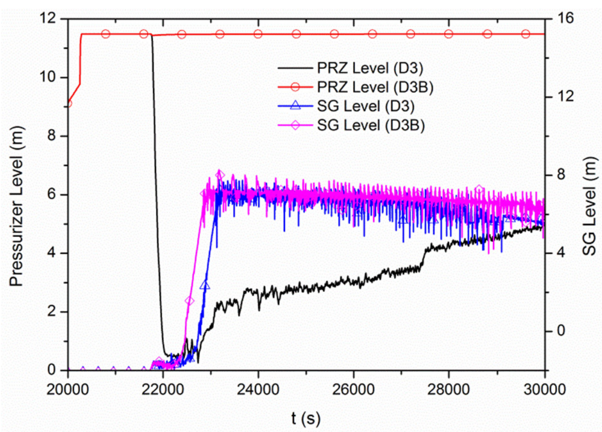

Fig. 33. Pressurizer level and SG level (D3 vs. D3B).

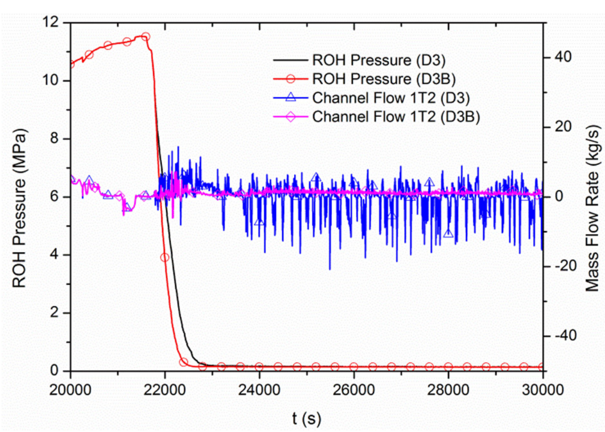

Fig. 34. ROH pressure and channel flow (D3 vs. D3B).

and varying the resistance among them. Two additional cases were simulated:

Case F1: the U-tubes of a SG in the 20-group model are grouped into four pathways by their elevation. No additional resistances are applied to those flow paths. The modeling assumptions are assumed to be the same as C1.

Case F2: same as F1 but three out of four paths are "blocked" during IBIFs (at 4000 s) by reducing area and increasing the form loss factors at the corresponding inlet/outlet junctions.

The comparison between C1 and F1 shows that the results are not significantly affected by the U-tube grouping scheme: continuous natural circulation breaks down at almost the same time; there is no appreciable difference in the predicted IBIF phenomena between the two cases. In case F2 part of the U-tubes are "blocked" during the transient resulting in higher steam generator flow resistances and greater vapor velocity at some of the U-tube inlets/outlets. However, this extreme case (3/4 of the U-tubes blocked) did not impair fuel cooling and the "liquid-hold-up" issue in the simulation by Harwood and Baschuk (2015) (described in Section 1) is not observed. The RELAP5 predicted IBIFs are much stronger, and the steam entering the U-tubes does not prevent the downward flow of condensed liquid. Some parameters of interest such as the SG level and the ROH pressure are not sensitive to the additional flow resistances of the U-tubes.

The predicted IBIF frequencies in channels of core pass one are shown in Table 9 for case C1, F1 and F2. The results show that IBIF frequencies are more sensitive to the decay power level and the elevation of fuel channels than to the U-tube grouping and flow resistances.

5. Conclusions

A detailed model of a 900 MW CANDU plant has been created using RELAP5/MOD3.3 including the PHTS, the feed and bleed system, the secondary side, the moderator system, and the shield water cooling system. The 480 fuel channels were grouped into 4, 8, and 20 characteristic channels to investigate the sensitivity of event timing to channel grouping. The models were benchmarked against the 1993 LOF event at Darlington NGS. The RELAP5 predictions agreed well with the station measurements. The models were then used to simulate the extended SBO accidents. Five accident scenarios with/without crash-cooling and with different SG water make-up options were simulated.

For the non-crash-cool case, the results predicted by the three models (4, 8 and 20 groups) are generally close: the SGs were depleted at around 5.1 h; the moderator became saturated at 5.0–5.5 h; the BC relief valve first opened at about 5.5 h, and the ROH/RIH became voided at about 6.0 h. The 8-group and 20-group models predicted interchannel flow phenomena after U-tube vapor lock, while the 4-group model which only has one characteristic channel per core pass is constrained to unidirectional flow. The channel flow in the 4-group model was stagnant immediately following the vapor lock resulting in earlier channel heat-up compared to the other models. The results, e.g. SG tube dryout and RIH/ROH voiding timings, are reasonably close to those predicted by MAAP/CANDU in the work by Blahnik and Luxat (1993). One of the important differences, however, is the moderator response. In their paper the moderator level did not change until the fuel channels ruptured at around 8 h (Blahnik and

Table 9
IBIF[1] cycles per 1000 s in channels of core pass 1.

Case	Top						Bottom	
	1T1	1T2	1T3	1T4	1T5	1T6	1B1	1B2
C1	15	23	17	16	16	19	18	12
F1	13	25	23	19	18	20	12	13
F2	12	24	25	14	19	18	10	8

[1] Refer to Table 7 for the definition of an IBIF cycle.

Luxat, 1993), while in this paper the moderator started boiling much earlier and moderator relief action was predicted. This difference is driven by the partitioning in the decay power.

The effect of operator initiated crash-cooling was then studied in detail by simulating four crash-cool scenarios (C0 with infinite water supply to the SGs, C1 with SGECS and deaerator flow provided to the SGs, C2 with deaerator flow only, and C3 without any water make-up). Comparing the results of the four cases with that of non-crash-cool case, it is concluded that crash-cooling can increase the utilization of available water inventories and significantly delay the accident event progression. Although the breakdown of continuous natural circulation occurs earlier, IBIF heat transfer combined with passive deaerator inventory transfer will provide a heat sink for a much longer time period than the case with no operator action. With the intermittent venting of coolant in the channels, the fuel and the PT remain sufficiently cooled, and the small temperature oscillation during the IBIF phase predicted by the current RELAP5 model will not challenge the channel integrity. With the addition of water from the deaerator tank the complete boil-off of SGs is delayed to 11.5 h, and if the SGECS system is also available, the time can be further extended to 16.1 h. If the operators are successful in maintaining the SG inventory through EME or other actions, IBIFs can continue indefinitely.

In case C3 where crash-cooling was credited and the passive and active water sources from the deaerator and SGECS fail, the steam generators dried out at 3.2 h significantly earlier than that in the non-crash-cool case. Furthermore, the first opening of BC relief in case C3 is predicted to be at 4.6 h which is also earlier than in the non-crash-cool case. This emphasizes the importance of passive or active water make-up which plays a significant role in terminating the event progression.

The mechanisms of the predicted IBIF phenomenon are then investigated in detail. The flow in the channel is found to be primarily driven by the hydrostatic head when the large void formed in the stagnant channel reaches one of the two feeders. The results predicted by the 20-group model showed that the venting events tend to happen together in channels of the same core pass, albeit in differing directions. It is also found channels at higher elevation with higher power will have higher IBIF frequencies. This is consistent with observed IBIF behaviors in full scale CWIT and other experiments. Steam vented to the headers eventually rives to the steam generators and is condensed.

A number of sensitivity studies have also been carried out to determine the effect of delayed operator actions for crash-cool, the role of the pressurizer, and the sensitivity to U-tube grouping and flow resistance. The results suggest that in a SBO if crash-cooling and water make-up to the SGs are credited before the PHTS inventory is depleted to below 50% of its normal inventory, the IBIF heat sink to the steam generators can be established. It is also found that the predicted IBIFs are quite robust and not sensitive to the grouping and the flow resistance of U-tubes.

The limitation of the RELAP5 code in predicting IBIFs are also discussed, however given the robustness of the IBIF phenomena and their insensitivity to modeling parameters and event timings, it is likely that these limitations do not invalidate the conclusions of this work.

Acknowledgement

The work is financially supported by Canadian Nuclear Safety Commission (CNSC) under contract 87055-15-0226-2. Technical support from the RELAP/SCDAPSIM development team is greatly acknowledged. The authors also would like to express their heartfelt gratitude to L.J. Siefken at Innovative System Software, and Dr. J.C. Luxat at McMaster University for all the invaluable suggestions and assistances.

References

Jiang, J., 2015. Electrical system. In: The Essential CANDU. University Network of Excellence in Nuclear Engineering (UNENE), pp. 1–42.
Blahnik, C., Luxat, J.C., 1993. CANDU response to loss of all heat sinks, 9th ANS Meeting on Nuclear Thermalhydraulics.
Luxat, J.C., 2008. Thermal-hydraulic aspects of progression to severe accidents in CANDU reactors. Nucl. Technol. 167 (1), 187–210.
C. Harwood, J. Baschuk, Assessment of thermalhydraulic phenomena for external water make-up. In: 35th Annual Conference of CNS, 2015, pp. 1–12.
Wu, E., 1993. SOPHT Users Manual – DATA Specific to Darlington-A NGS.
Ingham, P.J., Luxat, J.C., Melnyk, A.J., Sanderson, T.V., Natural circulation in an integral CANDU test facility. In: IAEA-TECDOC-1149, 2000, pp. 201–212.
McCallum, C.K., Wedgwood, J.M., 1996. Description of the Cold Water Injection Test Facility. COG File COG-96255.
Karchev, Z., Kawaji, M., A Study of intermittent buoyancy induced flow phenomena in CANDU fuel channels. In: NURETH-13, 2009, pp. 1–10.
Spencer, J., 2010. CANDU Reactor Intermittent Buoyancy Induced Flow Analysis McMaster Univ. Master Thesis.
Lei, Q.M., Gulshani, P., 1998. Assessment of fuel fitness-for-service after standing-start process under Gentilly-2 shutdown conditions, 19th CNS Annual Conference.
Petoukhov, S.M., 2014. MAAP4-CANDU Simulation Results for CANDU6 Accident Management Measure: Steam Generator Secondary Side Water Make-up From Dousing Tank for the Station Blackout Scenario. in: PBNC-2014, pp. 1–22.
Blahnik, C., 1991. Modular accident analysis program for CANDU reactors, 12th CNS Annual Conference.
Hanna, B.N., 1998. CATHENA: a thermal–hydraulic code for CANDU analysis. Nucl. Eng. Des. 180, 113–131.
Information Systems Laboratories, RELAP5/MOD3.3 CODE MANUAL VOL. 1–8, NUREG/CR-5535/Rev P4, 2010.
Kim, I., Cho, Y., Lee, S., 1995. RELAP5 simulations of critical break experiments in the RD-14 test facility, 16th CNS Annual Conference, pp. 2–4.
International Atomic Energy Agency, Intercomparison and Validation of computer codes for thermalhydraulic safety analysis of heavy water reactors, 2004.
Allison, C.M., Hohorst, J.K., 2010. Role of RELAP/SCDAPSIM in nuclear safety. Sci. Technol. Nucl. Install. 2010, 1–17.
Dupleac, D., Mladin, M., Prisecaru, I., Oct. 2009. Generic CANDU 6 plant severe accident analysis employing SCAPSIM/RELAP5 code. Nucl. Eng. Des. 239 (10), 2093–2103.
Tong, L.L., Chen, J.B., Cao, X.W., Deng, J., Jul. 2014. Thermal hydraulic behavior under Station Blackout for CANDU6. Prog. Nucl. Energy 74, 176–183.
A. Bonelli, O. Mazzantini, D. Dupleac, E. Dinca, RELAP/SCDAPSIM/MOD3.6 – Development of Severe Accident Models for Heavy Water Reactors Including CANDU and ATUCHA-2. In: Proceedings of ICAPP, 2015.
Hedley, J.B., Chin, T., 2007. User's Manual GEOFAC. AECL 153-114160-UM-001.
Mathew, P.M., 1989. Emittance of Zr-4 sheath at high temperature in Argon and steam atmospheres, 10th Annual CNS Conference.
Aydogdu, K., 2004. Moderator-system and shield-cooling system heat loads after reactor shutdown for CANDU 6 reactors, 25th Annual Conference of CNS, pp. 1–17.
Whittier, A.C., Black, D.W., Boss, C.R., 1977. CANDU Channel Decay Power, AECL-5704.
Naundorf, D., Yin, J., Petruzzi, A., 2011. RELAP5 Simulation of Darlington Nuclear Generating Station Loss of Flow Event, International Agreement Report.
Soedijono, P., Osamusali, S., Tahir, A., Wan, P., 2001. A mechanistic model to predict ΔPHH under two-phase natural circulation flow and comparison against experimental results in RD-14M. In: 22nd Annual Conference of CNS, pp. 1–25.
D'Auria, F., Galassi, G.M., 1990. Characterization of instabilities during two-phase natural circulation in typical PWR conditions. Exp. Therm. Fluid Sci. 3 (6), 641–650.

4. SA Model Development and Validation

About this Paper

Citation:

F. Zhou, D. R. Novog, L. J. Siefken & C. M. Allison (2018): Development and Benchmarking of Mechanistic Channel Deformation Models in RELAP/SCDAPSIM/ MOD3.6 for CANDU Severe Accident Analysis, Nuclear Science and Engineering, DOI: 10.1080/00295639.2018.1442060

Contribution to Knowledge

This paper made a step towards the mechanistic modelling of CANDU severe accidents by replacing the threshold models in a severe accident code (RELAP/SCDAPSIM/MOD3.6) with the developed mechanistic models for several key severe accident phenomena. This includes models for pressure tube ballooning and sagging during the fuel channel heat-up phase, and models for the sagging and disassembly of fuel channel assemblies during the core disassembly phase.

The pressure tube ballooning and contact conductance models were modified from the MATLAB model developed by A. Cziraky [59] (whose work was originally based on the work by J. Luxat [60] and M. Yovanovich [61]). The pressure tube sagging model and the fuel channel sagging model were developed from scratch using classical beam theory (similar to the AECL code CREEPSAG described in the paper by G. Gillespie [62]). The models were benchmarked against some PT deformation tests with good agreement between model predictions and experimental measurements. In this paper, the detailed descriptions of models, and their benchmarking against experiments were presented as well as an extensive review of the relevant studies.

This work made important improvements in the RELAP/SCDAPSIM code (originally developed for LWRs) for application to CANDU severe accident analysis. With the modified MOD3.6 PT deformation phenomena can be mechanistically modeled, and the feedback on the thermal-resistance across the annulus gap is taken into account. The simple threshold model for predicting channel failure and channel disassembly has been replaced with more mechanistic treatments. The thermal and mechanical interactions between channels at different rows which can occur during the core disassembly phases of a CANDU severe accident have also been included based on the adaptation of several mechanistic models.

<u>Author's Contribution to Paper</u>

The author (F. Zhou) is the primary contributor to this paper. Research work for this paper was done in parallel with that of the first paper in Chapter 3. The original idea, which was determined by F. Zhou and the co-author (D.R. Novog), was to develop several mechanistic deformation models using Python, and to externally couple them with RELAP5/MOD3.3 for the simulation of later-stage SBO. A new version of the RELAP/SCDAPSIM code (i.e. MOD3.6) was being planned by Innovative System Software (ISS) to support the severe accident analysis for PHWRs. To take advantage of the existing severe accident models in MOD3.6 Zhou and Novog switched to MOD3.6 as the base for model development. In the fall of 2015, the co-author (C. M. Allison) provided Zhou and Novog with the source code of an early version of MOD3.6 and the code development training.

All background investigation, the development/programming/testing of the models, and the benchmarking against experiments were performed entirely by F. Zhou with guidance from D.R. Novog. The co-authors (L. J. Siefken and C.M. Allison) contributed significantly through technical and source-code support (especially L. J. Siefken). This paper also benefited from the existing models / modifications that were developed / made by L. J. Siefken and C.M. Allison in MOD3.6 for non-CANDU specific phenomena. The writing of the paper was primarily done by F. Zhou, with significant contribution to the editing of the paper from D.R. Novog, and input from C. M. Allison. The paper was submitted to Nuclear Science and Engineering on Nov. 30, 2017, and was accepted for publication on Feb. 14, 2018 after one minor revision.

NUCLEAR SCIENCE AND ENGINEERING · VOLUME 190 · 209–237 · JUNE 2018

DOI: https://doi.org/10.1080/00295639.2018.1442060

Development and Benchmarking of Mechanistic Channel Deformation Models in RELAP/SCDAPSIM/MOD3.6 for CANDU Severe Accident Analysis

F. Zhou,[a*] D. R. Novog,[a] L. J. Siefken,[b] and C. M. Allison[b]
[a]*McMaster University, Hamilton, Ontario, Canada*
[b]*Innovative Systems Software, Ammon, Idaho*

Received November 30, 2017
Accepted for Publication February 14, 2018

Abstract — *In different stages of postulated severe accidents in CANDU reactors, the fuel channels may experience a series of thermomechanical deformations, some of which may have significant impacts on accident progression; however, they have not been mechanistically modeled by integrated severe accident codes such as MAAP-CANDU and SCDAP/RELAP5. This paper focuses on the development and benchmarking of mechanistic models for pressure tube (PT) ballooning and sagging phenomena during the fuel channel heatup phase as well as for the sagging of fuel channel assemblies during the core disassembly phase. These models, which are based on existing phenomena in literature, are coupled with RELAP5 and/or integrated into RELAP/SCDAPSIM/MOD3.6 as new SCDAP subroutines to provide more robust treatment of the deformation phases of severe accidents.*

The ballooning of a PT will lead to contact with its calandria tube (CT) and occurs during conditions where the coolant pressure is moderately high. At initial contact the high contact thermal conductance and the large temperature difference between the two tubes result in a large transient heat flux that challenges the channel integrity through potential film boiling on the outer calandria surface if moderator subcooling is low. A one-dimensional ballooning and contact model (BALLON) has been developed. BALLON calculates the ballooning-driven transverse strain of PT and CT and modifies the effective conductivity of the annulus before and after contact.

Pressure tube sagging is the dominant deformation mechanism at low pressures and occurs at relatively high PT temperatures. A model based on simple beam theory (SAGPT) has been developed. SAGPT calculates the longitudinal strain and the deflection of PT, and it also determines PT-to-CT sagging contact. The sagging and disassembly of the entire fuel channel assembly occur when the fuel channels are uncovered and the moderator heat sink is lost; thus, the entire PT-CT assembly sags together, possibly contacting channels at lower elevations. A model named SAGCH is created to track fuel channel assembly sagging after moderator boil off and also determines the extent of channel-to-channel contact, channel disassembly, suspended debris bed characteristics, and eventual core collapse.

This paper presents detailed descriptions of the models, the coupling schemes, and their benchmark against experiments, together with an extensive review of relevant studies in the literature.

Keywords — *CANDU severe accident, mechanistic models, RELAP/SCDAPSIM/MOD3.6.*

Note — *Some figures may be in color only in the electronic version.*

*E-mail: zhouf5@mcmaster.ca

I. INTRODUCTION

The CANDU[a] reactor fuel channel consists of a Zr-2.5wt%Nb pressure tube (PT) containing 12 or 13

[a] CANDU is a registered trademark of AECL.

fuel bundles. The PT is surrounded by a Zircaloy-2 calandria tube (CT) that is contained in a large calandria vessel (CV) filled with heavy water acting as moderator. The two CT ends are rolled into the lattice tube ends at the inner tube sheets of the calandria, while the PTs are connected to the end fittings at two ends by rolled joints. The annulus between the PT and the CT is filled with CO_2 to insulate the high-temperature PT from the lower-temperature CT. Four garter springs within the annulus support the PT and prevent PT-to-CT contact during normal operation. Under accident conditions where channel heatup cannot be precluded, the fuel channel may undergo a variety of deformations since the range of accident conditions (pressures, temperatures, liquid stratification, and moderator liquid environment) may be diverse and dependent on system and operator responses.

If the internal pressure is high (>1 MPa), the dominant PT deformation mechanism when the PT experiences overheating is ballooning; i.e., the PT expands radially toward the CT as a result of transverse creep strain under hoop stress. If the circumferential temperature distribution of the PT is relatively uniform, the PT will balloon into contact with its CT establishing an effective heat pathway to the moderator. The PT under nonuniform temperature gradients will experience nonuniform transverse creep strain that may potentially lead to early PT failure before PT-to-CT contact occurs. If the average circumferential strain of the PT reaches approximately 16% (i.e., the strain required for the PT to balloon and fully contact the CT) before the local strain at a hot spot reaches the failure limit, PT failure is prevented provided that the CT remains sufficiently cooled.

A number of models have been developed by other researchers for ballooning of PTs. The majority of them use the creep strain rate equation for Zr-2.5wt%Nb developed by Shewfelt et al.[1] The TRAN II code assumes that the PT circumferential temperature is uniform and uses only the average temperature to predict transverse strain.[2] More advanced models, e.g., GRAD (Ref. 3) and NUBALL (Ref. 4), divide the circumference into sectors. The strain of each sector is calculated independently based on its local temperature and stress. It is often assumed that the PT remains circular during ballooning. Although, this circular assumption precludes the possibility of local PT-to-CT contact, these models are found to predict the ballooning of PT in experiments reasonably well. An improved model to predict noncircular PT deformation has been developed by Lei and Fan,[5] aiming to improve accuracy when circumferential temperature gradients are large and the model allows the hottest area of the PT to deform into contact with the CT first.

At initial ballooning contact, a large heat flux spike into the moderator is expected due to the high contact conductance and large temperature difference between the PT and the CT. This transient heat flux may exceed the critical heat flux (CHF) for the moderator fluid that cools the CT causing film boiling on the CT external surface. Depending on the moderator subcooling and the contact temperature, this film boiling may be characterized as either (a) complete film boiling, i.e., the entire surface covered in film, or (b) patchy film boiling, i.e., patches of film surrounded by an area of nucleate boiling. A number of PT contact boiling experiments have been conducted since the 1980s to determine the moderator subcooling requirements necessary to demonstrate the moderator heat sink capability during accidents[6–9] and/or to evaluate the CT strain acceptance criteria.[10] A review of some of the experiments is carried out in Sec. IV.A of this paper. These experiments showed that in most cases film boiling patches will be cooled and rewet quickly due to heat transfer to surrounding regions of nucleate boiling.[6,7] However, for cases at low moderator subcoolings and high heat fluxes, rewetting may be prevented causing both the PT and the CT to overheat, strain, and fail.[8,10]

Gillespie[6] developed a one-dimensional (1-D) program called WALLR to predict the transient behavior following PT-CT contact. The heat conduction solutions across the PT and the CT were obtained using a finite element method imposing a specified incident heat flux on the PT inside surface. The heat transfer correlation for the CT outside surface was defined for four flow regimes, i.e., subcooled, nucleate boiling, transition boiling, and film boiling. Zuber's correlation[11] was used to predict the CHF for saturated water whereas Thibault's correlation[12] was used to account for subcooling effects. After PT-CT contact, the model used a constant contact conductance of 11 $kW/m^2{\cdot}K$ that resulted in the correct qualitative prediction of film boiling for experiments with an internal pressure greater than 1 MPa. However, the rewetting of film was not correctly predicted.

Gillespie et al.[7] later developed a similar model named CONTACT that was used to predict a new experimental test conducted in nearly saturated water. In this test, film boiling occurs over the entire CT circumference resulting in relatively uniform temperature. The model with a constant contact conductance of 11 $kW/m^2{\cdot}K$ successfully predicted the heatup, the contact timing/temperature, and the onset of film boiling. However, during film boiling the heat flows were not accurately modeled with the PT temperature being underpredicted and the CT temperature being overpredicted, indicating that the actual contact conductance during film boiling was lower than 11 $kW/m^2{\cdot}K$.

Luxat[13] developed a lumped-parameter model to study the heat transfer process during PT-CT ballooning contact.

He postulated that the contact conductance between the PT and the CT is high at initial contact but will decrease rapidly thereafter due to changes in the thermal expansion of two tubes during the temperature transient. The modified Zuber's correlation[14] was suggested for saturated pool boiling CHF with the Ivey and Morris correction factor[14] to account for subcooling. It was found that by using the minimum film boiling temperature method, the measured duration of dryout time was well predicted and that the film boiling behavior is governed by the postcontact heat transfer to the PT as well as by the moderator subcooling. If the CT did not quench and the postdryout CT temperature is sufficiently high, channel failure will occur. A CT quench limit curve and a fuel channel integrity map were then provided.

This approach was extended by Cziraky[15] for PT-CT ballooning contact. The contact pressure was iteratively solved by equating the creep strain rate equations of the PT and the CT. The correlation developed by Yovanovich[16] was then used to calculate the contact conductance for both the initial-contact and the postcontact phases. This approach predicted very high contact conductance at initial contact followed by a rapid decrease in conductance, which is consistent with experiments.[17,18]

Dion[19] recently continued these developments by improving the heat transfer modeling on the CT external surface. In his work two different approaches were used to calculate the heat transfer coefficient on the CT under film boiling conditions. First, the pool film boiling correlation by Gillespie and Moyer[20] was used after CHF is exceeded, and the minimum film boiling temperature correlation by Bradfield[21] was used to determine quenching. The model accurately predicted the PT and CT temperature transient for most tests with and without sustained film boiling[8] but failed to predict the test where quench occurred shortly after initial dryout. Second, a mechanistic film boiling model based on the work by Jiang and Luxat[22] was used to calculate the energy balance across the film and predict the film thickness. Better results were obtained with the second approach, and the quenching was accurately predicted.

During the fuel channel heatup phase when the internal pressure is low (<1 MPa), the dominant deformation mechanism is PT sagging. Sagging occurs during $\alpha + \beta \rightarrow \beta$ phase transformation; thus, the temperature at which the deflection becomes noticeable is higher than that associated with ballooning phenomena. As the PT sags downward, it will contact its CT. The contact pressure and contact area are much smaller compared to ballooning contact. In the short term or during the accident, this sagging contact is less of a concern as it is not likely to cause extensive film boiling on the CT outer surface. However, if sagging contact occurs during normal operation, the contact may cause significant changes in thermal field inside the PT, which results in hydrogen migration and hydride blister formation leading to PT failure after a prolonged period of time.[23]

CREEPSAG is a computer program developed by Atomic Energy of Canada Limited[24] (AECL) to analyze the bending deflection of a PT. It uses beam theory and simplifies the PT into a long thin beam with two fixed ends (also supported by garter springs). The support forces at the garter springs and the two rolled joints are determined prior to the calculation of tube deflection at each time step. The longitudinal creep strain rate in CREEPSAG is based on the work by Shewfelt and Lyall.[25]

PT-CT ballooning/sagging contact lowers the maximum fuel assembly temperatures and delays channel failure by allowing heat flow to the surrounding moderator liquid. Under prolonged accident conditions, the heat deposited into the moderator may initiate boiling, thereby depleting the moderator inventory and lowering the liquid level. As the moderator level decreases, channels at higher elevations in the calandria are uncovered. The uncovered channel assembly will then quickly heat up (since moderator liquid contact with the channel is lost), sag, and contact the lower channels. As the degree of channel sagging increases, the fuel channel may separate at its bundle junctions transferring its load to the lower-elevation channels.

When simulating a postulated severe accident, many existing computational tools utilize user-input threshold temperatures to determine PT-to-CT contact, channel failure, and disassembly, e.g., in MAAP-CANDU (Ref. 26), ISAAC (Ref. 27), and SCDAP/RELAP5 (Refs. 28 and 29). While such threshold models are simple and easy to integrate in large computer programs, they preclude best-estimate analyses and do not easily allow the quantification of uncertainty. To quantitatively study the impact of these phenomena on accident progression, three mechanistic models that can be coupled with the system code RELAP5—i.e., BALLON, SAGPT, and SAGCH—have been developed:

1. BALLON calculates the transverse strain of the PT and the CT and the contact conductance after ballooning contact.

2. SAGPT calculates the longitudinal strain and the deflection of the PT and determines the PT-CT sagging contact.

3. SAGCH models the sagging of an entire fuel channel assembly after uncovery, determines channel-to-channel contact, and calculates CT-CT contact heat transfer.

Two different coupling methods are used that transfer the local thermal-hydraulic conditions from RELAP to the mechanistic models. The first one uses a Python script to externally couple these models with RELAP5/MOD3.3 (Ref. 30) in which the PT-annulus-CT structure is represented by a RELAP5 heat structure. Such external coupling allows for easy integration with existing RELAP5 executables and for testing of individual models.

In the second coupling method, these models are integrated into the RELAP/SCDAPSIM/MOD3.6 source code. The RELAP/SCDAPSIM code is being developed at Innovative Systems Software as part of the international nuclear technology program called SDTP (SCDAP Development and Training Program).[31] The as-received version, i.e., MOD3.6, is being developed to support the analysis of pressurized heavy water reactors (PHWRs) under severe accident conditions.[32] The models are integrated using new SCDAP subroutines, and the PT-annulus-CT is represented by the SCDAP shroud component, which gains additional capabilities to model two-dimensional (2-D) conduction and various severe accident phenomena. Direct integration of the models into the SCDAP source code allows for efficient coupling reducing the computational overhead. The main purposes of this paper are to introduce these models and the two coupling methods and to benchmark them against several PT deformation experiments.

II. MODEL DESCRIPTION

II.A. Model for PT Ballooning: BALLON

Since the 1-D RELAP5 code cannot predict the circumferential temperature variation on the PT, the 1-D PT ballooning model BALLON, which uses the average temperature along the PT circumference and predicts the average strain, is developed (Fig. 1). The transverse strain is calculated independently at each axial location of a channel. The thin-wall assumption is used when calculating the hoop stresses since the thicknesses of the PT and the CT are relatively small compared to their diameters.

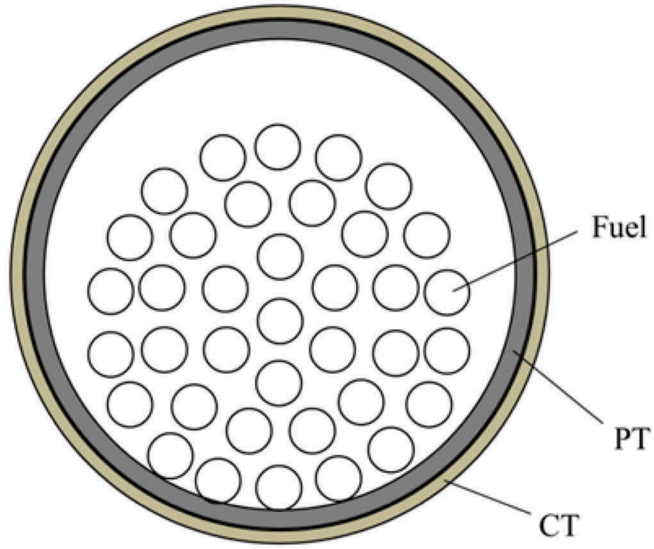

Fig. 1. The PT ballooned into contact with the CT.

II.A.1. Pressure Tube Creep Strain Rate Equation

For temperatures below 450°C, the creep strain rate of the PT is assumed to be zero. For temperatures between 450°C and 850°C, the creep deformation of the PT is due to two mechanisms, i.e., power law creep in α-phase and grain boundary sliding.[1] Thus, the creep rate is the sum of two terms:

$$\begin{aligned}\dot{\varepsilon}_{pt} &= \dot{\varepsilon}_{\alpha} + \dot{\varepsilon}_{gb} \\ &= 1.3 \times 10^{-5}\sigma_{pt}^{9}\exp\left(-\frac{36600}{T}\right) \\ &\quad + \frac{5.7 \times 10^{7}\sigma_{pt}^{1.8}\exp\left(-\frac{29200}{T}\right)}{\left[1 + 2 \times 10^{10}\int_{t1}^{t}\exp(-29200/T)dt\right]^{0.42}} , \qquad (1)\end{aligned}$$

where t_1 is the time when $T = 700°C$ and the denominator of $\dot{\varepsilon}_{gb}$ is to account for the hardening due to grain growth for temperatures above 700°C.

For temperatures between 850°C and 1200°C, the creep rate equation of the PT is again the sum of two terms[1]:

$$\begin{aligned}\dot{\varepsilon}_{pt} &= \dot{\varepsilon}_{\beta} + \dot{\varepsilon}_{gb} \\ &= 10.4\sigma_{pt}^{3.4}\exp\left(-\frac{19600}{T}\right) \\ &\quad + \frac{3.5 \times 10^{4}\sigma_{pt}^{1.4}\exp\left(-\frac{19600}{T}\right)}{1 + 274\int_{t2}^{t}\exp\left(-\frac{19600}{T}\right)(T - 1105)^{3.72}dt} , \qquad (2)\end{aligned}$$

in which $\dot{\varepsilon}_{\beta}$ is due to power law creep in β-phase and $\dot{\varepsilon}_{gb}$ is due to grain boundary sliding. The denominator of $\dot{\varepsilon}_{gb}$ is to account for the hardening caused by rapid phase transformation above 850°C, and t_2 is the time when $T = 850°C$. Because $\dot{\varepsilon}_{gb}$ decreases rapidly, this term becomes negligible for temperatures above 950°C. Unless otherwise noted, T in all the equations of this paper is in the unit of kelvin.

II.A.2. Calandria Tube Creep Strain Rate Equation

The PT and the CT are made of different Zr alloys, i.e., Zr-2.5%Nb for the PT and Zr-2 for the CT. The transverse creep rate equation of the CT for temperatures below 850°C (for α-phase Zr-2) is the sum of a dislocation creep term and a grain boundary sliding term[33]:

$$\dot{\varepsilon}_{ct} = \dot{\varepsilon}_d + \dot{\varepsilon}_{gb} \ . \tag{3}$$

The dislocation creep term is given by the following empirical correlations:

$$\dot{\varepsilon}_d = 22000(\sigma_{ct} - \sigma_i)^{5.1}\exp(-34500/T_{ct}) \tag{4}$$

and

$$\sigma_i(t) = 1.4 + \int_0^t \left[110\,\dot{\varepsilon}_d - 3.5 \times 10^{10} \times \sigma_i^{1.8}\exp(-34500/T_{ct})\right]dt \ , \tag{5}$$

where σ_i is the internal stress in α-phase Zr-2. The grain boundary sliding term is given by the following correlation:

$$\dot{\varepsilon}_{gb} = 140\sigma_{ct}^{1.3}\exp(-19000/T_{ct}) \ . \tag{6}$$

II.A.3. Contact Conductance

Accurate prediction of the contact conductance is important not only in determining whether CHF is exceeded at initial contact but also in predicting postcontact PT/fuel temperatures and quenching. The contact conductance model used in this paper is based on the mechanistic model developed by Yovanovich,[16] in which the interfacial conductance is assumed to be the sum of two components, i.e., h_c due to metal-to-metal contact and h_g the conductance across the gas gap:

$$h = h_c + h_g \ , \tag{7}$$

$$h_c = 1.25\frac{k_s m}{\sigma}\left(\frac{P_c}{H_c}\right)^{0.95} \ , \tag{8}$$

and

$$h_g = \frac{k_g f_g}{Y + \alpha\beta\Lambda} \ , \tag{9}$$

where

P_c = contact pressure

m = mean surface asperity slope

σ = surface roughness

H_c = contact microhardness or effective hardness

Y = mean plane separation

$\alpha, \beta, \Lambda, f_g$ = correction terms

and H_c can be explicitly calculated:

$$\frac{P_c}{H_c} = \left[\frac{P_c}{1.62c_1(\sigma/\sigma_0 m)^{c_2}}\right]^{1/(1+0.071c_2)} \ , \tag{10}$$

in which c_1, c_2 are the Vickers correlation coefficient and the Vickers size index. Y is approximated using the following correlation:

$$\frac{Y}{\sigma} = 1.184\left[-\ln\left(3.132\frac{P_c}{H_c}\right)\right]^{0.547} \ . \tag{11}$$

Thus, in Yovanovich's model the conductance is a strong function of the contact pressure and contact microhardness. The same approach as in Cziraky's model[15] is used to estimate the contact pressure between two pipes, i.e., by equating the creep strain rate of the PT with that of the CT ($\dot{\varepsilon}_{pt} = \dot{\varepsilon}_{ct}$) and iteratively solving the equation for contact pressure.

II.A.4. Pressure Tube/Calandria Tube Failure Criteria

The PT failure criterion by Shewfelt and Godin[34] was validated for a wide range of experimental conditions; i.e., the PT is assumed to fail when the local transverse strain at any point exceeds the following:

$$\varepsilon_f = -\frac{1}{n}\ln\left[1 - \left(\frac{w_0 - d}{w_0}\right)^n\right] \ , \tag{12}$$

where

w_0 = initial wall thickness

d = maximum possible depth of a local defect

n = creep stress exponent.

However, Eq. (12) is a local failure criterion and cannot be used directly by BALLON, which is a 1-D model.

Experiments[3] have shown that for moderate circumferential temperature variation (30°C to 70°C), the specimens normally did not fail until the average creep strain of 20%

was reached (i.e., larger than the strain required for the PT to balloon and fully contact with the CT); for tests with more severe circumferential temperature distribution (>100°C), the specimens all failed at an average creep strain of less than 20%. The experiments were conducted in the absence of a CT; thus, the effect of CT constrain was not taken into account. The results confirmed that the PT-to-CT contact can be made before PT failure when no large temperature gradient is present. The model in the present work uses a user-input PT failure strain with its default value set to 20%.

After PT-to-CT contact, there are two possibilities. First, if the heat removal from the CT is sufficient to balance local energy deposition, expansion ceases due to the reduced temperatures. Second, if the heat removal is not sufficient, the PT will continue to expand together with its CT until channel failure occurs. An additional user-input CT transverse failure strain has been implemented in the model to determine postcontact channel failure. The default value is 2%, which is selected by the CANDU reactor industry based on experimental evidence from a number of full-scale contact boiling tests.[6,7] Results from new contact boiling tests conducted recently[10] also show that the experimental conditions leading to 2% CT strain are very close to the channel failure conditions.

II.A.5. CHF and Heat Transfer Correlations in RELAP5

RELAP5/MOD3.3 (hereinafter to be referred to as MOD3.3) has a large number of wall heat transfer correlations for 12 heat transfer modes, e.g., nucleate boiling, transition boiling, and film boiling. The code allows the user to specify the types of flow field (or hydraulic geometry). It uses built-in logic to select the appropriate heat transfer modes and heat transfer correlations for a specified geometry.[30] The default geometry (see Table I), i.e., type-101, is used for most situations, and all the other types modify some of the standard correlation of type-101.

Type-101 uses the Chen correlation[35] for both saturated and subcooled nucleate boiling. The subcooled liquid condition was taken into account using the bulk liquid temperature as the reference temperature for the convective part.[30] Chen et al.'s transition boiling model[36] was used for transition boiling. For film boiling, three heat transfer mechanisms are considered including conduction across a vapor film blanket next to a heated wall, convection to flowing vapor and between the vapor and droplets, and radiation across the film to a continuous liquid blanket or dispersed mixture of liquid droplets and vapor.[30] The Bromley correlation[37] was used as a model basis for conduction, the Dittus-Boelter with gas properties for convection, and the Sun et al. correlation[38] for radiation. The 1986 AECL-UO CHF lookup table by Groeneveld et al.[39] was used to predict CHF, and multiplying factors are applied to modify the table value.

The CHF lookup table in type-101 was mainly developed from small-diameter-tube data; thus, it may not fully represent the fluid conditions on the external surface of the CT (131 mm in diameter). Type-134 in MOD3.3, i.e., for horizontal tube bundles, is more representative of such conditions. This geometry type differs from type-101 only in the nucleate boiling, CHF, and natural convection correlations.[30] The Zuber correlation[11] for pool boiling CHF was used with the hydrodynamic boiling stability number K set to 0.14, i.e.,

$$CHF_{Tube} = 0.14 h_{fg}\left[\sigma g\left(\rho_f - \rho_g\right)\right]^{0.25}\left(\rho_g\right)^{0.5} , \qquad (13)$$

where

σ = liquid surface tension

g = gravitational constant

h_{fg} = difference between saturated vapor and saturated liquid enthalpy.

The subcooling effect on CHF is taken into account using the Ivey and Morris correction factor.[41] The Folkin and Goldberg[42] correlation was then used to account for liquid depletion:

TABLE I

Relevant Wall Heat Transfer Correlations in RELAP5/MOD3.3*

Geometry Type	Modes of Heat Transfer			CHF
	Nucleate Boiling	Transition Boiling	Film Boiling	
101 (default) 134	Chen[35] Forster and Zuber[40]	Chen et al.[36] Chen et al.[36]	Bromley[37] Bromley[37]	Lookup table[39] Zuber[11]

*Reference 30.

$$\mathrm{CHF}_{Bundle} = \mathrm{CHF}_{Tube}(1 - 1.175\alpha)\ . \quad (14)$$

Because the Zuber correlation with the Ivey and Morris correction factor is suggested by Luxat[13] and other researchers[19] for CHF prediction in the PT-to-CT contact boiling problems, type-134 is used on the outside surface of the CT heat structure in the external coupling method of this study (i.e., externally couple BALLON with MOD3.3).

While SCDAP in MOD3.6 uses the same heat transfer correlation package as MOD3.3, it does not allow the user to specify alternative geometries (i.e., correlations) for the outside of the shroud component. The default type is thus still used for the shroud component to simulate the CT in MOD3.6 (i.e., the CHF lookup table). Thus, the prediction of CHF on the outer surface of the CT may be inaccurate as compared to the external coupling method discussed above. To allow more accurate modeling of heat transfer behaviors from the CT to moderator, modifications are needed in the future for the outside surface of the shroud component to replace the default component with more flexible CHF and heat transfer correlations.

II.B. Model for PT Sagging: SAGPT

II.B.1. Basic Theory

Sagging of the PT is caused by longitudinal bending stress when the PT experiences overheating (Fig. 2). Table II summarizes the estimated weights of a CANDU reactor fuel channel and its contents. The loads causing it to sag are its own weight, the weight of the coolant (if there is any left), and the weight of the fuel bundles. Besides, the supports at the two ends of the PT are also supported by four evenly spaced garter springs (or spacers, with a distance of ~1 m). The model SAGPT is based on simple beam theory, and the PT is represented by a beam with two fixed ends consistent with the literature.[24] The load on the PT is assumed to be uniformly distributed and is estimated to be 588 N/m according to Table II (excluding the weight of the CT).

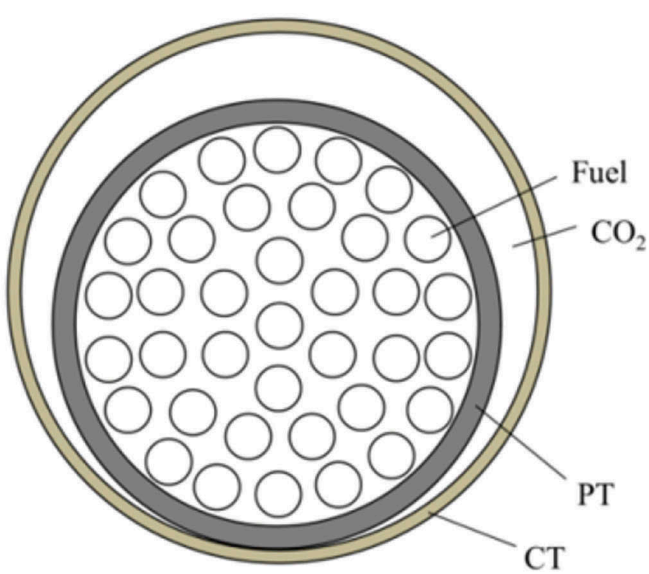

Fig. 2. The PT sagged into contact with the CT.

TABLE II

Estimated Weights of the Fuel Channel and Contents

Component/Item	Weight (kg)
Pressure tube (Zr-2.5wt%Nb)	58.8
Calandria tube (Zr-2)	22.3
Fuel bundle	283.8
Coolant	0 to 16.6
Other (garter springs, etc.)	~0

Spacers are assumed to be rigid in this work; i.e., they are not allowed to move or deform. The CT is assumed to be perfectly horizontal and provides supports to the PT via the four spacers. In the newer CANDU reactor designs, the spacers are tightly fitting springs made of Inconel X750. The PT sagging experiments showed that the garter springs were easily buckled during high-temperature tests leading to local deflection of the PT at the spacers.[24] PT-to-CT contact is desirable for mitigating accident consequences because the contact establishes the moderator as a heat sink and lowers the maximum channel temperature (provided that the channel is still submerged in moderator). The rigid spacer assumption is likely to delay contact thereby overpredicting the PT temperature at contact and the time to contact and is thus considered conservative. Future work will replace the rigid spacer assumption with a mechanistic spacer deformation model.

The deflection of the PT is the sum of elastic and plastic bending. The curvature of the beam due to elastic strain is

$$K_{el}(x,t) = \frac{M(x,t)}{E(x,t)I(x)}\ , \quad (15)$$

where

$M(x,t)$ = bending moment at x
$I(x)$ = moment of inertia of the pipe
$E(x,t)$ = Young's modulus, which is a function of temperature.

The longitudinal stress across a section at location x where the bending moment is $M(x)$ can be expressed as follows:

$$\sigma(x,t) = -\frac{M(x,t)c}{I(x)} , \tag{16}$$

where c is the distance to the centroid of the cross section. With the above stress, the longitudinal creep strain can be calculated by integrating the creep strain rate equation. The curvature of the beam due to plastic strain is

$$K_{pl}(x,t) = -\frac{\varepsilon(x,t)}{c} = -\frac{\int_0^t \dot{\varepsilon}(x,t)dt}{c} . \tag{17}$$

The total curvature is then the sum of elastic curvature and plastic curvature, i.e.,

$$\begin{aligned} K_t(x,t) &= K_{el}(x,t) + K_{pl}(x,t) \\ &= \frac{\frac{d^2y}{dx^2}}{\left[1+\left(\frac{dy}{dx}\right)^2\right]^{3/2}} \approx \frac{d^2y}{dx^2} . \end{aligned} \tag{18}$$

Deflection y can be calculated by integrating twice the curvatures along x.

II.B.2. Longitudinal Strain Rate Equation

The maximum bending stress in the center of the PT is about 1 MPa, which is significantly less than the hoop stress that may cause the PT to balloon (~12 MPa when the internal pressure is 1 MPa). The stress due to bending is thus insufficient to sustain plastic flow on its own, and the PT sagging mainly occurs during $\alpha + \beta \rightarrow \beta$ phase transformation,[25] i.e., between 610°C and 925°C. The internal stress caused by phase transformation together with the stress due to bending produces longitudinal strain. The contact between the PT and the CT due to sagging is normally made at PT temperatures well below 925°C (Ref. 24), implying that the PT is likely to have sagged into contact with its CT before significant Zr-steam reactions take place.

The longitudinal strain rate equation used in SAGPT is developed by Shewfelt and Lyall.[25] It can be expressed as follows:

$$\dot{\varepsilon} = 8 \times 10^{10} \sigma \exp\left(-\frac{26670}{T}\right)\left(K_2 - \frac{\varepsilon}{\sigma}\right)^{2.4} , \tag{19}$$

where K_2 is a function of temperature given by Table III. Between 800°C and 900°C, K_2 is obtained by linear interpolation between the two adjacent values.

This creep strain rate equation is based on data from constant-temperature and constant-stress experiments, while both the temperatures and the stresses are likely to change with time as the PT sags. Validation tests have been carried out by Shewfelt and Lyall[25] to validate the equation during actual transients. In these tests, the PT specimens were heated up at different rates but under constant stress. The data were compared to that predicted by the creep strain rate equation, and excellent agreement was observed.

In Eq. (19), $\frac{\varepsilon}{\sigma}$ is used to estimate the current volume fraction of β-phase at a given time because according to De Jong and Rathenau,[43] the strain caused by a phase transformation under constant stress varied linearly with the amount of material transformed, i.e.,

$$\varepsilon = K_1 \sigma (F - F_0) , \tag{20}$$

where F and F_0 are the current and the initial volume fractions of β-phase, respectively.[25] However, the linear relationship between the strain ε and $(F - F_0)$ no longer exists when σ is varying with time. To apply Eq. (19) to a situation where both the temperature and the stress are changing with time, the creep strain rate equation is modified in the current paper:

$$\dot{\varepsilon} = 8 \times 10^{10} \sigma(t) \times \exp\left(-\frac{26670}{T(t)}\right)\left(K_2 - \frac{\varepsilon_c}{\sigma_c}\right)^{2.4} , \tag{21}$$

TABLE III

Constant K_2 in the Longitudinal Creep Strain Rate Equation

Temperature (°C)	K_2 (MPa^{-1})
$T < 700$	0.0
$700 < T < 800$	0.0119
800	0.0119
825	0.0114
850	0.0167
875	0.0134
900	0.0100
$900 < T < 950$	0.0100
$T > 950$	0.0

where ε_c is the strain caused by constant stress σ_c under the same temperature transient $T(t)$, i.e.,

$$\varepsilon_c = \int_0^t \dot{\varepsilon}_c \, dt = \int_0^t \left[8 \times 10^{10} \sigma_c \times \exp\left(-\frac{26670}{T(t)} \right) \times \left(K_2 - \frac{\varepsilon_c}{\sigma_c} \right)^{2.4} \right] dt \ . \tag{22}$$

This is based on the fact that the rate of change of the volume fraction of β-phase is independent of the applied load and is a function of only temperature.

II.B.3. Boundary Conditions

The support reactions at two fixed ends and at the four garter springs are unknown. The six boundary conditions that are used to solve for the six unknowns can be expressed as follows:

$$\Delta\theta = \int_0^L K_{el}(x,t) + K_{pl}(x,t) dx = 0 \tag{23}$$

and

$$\Delta y_i = \int_0^{Li} \left[K_{el}(x,t) + K_{pl}(x,t) \right] (L_i - x) dx = 0 \ , \quad i = 1,\ 2,\ 3,\ 4,\ 5 \ . \tag{24}$$

$L_{1,\,2,\,3,\,4}$ are the distances from four garter springs to the left end while L_5 is the distance from the right end to the left ($L_5 = L$). Equation (23) means the change of slope from one end to the other is zero, while Eq. (24) means no vertical displacement is allowed at the garter springs as well as at the two fixed ends. The resulting linear equations are then solved using the Gauss-Elimination method. With the six support reactions, the bending moment at any location along the PT, i.e., $M(x)$, can be determined. The curvatures due to elastic and plastic strain are then calculated using Eqs. (15) through (18), and the deflections are found by integrating the curvatures along the axial direction.

II.C. Sagging of Uncovered Channels: SAGCH

When a fuel channel is submerged in the moderator, the CT is sufficiently cooled and thus has the strength to hold the PT and the fuel bundles. After the loss of moderator heat sink, the fuel and the PT heat up quickly together with the CT, which will soon lose its strength causing the entire fuel channel assembly to sag. Since the fuel channels in a CANDU reactor are vertically aligned (arranged in 24 rows and 24 columns for a 900-MW CANDU reactor), the sagged channel will eventually contact the lower channel transferring both heat (if at a higher temperature than the lower channel) and weight to the supporting channel. The supporting channel if also uncovered will sag under its own weight and the weight of the above channels.

As sagging increases, channel segments may separate near the individual bundle junctions[44] due to localized strain. These disassembled core parts relocate downward either to the bottom of the CV or fall onto the lower channel to form a suspended debris bed that is supported by the channels below the water level. When the mass of the suspended debris bed exceeds the strength of the supporting channels, the remaining channels are pulled out from one or both of their rolled joints at the two reactor faces, resulting in a core collapse to the bottom of the CV.

A model named SAGCH has been developed to mechanistically predict these phenomena during the core disassembly phase.[45] In the model, the entire channel is simplified as one beam with two fixed ends. The interactions between the fuel bundles and the PT as well as between the PT and the CT are not considered. Rather, they are modeled as a single structure. The Young's modulus of Zircaloy as a function of temperature (used by both the PT and the CT) is taken from Ref. 46, and the effects of oxidation, cold work, and fast neutrons on material properties are not taken into account. The load on the channel prior to any channel-to-channel contact is assumed to be uniformly distributed and is estimated to be 620 N/m (based on Table II). Since the longitudinal creep strain rate equation for the CT material (Zircaloy-2) is currently unavailable in the open literature, the CT is assumed to follow the same creep strain law as the PT, and Eq. (21) is used in the model.

Two boundary conditions are used: (1) The tangents to the deflection curvature at both ends are horizontal, and (2) the deflections at two ends are zero. These two boundary conditions are interpreted as follows:

$$\Delta\theta = \int_0^L K_{el}(x,t) + K_{pl}(x,t) dx = 0 \tag{25}$$

and

$$\Delta y = \int_0^L \left[K_{el}(x,t) + K_{pl}(x,t)\right](L-x)dx = 0 \ . \qquad (26)$$

The additional assumptions used in SAGCH are the following:

1. The buoyancy force acting on the CT is neglected since significant sagging of the fuel channel occurs only after its uncovery.

2. The interaction force between the two contacting channels is not dynamically calculated. To simplify the interaction, all the weight of the contacting part of the upper channel is assumed to be transferred to the lower channel.

III. COUPLING SCHEME

III.A. External Coupling with RELAP5/MOD3.3

To couple the above deformation models with system thermal hydraulics, two different methods were developed, one of which is the external coupling method taking advantage of the "strip" and "restart" options of RELAP5/MOD3.3. Figure 3 shows the flowchart of the external method. The RELAP5 input deck is adapted as follows:

1. A three-layer RELAP5 normal heat structure is used to represent the PT, annulus gap, and CT.

2. The material properties of the annulus (CO_2) are set as constants for a given time step so that they can be easily updated during restart.

3. External heat sources/sinks are added to the CT heat structure to model heat transfer between channels after channel assembly sagging and CT-to-CT contact.

4. Trip valves are used to connect the hydraulic volumes of the fuel channel and moderator; these valves remain closed until the PT mechanistic failure criteria are exceeded.

5. The conductivities of the annulus gap, the external heat sources/sinks, and the trip cards used to open the valves are updated during each coupling step.

As shown in Fig. 3, the script starts with an initial state simulation (for a specified time t_0) after which relevant data including the temperatures of the PT and the CT, the pressures of the fuel channel and the CV, etc., are stripped from the RELAP5 output files and written to a strip file. The script then uses the strip file data to calculate the PT/CT deformation (transverse and longitudinal strain, etc.). The geometries and strain of the PT and the CT are stored as global variables and are shared among the BALLON, SAGPT, and SAGCH models. To account for the reduced heat resistance across the annulus gap during ballooning or sagging, the effective conductivity k of the annulus region is updated based on the latest PT-CT geometries and is updated during each coupling step. The radiation across the annulus gap is modeled separately with the RELAP5 surface-to-surface radiation model.

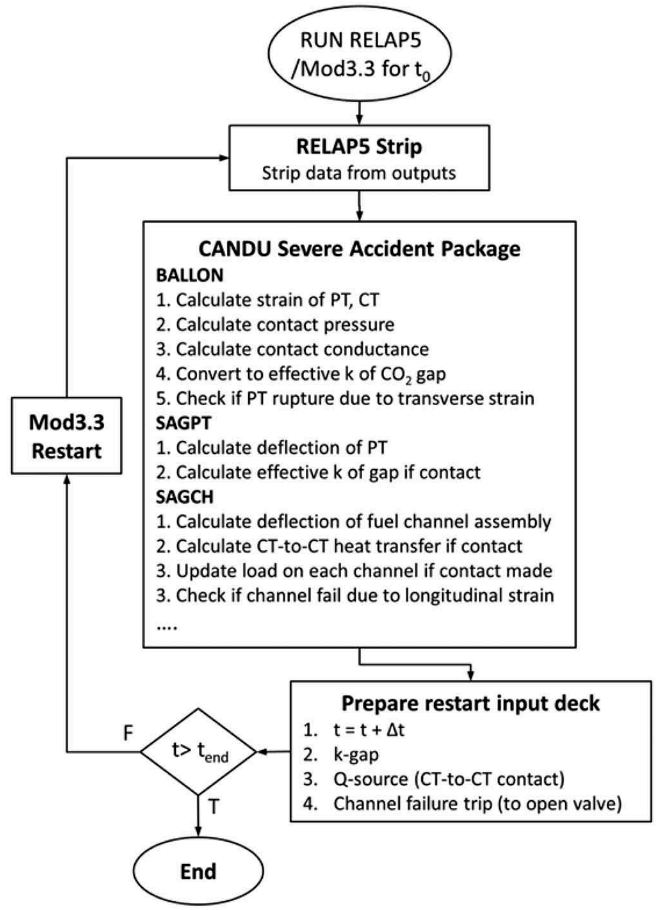

Fig. 3. Flowchart for external coupling.

III.B. Modified RELAP/SCDAPSIM/MOD3.6

The above external coupling method is limited by the characteristics of the RELAP5 heat structure: (1) The RELAP5 heat structure solves the heat conduction equations only in the radial direction; (2) there is a lack of models for other important severe accident phenomena such as the oxidation of Zircaloy and the liquefaction, relocation, and solidification of molten materials; and (3) the material properties of the annulus gap are shared by all axial nodes of a RELAP5 heat structure, which precludes the possibility of modeling local PT-CT contact heat transfer.

To resolve these issues, after testing each of the above developed models externally, each is then integrated into RELAP/SCDAPSIM/MOD3.6 (hereinafter to be referred to as MOD3.6) as new SCDAP subroutines. MOD3.6 is an integration of the RELAP5 code for thermal hydraulics, the SCDAP code for severe accident phenomena, and the COUPLE code for light water reactor lower vessel problems. The benefit of combining these mechanistic models with MOD3.6 is substantial. The SCDAP core components have several advantages over the RELAP5 heat structures: (1) The heat conduction equations are 2-D in both radial and axial directions; (2) there are well-developed severe accident models that can be used to model material oxidation, cladding deformation, fuel rod liquefaction, and relocation and other severe accident phenomena; and (3) several PHWR specific modeling improvements have already been implemented in MOD3.6, e.g., new modifications that have been made to account for the radiation heat transfer across the PT-CT annulus.[32]

When applying SCDAP/RELAP5 to CANDU reactors, a common approach is to use the SCDAP shroud component to represent the PT-CO_2-CT structure (e.g., in Refs. 28 and 47) due to their similarities in geometry and arrangement. The three mechanistic channel deformation models BALLON, SAGPT, and SAGCH are thus integrated into the SCDAP code mostly in the shroud-related subroutines. Figure 4 shows a detailed flow map of the newly added models in SCDAP.

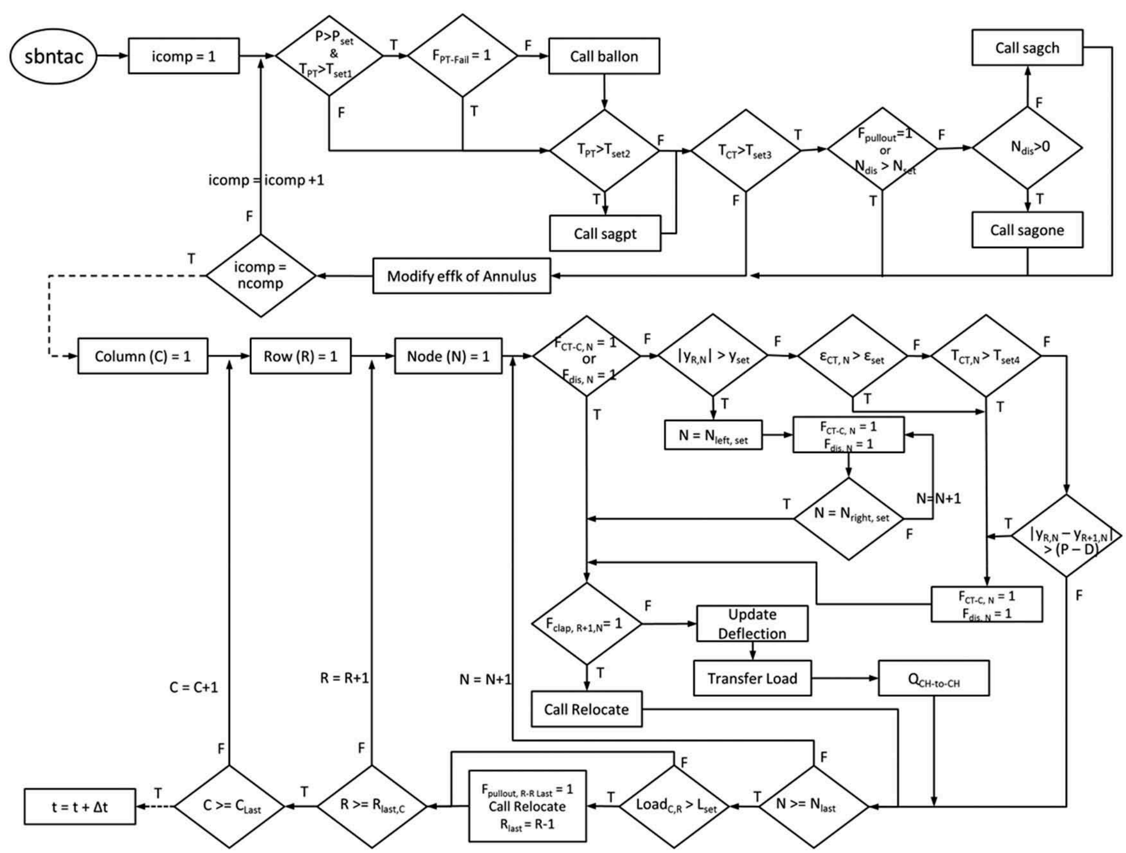

$F_{PT\text{-}C}$: PT-CT contact flag;
$F_{CT\text{-}C}$: CT-CT contact flag;
$F_{PT\text{-}Fail}$: PT rupture/breach flag;
F_{dis}: Channel (Ch.) disassemble fag;
F_{clap}: Flag indicating if the node has relocated to CV bottom;
$F_{pullout}$: Flag indicating if the channel has been pulled out;
N_{dis}: Number of Ch. segments that have disassembled;
N_{set}: Input number, if $N_{dis}>N_{set}$ stop tracking Ch. Sagging;
T_{set1}: Input T above which PT ballooning is significant;
T_{set2}: Input T above which PT sagging is significant;
T_{set3}: Input T above which Ch. sagging is significant;
T_{set4}: Zr melting temperature (default = 2033K);
P_{set}: Input P above which PT ballooning is significant;
ε: Longitudinal strain of CT;
ε_{set}: Input failure strain that may cause disintegration;
y_N: deflection of current node;
y_{set}: Input maximum allowed deflection before the channel disintegrate, and channel segments between $N_{left,set}$ to $N_{right,set}$ disassemble and relocate downward;
P: Lattice Pitch;
D: Diameter of CT;
C_{Last}: total number of columns;
R_{Last}: total number of rows left in current column;
N_{Last}: total number of axial nodes;
$Load_{C,R}$: load on current row (R) of column C;
L_{set}: Input maximum load the channel can support;

Fig. 4. Flowchart of new CANDU reactor severe accident models in RELAP/SCDAPSIM/MOD3.6.

III.B.1. Pressure Tube Deformation and Failure at High Pressure

Most of the modifications are made in "sbntac," which is the subroutine to drive all SCDAP components.[29] The PT ballooning phenomenon is modeled in the new subroutine "ballon," in which the gap distance between the PT and the CT are tracked and the contact pressure is calculated if contact has been made. The contact pressure is later used to calculate the PT-to-CT contact conductance using Eqs. (7), (8), and (9). The contact conductance is then converted to the effective conductivity of the annulus gap, and the corresponding material properties are updated. Users are allowed to input the pressure and the temperature thresholds (i.e., P_{set} and T_{set1} in Fig. 4), below which PT ballooning is considered insignificant and ballon will not be called. Otherwise, it will be called when the PT is predicted to fail. After channel failure, a trip valve if present in the input deck can be opened to establish a hydraulic connection between the fuel channel and the CV.

In the event of a station blackout, there is a period of time during the heat transport system inventory depletion phase when the coolant in the fuel channel is stagnant and horizontally stratified.[48] The top portion of the fuel channel is thus exposed to superheated steam and will experience high temperatures, while the lower portion is relatively cool. This leads to potentially large circumferential temperature gradients on the PT, and the PT may rupture early due to nonuniform creep strain before it contacts its CT. If the PT balloons into full contact with the CT without failure, the contact establishes the moderator as a heat sink, and PT failure will be delayed until such time as the heat transfer on the outside surface of the CT is deteriorated (e.g., as a result of fuel channel uncovery or sustained film boiling).

However, neither the RLEAP5 heat structures nor the SCDAP component solves the heat conduction in the circumferential direction, and only the average temperatures are used to calculate the creep strain of the PT and the CT. Thus, the current MOD3.6 code is not able to predict early channel failure under stratified flow conditions. This is also due to the limitations of the current version of the RELAP5 code on volume averaging and on horizontal heat structures. However, to examine the effect of early failures on accident progression, the user can lower the input PT failure strain to trigger early failure of a fuel channel assembly due to potential large circumferential temperature gradients.

The subroutine "sagpt," which is used to model sagging of the PT, is called after ballon is completed. The two subroutines sagpt and ballon share geometric variables such as the radius and the deflections of the PT. Thus, the code allows ballooning and sagging to occur simultaneously. By default, the 6-m-long PT in sagpt is discretized into 60 evenly spaced axial nodes with the four spacers located at 1.5, 2.5, 3.5, and 4.5 m, respectively. The number of nodes and the locations of the spacers can be easily changed from the input card. In sagpt the deflection of the PT at each node is calculated and is compared to the gap distance at the same location (which is updated in ballon) to determine whether the PT has sagged into contact with its CT.

In the PT sagging experiments by Gillespie et al.[24] the PT-to-CT contact developed into a contact patch approximately 0.5 m long (when the two garter springs are at a distance of 1.0 m) quite rapidly following initial contact, and the final measured maximum contact angle was about 20 deg. Given this rapid deformation, the transient growth of the contact patch is not dynamically modeled in sagpt. Rather, constant contact area and contact conductance are applied to the node where contact has occurred, as well as to its nearby nodes within the 0.5-m length of a bundle, and the model stops updating the creep strain of these nodes. The PT, however, is still allowed to deform and sag at other locations as such contact can be made at multilocations. The default contact length, contact angle, and contact conductance are 0.5 m, 10 deg, and 5.0 $kW/m^2 \cdot K$, respectively, which can also be changed via input cards. Since the heat conduction solution of the shroud component is 2-D (in the radial and the axial directions), the contact area and the conductance are converted to an effective conductivity of the annulus gas for the entire circumference of the corresponding axial nodes.

III.B.2. Channel Sagging and Disassembly

The subroutine "sagch" models the sagging of an entire fuel channel assembly. Before the channel contacts the lower assembly, it is modeled as one beam with two fixed ends (Fig. 5a). After channel-to-channel contact, there is interaction force between the two channels. If a channel is predicted to contact its lower channel at a certain axial node, this node is assumed to have disengaged from the rest of the channel with all the weight in the affected node transferred to the lower channel (Fig. 5b). The deflection/position of this node is updated according to the lower channel, while the deflections of the rest of the channel are updated in another subroutine "sagone," which considers a segment of the assembly from the fixed end to the position of contact thus modeling the channel as two separate beams each with one fixed end (Fig. 5c). Once the next node of the assembly contacts the lower channel, it also disengages, and its mass is transferred to the lower channel. In this manner the contact area increases node by node.

After the deflections of all the channels are updated in sagch and sagone, nested loops are used to calculate

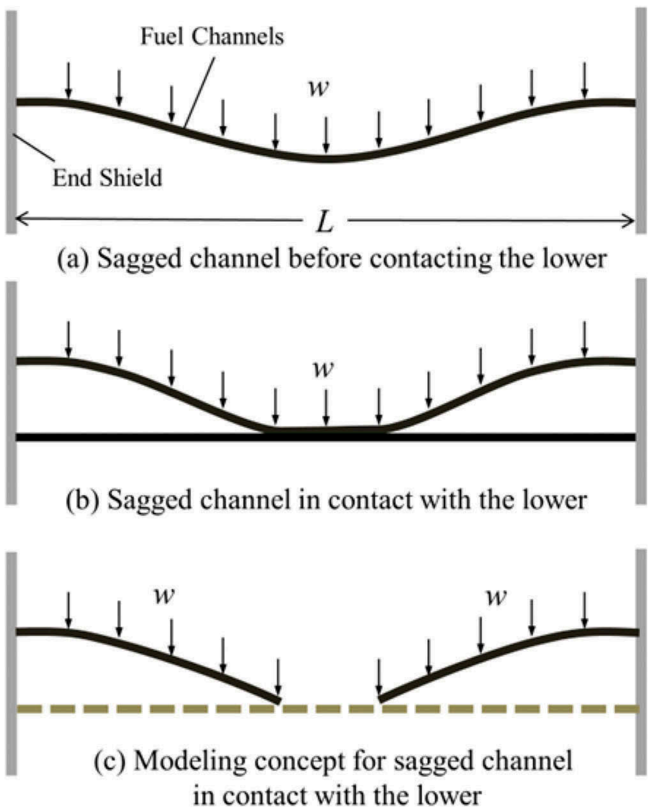

Fig. 5. Sagging of uncovered channels.

the nodal location of all channels in every column in the core in order to determine channel-to-channel contact, debris bed loads, disassembly of core parts, and core collapse (Fig. 4). A number of criteria are used to determine disassembly of a fuel channel or a segment of the channel assembly:

1. When the CT temperature of an axial node exceeds a user-input threshold (by default, the Zircaloy melting temperature, 2033 K), the corresponding node disassembles.

2. When the longitudinal strain of a node exceeds a user-input value (by default, 0.2), the corresponding node disassembles.

3. The channel is likely to have broken apart when it sags more than a distance of two to three lattice pitches.[49] Thus, an additional criterion is used to limit the extent of channel sagging when the maximum displacement of a node exceeds a user-input value (by default, two lattice pitches) at which point all nodes between N_{left} and N_{right} disassemble. N_{left} and N_{right} are user input (by default, the nodes corresponding to the third and tenth fuel bundles). This is based on the experimental evidence from the Core Disassembly Test Facility (CDF) at AECL. The posttest examination of a two-row channel test showed hot tears on the bottom side of a sagged channel about two bundle lengths away from the supporting ends.[50]

Similar to channel-to-channel sagging contact, after a node of the upper channel disassembles into contact with the lower channel, the weight of the node is transferred to the lower channel, and the deflection is updated according to the lower channel. If the lower channel has already collapsed, this node directly relocates to the bottom of the CV to join the terminal debris bed by calling the subroutine "relocate." Within the nested loops, the heat transferred from one channel to the other after contact is calculated and is taken into account by adding a heat source/sink term to the CT before the heat conduction equations are solved (Fig. 4).

III.B.3. Core Collapse and End Stub Behavior

The loads on all intact channels are updated every time step and are then compared to a user-input threshold to determine whether a channel has been pulled out from its rolled joint at the two ends. The buoyancy force acting on the submerged supporting channel is not taken into account when determining whether the threshold load has been exceeded. If this threshold is exceeded, all the channels below this channel in the same column are also pulled out. These pulled-out channels together with the supported suspended debris are then relocated to the bottom of the CV, i.e., core collapse in the subroutine relocate. It is also assumed that collapsing of a column will not affect the adjacent columns. Early studies showed that a submerged channel can support up to seven additional channels before it is pulled out of its rolled joint.[44] This number is used in MAAP4-CANDU to estimate the maximum suspended debris mass, i.e., 25 000 kg for most of the two-loop CANDU reactor plants (equivalent to 70 dry fueled channels).[27] In MAAP5-CANDU, a new version currently being developed to improve severe accident modeling in a CANDU reactor, this simple threshold value has been replaced with a more mechanistic criterion based on static beam loading calculation.[49] The maximum load on a single channel in MAAP5-CANDU is given by Eq. (27):

$$W_{chan\ max} = \frac{I_0 \sigma_{UTS}}{R_{CTo}} \left[\frac{12L}{L^2 + 2aL - 2a^2} \right] \{N\} , \qquad (27)$$

where

L = length of the CT

a = length of one side of the CT that is unloaded

R_{CTo} = CT outer radius

I_0 = moment of inertia of the CT, i.e., $I_0 = \frac{\pi}{16}\left(R^4_{CTo} - R^4_{CTi}\right)$

σ_{UTS} = ultimate tensile stress (UTS) of the CT at a given temperature and can be estimated using Eq. (28):

$$\sigma_{UTS} = \sigma_{UTS0} - 1.08\left(T_{CT,\,ave} - 273.15\right)\{\text{MPa}\}\,, \qquad (28)$$

where σ_{UTS0} is the UTS of a CT at 0°C and $T_{CT,\,ave}$ is the average CT temperature. This mechanistic core collapse criterion has been implemented in MOD3.6. The user can also overwrite it with a simple threshold criterion for comparison to other severe accident codes that utilize such metrics.

The end stubs of the upper channels (those are not pulled out) are left on the tube sheet after core collapse. Two modeling options are available to decide the behavior of fuel bundles in the end stubs (the user can easily switch between the two by input card to examine sensitivities or uncertainties):

1. In the first option, the fuel bundles in the end stubs will slide out and relocate to the bottom of the CV after core collapse. Only the segments of the PT and the CT are left behind.

2. In the second option, the fuel bundle in the end stub will not slide out regardless of the slope of the PT holding it. In this case, the end stubs will continuously heat up and may disassemble/relocate downward at a later time if any of the aforementioned disassembly criteria are met. The heat conducted from the end stubs to the end shield is estimated to be negligible and thus is not modeled.

In the current modeling, the channel segments after disassembly will be completely supported by the lower channel of the same column (if present) to form a suspended debris bed until core collapsing occurs. However, there are other possible core disassembly pathways that are currently not considered; e.g., a portion of the debris may fall through the space available between the adjacent fuel assemblies and be relocated directly to the CV bottom. However, given the large number of reactivity mechanism supporting structures and instrumentation structures, the amount of lateral movement of the debris is limited. Future work may add these options to assist sensitivity studies in this area.

IV. MODEL BENCHMARK

The three developed mechanistic models BALLON, SAGPT, and SAGCH are benchmarked independently against experiments. The relevant experiments selected for model benchmarking are reviewed in Sec. IV.A. The results predicted by the models are presented in Secs. IV.B and IV.C.

IV.A. Review of Relevant Experiments

IV.A.1. Contact Boiling Tests by Gillespie in 1980s

Gillespie (1981) (Ref. 6) conducted a number of contact boiling tests at the AECL Whiteshell Laboratories. The experimental apparatus consisted of a 1.5-m PT surrounded by a 1.8-m CT (Fig. 6). The annulus between the PT and the CT was filled with CO_2. The PT was pressurized with helium and was internally heated by a 1-m electric heater. The CT was immersed in water that was heated by submerged steam lines. Prior to the test, the water in the tank was heated to the desired temperatures, and the pressure was raised to the desired value. The temperatures of the PT and the CT were monitored by thermocouples spot-welded to the surfaces.

The results of 13 tests with different combinations of heater power, internal pressure, and water temperature are reported in Ref. 6 (refer to Table IV for test conditions and results). The internal pressure in the experiments covered a range from 0.5 to 4 MPa and water subcooling from 15°C to 33°C. In all tests the film boiling occurred in patches that eventually rewet due to the heat conduction from regions of film boiling to regions of nucleate boiling. The other important observations are the following:

1. Temperature variation existed along the PT circumference. The top portion was hotter than the lower portion due to internal natural convection of helium. Thus, except for

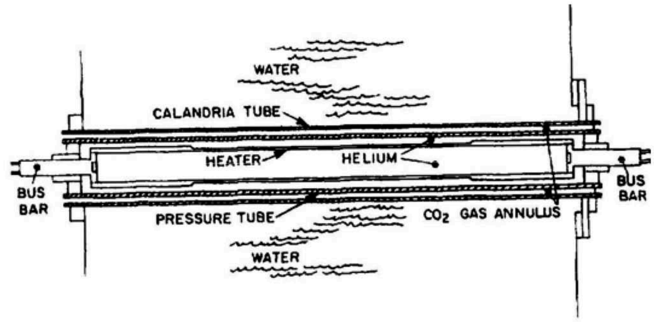

Fig. 6. Contact boiling experimental apparatus by Gillespie.[6]

TABLE IV

Experimental Conditions for Selected Contact Boiling Tests

Experiment	Test Code	Heater Power (kW/m)	Internal Pressure (MPa)	Water Temperature (°C)	Pressure Tube Contact Temperature (°C)	Measured CT Maximum Temperature (°C)	Type of Film Boiling	Time to Quench (s)	Time of Failure (s)
Gillespie, 1981 (Ref. 6)	G1	66[a]	4	67	760	112	No film	—	—
	G2	57[a]	4	85	760	495	Patchy film	30	—
	G3	66[a]	1	74	860	548	Patchy film	16	—
	G4	66[a]	1	67	860	117	No film	—	—
	G5	57[a]	2.5	77	760	110	No film	—	—
	G6	62[a]	4	81	750	117[b]	Patchy film	10	—
	G7	66[a]	2.5	77	820	305	Patchy film	6	—
	G8	66[a]	2.5	77	800	360	Patchy film	10	—
	G10	62	4	85	750	270	Patchy film	12	—
	G11	62	2.8	85	820	549	Patchy film	25	—
	G12	84	1	85	1000	730	Patchy film	520	—
	G13	28	0.5	71	1070	109	No film	—	—
Gillespie et al., 1982 (Ref. 7)	G16	54 to 62	2	99	800	~750	Complete film	~318	—
Luxat, 2001 (Ref. 8)	HPCB2	120	6.6	70.2	715 to 750	280	No film	—	—
	HPCB8	141	10.0	42.0	—	—	—	—	84[c]
	HPCB12	135	6.5	71.6	715 to 755	220	No film	—	—
	HPCB13	68	4.0	80.1	760 to 780	440	Patchy film	~7	—
	SUBC1	200	3.5	80.0	780 to 850	740	Complete film	∞	75
	SUBC2	195	3.5	77.0	810 to 895	675	Complete film	∞	97
IAEA, 2013 (Ref. 9)	ICSP	149	3.5	70.0	820 to 920	>650	Patchy film	25	—

[a]Heater power was turned off as soon as possible after contact.
[b]Thermocouple outside the film boiling area.
[c]Pressure tube fail prior to the contact with CT.

tests with low pressure (≤1 MPa), the PT top normally contacts the CT first.

2. Film boiling did not occur over the portion of the CT where the first contact was made. The first contact was too light to result in a sufficiently high contact conductance for the initial heat flux to exceed the local CHF. Film boiling occurred after the PT had expanded fully to fill the CT and in the area where contact was last made.

Gillespie et al. (1982) (Ref. 7) later added another case (test G16 in Table IV) where the test was conducted at nearly saturated water (99°C). The film boiling thus occurred completely over the entire CT surface resulting in relatively uniform temperature. This test is suitable for the benchmark of the 1-D model.

IV.A.2. New Contact Boiling Tests

The experiments used by Dion[19] for his model validation were conducted by Luxat[8] in association with Ontario Power Generation. Luxat's experimental apparatus (Fig. 7) consisted of a section of CANDU reactor fuel channel (approximately 1.7 m long) submerged in a pool of water. Inside the PT a 0.95-m-long, 19-mm-radius graphite heater was placed off center (toward the bottom) to promote a circumferentially uniform temperature distribution on the PT. Argon was supplied to the inside of the PT. A total of six tests were performed with a pressure ranging from 3.5 to 10 MPa and water subcooling from 19.9°C to 58.0°C (Table IV). In one of the tests, i.e., HPCB8, where the pressure was at 10 MPa, the PT ruptured before it contacted the CT. For the two tests conducted at 20°C and 23°C, subcooling with high heater power (i.e., SUBC1 and SUBC2), sustained film boiling occurred, and the CT failed shortly after contact. For the other tests, either no film boiling occurred or the film quenched shortly after contact.

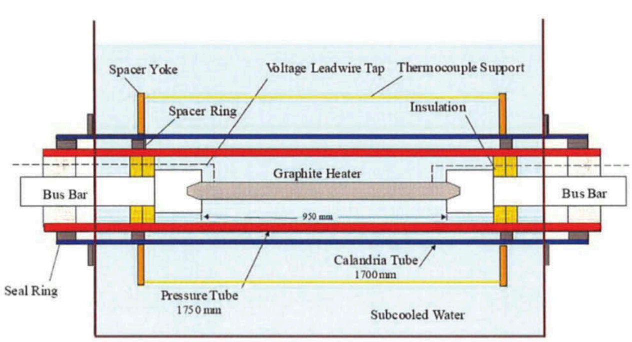

Fig. 7. New contact boiling experimental apparatus.[8,9]

Recently, a new test was conducted at the AECL Chalk River Laboratories under the International Atomic Energy Agency (IAEA) International Collaborative Standard Problem (ICSP) program.[9] The test section was almost identical to that used by Luxat.[8] The reported dimensions of the open water tank were 750-mm height, 1425-mm length, and 600-mm width with the CT placed approximately 425 mm from the bottom of the tank and 180 mm below the surface of the water (Fig. 7). The test conditions and results are again summarized in Table IV. In this test, initial contact occurred at 72 s resulting in 25% patchy film boiling for 25 s until full rewet. The reported maximum CT hoop strain (averaged around the circumference) was less than 0.4%.

IV.A.3. Pressure Tube Creep Sag Tests

Gillespie et al. (1984) (Ref. 24) carried out another set of experiments to investigate the creep bending of the PT. In these experiments (Fig. 8), a 3-m-long PT segment was rolled into the end fittings at two ends. The heaters and other materials in the PT had the same weight per meter as the CANDU reactor fuel bundles. The PTs were not pressurized. Thermocouples were spot-welded to the surface of the PT to record temperatures. The power of the heaters was varied to obtain a linear temperature ramp at the center plane of the PT. Linearly varying deflection transformers (LVDTs) were

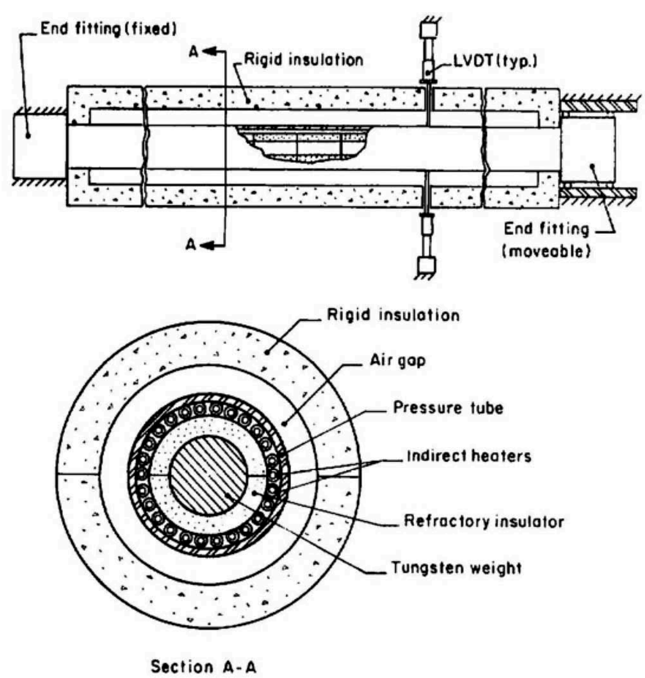

Fig. 8. Experimental apparatus for PT creep sag tests.[24]

used to record the deflections of the PT. Two series of tests were carried out: series 1 and series 2.

In the series 1 tests, the PT was surrounded by a 30-mm air gap and then by solid insulation. The test conditions are summarized in Table V. Although there was a steep temperature gradient near the two rolled joints, the temperature was nearly uniform over the central 2.6 m (except for experiment 1.6, where an axial temperature gradient was imposed).

In the series 2 tests, the solid insulation was replaced with a CT so that the PT contacted the CT during the tests. The test section was then placed in a water tank. Experiments 2.1 and 2.2 (Table VI) did not use garter springs, while experiments 2.3 and 2.4 both used two normal garter springs that were found to have deformed significantly during the test. Similar behaviors were also observed for the garter springs in the series 1 tests. Experiment 2.5 thus replaced the normal garter springs with 25-mm-long solid spacers. This resulted in a longer time to contact and thus a higher contact temperature. The water temperatures in some of the tests were set near saturation. Thus, the sagging contact caused patches of film boiling at the CT bottom. These dryout patches quenched shortly due to heat conduction to regions of nucleate boiling, but this resulted in oxide patches on the CT surface, which was a good indication of the contact width. The measured maximum width of the oxide patch was 20 mm (equivalent to 20 deg).

IV.B. BALLON Benchmark

IV.B.1. Model Descriptions for BALLON Benchmark

To benchmark BALLON, the contact boiling experiments introduced in Secs. IV.A.1 and IV.A.2 are simulated using the two coupling methods described in Secs. III.A and III.B, i.e., MOD3.3 externally coupled to BALLON (to be referred to as MOD3.3) and MOD3.6 with built-in deformation models (to be referred to as MOD3.6).

Figure 9 shows the RELAP5 nodalization of the fuel channel and water tank for the IAEA contact boiling tests[9] (used by both MOD3.3 and MOD3.6). The volume inside the PT is represented by a pipe component with 12 hydraulic cells initially filled with noncondensable gas (argon). The six central cells are linked to the surface of the 0.9-m-long graphite heater that is represented as a RELAP5 heat structure in MOD3.3 and a SCDAP simulator component in MOD3.6. The power along the heater is assumed to be uniformly distributed. The PT-CO_2-CT structure is modeled with a three-layer RELAP5 heat structure in MOD3.3 and the SCDAP shroud component in MOD3.6 with their inner surface linked to the cells of the channel and the outer surface to those of the water tank. The material properties for the graphite heater and the Zircaloy used in these models are as recommended by the IAEA ICSP workshop.[51] The same nodalization/input model is also used for the experiments by Luxat[8] because of the similarities in heater material and geometry. The channel power, the internal pressure, and the water temperature are varied for each test according to the test conditions in Table IV.

Different heater sizes and materials were used in the contact boiling tests by Gillespie[6] and Gillespie et al.,[7] and not enough details were provided in the literature. Thus, for these tests, the diameter and the specific heat capacity of the heater are modified to match as closely as possible the reported temperature ramps in tests G12 and G16, and the same input parameters are then used for all the other tests.

TABLE V

Experimental Conditions for Series 1 Tests

Experiment	Temperature Ramp (°C/s)	Garter Springs: Number	Garter Springs: Location (m)	LVDT Location (m)	Measured PT Temperature (°C)
1.1	3.0	0	—	1.5	820[a]
1.2	2.7	0	—	1.5	810[a]
1.3	3.3	1	1.5	1.0	890[b]
1.4	3.1	1	1.5	1.0	820[b]
1.5	2.8	1	1.5	1.0	860[b]
1.6	3.0[c]	0	—	1.5	890[a]

[a]Deflection is 20 mm.
[b]Deflection is 10 mm.
[c]Varied from 2.8 to 3.4 along the tube.

TABLE VI

Experimental Conditions for Series 2 Tests

Experiment	Temperature Ramp (°C/s)	Garter Springs		Water Temperature (°C)	Contact Temperature (°C)
		Number	Spacing (m)		
2.1	2.7	0	—	—	780
2.2	3.9	0	—	90	700
2.3	2.9	2	1.2	91	810
2.4	3.8	2	1.0	93	870
2.5[a]	2.4	2	1.0	93	940

[a]Solid spacer used to prevent garter spring deformation.

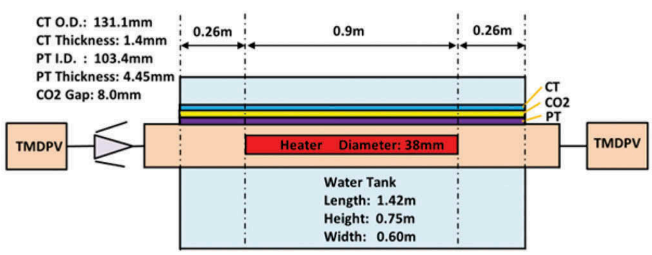

Fig. 9. RELAP5 model of the experimental apparatus for the new contact boiling tests.

IV.B.2. Contact Boiling Tests: BALLON Predictions

The results predicted by the RELAP5 heat structures with MOD3.3 and those by the SCDAP heat structures with MOD3.6 are summarized in Table VII. The predicted PT contact temperatures in most of the tests are reasonably close to the measured temperatures except for tests G12 and G13 where the PTs in the experiments contacted the CTs at very high temperatures. No significant differences between MOD3.3 and MOD3.6 in the predicted contact temperatures were observed.

The first eight tests (G1 through G8) of Gillespie's experiments were designed to investigate the occurrence of film boiling; thus, the heater power was turned off as soon as possible after contact. In tests G1, G4, and G5 with low contact temperature and/or high water subcooling, no film boiling was observed experimentally. MOD3.3, however, predicted film boiling in all the tests (Table VII). MOD3.6 showed better performance, and no film boiling was predicted in G1.

Figure 10 shows the contact boiling curves generated with data from the experiments in the 1980s (Refs. 6 and 7). The data from new contact boiling tests were also included. The predicted CHF limits (or curves) above which film boiling occurs are plotted. WALLR (Ref. 6) with a contact conductance of 11 kW/m^2·K correctly predicted the occurrence of film boiling for contact temperatures below 900°C. The film boiling curve by MOD3.3 with Yovanovich's model (MOD3.3 in Fig. 10) was significantly lower than that by WALLR. Since the CHF correlations of MOD3.3 (i.e., Zuber's correlation with the Ivey and Morris correction factor; type-134; see Sec. II.A.5) is similar to those used by WALLR, this difference is attributed to the contact conductance model.

Under these test conditions Yovanovich's model at initial contact predicts a peak conductance greater than 20 kW/m^2·K, which is likely to be overestimated as similar phenomena were also observed in the work by Dion.[19] A possible explanation is that Yovanovich's model was developed based on experiments conducted at low to moderate temperatures,[52] while the PT temperature at initial contact is high (typically greater than 750°C; see Table IV). In Yovanovich's model the contact conductance increases with increasing pressure-to-microhardness ratio. The Meyer hardness of Zircaloy (which is used to calculate the contact microhardness) decreases rapidly with increasing temperature.[46] The accuracy of the model used in this study with extremely low Meyer hardness at high temperatures can be questioned. After applying a maximum limit of 11 kW/m^2·K to the predicted contact conductance, MOD3.3 showed better agreement with the experiments (see MOD3.3b in Fig. 10). More research is recommended to extend the applicability of the Yovanovich model to avoid this overprediction.

However, MOD3.6 using Yovanovich's model without the 11 kW/m^2·K limit showed improved predictions compared to MOD3.3. This is because the SCDAP shroud component in MOD3.6 uses its default correlations to predict CHF as opposed to Zuber's correlation in MOD3.3. The overestimation of contact conductance at initial contact is thus mitigated by the overprediction in CHF in MOD3.6.

TABLE VII

Contact Boiling Tests Predicted by MOD3.3 and MOD3.6

Experiment	Test Code	Pressure Tube Contact Temperature (°C)			Calandria Tube Maximum Temperature (°C)			Time to Quench (s)			Maximum CT Strain (%)	
		Measured	MOD3.3	MOD3.6	Measured	MOD3.3	MOD3.6	Measured	MOD3.3	MOD3.6	MOD3.3	MOD3.6
Gillespie, 1981 (Ref. 6)	G1	760	766	765	112	492	169	—	18	—	0.01	0.00
	G2	760	760	761	495	523	536	30	32	33	0.05	0.08
	G3	860	853	849	548	587	608	16	27	33	0.01	0.01
	G4	860	852	848	117	572	576	—	22	25	0.00	0.00
	G5	760	788	790	110	529	544	—	25	28	0.01	0.03
	G6	750	765	762	117	514	524	10	27	29	0.04	0.05
	G7	820	797	794	305	536	548	6	26	29	0.02	0.04
	G8	800	797	794	360	536	548	10	26	29	0.02	0.04
	G10	750	763	764	270	530	583[a]	12	∞	∞	0.37[b]	2.0
	G11	820	791	786	549	548	606[a]	25	∞	∞	0.28[b]	2.0
	G12	1000	881	883	730	837[a]	842[a]	520	∞	∞	2.0	2.0
	G13	1070	852	845	109	539	569	—	21	32	0.00	0.00
Gillespie et al., 1982 (Ref. 7)	G16	800	810	802	750	821	690	318	353	315	52.3[c]	43.4[c]
Luxat, 2001 (Ref. 8)	HPCB2	715 to 750	745	750	280	485	164	—	19	—	0.10	0.00
	HPCB8	—	—	—	—	—	—	—	—	—	—	—
	HPCB12	715 to 755	756	750	220	493	164	—	23	—	0.18	0.00
	HPCB13	760 to 780	757	759	440	504	170	7	16	—	0.03	0.00
	SUBC1	780 to 850	803	810	740	669	615	∞	∞	∞	2.0	2.0
	SUBC2	810 to 895	796	807	675	618	588	∞	∞	∞	2.0	2.0
IAEA, 2013 (Ref. 9)	ICSP	820 to 920	790	799	650	540	174	25	37	—	0.36	0.00

[a]Calandria tube temperature at failure (CT strain > 2%).
[b]Sustained film boiling is predicted, but channel did not fail at the end of the simulation (350 s).
[c]Artificially high failure strain is used to prevent channel failure.

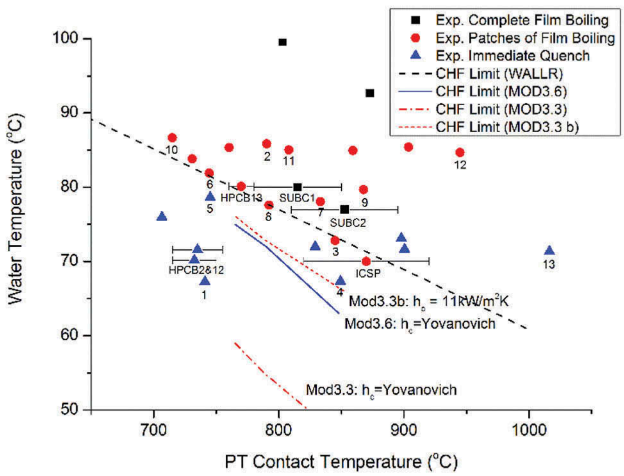

Fig. 10. Contact boiling curves showing relevant experiments (some data are from figure 2 in Ref. 9).

In Gillespie's experiments film boiling occurs in patches in all the tests except for test G16 where the tank water was near saturation. The patchy film boiling allows heat to be conducted from the dryout area to the area of nucleate boiling reducing the duration of film boiling. The 1-D models (MOD3.3 and MOD3.6) used here cannot predict such patchy film boiling phenomena. Film boiling, if predicted to occur, will cover the entire circumference. Furthermore, lacking the correct quench mechanism in RELAP5 leads to overestimation of the quench time as seen in Table VII.

Figure 11 shows the predicted and measured PT temperatures in test G12 where the heater power was left on after contact. In this test film boiling occurred on the top and the sides of the CT, while the bottom was in nucleate boiling with temperatures less than 130°C. The top-to-bottom heat conduction enhanced heat removal from the tube causing the tube to rewet. The CT top rewet at around 900 s, while the sides rewet much earlier since they are closer to the area of nucleate boiling. No significant CT deformation was observed experimentally even after more than 500 s of patchy film boiling. Both MOD3.3 and MOD3.6, however, fail to predict rewet. The CT experiences prolonged sustained film boiling, and failure is predicted to occur at approximately 150 s after contact. The failure of the code to predict quench is again attributed to 1-D simplification of the models and lack of a proper quench mechanism on large-diameter-tube surfaces.

Test G16, however, was performed in nearly saturated water. Film boiling thus occurred over the entire circumference after contact. The heater power was held constant at 54 kW/m for the first 250 s. The measured CT temperature during film boiling initially increased until the heat removed by water through the film balanced the incident heat flux on the PT, and then, it decreased slowly due to the increase in heat transfer area as the CT radially expanded (Fig. 12). The heater power was increased to 56 kW/m at 250 s and further to 62 kW/m at 300 s. The measured temperatures thus started to increase again but dropped rapidly at around 340 s due to heater failure.

The PT/CT temperatures predicted by MOD3.3 closely follow the temperatures measured at the PT/CT bottom until around 180 s when the CT strain becomes significant (Figs. 12 and 13). The increase in heat transfer area is not taken into account in MOD3.3, resulting in the overestimation of temperatures after 180 s. The temperatures predicted by MOD3.6 are lower than those predicted by MOD3.3. The measured final strain of the CT was 15%, which is significantly lower than that predicted by the models (Table VII).

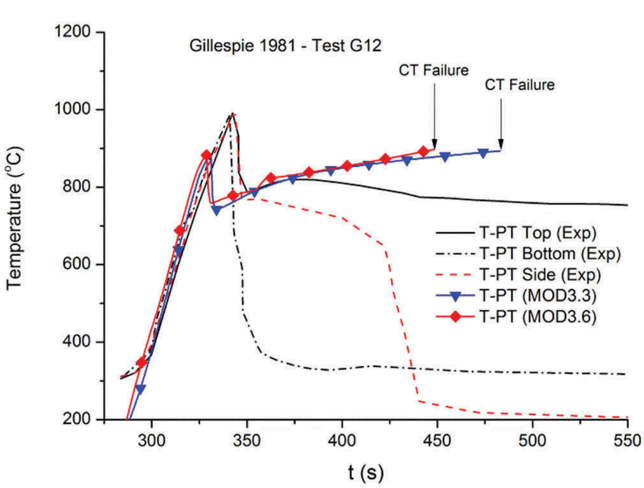

Fig. 11. Measured and predicted PT temperatures in test G12.

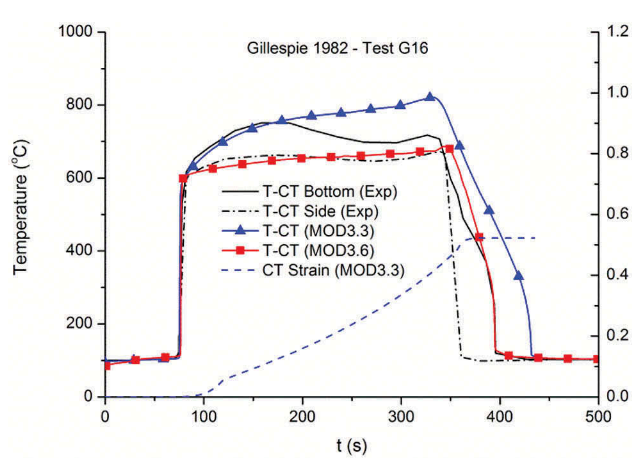

Fig. 12. Measured and predicted PT temperatures in test G16.

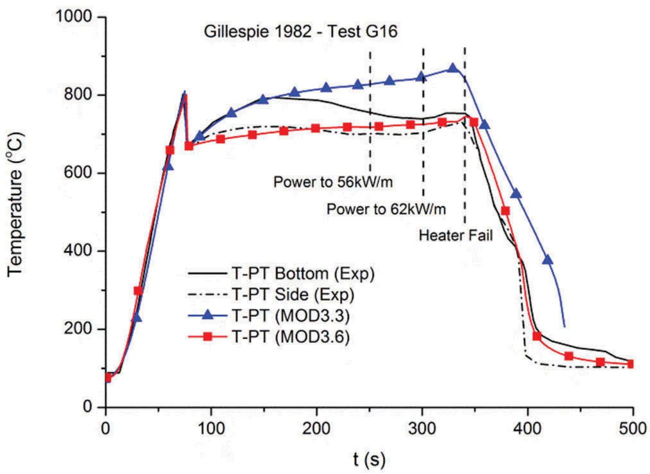

Fig. 13. Measured and predicted CT temperatures and strain in test G16.

Modeling of the new contact boiling tests conducted by Luxat[8] showed good agreement (Figs. 14 through 21). The PT heatup rates and contact temperatures predicted by MOD3.3 and MOD3.6 are very close to those measured in the experiments. MOD3.3 again predicted film boiling in all the tests including HPCB2 and HPCB12 where no film boiling occurred experimentally (Figs. 14 and 15). In test HPCB13, patchy film boiling occurred and lasted for less than 10 s. The duration of film boiling was closely predicted by MOD3.3 (Figs. 16 and 17). MOD3.6, however, failed to predict film boiling in HPCB13.

For tests SUBC1 and SUBC2 where sustained film boiling occurred, both MOD3.3 and MOD3.6 correctly predicted the occurrence of dryout (Figs. 18 through 21). The predicted PT and CT temperatures during film boiling also fall into the experimental range. However, the PT/CT

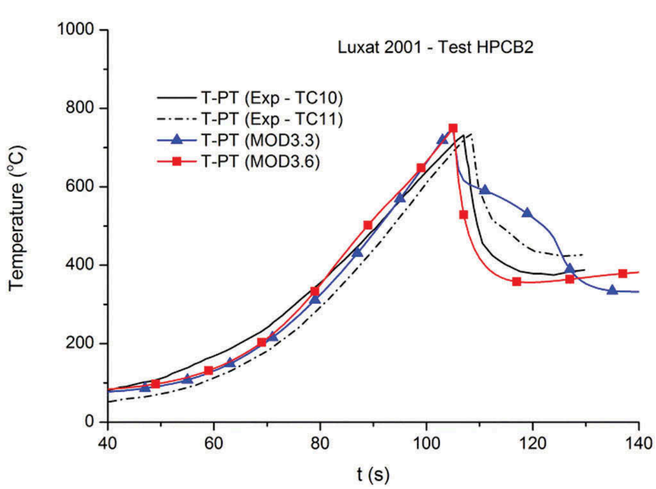

Fig. 14. Measured and predicted PT temperatures in test HPCB2.

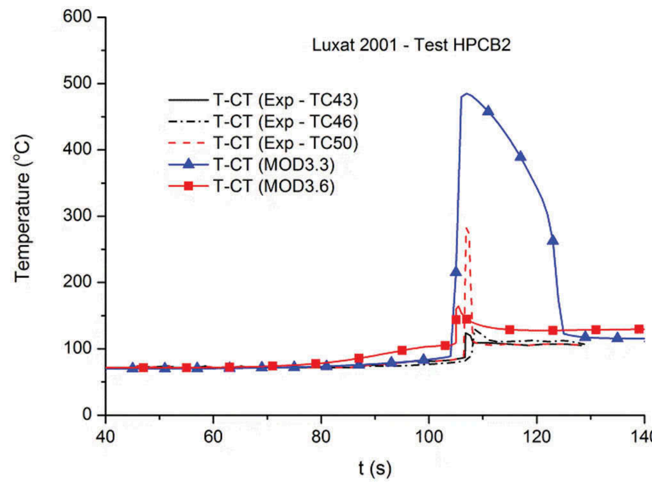

Fig. 15. Measured and predicted CT temperatures in test HPCB2.

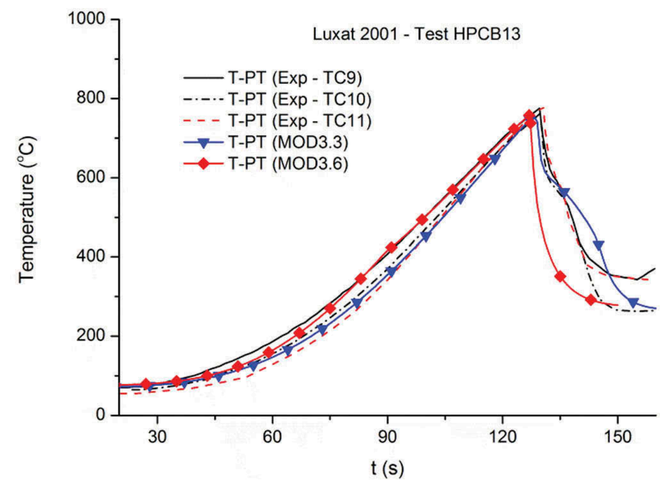

Fig. 16. Measured and predicted PT temperatures in test HPCB13.

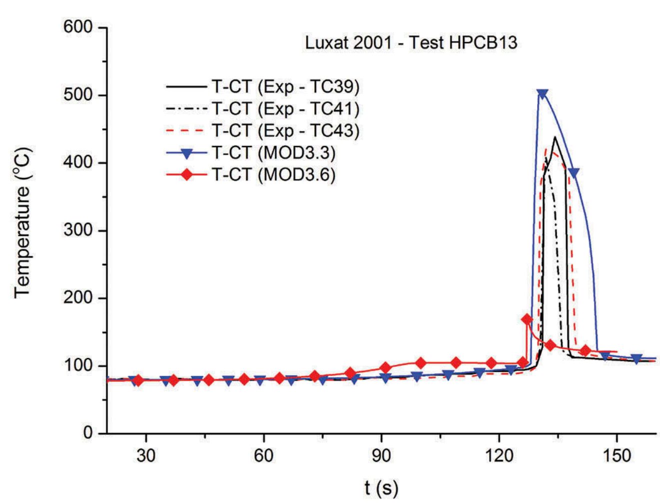

Fig. 17. Measured and predicted CT temperatures in test HPCB13.

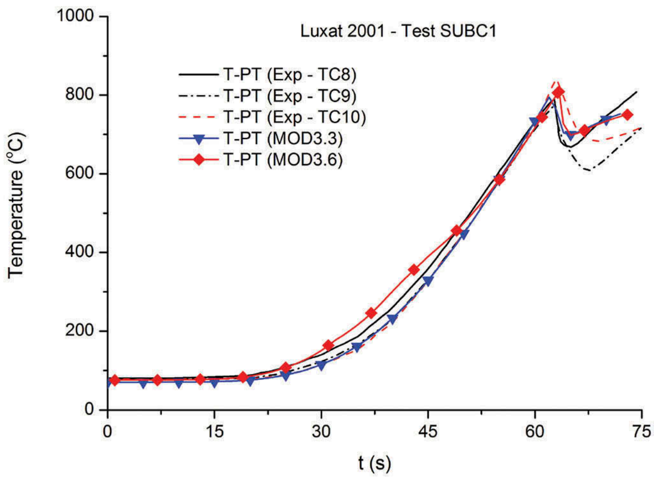

Fig. 18. Measured and predicted PT temperatures in test SUBC1.

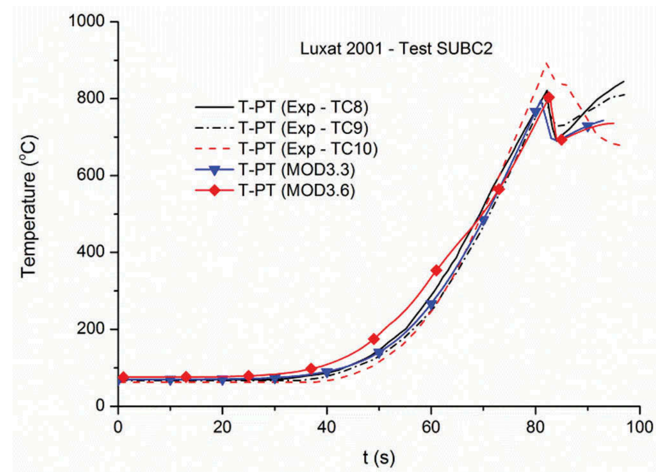

Fig. 20. Measured and predicted PT temperatures in test SUBC2.

heatup rates during film boiling were underpredicted by both MOD3.3 and MOD3.6, suggesting that the heat transfer coefficient under film boiling may be overestimated by RELAP5 in these two cases. In the experiments, the CT failed at 75 s in SUBC1 and 97 s in SUBC2 (Table IV). With a CT failure strain of 2%, failure of CT predicted by MOD3.3 and MOD3.6 occurred slightly earlier than in the experiments (Figs. 19 and 21).

The results of the IAEA ICSP test are shown in Figs. 22 and 23. In this test, the heater power was ramped up to 143 kW within 20 s; then, it was linearly increased to 149 kW at which point (~140 s) power was rapidly reduced to zero. The predicted contact temperatures by MOD3.3 and MOD3.6 were both lower than that in the experiment (Table VII), while the predicted contact times agree well with the measured one (i.e., 72 s). The underestimation in

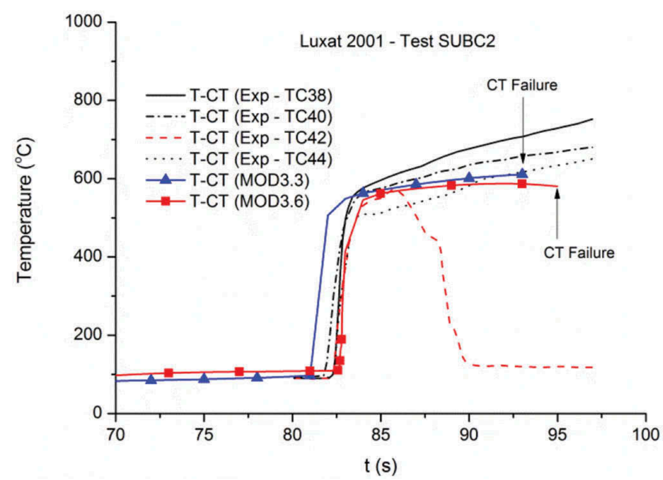

Fig. 21. Measured and predicted CT temperatures in test SUBC2.

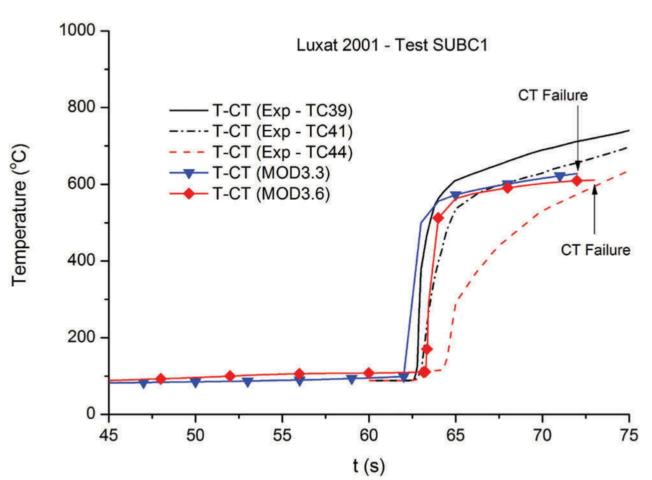

Fig. 19. Measured and predicted CT temperatures in test SUBC1.

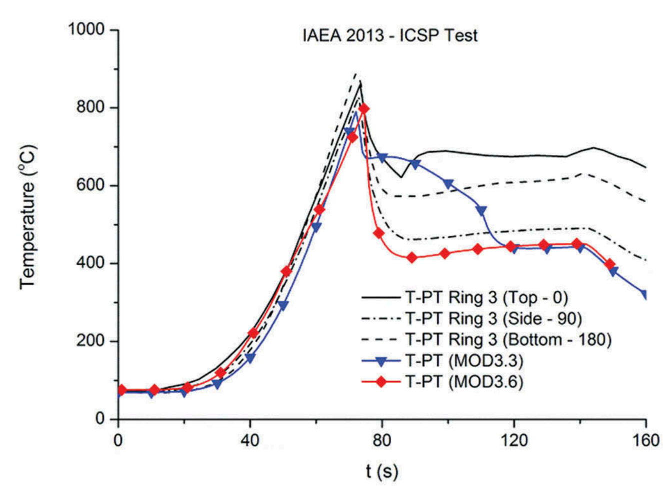

Fig. 22. Measured and predicted PT temperatures in IAEA ICSP test.

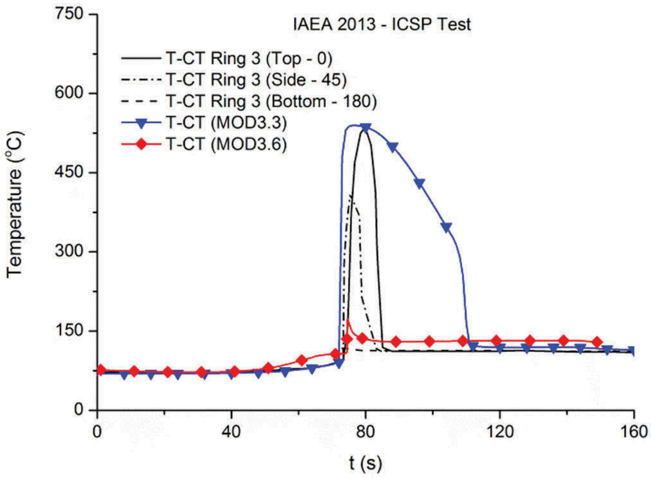

Fig. 23. Measured and predicted CT temperatures in IAEA ICSP test.

the contact temperature is consistent with studies done by the participants of the IAEA ICSP meeting.[53]

In the ICSP test, patchy film boiling existed for 25 s until full rewet. The film boiling predicted by MOD3.3, however, lasted for 37 s. The overestimation of the quench time is consistent with the code behavior discussed earlier for Gillespie's contact boiling tests. Nevertheless, the final CT average strain predicted by MOD3.3 (i.e., 0.36%; see Table VII) is close to the reported maximum CT strain (i.e., less than 0.4%).

The maximum CT temperature in the ICSP test is closely predicted by MOD3.3 (Fig. 23). MOD3.6 fails to predict the occurrence of film boiling; thus, the maximum CT temperature was significantly underestimated (Table VII). The failure of MOD3.6 to predict film boiling is attributed to the inappropriate CHF correlations being used by the CT outside surface within the SCDAP shroud component (i.e., the lookup table). The ICSP test was designed to have its test conditions located near the moderator subcooling limit, i.e., the boundary between immediate quench and patchy film boiling,[9] where accurate prediction of contact conductance and CHF becomes more important. Nevertheless, the PT temperatures after quench predicted by MOD3.3 and MOD3.6 are almost identical and are close to those measured at the PT/CT bottom (Fig. 22), implying that the predicted postcontact PT-CT contact conductance and nucleate boiling correlation are reasonably close to the actual values (at least for the tube bottom).

IV.B.3. Pressure Tube Temperature at Failure: BALLON Prediction

A series of PT ballooning tests was conducted at Ontario Hydro Research Laboratories in the 1980s (Refs. 54 and 55). Two sets of experiments were performed. In the first set of tests, PT segments of 0.6-m length were pressurized by either inert gas or steam. The variation of temperature around the circumference was thus small (of the order of 50°C). The PT heatup rate was in the range 1°C/s to 25°C/s with the internal pressure up to 5 MPa. The temperatures at which very rapid straining of the PT occurred were taken as the failure temperature of the PT. In the second set of tests, the PT segments before heatup were partially filled with water to generate large circumferential temperature variation. The temperature distribution, the PT strains, and the failure temperatures were then measured.

These tests have been used to validate computer codes such as NUBALL (Ref. 4). To validate the PT failure criteria used in this paper, some of the tests were simulated using BALLON. Since BALLON is a 1-D PT ballooning model, only the low-temperature-gradient tests are selected.

In typical analyses with BALLON, the PT is assumed to fail when the average creep strain exceeds a user-input value (default is 20%). To be consistent with NUBALL and the experiments, the PT failure strain in this validation case is overwritten to 100%. The PT failure temperatures as a function of internal pressure predicted by BALLON are shown in Fig. 24, and the results predicted by NUBALL in Ref. 4 are also plotted for comparison. The failure temperatures predicted by BALLON agree well with the data from the experiments, and the failure curves predicted by BALLON are quite similar to those of NUBALL. It is also noted that the predicted failure temperature is not sensitive to the failure criteria due to the accelerated strain prior to the failure. The degree of the agreement illustrated in Fig. 24 can be achieved by

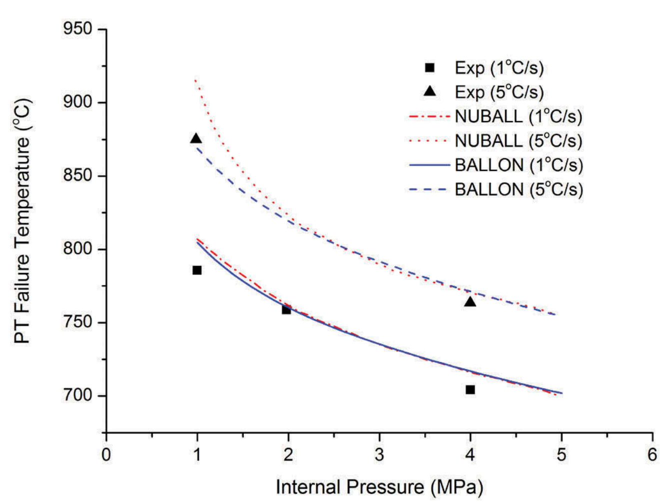

Fig. 24. Pressure tube failure curves at different heatup rates.

using any average failure strain higher than 20%. This confirmed that the used failure criterion, i.e., an average creep strain of 20%, is reasonable when severe circumferential temperature distribution is not present. For cases where large circumferential temperature gradients are expected, the suggested PT failure strain (averaged around the circumference) is 6%, which is the lower-bound PT failure strain in PT deformation tests with relatively large circumferential temperature gradients.[3]

IV.C. SAGPT Benchmark

The experiments by Gillespie et al.[24] (refer to Sec. IV.A.3 for details) are used to benchmark the PT sagging model SAGPT. Section IV.C.1 presents the predicted results for series 1 tests (Table V) where the PT was allowed to sag freely, while Sec. IV.C.2 is for series 2 tests (Table VI) where PT-to-CT contact was made and the PT temperature at contact was the main interest.

IV.C.1. Deflections of PT with and Without Garter Springs: SAGPT Prediction

In order to model the series 1 tests, SAGPT is modified from typical CANDU reactor geometries in order to represent the experimental apparatus: (1) The gap distance between the PT and the CT is increased to 30 mm; (2) the length of the PT is reduced to 3 m; and (3) the number of garter springs is reduced from four to one in experiments 1.3, 1.4, and 1.5 and to zero for the rest of the tests. Although the measured temperature was nearly uniform over a large portion of the PT, temperature gradients occurred at the two ends of the PT due to heat losses. Because of the lack of information in Ref. 24 regarding this nonuniformity, the heatup rates along the entire PT are assumed to be uniform. The sensitivity to the temperature uniformity is investigated for experiments 1.1 and 1.2 by lowering the heatup rates at the two ends by 20% (over a length of 0.25 m) to account for the heat loss due to axial conduction. All six tests have been simulated using SAGPT, while only experiments 1.1 and 1.2 are repeated using MOD3.6. The measured and the predicted PT temperatures are shown in Table VIII. The predictions by the code CREEPSAG in Ref. 24 are also included for comparison.

In tests where the spacer was not used, i.e., experiments 1.1, 1.2, and 1.6, the temperatures predicted by SAGPT agree well with the experimental data. The slight underestimation of contact temperature in experiments 1.1 and 1.2 is attributed to the uniform axial temperature assumption used in the predictions. Lowering the heatup rate by 20% at the two ends in SAGPT resulted in predictions that qualitatively align with the measurements (F = 0.8 in Table VIII). Figure 25 shows the measured and the predicted displacements at the LVDT (1.5 m) in experiment 1.2. It can be seen that with a uniform heatup rate (i.e., F = 1.0), the PT displacement at the center was overpredicted by SAGPT. After taking into account the axial heat loss, excellent agreement between SAGPT and CREEPSAG is observed noting that the CREEPSAG code used direct measurements from the thermocouples at five axial locations.[24] Both models show some discrepancies between the measured and the predicted displacement during the first 100 s. This is attributed to the creep

TABLE VIII

Measured and Predicted PT Temperatures at Given Deflections*

Experiment	Measured Temperature	SAGPT (F = 1.0[a])	SAGPT (F = 0.8[b])	MOD3.6 (F = 1.0[a])	Reference 24
1.1	820[c]	794	821	797	800
1.2	810[c]	790	816	790	830
1.3	890[d]	917	—	—[e]	880
1.4	820[d]	911	—	—[e]	940
1.5	860[d]	900	—	—[e]	890
1.6	890[c]	900	—	—[e]	870

*In units of degree Celsius.
[a]F = 1.0: uniform temperature along the PT.
[b]F = 0.8: At the two ends the PT heatup rates are assumed to be 80% of the center over a length of 0.25 m.
[c]Deflection is 20 mm.
[d]Deflection is 10 mm.
[e]Experiments 1.3 through 1.6 are not modeled with MOD3.6 because the number of spacers is not allowed to change in MOD3.6 and the user cannot impose arbitrary axial temperature gradients.

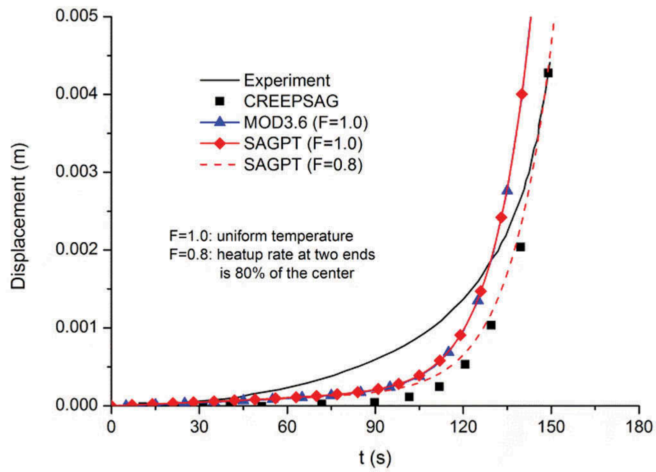

Fig. 25. Measured and predicted PT displacement at LVDT in experiment 1.2.

strain rate equation used in these models as it is likely that Eq. (19) is inaccurate at low temperatures [as in the experiments used to determine the correlations, very little strain was measured below 700°C (Refs. 24 and 25)]. However, as the temperature increases, the creep strain rate increases rapidly, and thus, there is good agreement at the latter stages of the transient.

In tests where the spacer was used, the temperatures are overestimated, especially in experiment 1.4. This is attributed to the rigid garter spring (spacer) assumption used in SAGPT. In the experiments the PTs were found to have deformed locally at the spacers, and the spacers also buckled, while in SAGPT the spacer geometry is assumed fixed. CREEPSAG also showed the same behavior as SAGPT. Figure 26 shows the predicted PT profile in experiment 1.3. The deflections of the PT are negligible when temperatures are below 700°C and increase rapidly at temperatures around 850°C. In this test the LVDT was located at 1 m. SAGPT predicts a PT temperature of 917°C when the deflection at the LVDT reaches 10 mm (slightly higher than the measured temperature). Given the behavior in experiment 1.4, an important phenomenon in sag is garter spring deformation. A mechanistic spacer deformation model is thus needed.

In experiment 1.6 an axial temperature gradient was imposed by varying the heatup rate along the PT. The imposed temperature at one end (x = 0 m) was higher than that at the other end (x = 3 m) resulting in asymmetric PT deflections. The displacements of the PT at various locations at the time of 212 s were recorded. The measured and the predicted PT profiles are shown in Fig. 27. The magnitude and location of the maximum displacement are well predicted by SAGPT, while the deflections on the right side are underpredicted.

IV.C.2. Pressure Tube–to–Calandria Tube Sagging Contact: SAGPT Prediction

In the series 2 tests, the PT is contained in the CT with a gap distance of 8 mm. The PT temperature was recorded when PT-to-CT contact was made. Only tests without the garter springs (i.e., experiments 2.1 and 2.2 in Table VI) are selected for the model benchmark because in the other tests the garter springs buckled and the localized deflection at the garter springs was up to half the distance between the tubes. The measured and the predicted PT contact temperatures are shown in Table IX.

In experiment 2.1, there is excellent agreement between the predicted and the measured contact temperatures. However, in experiment 2.2, the contact temperature was overpredicted by both SAGPT and CREEPSAG. The results predicted by SAGPT clearly show an upward trend in the contact temperature with an increase in the heatup rate, which was not observed in the experiments. This discrepancy might be due to the uncertainties in the experiments, especially in determining the timing of

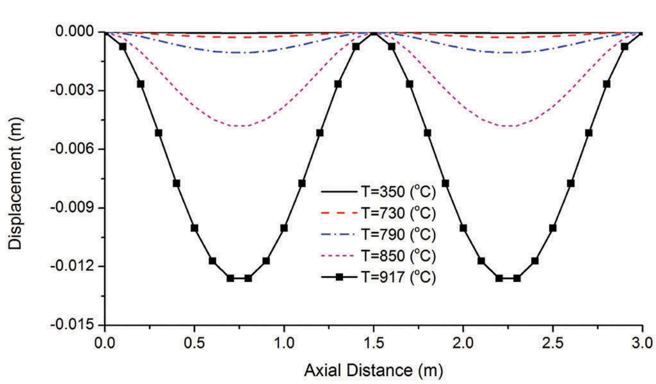

Fig. 26. Pressure tube profile predicted by SAGPT during temperature ramp in experiment 1.3.

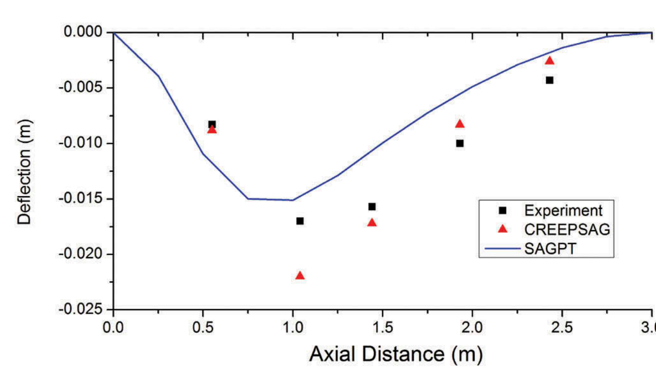

Fig. 27. Measured and predicted asymmetric PT deflections at 212 s in experiment 1.6.

TABLE IX

Measured and Predicted PT Temperatures at PT-CT Sagging Contact

Experiment	Contact Temperature Measured (°C)	SAGPT (°C)	CREEPSAG (°C)[24]
2.1	780	781	770
2.2	700	796	770

initial contact (contact was assumed when the maximum LVDT recorded deflection was reached) or in the limitations in the models discussed previously.

IV.D. SAGCH Verification

Because of a lack of relevant experimental data from the open literature, the SAGCH model has not been explicitly validated. Given the similarity in phenomena for the PT and the entire assembly sagging, the models are similar, albeit the material properties in application may differ. The SAGCH models have been verified by simply modifying the geometries of the channel in the model to represent a PT with no support from the spacers and then to reproduce some PT sagging tests (e.g., similar to the verification of PTSAG against experiments 1.1, 1.2, 2.1, and 2.2). Consistent results were predicted by SAGCH and SAGPT for the same experimental data.

The experimental data from the CDF (Refs. 56 and 57) at AECL are ideal for future validation of SAGCH. In the CDF, the CANDU reactor fuel channel is scaled down to a one-fifth linear scale while maintaining the same stress level at the channel center plane (i.e., 14.5 MPa). The scaled channel in the CDF tests consists of 12 simulated fuel bundles and a pipe representing the ballooned PT and the CT surrounding it. The pipe is made of Zr-2.5wt%Nb. The CDF test results show significant strain localization at the bundle junctions along the bottom side of the channel.[57] This phenomenon is currently not considered in the SAGCH model, while neglecting the effect of strain localization is expected to underpredict the magnitude of sagging [by about 25% (Ref. 56)]. Special treatment is thus needed in the future to account for this stress concentration near the bundle junctions. A simple approach (which has been proven effective in reproducing the experiments by other researchers[56]) is to multiply the creep strain rate equation by a constant factor in the stress concentration regions near the bundle junctions. However, additional mesh refinement is needed at these regions of interest along with the appropriate new subroutines.

V. CONCLUSION AND FUTURE WORK

Three mechanistic channel deformation models—i.e., BALLON, SAGPT, and SAGCH—that can be coupled with the thermal-hydraulic code RELAP5 have been developed to model the PT ballooning/sagging and the channel sagging/disassembly phenomena in a postulated severe accident of CANDU reactors. A Python script has been developed to externally couple these models with RELAP5/MOD3.3. The models have also been integrated into RELAP/SCDAPSIM/MOD3.6 as new SCDAP subroutines. The detailed descriptions of the models, the coupling schemes, and the modified MOD3.6 are presented in this paper. The models were benchmarked against several PT deformation experiments. The model predictions agreed well with the experimental data.

BALLON was first coupled with RELAP5 (using both MOD3.3 and MOD3.6) to simulate a number of contact boiling tests. The predicted contact temperatures agreed well with the measured temperatures. MOD3.3 with a RELAP5 heat structure predicted film boiling after contact in almost all the tests, while in reality no film boiling was observed in tests with low power and/or high moderator subcooling. The failure of MOD3.3 in predicting the occurrence of film boiling is attributed to the overestimation of contact conductance by Yovanovich's model at initial contact. This effect is partially compensated by the overprediction of CHF in MOD3.6.

In tests where film boiling occurred in patches, the time to quench was overpredicted by both MOD3.3 and MOD3.6. In experiments the heat conduction from the patchy film boiling regions to areas of nucleate boiling enhanced heat removal from the CT and reduced the duration of dryout. This 2-D phenomenon cannot be captured by MOD3.3 and MOD3.6, both of which are 1-D codes. Thus, the models currently are conservative in predicting the occurrence in film boiling and the duration of film boiling. Additional quench correlations may be used for future work to better predict the time to quench.

In tests where the entire CT surface was in sustained film boiling or where no film boiling occurred (or after the quench of dryout patches), the predicted PT and CT temperatures during the postcontact phase are reasonably close to the measured temperatures. Yovanovich's model thus can be used to calculate the contact conductance for the postcontact phase.

BALLON was also used to predict the PT failure temperatures in experimental tests with different heatup rates and internal pressures up to 5 MPa. The results suggest a PT failure strain of 20% (averaged over the circumference) for tests with small circumferential temperature gradients.

The SAGPT sagging models were used to model several low-pressure PT deformation tests. In tests where garter springs or spacers were used, the models were found to overestimate the temperatures at a given deflection (or at PT-CT contact). This is because in the current model the spacers are assumed to be rigid; i.e., they are not allowed to move or deform, while in the experiments they were found to have buckled under high temperatures. To better predict PT sagging, a mechanistic spacer deformation model is thus needed.

Nomenclature

c = distance to the centroid of cross section (m)

c_1 = Vickers correlation coefficient (GPa)

c_2 = Vickers size index

d = maximum possible depth of local defect (μm)

E = Young's modulus (N/m^2)

f_g = correction term

H_c = contact microhardness (GPa)

h = conductance (W/m^2·K)

I = moment of inertia (m^4)

K_{pl}, K_{el} = plastic curvature and elastic curvature, respectively (m^{-1})

k_g = thermal conductivity of the gas (W/m·K)

k_s = effective thermal conductivity of the joint

M = bending moment (N·m)

m = mean surface asperity slope

n = creep stress exponent

P_c = contact pressure (GPa)

T = temperature (K)

t = time (s)

w_0 = initial wall thickness (μm)

x = axial distance (m)

Y = mean plane separation (μm)

y = deflection in the vertical direction (m)

Greek

α = accommodation parameter

β = fluid parameter

ε_f = PT failure strain

ε_{pt} = creep strain

$\dot{\varepsilon}_{pt}$ = creep strain rate of PT (s^{-1})

$\dot{\varepsilon}_{ct}$ = creep strain rate of CT

$\dot{\varepsilon}_{\alpha}$ = creep strain rate of PT due to power law creep in the α-phase (s^{-1}).

Λ = mean free path (μm)

σ_{pt}, σ_{ct} = stress of PT and CT, respectively (MPa)

σ = surface roughness (μm)

σ_0 = reference roughness (equals to 1μm)

ORCID

D. R. Novog http://orcid.org/0000-0003-4809-3472

References

1. R. S. W. SHEWFELT, L. W. LYALL, and D. P. GODIN, "A High-Temperature Creep Model for Zr-2.5 wt% Nb Pressure Tubes," *J. Nucl. Mater.*, **125**, 228 (1984); https://doi.org/10.1016/0022-3115(84)90548-8.
2. R. S. W. SHEWFELT, D. P. GODIN, and L. W. LYALL, "Verification of High-Temperature Transverse Creep Model for Zr-2.5 wt.%Nb Pressure Tubes," AECL Report 7813, Atomic Energy of Canada Limited (1984).
3. R. S. W. SHEWFELT and D. P. GODIN, "Verification Tests for GRAD, A Computer Program to Predict the Non-Uniform Deformation and Failure of Pressure Tubes During a Postulated LOCA," AECL Report 8384, Atomic Energy of Canada Limited (1985).
4. P. KUNDURPI, "Validation of Computer Code NUBALL for Simulation of Pressure Tube Asymmetric Ballooning Behaviour," *Proc. 2nd Int. Conf. Simulation Methods in Nuclear Engineering*, Montreal, Quebec, Canada, October 14–16, 1986, Canadian Nuclear Society (1986).
5. Q. M. LEI and H. Z. FAN, "An Improved Model to Predict Nonuniform Deformation of Zr-2.5 NB Pressure Tubes," *Proc. 18th Annual CNS Conf.*, Toronto, Ontario, Canada, June 8–11, 1997, Canadian Nuclear Society (1997).
6. G. E. GILLESPIE, "An Experimental Investigation of Heat Transfer from a Reactor Fuel Channel to Surrounding Water," *Proc. 2nd Annual CNS Conf.*, Ottawa, Canada, June 10, 1981, Canadian Nuclear Society (1981).
7. G. E. GILLESPIE, R. G. MOYER, and P. D. THOMPSON, "Moderator Boiling on the External Surface of a Calandria Tube in a CANDU Reactor During a Loss-of-Coolant Accident," *Proc. Int. Mtg. Thermal Nuclear Reactor*

Safety, Chicago, Illinois, August 29–September 2, 1982, p. 1523, U.S. Nuclear Regulatory Commission (1982).

8. J. C. LUXAT, "Analysis of High Pressure Contact Boiling Tests," Ontario Power Generation (2001).
9. T. NITHEANANDAN, "Proposal for the IAEA International Collaborative Standard Problem on HWR Moderator Subcooling Requirements to Demonstrate Backup Heat Sink Capabilities of Moderator During Accidents," International Atomic Energy Agency (2012).
10. M. EI-HAWARY et al., "New Contact Boiling Experiments to Evaluate Calandria Tube Strain Acceptance Criteria," *Proc. 35th Annual CNS Conf.*, Saint John, New Brunswick, Canada, May 31–June 2, 2015, Canadian Nuclear Society (May 2015).
11. N. ZUBER, "Hydrodynamic Aspects of Boiling Heat Transfer," AECU-4439, Atomic Energy Commission (1959).
12. J. THIBAULT, "Boiling Heat Transfer Around a Horizontal Cylinder and in Tube Bundles," PhD Thesis, McMaster University (1978).
13. J. C. LUXAT, "Mechanistic Modeling of Heat Transfer Processes Governing Pressure Tube-to-Calandria Tube Contact and Fuel Channel Failure," *Proc. 23rd Annual CNS Conf.*, Toronto, Ontario, Canada, June 2–5, 2002, Canadian Nuclear Society (2002).
14. L. H. K. LEUNG and D. C. GROENEVELD, "Compendium of Thermalhydraulic Correlations and Fluid Properties," COG-90-86, CANDU Owners Group (1991).
15. A. CZIRAKY, "Pressure Tube-Calandria Tube Thermal Contact Conductance," Master Thesis, McMaster University (2009).
16. M. M. YOVANOVICH, "Micro and Macro Hardness Measurements, Correlations, and Contact Models," *Proc. 44th AIAA Aerospace Sciences Mtg.*, Reno, Nevada, January 9–12, 2006, American Institute of Aeronautics and Astronautics (Jan. 2006).
17. P. NEAL and C. FRASER, "Contact Boiling Experiment SUBC3," COG-02-2018, CANDU Owners Group (2003).
18. H. Z. FAN, Z. BILANOVIC, and T. NITHEANANDAN, "Use of CATHENA to Model Calandria-Tube/Moderator Heat Transfer After Pressure-Tube/Calandria-Tube Ballooning Contact," *Proc. 6th Int. Conf. Simulation Methods in Nuclear Engineering*, Montreal, Quebec, Canada, October 12–15, 2004, Canadian Nuclear Society (2004).
19. A. DION, "A Mechanistic Model to Predict Fuel Channel Failure in the Event of Pressure Tube Overheating," Master Thesis, McMaster University (2016).
20. G. E. GILLESPIE and R. G. MOYER, "An Experimental Determination of Heat Transfer from Large Cylinders: Film Boiling in Subcooled Water," Atomic Energy of Canada Limited (1984).
21. W. S. BRADFIELD, "On the Effect of Subcooling on Wall Superheat in Pool Boiling," *Trans. Am. Soc. Mech. Eng. J. Heat Transf.*, **89**, *3*, 269 (1967); https://doi.org/10.1115/1.3614378.
22. J. T. JIANG and J. C. LUXAT, "Mechanistic Modeling of Pool Film-Boiling and Quench on a CANDU Calandria Tube Following a Critical Break LOCA," *Proc. Int. Youth Nuclear Congress*, Interlaken, Switzerland, September 21–26, 2008.
23. M. SHOUKRI and A. M. C. CHAN, "On the Thermal Analysis of Pressure Tube/Calandria Tube Contact in CANDU Reactors," *Nucl. Eng. Des.*, **104**, *2*, 197 (1987); https://doi.org/10.1016/0029-5493(87)90299-8.
24. G. E. GILLESPIE, R. G. MOYER, and G. I. HADALLER, "An Experimental Investigation of the Creep Sag of Pressure Tubes Under LOCA Conditions," *Proc. 5th Annual CNS Conf.*, Saskatoon, Canada, June 4–5, 1984, Canadian Nuclear Society (1984).
25. R. S. W. SHEWFELT and L. W. LYALL, "A High-Temperature Longitudinal Strain Rate Equation for Zr-2.5 wt%-Nb Pressure Tubes," *J. Nucl. Mater.*, **132**, 41 (1985); https://doi.org/10.1016/0022-3115(85)90391-5.
26. S. M. PETOUKHOV, "MAAP4-CANDU Analysis of a Generic CANDU 6 Station: Preliminary Results for a Large LOCA Scenario," *Proc. 23rd Annual CNS Conf.*, Toronto, Ontario, Canada, June 2–5, 2002, Canadian Nuclear Society (2002).
27. "Analysis of Severe Accidents in Pressurized Heavy Water Reactors," TECDOC 1594, International Atomic Energy Agency (2008).
28. D. DUPLEAC, M. MLADIN, and I. PRISECARU, "Generic CANDU 6 Plant Severe Accident Analysis Employing SCAPSIM/RELAP5 Code," *Nucl. Eng. Des.*, **239**, *10*, 2093 (Oct. 2009); https://doi.org/10.1016/j.nucengdes.2009.05.007.
29. SCDAP/RELAP5 DEVELOPMENT TEAM, "SCDAP/RELAP5/MOD3.3 Code Manual," NUREG/CR-6150, U.S. Nuclear Regulatory Commission (1997).
30. "RELAP5/MOD3.3 Code Manual Vol. 1-8," NUREG/CR-5535/Rev P4, U.S. Nuclear Regulatory Commission (2010).
31. C. M. ALLISON and J. K. HOHORST, "Role of RELAP/SCDAPSIM in Nuclear Safety," *Sci. Technol. Nucl. Install.*, **2010**, 1 (2010); https://doi.org/10.1155/2010/425658.
32. A. BONELLI et al., "RELAP/SCDAPSIM/MOD3.6—Development of Severe Accident Models for Heavy Water Reactors Including CANDU and ATUCHA-2," *Proc. ICAPP 2015*, Nice, France, May 3–6, 2015.
33. R. S. W. SHEWFELT and L. W. LYALL, "A High-Temperature Creep Model for Zircaloy-2 Calandria Tubes," COG-88-37, CANDU Owners Group (1988).

34. R. S. W. SHEWFELT and D. P. GODIN, "The Effect of Axial Scratches on the Ductile Creep Rupture of Internally Pressurized Thin-Walled Tubes," *Res. Mech.*, **13**, 1 (1985).

35. J. C. CHEN, "A Correlation for Boiling Heat Transfer to Saturated Fluids in Convective Flow," *Process Des. Dev.*, **5**, 322 (1966); https://doi.org/10.1021/i260019a023.

36. J. C. CHEN, R. K. SUNDARAM, and F. T. OZKAYNAK, "A Phenomenological Correlation for Post-CHF Heat Transfer," NUREG-0237, U.S. Nuclear Regulatory Commission (1977).

37. L. A. BROMLEY, "Heat Transfer in Stable Film Boiling," *Chem. Eng. Prog.*, **46**, 221 (1950).

38. K. H. SUN, J. M. GONZALEZ-SANTALO, and C. L. TIEN, "Calculations of Combined Radiation and Convection Heat Transfer in Rod Bundles Under Emergency Cooling Conditions," *J. Heat Transfer*, **98**, 414 (1976); https://doi.org/10.1115/1.3450569.

39. D. C. GROENEVELD, S. C. CHENG, and T. DOAN, "1986 AECL-UO Critical Heat Flux Lookup Table," *Heat Transfer Eng.*, **7**, *1–2*, 46 (1986); https://doi.org/10.1080/01457638608939644.

40. H. K. FORSTER and N. ZUBER, "Dynamics of Vapor Bubbles and Boiling Heat Transfer," *AIChE J.*, **1**, *4*, 531 (1955); https://doi.org/10.1002/(ISSN)1547-5905.

41. H. J. IVEY and D. J. MORRIS, "On the Relevance of the Vapor Liquid Exchange Mechanism for Subcooled Boiling Heat Transfer at High Pressures," AEEW-R137, Atomic Energy Establishment Winfrith (1962).

42. B. S. FOLKIN and Y. N. GOLDBERG, "Simulation of Free Convection Boiling Crisis in Vapor Blanketing of a Horizontal Tube Bundle," *Heat Transfer Sov. Res.*, **12**, *3*, 77 (1980).

43. M. DE JONG and G. RATHENAU, "Mechanical Properties of Iron and Some Iron Alloys While Undergoing Allotropic Transformation," *Acta Metall.*, **7**, *4*, 246 (1959); https://doi.org/10.1016/0001-6160(59)90017-3.

44. C. BLAHNIK, J. C. LUXAT, and S. NIJHAWAN, "CANDU Response to Loss of All Heat Sinks," *Proc. 9th Topl. Mtg. Nuclear Thermal Hydraulics*, San Francisco, California, 1993.

45. F. ZHOU et al., "Coupling RELAP5 and Pressure Tube Deformation Models to Analyze the Thermal-Mechanical Phenomena in CANDU Severe Accidents," *Proc. 36th Annual CNS Conf.*, Toronto, Ontario, Canada, June 19–22, 2016, Canadian Nuclear Society (2016).

46. SCDAP/RELAP5 DEVELOPMENT TEAM, "SCDAP/RELAP5/MOD3.2 Code Manual Volume IV: MATPRO—A Library of Materials Properties for Light-Water Reactor Accident Analysis," U.S. Nuclear Regulatory Commission (1997).

47. L. L. TONG et al., "Thermal Hydraulic Behavior Under Station Blackout for CANDU6," *Prog. Nucl. Energy*, **74**, 176 (July 2014); https://doi.org/10.1016/j.pnucene.2014.03.003.

48. J. C. LUXAT, "Thermal-Hydraulic Aspects of Progression to Severe Accidents in CANDU Reactors," *Nucl. Technol.*, **167**, *1*, 187 (2008); https://doi.org/10.13182/NT09-A8862.

49. J. KENNEDY, P. MAKA, and M. CHAI, "MAAP5-CANDU Development," *Proc. 36th Annual CNS Conf.*, Toronto, Ontario, Canada, June 19–22, 2016, Canadian Nuclear Society (2016).

50. P. M. MATHEW, "Severe Core Damage Accident Progression Within a CANDU Calandria Vessel," presented at MASCA Seminar, Aix-en-Provence, France, June 10–11, 2004.

51. "Inputs and Assumptions for Pre-Test (Double-Blind) Calculation (Rev. 1, 27 November 2012)," presented at International Atomic Energy Agency First Workshop for the International Collaborative Standard Problem (ICSP) on Heavy Water Reactor (HWR) Moderator Subcooling Requirements, Ottawa, Canada, November 19–21, 2012; https://www.iaea.org/NuclearPower/Downloadable/WCR/ICSP-HWR-Moderator/summary.pdf (current as of Dec. 25, 2016).

52. A. A.-H. HEGAZY, "Thermal Joint Conductance of Conforming Rough Surfaces: Effect of Surface Micro-Hardness Variation," PhD Thesis, University of Waterloo (1985).

53. M. KRAUSE, "HWR Related Activities for 2014 TWG-HWR Meeting," International Atomic Energy Agency; https://www.iaea.org/NuclearPower/Downloadable/Meetings/2014/2014-11-25-11-27-TM-NPE/IAEA_HWR_Activities_(MKrause).pdf (2014) (current as of Dec. 25, 2016).

54. E. T. C. HO and A. DONNER, "Deformation Behavior of Zr-2.5% Nb Pressure Tubes Under Internal Pressure and Ramp Temperature Conditions," OHRD-84-100-K, Ontario Hydro Research Division (1986).

55. E. T. C. HO and A. DONNER, "Biaxial Deformation of Zr-2.5% Nb Pressure Tubes Partially Filled with Water at Elevated Temperatures," OHRD-85-243-K, Ontario Hydro Research Division (1985).

56. P. M. MATHEW et al., "Severe Core Damage Experiments and Analysis for CANDU Applications," *Proc. SMiRT 17*, Prague, Czech Republic, August 17–22, 2003, International Association for Structural Mechanics in Reactor Technology (2003).

57. P. M. MATHEW, V. G. SNELL, and M. BONECHI, "CANDU-Specific Severe Core Damage Accident Experiments in Support of Level 2 PSA," *Proc. SMiRT 16*, Washington, District of Columbia, August 12–17, 2001, International Association for Structural Mechanics in Reactor Technology (2001).

5. Simulation of Later Phase with MOD3.6

About This Paper

Citation:

F. Zhou and D.R. Novog, "Mechanistic Modelling of Station Blackout Accidents for a Generic 900MW CANDU Plant Using the Modified RELAP/SCDAPSIM/MOD3.6 Code", *Nucl. Eng. Des.*, vol. 335, April, pp. 71–93, 2018.

Contribution to Knowledge

This work is the culmination of the work done in this PhD and integrates the results from the papers in Chapter 3 and 4 to produce a full simulation of the SBO timeline. The mechanistic models added to MOD3.6 allow more robust treatment of the deformation processes during severe accident, and permit more physics-based sensitivity studies.

By extending the early-phase SBO simulation (presented in Chapter 3), the impacts of operator actions (i.e. crash-cooldown and different SG water make-up options) on the later-phase accident progression were investigated. These operator actions affected the accident progression mainly through the influence on the duration of the natural circulation phase. Shorter durations of natural circulation led to higher decay power levels for the later accident stages thus the acceleration of event progressions, and vice versa. However, similar hydrogen production and fission product releases were predicted for the four accident scenarios simulated. This paper also examined the sensitivities to a wide range of modelling parameters, e.g. core collapse criteria, and pressure tube failure strain. The results of these sensitivity studies revealed that the predicted hydrogen production and fission product releases until calandria vessel dryout are often sensitive to parameters that may affect the duration of the core disassembly phase and/or the temperature of the suspended debris bed.

Author's Contribution to Paper

The author (F. Zhou) is the primary contributor to this paper. Model development, model execution, data analysis, and writing of the draft paper were carried out entirely by F. Zhou. The co-author (D. R. Novog) also contributed significantly to this paper through guidance, expertise, suggestions, and editing of the paper. The paper was submitted to Nuclear Engineering and Design on February 27th 2018, and was revised and resubmitted on April 30th 2018. The paper was accepted for publication on May 6th 2018.

Nuclear Engineering and Design 335 (2018) 71–93

Contents lists available at ScienceDirect

Nuclear Engineering and Design

journal homepage: www.elsevier.com/locate/nucengdes

Mechanistic modelling of station blackout accidents for a generic 900 MW CANDU plant using the modified RELAP/SCDAPSIM/MOD3.6 code

F. Zhou*, D.R. Novog

McMaster University, Hamilton, Ontario, Canada

ARTICLE INFO

Keywords:
CANDU
Severe accident
RELAP/SCDAPSIM
Station blackout
Core disassembly

ABSTRACT

CANDU (CANada Deuterium Uranium) reactors have many unique design features that play important roles during a severe accident, however analysis of such features using Light Water Reactor (LWR) specific computer codes is challenging. Severe accidents in CANDU involve complex thermo-mechanical deformation phenomena which differ from the phenomena present during LWR accidents. For example, during complete station blackout scenarios with a failure of all emergency measures, the pressure tubes may balloon or sag into contact with the surrounding calandria tubes (CTs) establishing a thermal conduction pathway for heat rejection to the large moderator water volume. As the moderator liquid evaporates or boils its level decreases until fuel channels become uncovered in the calandria vessel. The uncovered channels heat up quickly and the entire fuel channel assembly (fuel, pressure tube and calandria tube) will sag and possibly disassemble. During the disassembly process some channel components may fall to the bottom of the calandria while others may form a suspended debris bed supported by channels which are still submerged in moderator liquid. These phenomena impact event-timing, accident progression, hydrogen production and fission product release.

In this work several mechanistic channel deformation models have been developed and integrated into RELAP/SCDAPSIM/MOD3.6 to provide a coupled treatment of the deformation phase for such postulated accidents. MOD3.6 is a new version of the RELAP/SCDAPSIM code being developed to support the analysis of Pressurized Heavy Water Reactors (PHWRs) under severe accident conditions. In this paper, the code system is used to simulate a postulated station blackout accident for a generic 900 MW CANDU plant. To reduce the uncertainty in the modeling of core disassembly and to overcome the memory constraints of the code, the simulation is broken into two phases with the first phase (i.e., from initiating event to the channel failure and depressurization) simulated using a full-plant RELAP5 model providing relatively high spatial fidelity of the entire heat transport system, and the second phase (i.e. continued from the end of the first phase until calandria vessel dryout) using alternative nodalization focusing on the calandria vessel and fuel channel components. The paper assesses the entire accident progression up to the point of calandria vessel dryout and performs sensitivity analysis on model parameters to assess their relative importance.

1. Introduction

The CANDU®[1] reactor (CANada Deuterium Uranium) is a pressure-tube type reactor using natural uranium as fuel, with a separate heavy-water coolant and moderator. A typical 900 MW CANDU reactor consists of two identical primary heat transport loops each in a figure of eight arrangement. A loop has two alternating-direction core passes with 120 fuel channels in each core pass. The two loops are symmetrical about the vertical symmetry plane of the calandria vessel (CV). Each fuel channel consists of a Zr-2.5%-Nb pressure tube (PT) surrounded by annulus insulating gas (CO_2) and a Zr-2 calandria tube (CT). The moderator surrounds each channel and is contained in a horizontally orientated large cylindrical calandria vessel. The PT is connected to the end fittings by rolled joints at the two ends, and separated from the CT by four evenly spaced garter springs in the annulus gap. The garter springs are designed to prevent PT-to-CT contact under normal operating conditions. This fuel channel design ensures only a small amount of thermal energy (about 4–5% (Aydogdu, 1998) is deposited into the moderator system. The calandria tube ends are rolled into the lattice tube ends of the two end shields at the axial ends of the calandria vessel. The end shields are filled with light water and steel balls to provide biological protection in the axial direction. Radial shielding is provided

* Corresponding author.
E-mail address: zhouf5@mcmaster.ca (F. Zhou).

[1] CANDU is a registered trademark of Atomic Energy of Canada Limited (AECL)

https://doi.org/10.1016/j.nucengdes.2018.05.009
Received 27 February 2018; Received in revised form 30 April 2018; Accepted 6 May 2018

Nomenclature

AECL	atomic energy of Canada limited
ASDV	atmospheric steam discharge valve
CANDU	CANada deuterium uranium
CSDV	condenser steam discharge valve
CT	calandria tube
CV	calandria vessel
ECC	emergency core cooling
EME	emergency mitigating equipment
ES	end shield
IBIF	intermittent buoyancy induced flow
ISAAC	integrated severe accident analysis code
LWR	light water reactor
MAAP	modular accident analysis program
MCST	maximum cladding surface temperature
MSSV	main steam safety valve
NGS	nuclear generating station
PHTS	primary heat transport system
PHWR	pressurized heavy water reactor
PSA	probabilistic safety assessment
PT	pressure tube
RIH	reactor inlet header
ROH	reactor outlet header
SBO	station blackout accident
SDS	shutdown system
SG	steam generator
SGECS	steam generator emergency cooling system
ST	shield tank

by the light-water filled shield tank which surrounds the calandria vessel.

The over-pressure protection of the primary heat transport system (PHTS) is mainly through the four 100% liquid relief valves, two connected to a reactor outlet header (ROH) of each loop. The liquid relief valves allow coolant to be discharged to the bleed condenser which is protected from over-pressure by its own spring-loaded relief valves. The pressure relief and over-pressure protection of the secondary side are provided by the atmospheric steam discharge valves (ASDVs), the condenser steam discharge valves (CSDVs), and the main steam safety valves (MSSVs). There is one ASDV on each steam line (four total), and three pairs of CSDVs which discharge steam to the condenser. The MSSVs are spring-loaded valves which can also be manually opened by the operators to initiate auto-depressurization of the secondary side system (often referred to as "crash-cooldown" because of the high rate of temperature and pressure reduction in both the primary and secondary sides).

The CANDU reactor has multiple heat sink provisions, some of which are passive and do not require electrical power to operate. In an accident where the electrical system is comprised but the PHTS remains intact, e.g. a station blackout (SBO), continuous or intermittent natural circulation allows decay heat to be effectively removed from the low-elevation core and deposited into the steam generators (SGs) provided that there is sufficient inventory in the secondary side (shell-side) of the SGs. If make-up water can be supplied to the steam generators heat removal from the core can continue indefinitely.

In a CANDU plant the main feedwater pumps provide inventory to the steam generators and run on Class IV power while the auxiliary feedwater pumps, powered by the Class III power, provide alternative steam generator inventory make-up (Jiang, 2015). The Emergency Water System powered by Emergency Power Supply system can also provide water to the SGs in the event that Class IV and III power are unavailable. These systems, however, will not be available in an extended SBO where Class IV, Class III and Emergency Power Supply are unavailable.

If crash-cooldown is initiated, the associated depressurization of the secondary side allows several passive low-pressure water sources for the SGs. For example, the deaerator tank can provide steam generator makeup for a significant period of time. Such makeup occurs through the feedwater control valves which fail open on loss of power thus allowing water in the high-elevation deaerator tank to flow by gravity into the SGs after crash-cooldown. Depending on the specific CANDU design, some stations, e.g. CANDU6, have a gravity-fed dousing tank system which is part of emergency water system, while some, e.g. Darlington Nuclear Generating Station (NGS) are equipped with the SG emergency cooling system (SGECS) consisting of two air accumulators and two water tanks. Both systems can passively provide make-up water to the SGs after initiation. As a response to the Fukushima Daiichi accident, emergency mitigating equipment (EME) such as portable pumps and power generators have also been implemented in the Canadian nuclear power plants providing alternative water make-up options.

A severe accident in CANDU involves an imbalance in the heat generation and removal, resulting in the damage of fuel or structures within the reactor core (Luxat, 2008). The severe accident sequences are often categorized into various core damage states according to their terminal location of the debris (Nijhawan et al., 1996). In the first core damage state, the fuel channels are submerged in the moderator and the damaged fuel is contained in the fuel channels with the PTs plastically deformed into contact with the CTs (via ballooning or sagging depending on the internal pressure as the PTs heat up). The contact arrests the deformation of the PTs since the CTs are cooled by the moderator. Early studies showed that the fuel bundles during this stage can be severely damaged with possible phenomena such as bundle distortion (slumping), oxidation of cladding, the relocation of molten Zircaloy and the dissolution of uranium dioxide (UO_2) by molten Zircaloy (Rosinger et al., 1985) (Akalin et al., 1985) (Kohn and Hadaller, 1985). Melting of UO_2 itself, however, is not likely (Simpson et al., 1996). This core damage state will remain stable indefinitely if the moderator heat sink remains available.

Given that the low-pressure moderator system can be easily replenished from outside sources, progression to more severe core damage states has low probability. In more severe events moderator inventory depletion, core disassembly and debris bed phenomena become important. Rogers (1984) and Blahnik and Luxat (1993) have carried out some pioneering work on the modeling of core disassembly process: Rogers assumed that the disassembled core parts will fall directly to the bottom of calandria vessel, while Blahnik proposed a more mechanistic model in which the uncovered channel will eventually sag into contact with the lower channel. In Blahnik's model the sagged or disassembled channels form a suspended debris bed which is eventually supported by channels that are still submerged in the moderator. As the supporting channels become uncovered they will sag causing the suspended debris bed to increase in size and relocate to the lower (cooled) channels. When the mass of the suspended debris bed exceeds the maximum load the channels can support, all the channels (except those in the periphery region) are assumed to collapse to the bottom of the calandria vessel. The end states of the core disassembly phase for all disassembly pathways are the same, i.e. a solid debris bed located the bottom of the calandria vessel externally cooled by the water in shield tank (Meneley et al., 1996). However, the different core disassembly pathways result in different hydrogen production and fission product release trajectories, and thus different decay heat levels in the terminal debris bed.

There are several widely used severe accident codes that were originally developed for Light-Water Reactors (LWR), including MAAP, MELCOR, and SCDAP/RELAP5. However, the unique design features of

CANDU (especially the horizontal fuel channel design) and the distinctive severe accident phenomena (as described above) prevent the straight forward application of these codes to the CANDU reactors. To adapt the MAAP code to CANDU, extensive works have been performed since 1988 by adding a large number of CANDU specific models to MAAP-LWR leading to the deployment of the MAAP-CANDU code (Blahnik, 1991). ISAAC (Integrated Severe Accident Analysis Code) (Kim et al., 1995) is also based on MAAP and is developed and mainly used in Korea.

The RELAP5 code and its variants have been used for CANDU reactors with some validation against CANDU-related experimental data (e.g. the RD-14M tests) and code-to-code comparisons with the Canadian code CATHENA (Kim et al., 1995) (International Atomic Energy Agency, 2004). The SCDAP/RELAP5 code (SCDAP/RELAP5 Development Team, 1997) is an integration of RELAP5 (thermal-hydraulics), SCDAP (severe accident phenomena) and COUPLE code (lower vessel LWR phenomena). The RELAP/SCDAPSIM code (originating from SCDAP/RELAP5) is being developed as part of the international nuclear technology program called SCDAP Development and Training Program (Allison and Hohorst, 2010). It has been used by researchers in Romania (Dupleac et al., 2009), China (Tong et al., 2014), and Argentina (Bonelli et al., 2015) in the safety analysis for the CANDU reactors. A new version of the code, RELAP/SCDAPSIM/MOD3.6 (hereinafter to be referred as MOD3.6), is being developed at Innovative System Software (ISS) to support the analysis of Pressurized Heavy Water Reactors (PHWRs) under severe accident conditions. However, in the standard version of MOD3.6, models for many CANDU severe accident phenomena, especially during the core disassembly phase, are still lacking. The occurrences of thermal–mechanical deformations during the channel heat-up phase, e.g. PT ballooning/sagging and PT failure, are determined using user-input threshold numbers similar to MAAP4-CANDU code and the ISAAC code. For example pressure tubes are assumed to balloon when some criteria related to temperature and pressure are exceeded with no prediction of the phenomena related to deformation. While such threshold models are simple and easy to integrate into large computer programs, they preclude best-estimate analyses and do not easily allow the quantification of uncertainty. Mechanistic deformation models for CANDU fuel channels have been developed by other researchers (e.g. PT ballooning (Shewfelt et al., 1984) (Shewfelt and Godin, 1985) (Kundurpi, 1986) (Luxat, 2002), PT-to-CT contact conductance model (Cziraky, 2009), channel failure (Dion, 2016), PT sagging models (Gillespie et al., 1984), and channel sagging models (Mathew et al., 2003), but their use in integrated severe accident codes is limited. The sensitivity of accident progression and emergency mitigating actions to these models is currently not available in open literature.

Recently three mechanistic channel deformation models have been developed and validated to replace the threshold-based models in MOD3.6 by Zhou et al. (2018). The BALLON model calculates the transverse strain (which results in the change in diameter) of the pressure tube, determines the effective conductivity of the annulus before and after contact, and also predicts channel failure. The SAGPT model calculates the longitudinal strain and the deflection of PT, and also determines PT-to-CT sagging contact characteristics. The SAGCH model tracks sagging of fuel channel assembly after uncovery during the moderator boil-off phase, and determines channel-to-channel contact characteristics, channel disassembly, and core collapse.

In this paper the modified MOD3.6 code is used to simulate a postulated station blackout accident for a generic 900 MW CANDU plant providing an integrated prediction of the accident progression up to the point of calandria vessel dryout. At the end of simulated transient there is a terminal debris bed sitting on the bottom of the calandria vessel with no water present. The subsequent in-vessel retention phase of the accident is beyond the scope of this study. The application of RELAP/SCDAPSIM for CANDU in-vessel retention studies have been conducted by Dupleac et al. (2008), Mladin et al. (2010), Dupleac et al. (2011), and Nicolici et al. (2013).

To reduce the uncertainty in the modeling of core disassembly and to overcome the memory constraints of the code, the simulation is broken into two phases with the first phase (i.e., from initiating event to the channel failure and depressurization) simulated using relatively high-fidelity nodalization of the entire heat transport system (as described in Section 2.2.1), and the second phase simulated using nodalizations focused on in-core components, the calandria vessel, end shields and calandria vault (as described in Section 2.2.2). The full-plant RELAP5 model has been used to simulate a postulated SBO accident with the loss of Class IV, Class III, and Emergency Power Supply by Zhou and Novog (2017) with a focus on the natural circulation behavior during the early phase of accident where significant PT deformation can be precluded. The core disassembly nodalization was developed specifically for this work.

2. Model description

2.1. Models for severe accidents phenomena

The detailed description of the newly added deformation models in MOD3.6 and their validations against experiments can be found in (Zhou et al., 2018), thus will not be repeated here. The following two sections describe the models of other important severe accident phenomena in MOD3.6 and the minor modifications (if any) made to these models.

2.1.1. Oxidation, cladding deformation and fission product release

The oxidation of Zircaloy in RELAP/SCDAPSIM is assumed to follow the parabolic rate equation and is subject to three limits (SCDAP/RELAP5 Development Team, 1997): 1) Oxidation is terminated when the material is fully oxidized; 2) Oxidation is limited by the availability of steam; 3) Oxidation is limited by the diffusion of water vapor. For the ballooned and ruptured fuel cladding the oxidation rates are doubled in failed regions assuming the inside and outside of cladding oxidize at the same rates. Since both the CANDU pressure and calandria tubes are made of Zircaloy, modifications have been made in this work to account for the oxidation on both the PT inner surface and CT outer surface. Similar to cladding failure, after the PT and/or the CT is breached oxidation rates are doubled, i.e. the inside and outside surfaces of the PT and the CT oxidize at the same rates.

The cladding deformation in RELAP/SCDAPSIM uses the so-called "sausage deformation model" which is based on theory of Hill (1950) and the Prandtl-Reuss equations (Mendelson, 1968). Circumferential temperature gradients on the cladding are not taken into account and the cladding is assumed to deform like a membrane. The deformation stops once the outer diameter of the cladding is equal to the fuel rod pitch or once the cladding is breached. The users can input the rupture strain at which the cladding will rupture, the limit strain for rod-to-rod contact, and the strain threshold for double-sided oxidation (i.e. the strain above which steam can enter the gap freely to react with the inner surface after cladding failure) (Hohorst, 2013). The code also takes into account the flow blockage caused by the ballooning of the cladding. The fuel rod internal gas pressure is computed from perfect gas law. The gas volume considered in the code includes the plenum volume, fuel void volume as fabricated, and the additional gap volume due to cladding ballooning (SCDAP/RELAP5 Development Team, 1997).

The fission product release from fuel to the gap is modeled using a combination of the theoretical model developed by Rest (1983) for xenon (Xe), krypton (Kr), cesium (Cs), iodine (I) and tellurium (Te), and empirical models for other fission products (SCDAP/RELAP5 Development Team, 1997). After cladding failure cesium and iodine released from the gap are assumed to combine and form cesium iodide, with any leftover cesium reacting with water or any leftover iodine being released as I_2 (SCDAP/RELAP5 Development Team, 1997). The hydrogen and the energy released during cesium-water interaction are both accounted for in the model. Release of less volatile fission products is based on the CORSOR-M model in NUREG/CR-4173 (Kuhlman, 1985). Once the fuel has been liquefied, xenon, krypton, cesium and iodine are instantaneously released to the gap, while the release of less volatile species is not affected by liquefaction (SCDAP/RELAP5 Development Team, 1997).

2.1.2. Fuel rod liquefaction, relocation and solidification

Fuel rod liquefaction and relocation in SCDAP is modeled using the LIQSOL (LIQuefaction-flow-SOLidication) model which models the change in fuel rod configuration due to melting taking into account the oxidation and heat transfer of the liquefied cladding-fuel mixture during relocation (SCDAP/RELAP5 Development Team, 1997). The methodology is performed in three steps:

1) Calculate where the cladding and fuel have been liquefied. The liquefied mixture is assumed to be contained in the cladding oxide shell.
2) Calculate when and where the cladding oxide shell is breached. If the cladding is less than 60% oxidized, the oxide shell can contain the molten mixture until its temperature exceeds 2500 K (both 60% and 2500 K are the default and can be changed from input card). If the cladding is more than 60% oxidized, the oxide shell does not fail until its melting temperature is reached.
3) Calculate the relocation of the liquefied mixture due to gravity and the oxidation/heat transfer while it is slumping, and also predict when it has stopped slumping due to solidification. Drops of slumping materials are assumed to flow at constant velocity of 0.5 m/s in the shape of hemisphere with radius of 3.5 mm.

SCDAP is originally developed for LWR with vertical fuel rods, thus it models the melt of fuel rods as phenomena similar to burning of candles, i.e. drops of melt flow down axially until they solidify when reaching a cooler surface. The LIQSOL model is based on observations of the fuel rods behavior primarily obtained from CORA experiments (Hagen et al., 1988; Hagen, 1993). However, in CANDU reactors where the fuel bundles are placed horizontally in PTs the melting process has a different phenomenology. The 37 fuel elements are held together by the welded endplates at the two bundle ends, and separation of the elements from each other and from the PT is provided by the spacer and bearing pads that are brazed to the fuel cladding (Tayal and Gacesa, 2014). Experiments have shown that as the CANDU fuel channel heats up fuel elements will first sag into contact and fuse with each other to form a closely packed bundle (i.e. bundle slumping) before significant cladding and fuel melting takes place (Kohn and Hadaller, 1985). Bundle slumping increases the area of element surface in contact with the inside bottom of the PT which leads to more non-uniform circumferential temperature gradients in the PT increasing the likelihood of premature channel failure. The inter-element contact limits the steam access to the interior of sub-channels, and also leads to a unique melt relocation pattern: because the ZrO_2 layer is thinner in the contact area due to localized steam starvation, the oxide shell is most likely to rupture in the vicinity of an inter-element contact (Akalin et al., 1985). After the breach of oxide shell, capillary forces then rapidly move the molten material into the inter-element cavities, resulting in a small "pool" of melt (Akalin et al., 1985).

While the liquefaction and relocation process for such horizontal close-packed geometries are well described in the paper by Akalin et al. (1985), the detailed modeling of such process is difficult. Mladin et al. (2008) modified the RELAP/SCDAPSIM/ MOD3.4 code to analyse the early degradation of a fuel assembly in a CANDU fuel channel. Their models allow molten fuel inter-element relocation and fuel-to-PT relocation. Resizing of sub-channels inside a fuel channel during slumping and contact heat transfer among fuel elements were also accounted for. However, to use their models the 37 elements of a fuel bundle need to be modeled using a large number of SCDAP fuel components. While such detailed treatment is possible for single channel analyses, the number of components required for full-core simulations becomes intractable. In this study CANDU specific bundle slumping and fuel relocation are not considered in detail and the original LIQSOL model is used with the molten drop slumping velocity set to zero to avoid relocation in the axial direction (i.e. horizontally along the CANDU fuel bundle). The temperature at which the oxide shell fails is set to 2500 K, and the fraction of cladding oxidation for a stable oxide shell is set to 20% (recommended value in (SCDAP/RELAP5 Development Team, 1997). The implications of these assumptions are:

1) By precluding bundle slumping during the channel deformation and relocation phase, the amount of energy generation due to oxidation and the subsequent hydrogen generation will be over-predicted since the simulations allow much more steam access to cladding materials than the more realistic case where steam flow is hindered by subchannel deformations.
2) By precluding molten material relocation, the oxidation heat loads will be over-predicted, because inter-element relocation reduces the surface area available for Zr-steam reaction by allowing molten cladding to change from its original geometry into small pools with much smaller surface to volume ratio (Akalin et al., 1985).

Therefore, these assumptions provide an overall conservative estimate with regards to oxidation heat loads and hydrogen production for these phases of the accident. For subsequent phases of the accident differing conservative assumptions may be applicable.

It is also important to note (based on experimental observations (Akalin et al., 1985) inter-element relocation is most pronounced when the fuel heat-up rate is high (in excess of 10 °C/s). This is because at high heat-up rates the ZrO_2 layer will be thinner at the time when the remaining cladding becomes molten, and more low-oxygen Zr melt is available to dissolve the oxide layer. For the SBO scenarios analysed in this study, fuel channel heat-up occurs after SG dryout at low decay heat level, thus the fuel heat-up rates are considerably lower than 10 °C/s. Assuming no melt relocation is expected to cause less uncertainty in this study than in a scenario where the fuel heat-up rate is much higher, e.g. a Loss-of-Coolant Accident (LOCA).

Dupleac and Mladin (2009) investigated the effect of CANDU fuel bundle and fuel channel modeling using RELAP/SCDAPSIM by comparing four fuel channel models with increasing level of detail. The simplest model is similar to the current representation of fuel channel in this study, i.e. all the fuel elements were assumed to have the same average power and behave in the same manner. The most complicated model divided the fuel channel into four pathways with cross-flow junctions simulating the possible inter-sub-channel communication, and used the new model developed by Mladin et al. (2008) to account for bundle slumping and melt relocation. It was shown that for fast transients such as Large Break LOCA the hydrogen generated was influenced by the models employed, i.e. the simplest model over-predicted hydrogen production by about 27% compared to the model by Mladin et al. (for the medium-power channel). However, for slow transient, like SBO, the differences were much smaller. A sensitivity study is performed (discussed in Section 4.3) where the oxidation rate on the fuel surfaces is reduced in order to mimic the case where steam flow to a portion of the bundle interior is limited and shows that overall the timing of the event is not significantly altered which is consistent with the conclusions in the work by Dupleac and Mladin (2009).

2.2. RELAP5 nodalization of 900 MW CANDU plant

2.2.1. RELAP5 nodalization for early phase of SBO

The early phase of the SBO accident (i.e. from initiating event to the channel failure and PHTS depressurization) is simulated using a full-plant RELAP5 model which includes the primary heat transport system,

F. Zhou, D.R. Novog *Nuclear Engineering and Design 335 (2018) 71–93*

the feed and bleed system, the secondary side, the moderator system, and the shield-water cooling system. The 480 fuel channels were grouped into 20 characteristic channels by both elevation and channel power with the core divided into five vertical nodes (Fig. 1).

The power is calculated using the RELAP5 reactor kinetic model taking into account both fission product decay and actinide decay. The fission product decay modeling is based on the built-in 1979 ANS standard data (ANS79-3) for daughter fission products of U-235, U-238, and Pu-239. The relative heat load distributions among various systems (i.e. the PHTS fuel/coolant, the moderator, and the shield water) are calculated based on the reported values for CANDU 6 (Aydogdu, 2004), due to the unavailability of CANDU 900 data in literature. However, considering the similarities in design, the relative heat loads should be similar between a CANDU 6 and a CANDU 900. The changes in relative heat loads from fission products and actinide decay is considered as a function of time in this work, and energy from actinide decay is all deposited into coolant or the fuel due to the fact that low-energy gamma photons are most likely to be thermalized within the channels (Table 1). These subtle differences greatly impact the heat loads to the moderator during the early stages of the accident as discussed in Section 3.2.7.

More details about this full-plant model can be found in Zhou and Novog (2017) where the model was benchmarked against the 1993 loss-of-flow event at Darlington NGS. Table 2 summarized the key input parameters of the model and the initial conditions prior to the transient.

In the previous work by Zhou and Novog (2017) the fuel and fuel channels were modeled using RELAP5 heat structures, and due to the lack of channel deformation models in MOD3.3 the simulations were terminated prior to the heat-up/deformation of fuel channels. In this paper, the RELAP5 heat structures for the fuel channels are replaced with the SCDAP fuel and shroud components allowing various severe accident phenomena such as cladding/PT deformation and failure to be modeled. Trip valves connecting the channel and the calandria vessel are added and will open to simulate channel rupture into the calandria vessel.

2.2.2. *RELAP5 nodalization for core disassembly phase*

The core disassembly in CANDU involves the boil-off of moderator and the heat-up, sag and disassembly of uncovered channels. Channels at different elevations will heat up at different times/at different rates depending on their uncovery times/channel power, and there will be interactions (heat and mechanical load transfer) between channels at different rows. Therefore, it is ideal to increase the channel resolution in the model, especially in terms of elevation. The limitation of the full-plant model used in (Zhou and Novog, 2017) is that its channel grouping scheme is not sufficiently fine to capture the core disassembly phase phenomena. This full-plant model utilizes approximately 800 hydraulic components (i.e. near the current RELAP limit of 999). Significantly finer representation of core components for the disassembly phase is thus not possible.

To circumvent this issue modeling of the disassembly phase takes advantage of the change in component importance after the first channel rupture. In particular, after the first channel rupture the thermal–hydraulic response above the CANDU headers, the feed and bleed system, and the secondary side have little influence on the further progression of accident. Therefore a new nodalization can be adopted post-channel rupture where the initial conditions for such a model are inherited from the full-plant simulations after first channel rupture and prior to significant core degradation.

As noted previously, during the disassembly phase higher fidelity nodalization is needed with respect to channel location/elevation to allow for more accurate treatment of the moderator boil off phenomena as well as to capture channel-to-channel interactions (i.e., fuel channels sagging into contact with lower elevation channels). Full representation of all 480 channels would still exceed the RELAP limits so the following further simplifications are made:

1) Symmetry boundaries are applied such that only half of the core is modeled and 88 channel groups are arranged in 14 rows and 8

Table 1
Heat Loads in the 900 MW CANDU Model.

	Fission	FP Decay	Actinides Decay
To Moderator	4.202%	8.752%	0%
To Shield Water	0.181%	0.198%	0%
To Coolant	95.617%	91.050%	100%
Total	100%	100%	100%

Note: the heat loads to moderator and shield water in this table do not include the heat loss from the fuel channels which are calculated separately with heat structures.

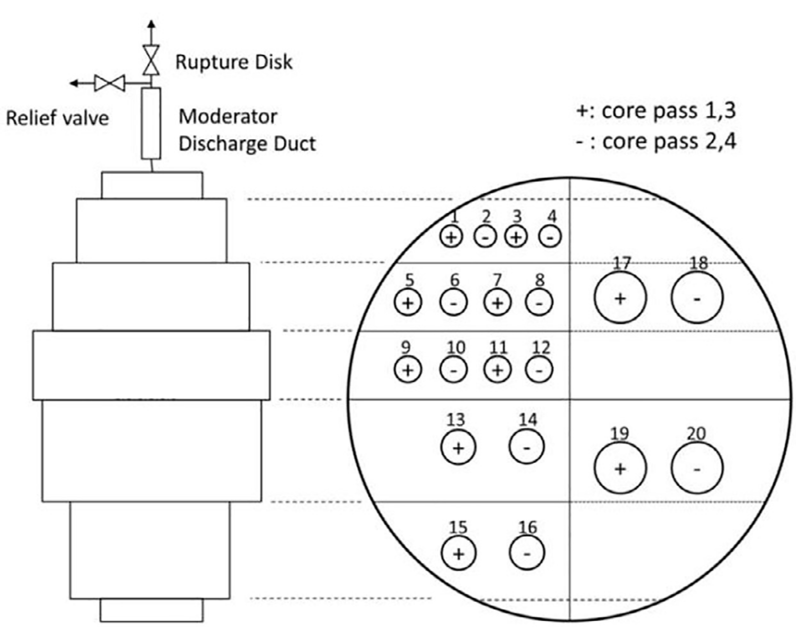

Loop	Pass		Code	No. of CHs	Power Av. (kW)
1	1	1	1T1	10	4218.7
		3	1T2	5	5976.6
		5	1T3	11	6153.1
		7	1T4	11	4971.5
		9	1T5	12	6365.6
		11	1T6	12	5460.4
		13	1B1	35	5853.6
		15	1B2	24	4971.5
	2	2	2T1	9	4281.6
		4	2T2	5	5907.4
		6	2T3	10	5141.2
		8	2T4	11	6171.3
		10	2T5	12	5465.9
		12	2T6	12	6362.6
		14	2B1	35	5916.9
		16	2B2	26	4857.2
2	3	17	3T	59	5600.7
		19	3B	61	5484.0
	4	18	4T	61	5532.9
		20	4B	59	5513.6
Total				480	2651MW

Fig. 1. Nodalization of Calandria Vessel and Channel Grouping Scheme (20-Group Model) (Zhou and Novog, 2017).

Table 2
Key Input Parameters for the 900 MW CANDU under Normal Operating Conditions.

Input Parameter	Value
Thermal Power (MW)	2651
No. of Fuel Channels in the core (−)	480
ROH pressure (kPa)	9921
SG pressure (kPa)	5050
Liquid Relief Valves setpoint (kPa)	10,551
Bleed Condenser pressure (kPa)	1720
Bleed Condenser relief valve setpoint (kPa)	10,270
ASDV setpoint (kPa)	5085
CSDV setpoint (kPa)	5050
Calandria Vessel steam relief valve setpoint (kPa)	165
Calandria Vessel rupture disks burst pressure (kPa)	239
Shield Water rupture disk burst pressure (kPa)	170
ROH coolant temperature (°C)	310.6
RIH coolant temperature (°C)	264.5
Feedwater inlet temperature (°C)	178.0
Moderator temperature (°C)	59.0
End Shield water temperature (°C)	55.6
Shield Tank water temperature (°C)	60.2
PHTS inventory (without Pressurizer) (m^3)	213
Pressurizer inventory (m^3)	64
Moderator inventory in Calandria Vessel (m^3)	287
No. of Loops, SGs, and Pumps (−)	2, 4, 4
SG inventory (per SG) (Mg)	91.9
End Shield water inventory (Mg)	23.6
Shield Tank water inventory (Mg)	743
Deaerator Tank inventory (Mg)	319.2
SGECS Tank inventory (per tank) (Mg)	69.5
UO_2 mass in the core (Mg)	125.3
Zircaloy (Cladding, PT, and CT) mass in the core (Mg)	49.8
Pressuriser level (m)	6.5
SG level (m)	14.4
Bleed Condenser level (m)	0.9

columns (Fig. 2). Fig. 3 shows the alterative channel grouping scheme which is only used in sensitivity study in Section 4.6. This symmetry condition assumes that the two loops of the reactor will disassemble and collapse with similar timings which is not necessarily valid (especially in accidents where asymmetric loop behaviors are expected, e.g. LOCA). However, the uncertainties caused by asymmetric core disassembly behaviors are expected to be smaller in the SBO accidents, given that the two loops will have similar thermal–hydraulic conditions.

2) Since earlier studies showed core collapse normally occurs prior to the moderator level dropping below 50% (Meneley et al., 1996), a reduced nodalization at the bottom of the core is used. Thus the maximum vertical resolution (12 rows) is given to the top half of the core while only 2 rows are assigned to the bottom half of the core. However, it is possible that in some accident scenarios core collapse may be delayed until the moderator level drops below 50%. In such case, it may be desirable to further divide the bottom half of the core.

A sufficient number of radial channel groups are also considered since these reflect differing channel powers and heat-up rates providing a total of 88 channel groups in the core disassembly nodalization. Each channel group will need at least two SCDAP core components, i.e. a fuel and a shroud component such that 176 SCDAP core components are needed. The transient is first run using the full-plant model and is terminated a few minutes after the first channel rupture (i.e. after PHTS depressurization and prior to channel heat-up). Then relevant initial and boundary conditions are passed to the core disassembly model and the transient is continued until the formation of terminal debris bed.

For vertical components, RELAP5 tracks liquid collapsed liquid height in detail. However, it has limitations on tracking liquid level in horizontal pipe components. In reality when the moderator level is decreasing fuel channels at higher elevations are uncovered earlier while fuel channels at lower elevation are still submerged in water. In contrast RELAP5 will utilize nucleate boiling correlations for all the heat surfaces in a volume, i.e. all CT outer surfaces within a node will involve nucleate boiling until such time as almost all the water in the calandria vessel is boiled off. Thus if the calandria vessel were simulated as a horizontal pipe component the impact of moderator level on channel cooling could not be determined accurately. To overcome this limitation the calandria vessel is subdivided into a series of vertical-oriented nodes with a variable diameter to capture the correct moderator inventory as a function of elevation. The moderator nodalization is divided into a number of cells corresponding to the channel grouping scheme, i.e. channels at different elevation are attached to different moderator nodes and the total moderator volume is conserved.

Fig. 4a shows the nodalization of the calandria vessel in the full-plant model where the calandria vessel is modeled using a vertical pipe with 7 cells (i.e., for the early portion of the accident where moderator volume does not influence behavior), while Fig. 4b is the new nodalizations for the core disassembly phase. In the disassembly model the top half of the calandria vessel is subdivided into 12 nodes to match one-to-one the channel grouping scheme in Fig. 2, while the bottom half remained unchanged. The end shield and the shield tank are similarly modeled using vertical-oriented pipe components (Fig. 5) at corresponding elevations to that in the calandria. The end shields are connected to the bottom of the topmost node of the shield tank. Thus the water level in the end shields will not change until the water in the shield tank drops to uncover the link between the end shield and shield tank. This will not occur within the scope of this study due to the large water inventory in the shield tank, although such phenomena may become important in the examination of terminal debris-bed cooling.

Fig. 6 shows all the heat transfer pathways in the core disassembly model. Each fuel channel structure consisting of the pressure tube, calandria tube and annulus gap is modeled using SCDAP shroud components with its inner surface attached to the fuel channel and the outer surface attached to the corresponding node in the calandria vessel. Similarly, the heat from the end fittings and the lattice tubes to the shield water is modeled using the appropriate linkages. RELAP5 heat structures are also used to represent the tube sheet and the calandria vessel shell so that the heat transfer between the end shield and the moderator, and between the moderator and the shield tank are considered. The standard RELAP correlations are applied to these structures.

3. Extended SBO accidents

In the previous study by Zhou and Novog (2017) five SBO scenarios with and without crash-cooling and with different water make-up options were modeled for a 900 MW CANDU plant using RELAP5/MOD3.3. All the simulations were terminated as soon as the channels increased significantly in temperature. The results revealed that operator interaction plays a significant role in the event timing in the early phases and can therefore vastly change the decay heat level at the time of channel heat-up and core disassembly. In this paper, the same SBO scenarios as shown in Table 3 are simulated using the modified MOD3.6. The simulations are continued until the formation of a terminal debris bed to investigate the impact of operator timing on late stage accident progression.

Case CD1 is defined as the reference case where operator initiated crash-cooldown is credited and both the gravity-driven deaerator flow and the SGECS are available. In case CD2 only the deaerator water is credited. Case CD3 examines the impact of crash-cooling without crediting any water make-up. CD4 corresponds to cases where no operator intervention is credited. All these four scenarios are simulated using the best-estimate full-plant models and assumptions while the sensitivity to model input parameters will be discussed separately in Section 4.

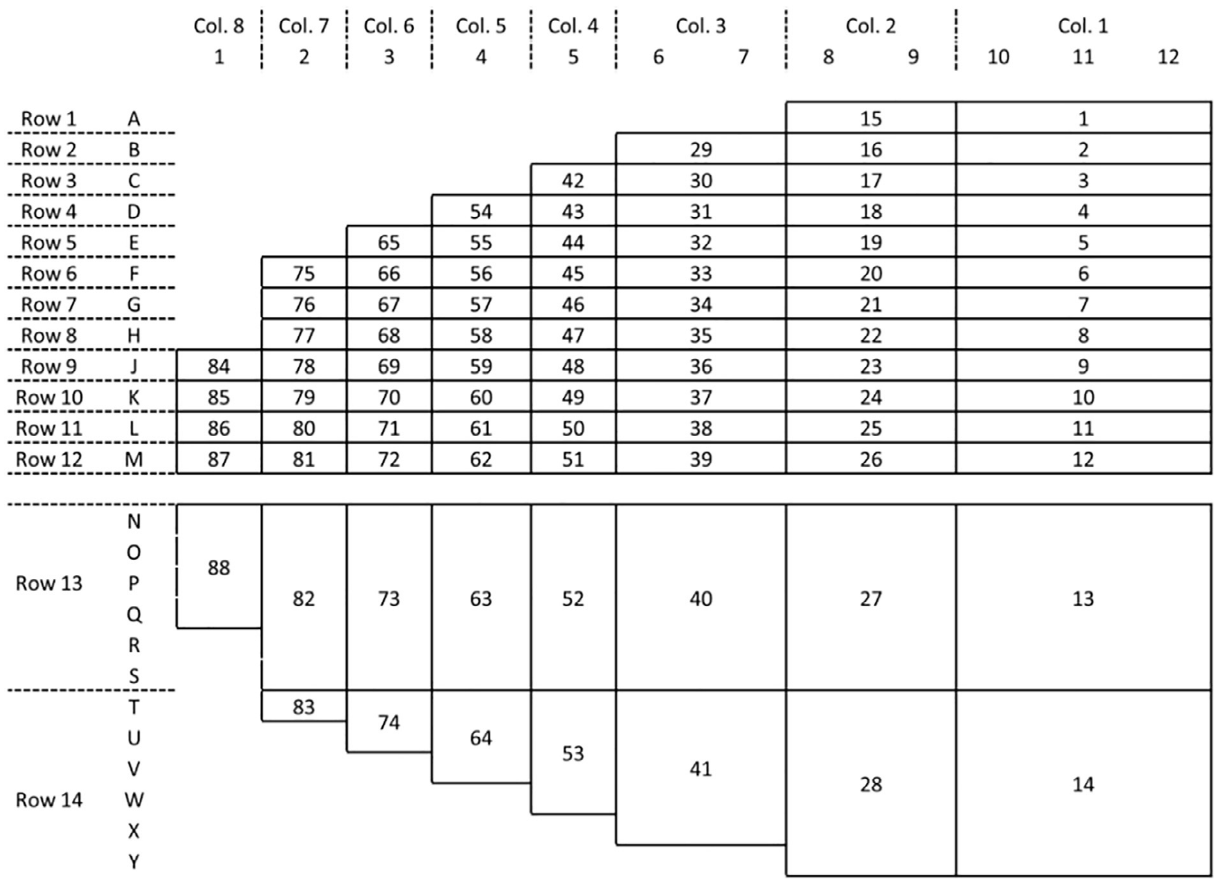

Fig. 2. Channel Grouping Scheme for Core Disassembly Phase (Reference Case).

3.1. Modelling assumptions

The modeling assumptions for thermal–hydraulic systems are consistent with the previous study (Zhou and Novog, 2017). Some of the important ones are listed below (refer to (Zhou and Novog, 2017) for more details):

1) Loss of Class IV power occurs at time zero. Class III power, and Emergency Power Supply are also lost leading to the loss of moderator cooling, shield tank and end-shield cooling and the loss of Emergency Core Cooling (ECC) components.
2) Class I and II powers are assumed available. However, it is important to note that for a typical CANDU plant when Class III power has been lost Class I power will be supplied from the batteries while Class II power is connected to Class I power via inverters. The batteries can last for about an hour (Jiang, 2015) (this number may vary depending on the specific site design). The loss of DC power can leads to the unavailability of equipment. For the transients in this study the systems dependent on DC power, e.g. SGECS, have already finished operation by the time the batteries are depleted.
3) Loss of turbine load is also initiated at time zero.
4) Following turbine trip, reactor power stepback to 60% is initiated by inserting the Mechanical Control Absorbers with 0.5 s delay. Sensitivity studies show no significant impact of absorber insertion on the long term transients.
5) The reactor Shutdown System 1 (SDS1) is tripped on low flow signal (inlet feeder flow drops below 71% of normal flow).
6) The CSDVs are available until the condenser vacuum is lost at approximately 13.5 s. ASDVs are assumed to be available.
7) Pressurizer steam bleed valve, liquid relief valves, and bleed condenser relief valves are assumed available.

The modeling assumptions for the thermo-mechanical deformation models are:

8) The loads applied to the PT (sagpt) and to the fuel channel (sagch) are assumed to be uniformly distributed and are set to 588 N/m and 620 N/m respectively (Zhou et al., 2018).
9) PT is assumed to fail when the average strain exceeds 20% which is the typical measured average transverse creep strain at failure in PT deformation tests with small circumferential temperature gradient (Shewfelt and Godin, 1985). The impact of early channel failure due to non-uniform temperatures or high pressure ballooning is investigated separately in Section 3.2.6 by performing sensitivity analysis, i.e. Case CD1F where a PT failure strain of 6% is imposed and the other modeling assumptions are identical to the reference case CD1.
10) Fuel cladding is assumed to fail if the fuel element average strain exceeds 5%. This cladding overstrain failure criterion (also used in codes such as ELOCA) is considered to be very conservative as it represents the potential onset of cladding ballooning rather than cladding failure (Lewis et al., 2009).
11) The four garter springs in the PT sagging model are assumed to be evenly spaced (with a distance 1 m) and located in the centre of the channel, i.e. they are located at 1.5 m, 2.5 m, 3.5 m, 4.5 m. The garter springs are assumed to rigid, while in reality they can deform under high temperatures (Gillespie et al., 1984). Assuming they remain rigid in the current model may contribute to a delayed PT-to-CT sagging contact thus the overestimation of PT temperatures.
12) After PT-to-CT sagging contact a constant contact area and a constant contact conductance are applied to the location of contact. The contact conductance is assumed to be 5.0 kW/m^2K with the

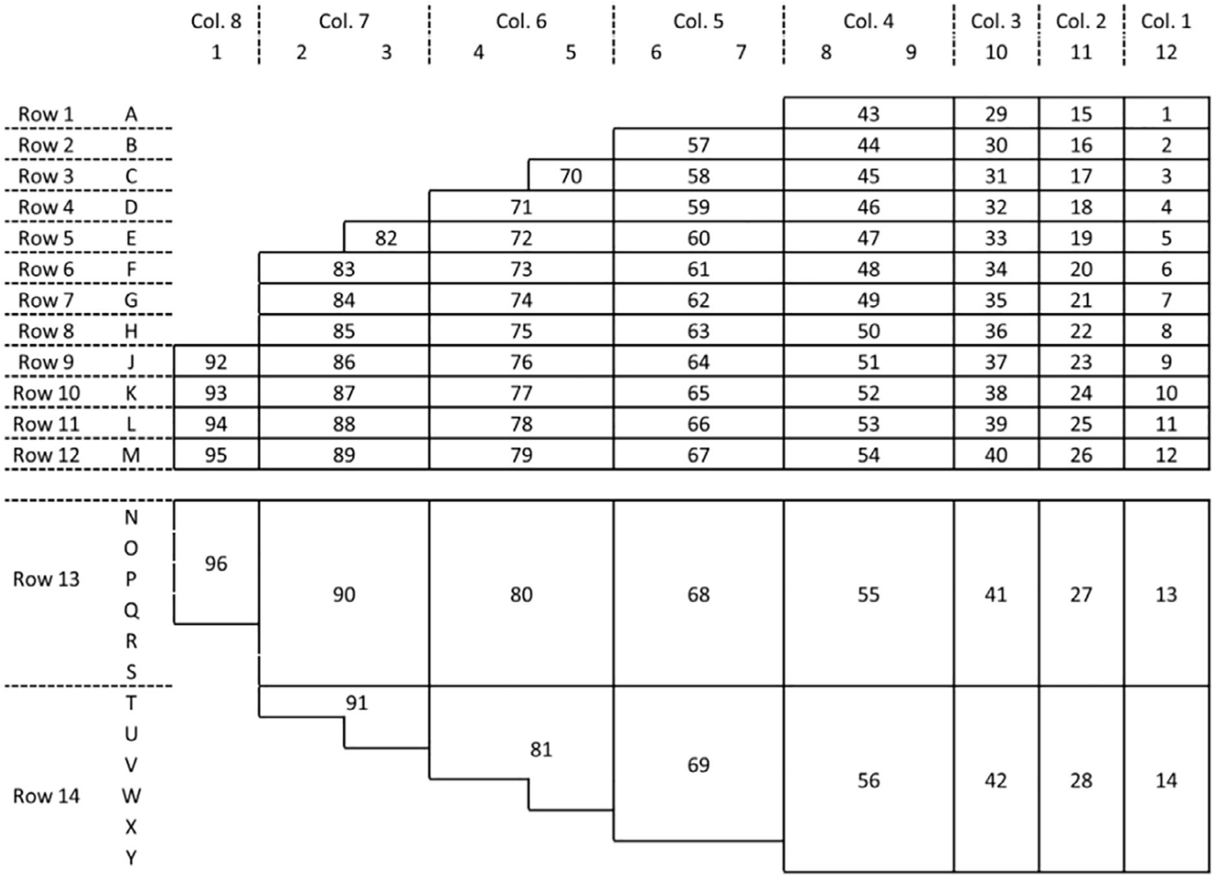

Fig. 3. Alternative Channel Grouping Scheme for Sensitivity Study.

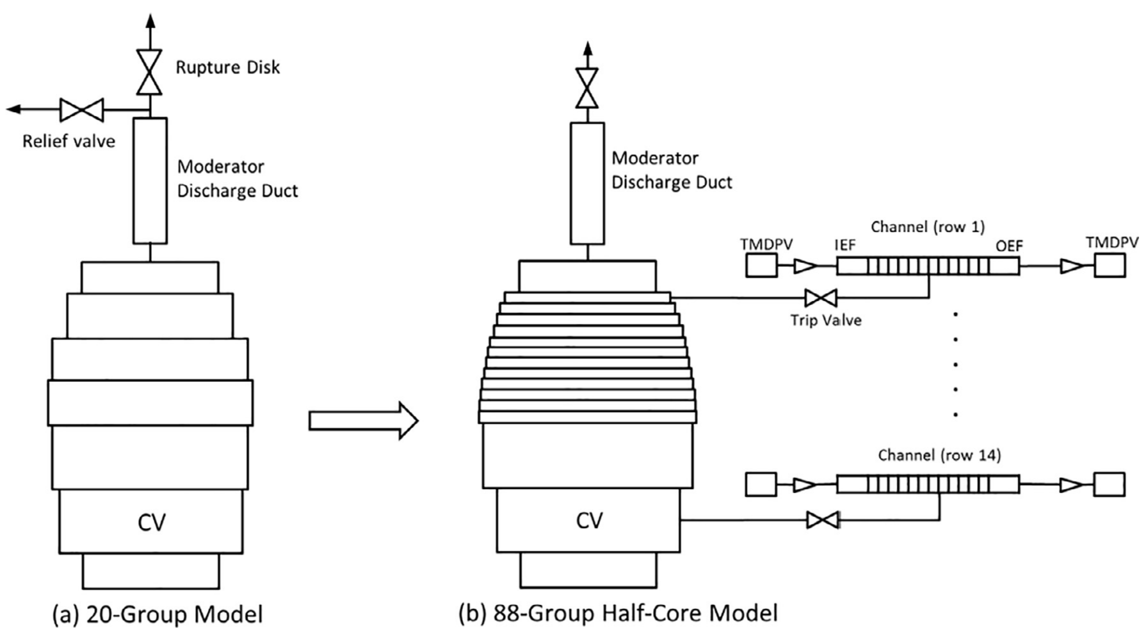

Fig. 4. Nodalization of Calandria Vessel for Early Phase (a) and Core Disassembly Phase (b).

contact length and contact angle set to 0.5 m and 10° (converted to effective conductivity of the annular gap and applied to the all nodes between two adjacent spacers of the contact location). In the PT sagging experiments by Gillespie et al. (1984) the PT contacted the CT in the central 0.5 m quite rapidly with a measured maximum contact angle of 20°. The value (i.e. angle) used in the modeling is thus conservative. Sensitivity to the contact angle is investigated and discussed in Section 4.2.

13) For channel-to-channel contact, the contact conductance and contact angle are set to 5.0 kW/m^2K and 15° respectively. The input of contact length is not necessary as the model allows the continuous tracking of contact area (Zhou et al., 2018). Sensitivity to the

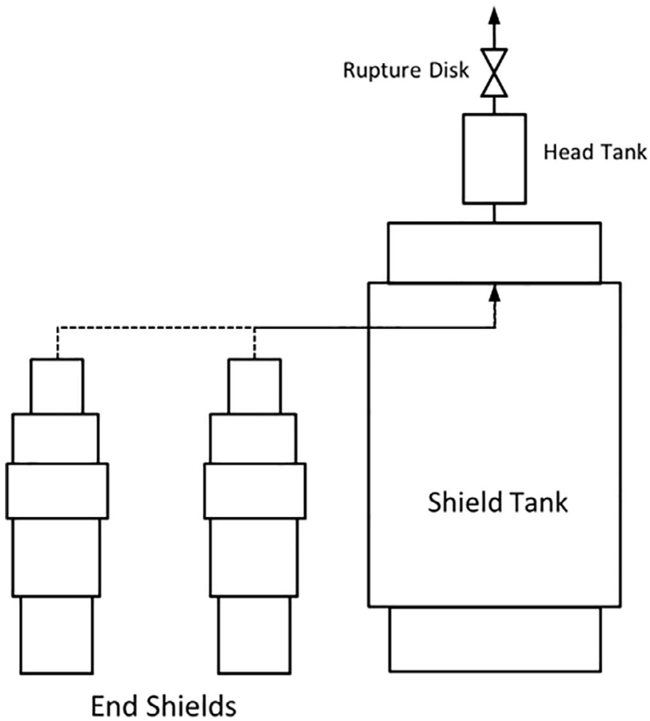

Fig. 5. Nodalization of the Shield Water Cooling System.

contact angle is addressed in Section 4.2.

14) When the maximum displacement of the channel exceeds 2 lattice pitches, the majority of the affected channel (3rd–10th bundles) will separate and relocate downward leaving small "stubs" of the channel connected to the tube sheet. This is based on experimental evidence from the Core Disassembly Test, i.e. post-test examination of a two-row channel test showed hot-tear on the bottom side of a sagged channel, at both sides, two bundle lengths away from channel end (Mathew, 2004). In addition, if the fuel channel experiences localized heat-up such that the CT temperature of a channel segment exceeds the melting temperature before significant sagging occurs (though unlikely), the corresponding segment is separated from the rest of the channel and relocated downward.

Table 3
Simulated SBO Scenarios.

Case	MSSV (timing)	Deaerator	SG ECS	EME	Note
CD1	Y (15 min)	Y	Y	–	crash-cool
CD2	Y (15 min)	Y	–	–	crash-cool
CD3	Y (15 min)	–	–	–	crash-cool
CD4	–	–	–	–	no crash-cool

15) After channel failure it is assumed that the bundles in the end stubs will not relocate regardless of the degree of sagging, and remain suspended at their original position even after the column collapses. The end stubs and the corresponding fuel bundles, however, will be relocated downward when the temperatures of the supporting CTs exceeds its melting point. Sensitivity to the behavior of the bundles in the end stubs is discussed in Section 4.4.

16) The maximum load a single fuel channel can support before the UTS of the CT is exceeded at the top of the CT is set to 3500 N/m (or 2143 kg) which is estimated using the mechanistic model from MAAP5-CANDU (Kennedy et al., 2016) for calculating maximum supportable load:

$$W_{chan\ max} = \frac{I_0 \sigma_{UTS}}{R_{CTo}} \left[\frac{12L}{L^2 + 2aL - 2a^2} \right] \{N\} \tag{1}$$

assuming that the ultimate tensile stress (σ_{UTS}) of cold-worked Zr-2 at 100 °C (moderator is likely to be saturated at the time of core collapse) is 661 MPa (Whitmarsh, 1962) and the unloaded length (a; length of one side of the CT that is unloaded) equals 0.5 m. L is the length of CT; R_{CTo} is the CT outer radius; I_0 is the moment of inertia of the CT. The maximum load a channel can support is sensitive to the unloaded length (or the spreading of the debris) as predicted by Eq. (1). Sensitivity to the core collapse criteria is discussed in Section 4.1.

3.2. Results and discussions

3.2.1. Early phase of SBO accident

The early phase of the four SBO scenarios (prior to any significant channel deformation) has been studied in detail by Zhou and Novog (2017), thus will not be repeated. A brief summary is presented in this Section since the timings of events in the early phase (Table 4) influence the later accident progression.

After the loss the Class IV power, the PHTS pumps rundown and

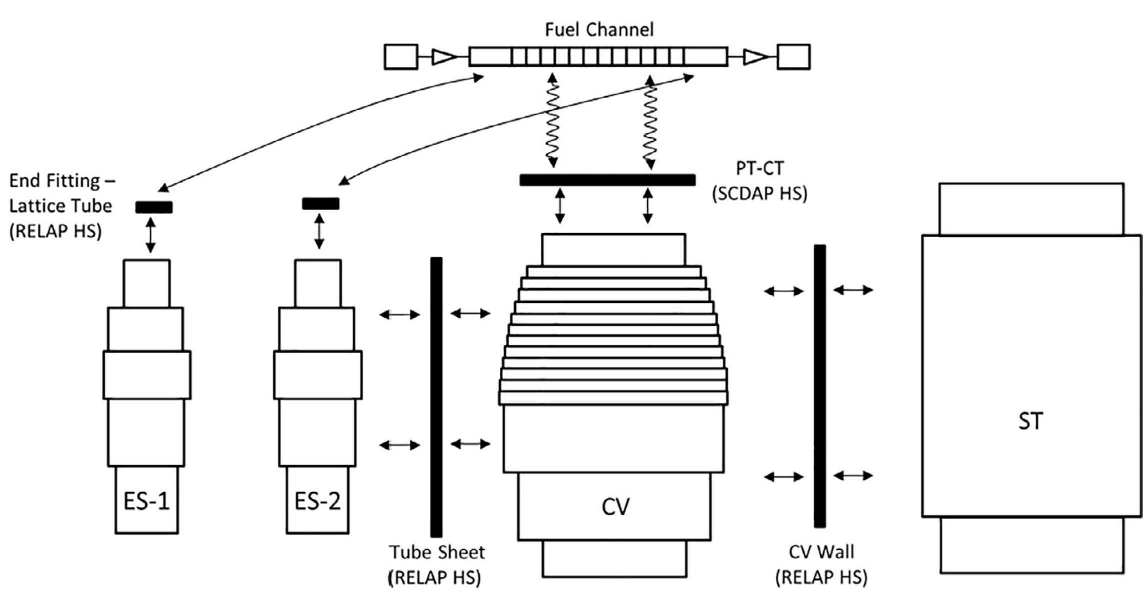

Fig. 6. Heat Flow Pathways in the Core Disassembly Model.

Table 4
Predicted Event Timings (seconds).

		CD1	CD1F[5]	CD2	CD3	CD4
Early Phase	Loss of Class IV	0.0	0.0	0.0	0.0	0.0
	Turbine Trip	0.0	0.0	0.0	0.0	0.0
	Emergency Stop Valve Close	0.28	0.28	0.28	0.28	0.28
	Reactor Stepback	0.5	0.5	0.5	0.5	0.5
	CSDV First Open	0.8	0.8	0.8	0.8	0.8
	SDS1 Trip	3.8	3.8	3.8	3.8	3.8
	Liquid Relief Valve First Open	4.6	4.6	4.6	4.6	4.6
	ASDV First Open	13.6	13.6	13.6	13.6	13.6
	MSSV Open	900	900	900	900	–
	SGECS Flow Begins	1196	1196	–	–	–
	Deaerator Flow Begins	1692	1692	1768	–	–
	IBIF Begins	2020	2020	2080	2050	–
	SG Dry	57,840 (16.07 h)	57,840 (16.07 h)	41,504 (11.53 h)	11,624 (3.23 h)	18,360 (5.10 h)
	Moderator Saturated[1]	41,808 (11.61 h)	41,808 (11.61 h)	40,848 (11.35 h)	19,509 (5.42 h)	19,720 (5.48 h)
	Bleed Condenser Relief Valve First Open	65,842 (18.29 h)	65,842 (18.29 h)	46,304 (12.86 h)	16,123 (4.48 h)	19,835 (5.51 h)
	Channel Stagnant[2]	66,572 (18.49 h)	66,572 (18.49 h)	48,275 (13.41 h)	16,522 (4.59 h)	20,623 (5.73 h)
PT Deform. Phase	RIH/ROH Void ($\alpha > 0.999$)	67,168 (18.65 h)	67,168 (18.65 h)	48,719 (13.53 h)	16,821 (4.67 h)	21,037 (5.84 h)
	1st PT-to-CT Balloon/Sag Contact	77,023 (21.40 h)	71,428 (19.84 h)	55,776 (15.49 h)	17,385 (4.83 h)	22,798 (6.33 h)
	Calandria Vessel Rupture Disk Open	76,056 (21.13 h)	69,995 (19.44 h)	54,365 (15.10 h)	23,358 (6.49 h)	25,700 (7.14 h)
	First Channel Failure[3]	77,081 (21.41 h)	69,986 (19.44 h)	55,954 (15.54 h)	24,542 (6.82 h)	26,867 (7.46 h)
Core Disassembly Phase	**Simulation Restart Point**	77,600	71,200	56,600	25,200	27,800
	1st CT-to-CT Contact	77,884 (21.63 h)	71,754 (19.93 h)	56,773 (15.77 h)	25,332 (7.04 h)	28,304 (7.86 h)
	Start of Core Collapse	80,475 (22.35 h)	76,541 (21.26 h)	59,102 (16.42 h)	27,653 (7.68 h)	31,700 (8.81 h)
	End of Core Collapse[4]	85,953 (23.88 h)	81,765 (22.71 h)	63,617 (17.67 h)	31,356 (8.71 h)	35,920 (9.98 h)
	Calandria Vessel Dry	94,436 (26.23 h)	90,334 (25.09 h)	72,062 (20.01 h)	38,826 (10.79 h)	42,535 (11.82 h)

[1] Moderator is assumed to be saturated when the average temperature exceeds 110 °C.
[2] Highest channel in core pass one of loop if more than one channel is present.
[3] Channel failure after the rupture disks open and fuel channel is uncovered.
[4] "End of core collapse" is defined as the collapse of all columns except column 8 (the outermost column, refer to Fig. 2.
[5] Pressure tube failure strain is set to 6% (as opposed to 20% in case CD1, 2, 3 and 4) to study the effect of early channel failure.

coolant flow rate decreases. Reactor power stepback is initiated by the insertion mechanical control absorbers shortly after turbine trip. When the inlet feeder flow drops below the SDS1 setpoint, the shutdown rods are inserted into the reactor core rapidly reducing the power to decay heat levels. The SG pressure increases after the close of Emergency Stop Valve. Steam on the secondary side is released first via CSDV to the condenser until condenser vacuum is lost then to the atmosphere through ASDVs. The SGs in a CANDU reactor are at a higher elevation than the reactor core. Continuous natural circulation on the primary side is thus established shortly after the pump inertia is exhausted. The PHTS pressure is stabilized at approximately 8.5 MPa when the natural circulation heat removal matches the decay heat generation.

In cases where crash-cool is credited (i.e. CD1 to CD3) the operator manually open MSSVs at 900 s (15 min) to depressurize the SG secondary side. The rapid depressurization causes the water in the SGs to vaporize resulting in an initial water level transient more severe than the non-crash-cool case CD4. In case CD1, the SGECS valve open when the SG pressure drops below 963 kPa at about 20 min, and water from the SGECS tanks is injected into the SGs by instrument air. As the pressure decreases further, at about 28 min the gravity-driven flow starts from the deaerator tank. In case CD2 where only the deaerator water is credited, deaerator flow starts at 29 min. The water make-up from the SGECS and/or the deaerator temporarily reverses the decreasing SG level.

Meanwhile, in cases CD1 to CD3 the depressurization of the SGs temporarily enhances heat removal from the primary side causing the primary-side temperature and pressure to decrease. Without ECC the pressure of the primary side eventually approaches that of the secondary side causing the impairment of SG heat removal effectiveness. Following a temporary flow enhancement the continuous natural circulation on the primary side breaks down at about 33–34 min. However, almost immediately after the disruption of continuous natural circulation, intermittent buoyancy induced flow (IBIF) begins in the fuel channels allowing vapor generated in the core to be vented to the SGs and condensed. The detailed behavior and the mechanism of IBIF phenomena have been discussed in (Zhou and Novog, 2017).

In all four cases (CD1 to CD4), the SG secondary side water is the primary heat sink during the early stage of the accident. Either continuous natural circulation or IBIF continues to remove heat from the core until the SG inventory is depleted. Without crash-cooldown (i.e. case CD4), the low-pressure water sources (e.g. SGECS and deaerator tank water) cannot be supplied to the SGs. The initial inventory of the SGs (about 92 Mg per SG) is predicted to provide about 5.10 h of heat sink capacity.

With crash-cooldown credited, various water make-up options to SGs become possible to extend the IBIF mode of natural circulation. In case CD1, with the combined make-up water from SGECS and the deaerator tank the SGs provide 16.07 h of heat sink capacity. For case CD2 where only passive flow from the deaerator tank is credited, the SGs provide 11.53 h of heat sink capacity. If the SG inventory can be maintained through external water make-up, IBIF will continue indefinitely. However, in case CD3, where crash-cooling was credited but water make-up from any source is unavailable, SGs dried out at 3.23 h significantly earlier than in case CD4.

After the SG heat sink is lost, the subsequent accident progressions are similar in the four cases, albeit at different times and decay heat levels. The PHTS is pressurized due to the heat removed from the fuel exceeding the heat sink capabilities (Fig. 7). Liquid relief valves then open discharging coolant into the bleed condenser which has already been isolated on high coolant temperature downstream of the bleed cooler. The bleed condenser pressure increases rapidly until it reaches the setpoint of its own relief valve. The PHTS pressure is then governed by the bleed condenser relief valve capacity. The time interval between SG dryout and the first opening of Bleed Condenser relief valve is much greater in the three crash-cool cases than the non-crash-cool case (CD4).

In case CD4, as coolant is lost through the liquid relief valves void in

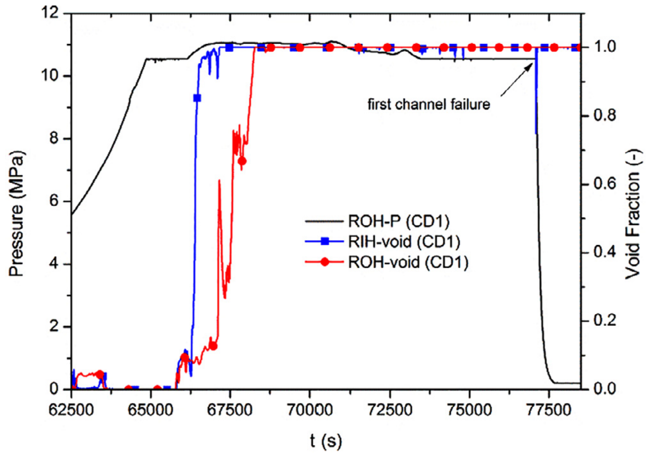

Fig. 7. ROH Pressure and RIH/ROH Void Fraction in Case CD1.

the PHTS increases. Flow resistance in the SG U-tubes thus increases leading to negative RIH-to-ROH pressure differential. When this pressure differential becomes large enough to overcome the hydrostatic head difference between the inlet and outlet feeder pipes, the flow in some fuel channels becomes reversed. At some point, continuous natural circulation through the SGs breaks down, but the interchannel flow phenomena will persist until the RIH or ROH becomes voided (5.84 h), i.e. the connections between the header and the feeder pipes are uncovered. Flow in the channel then stagnates. In the three crash-cool cases (CD1-3), IBIF ceases during the repressurization of PHTS, and interchannel flow phenomena are predicted until the headers become voided.

3.2.2. Pressure tube deformation phase

Once the coolant in channel is stagnant, void in the channels increases rapidly as the coolant boils off and the fuel channels begin to heat up. The PTs will then start to balloon since the internal pressure at the time of fuel channel heat-up is high (10–11 MPa, see Fig. 7). Ballooning is the dominant PT deformation mechanism at PHTS pressures greater than approximately 1 MPa. If the PT circumferential temperature gradient is small, the PTs are allowed to balloon into contact with the CTs. This establishes an effective thermal conduction pathway for heat rejection into the moderator. During this channel boil-off phase, the flow in channel is horizontally stratified. The PT under flow stratification may experiences high and potentially non-uniform temperatures which may cause early fuel channel failure before the PT-to-CT contact occurs.

In case CD1 to CD4, it is assumed that the all fuel channels will survive the PT ballooning phase, allowing heat rejection to the moderator. Historically, it is common to assume that the PTs in a SBO transient will always fail early and before contacting the CTs. This is because the PHTS pressure at the time of fuel channel heat-up in a SBO scenario is high (about 10 MPa depending on the bleed condenser relief valve setpoint and capacity), and the existing ballooning tests performed at such high pressures all showed early PT failure (Luxat, 2001). However these tests correspond to decay heat levels much greater than those present when crash cooling is credited and hence while failure is still likely it has not been universally demonstrated under scenarios involving crash cooling. Therefore in this analysis both full ballooning contact into the calandria tube and early PT-failure under high pressure are assessed. The impact of potential early channel failure is discussed separately in Section 3.2.6.

In all the four cases (CD1 to CD4) most of the PTs are found to have ballooned during this phase. PT deformation starts at a temperature greater than approximately 500 °C with PTs expanding radially under hoop stress towards the CTs (Fig. 8). The effective conductivity of the annulus gap is dynamically updated in the code to account for the change in geometry as the pressure tube to calandria tube gap decreases. The heat resistance across the annulus gas thus decreases with the decrease in PT-CT gap distance. For all the fuel channels in case CD1 and CD2 a local energy balance is reached and the PTs stop ballooning before they contact their CTs resulting in small gap distance between the two pipes (Fig. 8). Similar phenomenon is also observed in the low-power channels in case CD3 and CD4. This is different from the observations in the existing PT deformation experiments where the PTs all deformed quickly into contact with the CTs. This inconsistency is attributed to the very-low decay power level at the time of channel heat-up in this study. The heater power rating in experiments typically ranges from 30 to 200 kW/m with the majority of them above 60 kW/m (Dion, 2016; Gillespie, 1981; Nitheanandan, 2012) since such conditions are relevant for LOCA/LOECC and SBO cases with no-crash cooling. With the evolution of severe accident management, crash cooling has become a key operator action and leads to power ratings below 10 kW/m for all cases. Hence the conditions at channel heat-up in cases where crash-cooling is credited deviate from the more conservative test conditions in the past.

At the time of fuel channel heat-up all the channels are submerged in the moderator. The contact between PT and CT (or the decrease in gap distance for those partially ballooned channels) establishes the moderator as heat sink. The heat deposited into the moderator during this phase thus increases substantially (Fig. 9). The moderator steaming/evaporation rate soon exceeds the capacity of the relief valve of the cover gas system. The calandria vessel is thus pressurized to the rupture disk burst pressure (Fig. 10) and the rupture disks are predicted to open about 1.3–2.5 h after the main heat transport system headers become voided (Table 4).

The depressurization of the calandria vessel lowers the saturation point of the moderator leading to extensive bulk boiling. A large amount of moderator is expelled into the containment through the discharge duct resulting in a step change in moderator level (Fig. 10). After stabilization, in cases CD1 to CD4, between 4 and 6 rows of channels are predicted to be uncovered by the two-phase moderator level (enough to uncover the highest channel groups in the full-plant model) (Fig. 11). Considering the complexity of the moderator expulsion phenomena, the moderator level transients predicted by RELAP5 will have high uncertainties. Nevertheless, the predicted remaining moderator mass in the calandria vessel (i.e. about 60–61% in case CD1 and CD2, and about 64–65% in case CD3 and CD4) is fairly close to the number 63% predicted by MODBOIL (Rogers, 1989). MODBOIL is a CANDU-specific code used to predict the transient moderator expulsion behavior. The sensitivity of subsequent accident progression to the amount of moderator left after expulsion is discussed in Section 4.5.

Those uncovered channels heat up quickly with their PTs ballooning

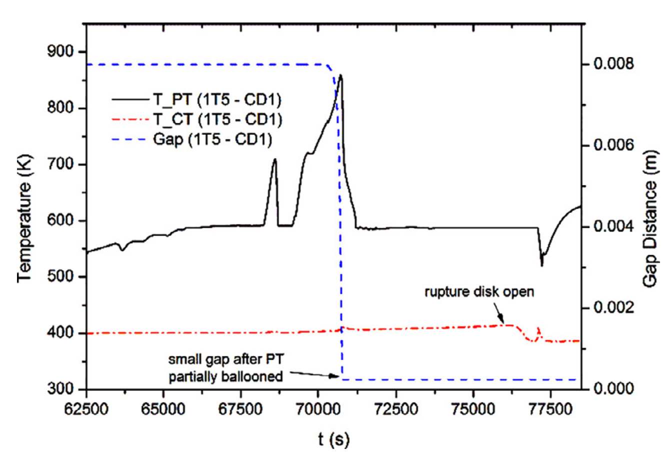

Fig. 8. PT, CT Temperatures and PT-to-CT Gap Distance at 7th Bundle in Channel 1 T5 in Case CD1 (refer to Fig. 1 for the channel grouping scheme of 20-group model, same below).

F. Zhou, D.R. Novog Nuclear Engineering and Design 335 (2018) 71–93

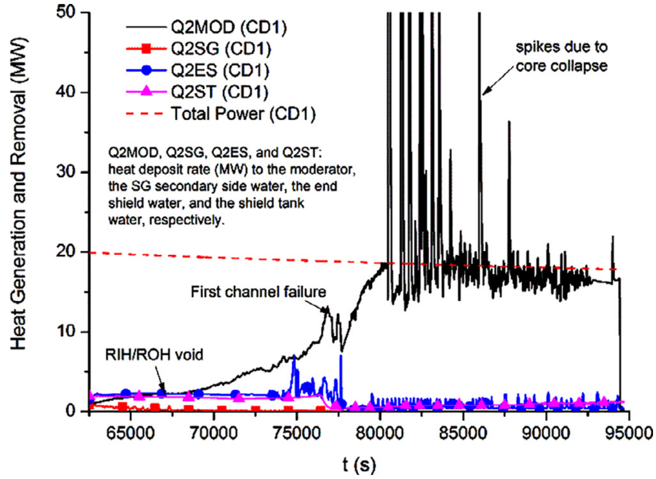

Fig. 9. Heat Generation and Removal Rate in Case CD1.

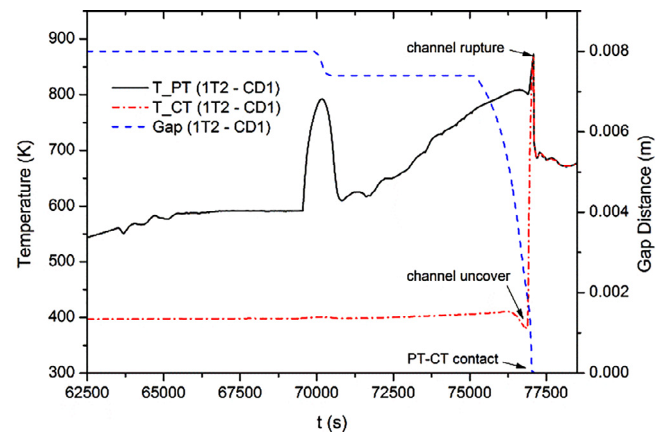

Fig. 12. PT, CT Temperatures and PT-to-CT Gap Distance at 10th Bundle in Channel 1 T2 in Case CD1.

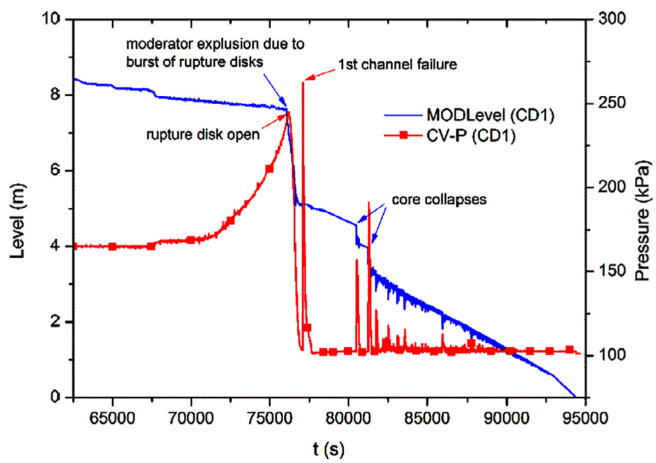

Fig. 10. Collapsed Moderator Level and Calandria Vessel Pressure in Case CD1.

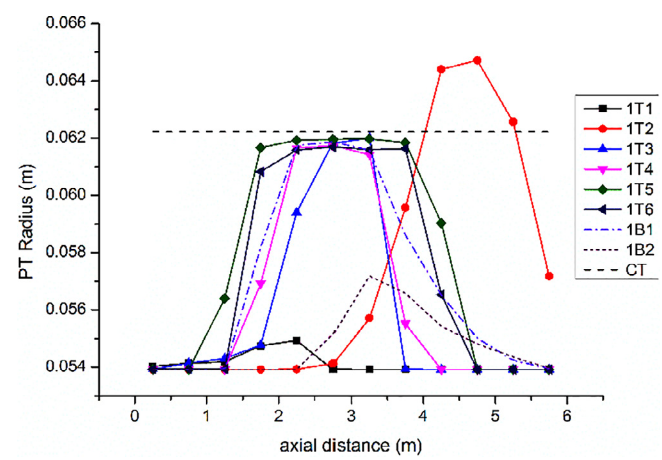

Fig. 13. Pressure Tube Axial Profiles of Channels in Core Pass 1 Prior to Core Disassembly in Case CD1 (t = 77,600 s).

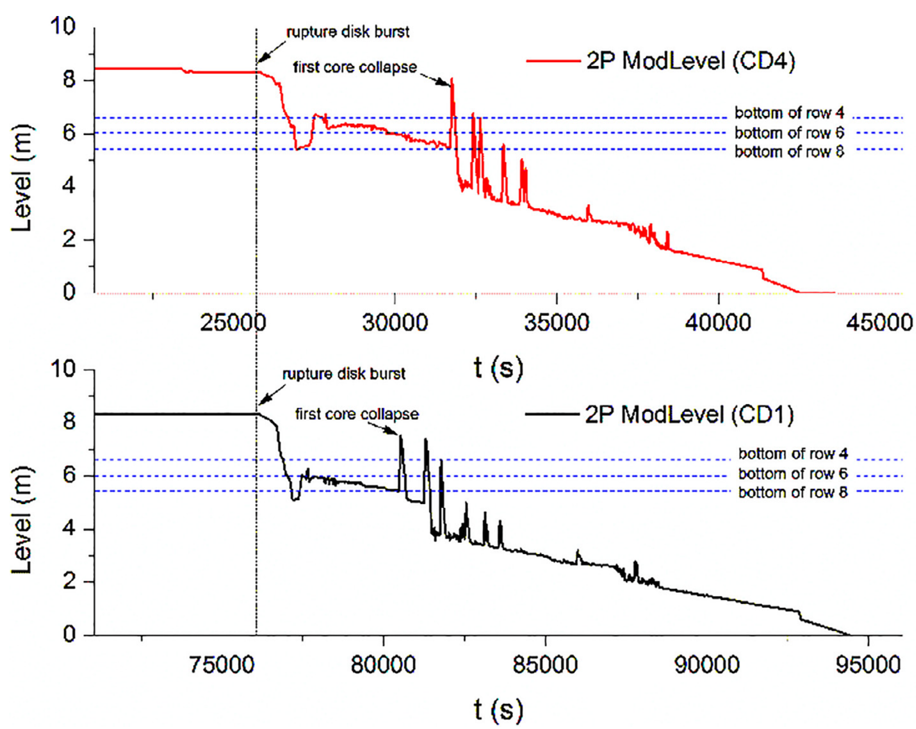

Fig. 11. Two-Phase Moderator Level in Case CD1 and CD4.

into contact with the CTs (if contact has not previously been made). After contact, the PTs continue to expand together with their CTs until the CT/PT failure strain is reached (Fig. 12). First channel failure occurs shortly after the rupture disks burst in all the four cases (Table 4), causing the calandria vessel pressure to spike (with a peak pressure of 262.6 kPa in case CD1, 265.0 kPa in case CD2, 272.3 kPa in CD3, and 275.3 kPa in CD4). The remaining coolant in the PHTS is discharged into the calandria vessel through the failed pressure tubes resulting in rapid depressurization (Fig. 7) which temporarily cools the fuel channels. As the PHTS pressure drops PT ballooning is terminated. Fig. 13 shows the PT radius along the axis after channel rupture for all the channels of loop one in case CD1. It can be seen that the PTs in all the channels except those with very low power have deformed significantly, and first failure occurs in one of the uncovered high-power channels, i.e. 1T2 (refer to Fig. 1 for the channel grouping scheme of the 20-group model).

3.2.3. Core disassembly phase

The temperatures of the fuel channels soon begin to increase again. For the submerged fuel channels in which the PTs have ballooned into contact with the CTs, the temperatures of the PT and fuel cladding are arrested well below the Zircaloy-steam reaction temperature. The PT temperatures may become high in the channel (or at locations) where the PT has not significantly ballooned. This causes the PT to sag into contact with the CT under the weight of the fuel bundles further establishing the moderator as heat sink.

For the uncovered fuel channels the CTs soon lose their strength at high temperatures and the fuel channel assemblies start to sag. The sagged channels eventually contact the lower elevation channels transferring both heat and mechanical load. First channel-to-channel contact occurs about 0.5 h after the opening of calandria vessel rupture disks in case CD1 and about 0.72 h in case CD4 (Table 4). If the lower channel is still submerged and is sufficiently cooled, heat from the sagged channel will be effectively conducted to the lower channel and is then removed by the moderator (Figs. 14 and 15). The water level in calandria vessel continues to decrease gradually with the continuous boil-off of moderator to uncover more channels (Fig. 11). When the supporting channel is uncovered it will also heat up, and sag under its own weight and the weight of the above channels, and contact a lower elevation channel.

Progressively, the number of sagged channels increases as the moderator level drops. As the degree of sagging increases the channels at higher elevation will start to separate at their bundle junctions i.e. channel disassembly. The disassembled channels then lay completely on the lower ones to form a suspended debris bed which is supported by the highest channel that is still submerged in water. Some debris may fall through the space available between adjacent cooled fuel assemblies. Such behavior is currently not modeled in this study, i.e. all mass of fractured fuel assemblies is temporarily held in the suspended debris bed. Allowing partial relocation of debris through the gaps between fuel channels would change the load on the supporting channels and possibly delay core collapse. Quenching of this debris may alter the moderator level transient. However, the presence of a large number of reactivity mechanism support structures and instrumentation structures would limit the amount of lateral movement of the debris. Thus the most probable scenario involves the formation of a large suspended debris bed involving most of the failed assemblies. It is also notable that partial relocation may become more important for scenarios involving higher suspended debris temperatures thus greater amount of metallic melt since molten material formed in the suspended debris bed may drip down to the bottom of the calandria vessel prior to core collapse.

Initially, the suspended debris bed mainly consists of coarse solid debris including the intact or slumped fuel bundles and the PT-CT segments. Heat is conducted downward through channel-to-channel contact resulting in a vertical temperature gradient that is largely dictated by the channel powers prior to collapse and the contact conductance/area models used to describe suspended debris bed behavior. The sensitivities to these model parameters are discussed in Section 4. The lowest channel that is in contact with the submerged channel is at relatively low temperature, while the upper channels/debris may experience continuous heat-up and exothermic Zr-steam reaction on surfaces of the CT, PT and fuel cladding (Fig. 14). The model assumes that there is no lateral movement of the suspended debris bed and no interactions between the neighboring columns.

With the continuous build-up of suspended debris bed the load on the supporting channels increases and the maximum core temperature also increases with time (Fig. 16). When the mass of the suspended debris bed exceeds the strength of a supporting channel, this channel together with the debris bed falls and impacts lower elevation channels. Since the combined mass exceeds the rolled joint capacity all remaining channels in that column relocate to the bottom of the core (i.e., the so-called core collapse phase). The end stubs of the channels above the supporting channel (typically 2–4 fuel bundles per channel) are left on the tube sheets while those below (and including) the supporting channel have no stubs. Core collapse is assessed for each column separately and the collapse of a column will not affect that the others, i.e. a columnar collapse model. In the four base cases (i.e. CD1-CD4), bundles in the stubs are assumed to remain suspended until the supporting CTs melt. Such assumptions give rise to the larger hydrogen production and hence more conservative estimates although the sensitivities are assessed in Section 4.4.

The elapsed time from first channel failure to the start of core collapse is relatively short in the three crash-cool cases, i.e. 0.94 h in case CD1, 0.86–0.88 h in case CD2 and CD3, as opposed to 1.35 h in the non-crash-cool case CD4 (Table 4). The difference in the elapsed time results from the different initial moderator levels at the start of the core disassembly phase. Fig. 11 shows the two-phase moderator level in case CD1 and CD4 (case CD2 and CD3 are similar to CD1). The number of rows that are initially uncovered in CD4 is 4–5 as opposed to 6 in the other cases. This leads to slightly different core disassembly pathways.

The calandria vessel is about half voided (see Fig. 10 for the collapsed water level) and about 8 rows of channels are stacked upon each other at the time of core collapse (Fig. 15). In case CD1 the peak core temperature, i.e. 2677 °C, is reached prior to the collapse of column 1 (Fig. 16). However, high temperatures are limited to a small number of channels, and the majority of suspended debris bed is well below 2600 °C the temperature above which significant UO_2 dissolution and the formation of metallic (U, Zr, O) melt are expected. Similar observations are also found in the other three cases with slightly different peak temperatures (2774 °C in CD2, 2839 °C in CD3, and 2751 °C in CD4). In all the cases a significant portion of the debris has exceeded

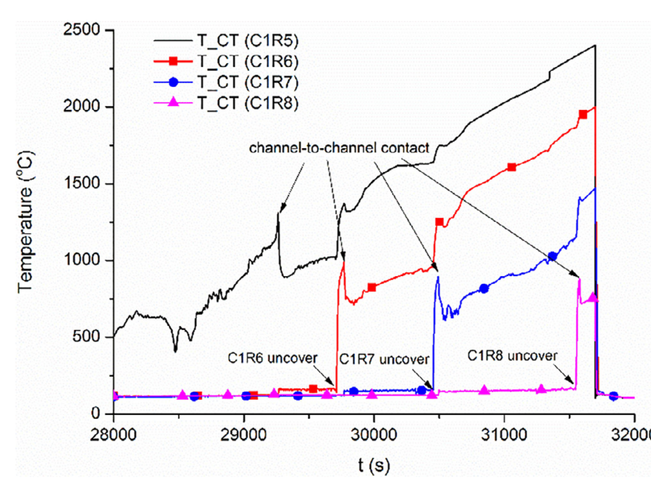

Fig. 14. Calandria Tube Temperatures at 7th Bundle in Column 1 Row 5–8 (Case CD4).

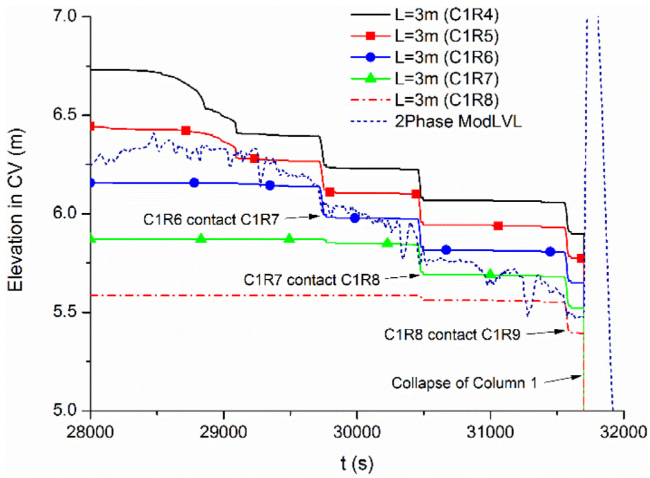

Fig. 15. Deflections at Channel Centre in Column 1 Row 4–8 and Two-Phase Water Level in Calandria Vessel (Case CD4).

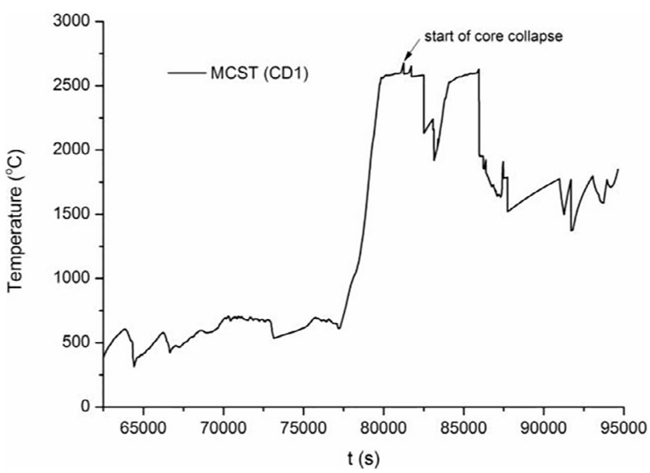

Fig. 16. Maximum Cladding Surface Temperature in Case CD1.

the Zircaloy melting point 1760 °C, implying that molten material relocation may occur. Lacking the evidence from integral severe accident experiments for CANDU reactors, the "inter-channel melt relocation" phenomena are currently not modeled. However melt location in this phase would have the effect of initiating core collapse earlier and terminating hydrogen production.

3.2.4. Hydrogen and fission product releases

During the core disassembly phase, if the fuel cladding has ruptured and/or the fuel channel (either the PT or CT) has been breached, oxidation occurs on both inside and outside surface of the fuel cladding and/or the PT and CT. After the fuel cladding failure, fission products in the gap are instantaneously released.

Table 5 shows the cumulative hydrogen and fission products release at the end of three accident stages. Most of the hydrogen is generated in the suspended debris bed (Fig. 17). The hot debris when suspended is in a steam rich environment due to the continuous boil-off of moderator, and such condition is favorable to Zr-steam reactions. The SCDAP model does not currently include restrictions on steam access to the interior portions of the debris bed, thus hydrogen formation and heat loads are over-predicted. Once the suspended debris is relocated to the calandria vessel bottom, it is quenched by the moderator thus no longer contributes to the hydrogen production. The end stubs left after core collapse and the peripheral channels (i.e. column 8 which will remain suspended for a long time) contribute a small fraction to the hydrogen loading. The total hydrogen release until calandria vessel dryout is 165.3 kg in case CD1, 175.2 kg in CD2, 173.2 kg in CD3, and 202.5 kg in CD4 (Table 5).

Fission products release starts to increase rapidly when the maximum cladding surface temperature (MCST) reaches approximately 2000 °C. The current model predicts that the majority of the released fission products (until calandria vessel dryout) are from the suspended debris bed. Once all the channels have been relocated to the calandria vessel bottom, the code predicts nearly zero release after this point (Fig. 18). Until calandria vessel dryout the total mass of fission products released are closely predicted in the three crash-cool cases (Xe and Kr: 0.922–0.937 kg, Cs and I: 0.513–0.522 kg), while the amount released in CD4 is much higher (Table 5). The higher hydrogen and fission products release in case CD4 is attributed to the longer duration of debris bed being suspended.

3.2.5. Moderator and shield water responses

After core collapse the corresponding fuel channels and debris are relocated to the calandria vessel bottom and all heat structure surfaces are exposed to the moderator fluid at the same instant. This leads to the rapid increase in the heat deposited into the moderator (Fig. 9 for CD1), which results in rigorous steaming of moderator causing the calandria vessel to temporarily pressurize (Fig. 10). Some moderator is expelled out of the calandria vessel through the discharge ducts following core collapse. The first few core collapses cause the small step changes in the moderator level as seen in Fig. 10. The level decreases quite smoothly thereafter. Eventually the debris is cooled by the moderator to a temperature close to moderator saturation temperature. Calandria vessel dryout occurred 4.82 h after the first channel failure in CD1, 4.47 h in CD2, 3.97 h in CD3 and 4.36 h in CD4 (Table 4). This elapsed time from channel failure to calandria vessel dryout is largely dictated by the decay heat level at the time of fuel channel heat-up as well as by the remaining calandria vessel inventory after the initial moderator expulsion when the rupture disks burst.

The end states of the core disassembly phase are the same in the four cases, i.e. a solid terminal debris bed sitting at the bottom of the calandria vessel externally cooled by the shield tank water and the end shield water with some end stubs left on the tube sheets. The simulations are all terminated as soon as the remaining moderator in the calandria vessel is completely boiled off. The shield tank is full of water which is still subcooled at the time of calandria vessel dryout (97.4 °C in CD1, 93.8 °C in CD2, 90.3 °C in CD3, and 89.0 °C in CD4). The end shield water start boiling quite early due to its relatively small volume and the considerable heat loss from the end fittings. Since the end shield and shield tank are connected, the end shield water level will not change until the shield tank water level is boiled down to uncover the end-shield-to-shield-tank connection which is beyond the scope of this study.

Table 5
Cumulative Hydrogen/Fission Product Release at the End of Three Accident Stages (kg).

		H_2	Xe + Kr	Cs + I
Phase 1[a]	CD1/CD2 /CD3/CD4	0.0	0.0	0.0
Phase 2[b]	CD1	158.2	0.932	0.519
	CD2	167.3	0.905	0.504
	CD3	152.6	0.893	0.497
	CD4	193.2	1.281	0.713
Phase 3[c]	CD1	165.3	0.937	0.522
	CD1F	158.6	0.671	0.374
	CD2	175.2	0.923	0.514
	CD3	173.2	0.922	0.513
	CD4	202.5	1.321	0.735

[a] from initiating event until first channel failure.
[b] from first channel failure until 1–7 columns collapse.
[c] from the collapse of 7th column until calandria vessel dryout.

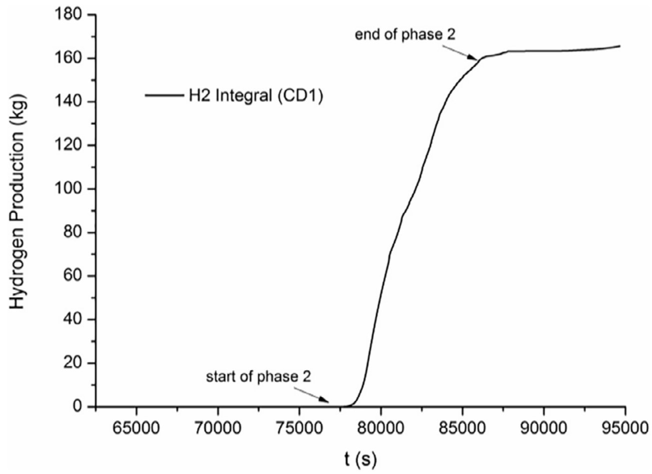

Fig. 17. Integral of Hydrogen Release in Case CD1.

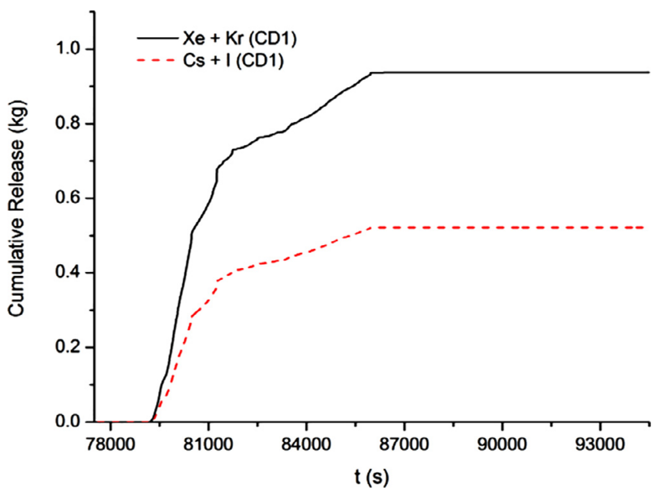

Fig. 18. Cumulative Fission Products Release in Case CD1.

3.2.6. Impact of early channel failure

There exist several hypothetical mechanisms wherein fuel channel integrity may be lost prior to the failure criteria expected during normal accident progression. These may occur from large circumferential temperature gradient on the PT during ballooning, asymmetric heat loads on the channel post contact, failure at a pre-existing flaw site or PT embrittlement, failure due to CT dryout on its outer surface, or local overheating driven by fuel bundle slumping. To examine the impact of premature channel failure case CD1F is simulated.

Case CD1F assumes that a channel will fail early due to potential PT non-uniform temperatures before the PT balloons into contact with its CT. The PT failure strain is set to 0.06 which is the lower-bound PT failure strain in PT deformation tests with relatively large circumferential temperature gradient (Shewfelt and Godin, 1985). First failure thus will occur before channel uncovery. All other models and assumptions are kept the same as CD1.

In case CD1F the first channel failure occurs in one of the highest power channels at 19.44 h shortly after the RIH/ROH becomes voided (Table 4). The calandria vessel pressure spikes up to 563.6 kPa which is still well below the calandria vessel failure pressure (Fig. 19). Calandria vessel rupture disks open for overpressure protection (only one of the four rupture disks is credited which is considered conservative as it results in greater peak load on the calandria vessel walls). Some moderator is expelled out of the calandria vessel. Meanwhile, the remaining PHTS coolant is discharged through the ruptured channel into the calandria vessel. Fig. 20 shows transient of the two-phase moderator level compared to the reference case. The number of channel rows that are initially uncovered is about four in CD1F as opposed to six in CD1. This leads to slightly different core disassembly pathways.

Since the PTs have not significantly deformed and the heat resistance of the annulus gap is still high, the PT temperatures increase leading to the increase in radiation heat transfer across the annulus gap. For some fuel channels, the PTs sag into contact with the CTs which establishes the moderator as heat sink provided that the CTs are still submerged in moderator. The heat deposited into the moderator increases considerably during this phase.

The subsequent accident progressions are similar. The core disassembly starts at 21.26 h (Table 4), about 1.09 h earlier than in the reference case (CD1). The calandria vessel dryout occurs at 25.1 h in CD1F, i.e. about an hour earlier than in CD1. The premature fuel channel failure thus acts to move up all the subsequent events. Less fission products releases are predicted in case CD1F as compared to case CD1 (Table 5) during this phase of the event. The total hydrogen productions until calandria vessel dryout in case CD1 and CD1F, however, are closely predicted (Table 5).

3.2.7. Comparison of modified MOD3.6 and MAAP-CANDU results

Blahnik and Luxat (1993) carried out a similar study in which they simulated a SBO accident with the loss of all electrical power for a unit of Darlington NGS using the MAAP-CANDU code. The SBO scenario in their analysis did not involve crash-cooldown, thus the PHTS pressure remained high until fuel channel failure.

Canadian Nuclear Safety Commission (CNSC) recently released the results of a similar study where a prolonged SBO scenario without operator intervention was simulated using the MAAP4-CANDU code for Darlington NGS (Canadian Nuclear Safety Commission, 2015). The analysis was performed by Ontario Power Generation (OPG) as part of their Level 2 Probabilistic Safety Assessment (PSA).

The input geometries/parameters and the modeling assumptions in the above two studies are similar to those used in case CD4 of this paper. A comparison is thus made among the results predicted by MAAP-CANDU, MAAP4-CANDU and the modified MOD3.6 code. The key event timings predicted by the three codes are shown in Table 6.

The timings of events during the early stage of accident, e.g. the SG dryout time, and the start of coolant relief, predicted by the MOD3.6 are close to those predicted by the two MAAP-CANDU codes. The Darlington Level 2 PSA also showed that a simple operator action would provide approximately 8–10 h of additional passive core cooling by supplying readily available water to the secondary-side SGs (Canadian Nuclear Safety Commission, 2015). This is consistent with the conclusion of this study that the combined water make-up from SGECS and the deaerator tank is able to extend the natural-circulation

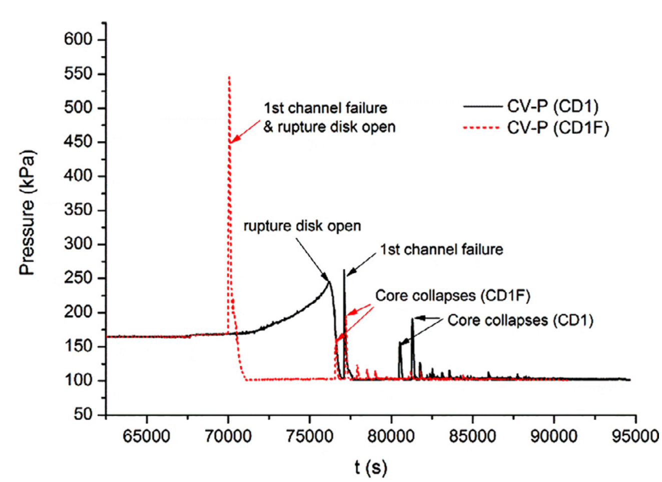

Fig. 19. Calandria Vessel Pressure in Case CD1 and CD1F.

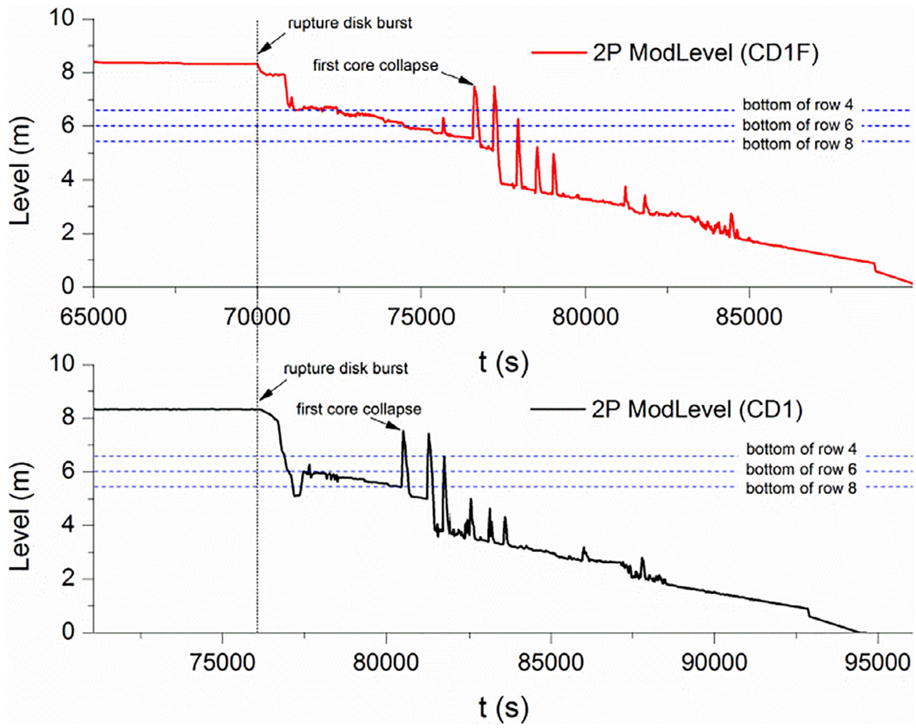

Fig. 20. Two-Phase Moderator Level in Case CD1 and CD1F.

mode of heat removal by up to 11 h.

The timings of header dryout and fuel-channel dryout predicted by these codes are also reasonably close. However, in Blahnik's work (Blahnik and Luxat, 1993) the moderator became saturated at about 7.5 h, while in case CD4 of this study the moderator starts boiling much earlier (i.e. 5.48 h). This difference is partially attributed to the improved decay heat partitioning used in this study as well as the more robust treatments of the radiation heat transfer and PT deformation phenomena.

Another important difference is in the timing of first channel failure. MAAP4-CANDU predicted fuel channel failure almost as soon as the fuel channel dryout began, i.e. at 6.4 h, due to non-uniform straining of the PT. MAAP-CANDU made the similar assumption that channel failure would occur after the remaining liquid in the feeders/channels was boiled off. The first fuel channel failure was predicted to be at 8.4 ± 1 h (the uncertainty stemmed from the timing of phase separation at the headers and the duration of channel boil-off). In MOD3.6 (case CD4), however, the PTs after dryout are allowed to balloon into contact with the CTs establishing the moderator as a heat sink. This delays the first channel failure to 7.46 h (i.e. after the initial moderator expulsion following the burst of calandria vessel rupture disks).

MAAP4-CANDU and its predecessors considers the core collapse on a per loop basis and typically models 18 characteristic channels per loop. When the suspended debris load in a given loop exceeds the user defined value (i.e. MLOAD) core collapse is triggered. Core collapse was predicted by MAAP-CANDU to occur at about 11 h in these two studies. The MLOAD value for most two-loop CANDU plants is typically 25,000 kg per PHTS loop, which is now considered very high and likely resulted in the delay in core collapse. Mod3.6 assumes that the channels collapse column by column independently. Core collapses thus occur within a time range between 8.81 and 9.98 h in case CD4. The load to trigger core collapse is estimated using Eq. (1) in this study and is thus considered more reasonable (more discussion can be found in the following Section 4.1).

The calandria vessel dryout in MOD3.6 is more than two hours earlier than the MAAP-CANDU code and four hours earlier than MAAP4-CANDU. The early calandria vessel dryout predicted by MOD3.6 might have resulted from the moderator expelled out of the calandria vessel during the earlier core collapses.

A sensitivity study is performed (i.e. Case CU1) by replacing the

Table 6
Comparison of Predicted Event Timings between Modified MOD3.6 and MAAP-CANDU (hours).

	MOD3.6 (CD4)	MAAP4-CANDU (Canadian Nuclear Safety Commission, 2015)	MAAP-CANDU (Blahnik and Luxat, 1993)
SG Dryout	5.10	5.0	5–6
Coolant Relief Starts	5.51[a]	–[d]	~6
RIH/ROH Voided	5.84	–[d]	6.5
First Channel Dryout	6.33[b]	6.4	–[d]
Moderator Start Boil	5.48[c]	–[d]	7.5
Calandria Vessel Rupture Disk Open	7.14	6.4	8.4 ± 1
First Channel Failure	7.46	6.4	8.4 ± 1
Core Collapse	8.81–9.98	10.7	~11
Calandria Vessel Dryout	11.82	16.0	~14

[a] The first opening of bleed condenser relief valve in MOD3.6.
[b] The first PT-to-CT ballooning contact in MOD3.6.
[c] When the average moderator temperature exceeds 110 °C in MOD3.6.
[d] Timings not reported.

current decay heat partitioning (based on Aydogdu (2004) with a constant heat load distribution (i.e. fuel channel 95.48%, moderator 4.34%, and shield water 0.18% of total power). All the other modeling assumptions are kept the same as case CD4. This leads to a decrease in relative heat load to the moderator by direct deposition and an increase in relative heat load to the fuel channels after reactor shutdown. The heat loss from the fuel channel to the moderator is calculated separately in both CD4 and CU1 by SCDAP heat structures taking into account both the radiation heat transfer across the annulus gap and the deformation of the pressure tubes. Such heat losses agree well with those observed under normal operating conditions. The results (see Table 7) show that in case CU1 the SG dryout occurred at 4.82 h slightly earlier than that in case CD4. The timings of the subsequent events such as the first bleed condenser relief action, reactor header void and the first PT-to-CT contact are advanced by approximately the same amount.

The timing of moderator saturation is delayed to 6.38 h as a direct result of the lower moderator deposition fraction. Thus the major contributor to differences in moderator heat-up rate between MAAP and RELAP stems from these assumptions. The calculated average moderator temperatures are plotted in Fig. 21. The gap between the two temperature curves initially increases with time until the fuel channels start to heat up. Although the moderator heat-up rate in case CU1 is lower prior to fuel channel heat-up, the heat-up (thus the deformation of PTs) starts earlier than in case CD4. When the PT deformation is initiated in case CU1, the moderator heat-up rate increases substantially bridging the gap between two cases. The differences in rupture disk burst timing and channel failure timing between case CD4 and CU1 are therefore small.

4. Additional sensitivity studies

There are large uncertainties in the modeling of CANDU severe accidents especially during the core disassembly phase. A number of sensitivity cases are thus performed to assess the sensitivities to various input parameters and modeling assumptions.

4.1. Sensitivity to core collapse criterion

A constant threshold load (estimated using Eq. (1)) is used in this study to determine core collapsing. The main input parameters to the equation such as the CT ultimate tensile stress and the unloaded length are subject to some uncertainties. Recently, the mechanistic core collapse model (i.e. Eq. (1)) became available in MOD3.6 (Zhou et al., 2018). To study the impact of this model and to quantify the sensitivity to the core collapse criterion, the following three cases are designed (Table 8):

- CS1: the threshold load is set to 3000 N/m or 1836 kg (reference case CD1: 3500 N/m or 2143 kg). All the other modeling assumptions are kept the same as CD1.
- CS2: same as CS1, but the threshold load is set to 4000 N/m or 2449 kg.
- CS3: instead of a constant threshold load, Eq. (1) is used directly to calculate the maximum supportable load. The unloaded length in the equation is dynamically updated by the channel sagging model.

The maximum load a single channel can support including its own weight as given by Eq. (1) is plotted against the unloaded length (solid line in Fig. 22). The maximum supportable load increases with the decrease in unloaded length, and reaches maximum of about 2500 kg when the unloaded length is zero (or the load is uniformly distributed along the entire fuel channel). On the other hand, shorter unloaded length (or greater contact length) means more weights from the above sagged/disassembled channels. The relation between the maximum number of supportable rows (excluding itself) and the unloaded length is shown in Fig. 22 (dash line) assuming that the load of any axial node (or channel segment) is all transferred to the lower node once contact is made.

The different threshold loads used in CS1 and CS2 result in different timing of core collapse. The maximum number of channels stacked on top of each other prior to core collapse also increases with the increase in threshold load. The peak temperature generally increases with increasing threshold load, and exceeds the melting temperature of UO_2 (2850 °C) in case CS2 with an unrealistically-large threshold load.

Case CS3 with the mechanistic core collapse criterion predicts results very similar to case CS1 in which a constant threshold load of 1836 kg is used. The careful examination of the core degradation map shows that the most likely unloaded length prior to core collapse predicted by the current model is between 1.25 m and 1.5 m. This corresponds to a loaded length of 6–7 bundle lengths and a calculated threshold load of 1795–1856 kg which is close to the number used in case CS1.

The results also show strong positive correlation between hydrogen release and the threshold load to trigger core collapse, i.e. the higher the threshold load the larger the hydrogen release (Fig. 23). The total hydrogen release until calandria vessel dryout is 143.3 kg in case CS1, and 204.3 kg in case CS2 (as opposed to 165.3 kg in case CD1). The fission products releases show similar behavior (Table 8). Less fission product releases are predicted in CS1 and CS3 implying that more fission products thus a greater heat load will be present in the terminal debris bed which will impose a higher risk of calandria vessel failure for the subsequent in-vessel retention phase. The hydrogen and fission production releases in case CS3 are again very close to that in case CS1 for the same reason.

Generally, the longer the debris is supported, the higher the suspended core temperature. The degree of cladding failure and fuel liquefaction also becomes more severe leading to greater fission products releases during this stage. This longer hold-up of suspended debris thus increases the uncertainties in the modeling as the partial relocation of debris (metallic melt) to the terminal debris bed is currently not modeled in MOD3.6. The calandria vessel dryout time, however, is not sensitive to the core collapse criterion (Table 8). The remaining moderator in the calandria vessel is depleted at almost the same time, i.e. at about 26.2–26.3 h, in the four cases (i.e. CD1 and CS1-3).

4.2. Sensitivity to contact angles

The contact conductance between PT and CT due to PT sagging contact and that between two CTs due to channel-to-channel contact are currently not mechanistically calculated. Instead, user-input constant contact angle and contact conductance are used. To examine the sensitivity to these parameters the following cases are simulated:

- CA1: The CT-to-CT contact angle is set to 25° (15° in the reference case CD1), while all other models and assumptions are kept the same as CD1.
- CA2: same as CA1, but the CT-to-CT contact angle is set to 5°.

Table 7
Sensitivity to Heat Load Partition.

		CD4 (Ref.)	CU1
Heat Load	Fuel Channel	Table 1	95.48%
	Moderator		4.34%
	Shield Water		0.18%
Steam Generator Dry		5.10 h	4.82 h
Moderator Saturated		5.48 h	6.38 h
Bleed Condenser Relief Valve First Open		5.51 h	5.19 h
Channel Stagnant		5.73 h	5.54 h
RIH/ROH Void		5.84 h	5.55 h
1st PT-to-CT Contact		6.33 h	6.00 h
Calandria Vessel Rupture Disk Open		7.14 h	7.35 h
First Channel Failure		7.46 h	7.61 h

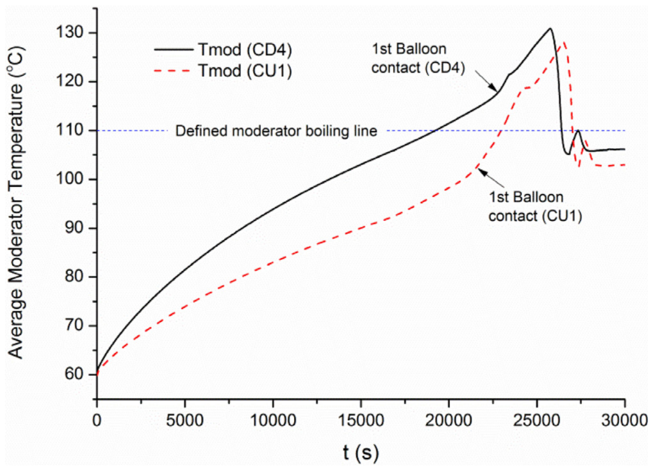

Fig. 21. Average Moderator Temperatures in Case CD4 and CU1.

Table 8
Sensitivity to Core Collapse Criteria.

	CD1 (Ref.)	CS1	CS2	CS3
Max Load (kg)	2143	1836	2449	Eq. (1)
Results				
Max Historical Core Temp. (°C)	2677.3	2605.2	3111.0	2603.4
Start of Core Collapse (s)	80,475	80,035	81,648	80,041
Calandria Vessel Dryout (s)	94,436	94,513	94,385	94,409
H_2 Release* (kg)	165.3	143.3	204.3	137.4
Xe + Kr* (kg)	0.937	0.566	1.756	0.520
Cs + I* (kg)	0.522	0.315	0.978	0.289

* Total release until calandria vessel dryout (same in the tables below).

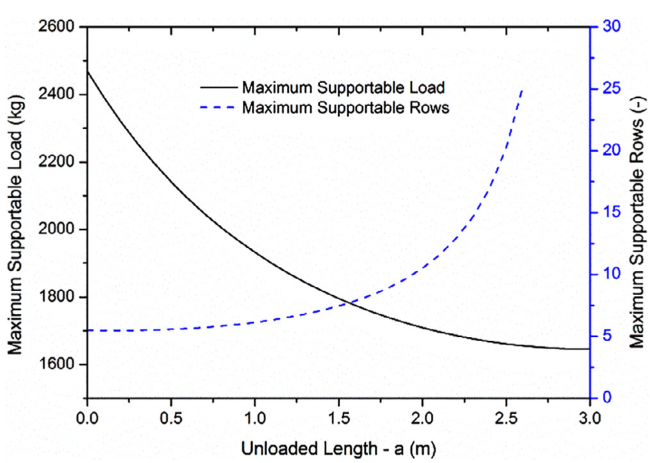

Fig. 22. Maximum Supportable Loads and Rows as a Function of the Unloaded Length (assuming constant σ_{UTS} of 661 MPa).

- CA3: The PT-to-CT contact angle is set to 20° (10° in CD1), while all other assumptions are kept the same as CD1.
- CA4: same as CA3, but the PT-to-CT contact angle is set to 5°.

Case CA1 and CA2 examine the sensitivity to the effectiveness of channel-to-channel contact heat transfer. In case CA1, the increase in contact angle by 10° does not lead to a significant change in the predicted core collapse starting time, calandria vessel dryout time, or hydrogen production (Table 9). The cumulative fission products releases, however, are much less than those in the reference case. On the other hand, the decrease in contact angle in case CA2 results in an appreciable increase in fission product release. This influence is mainly through its effect on the temperature distribution of the suspended

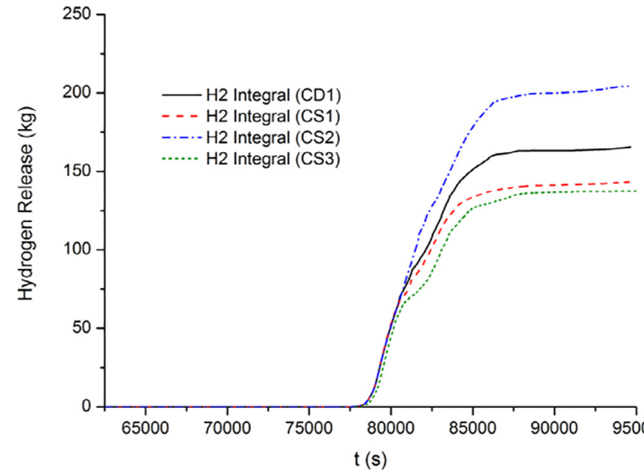

Fig. 23. Integral Hydrogen Releases in Case CD1 and CS1-3.

debris bed.

Case CA3 and CA4 study the sensitivity to the PT-to-CT contact angle following PT sagging contact. The input contact angle in case CA3 is twice of that in the reference case and in case CA4 the angle is 50% of that in the reference case. However, no appreciable differences are observed among the reference case and the two sensitivity cases. This is mainly because in the cases examined ballooning is the dominant PT deformation mechanism rather than sagging, and most of the PTs have already significantly ballooned prior to core disassembly before PT sagging contact can play a role in altering the conductivity of the annulus gap.

In reality the effectiveness of heat conduction in the suspended debris bed is subject to high level of uncertainties and can be affected by the weight, the deformation/compaction, and the liquefaction/solidification of the debris. The currently used contact conductance and angle are conservative and do not take into account the feedbacks from these phenomena. A more mechanistic model may be considered for future works.

4.3. Sensitivity to cladding oxidation multiplier

Bundle slumping may occur as the fuel channels heat up to form a close-packed geometry which limits steam access to the interior cladding surface of the subchannels. This phenomenon is currently not taken into account in the analysis. To investigate the effect of potential bundle slumping case CO1 is simulated (Table 10). In CO1 the oxidation rate on the fuel cladding surfaces is artificially reduced by multiplying a factor of 0.3 in order to mimic the case where steam flow to a portion of the bundle interior is limited due to bundle slumping. The value 0.3 is selected based on the study carried out by Dupleac and Mladin (2009) as discussed earlier. Oxidation on the PT inner or CT outer surfaces are not affected. All the other modeling assumptions are kept the same as

Table 9
Sensitivity to Debris Contact Angle.

	CD1 (Ref.)	CA1	CA2	CA3	CA4
CT-CT Contact Angle (°)	15	25	5	–	–
PT-CT Contact Angle (°)	10	–	–	20	5
Max. Historical Core Temp. (°C)	2677.3	2651.3	2900.8	2677.2	2678.6
Start of Core Collapse (s)	80,475	80,446	80,542	80,474	80,468
Calandria Vessel Dryout (s)	94,436	94,337	94,426	94,436	94,470
H_2 Release * (kg)	165.3	143.2	173.1	165.3	161.8
Xe + Kr * (kg)	0.937	0.481	1.647	0.937	0.900
Cs + I * (kg)	0.522	0.268	0.917	0.522	0.501

"–": same as the reference case (same in the tables below).

Table 10
Sensitivities to Oxidation and End Stub Bundle Behavior.

	CD1 (Ref.)	CO1	CE1	CE2
Cladding Oxidation Factor	1.0	0.3	–	–
End Stub Bundle Behavior	Option 1	–	Option 2	Option 3
Max. Historical Core Temp. (°C)	2677.3	2664.2	2676.6	2590.0
Start of Core Collapse (s)	80,475	80,897	80,476	80,445
End of Core Collapse[1] (s)	85,953	86,208	85,793	83,278
Calandria Vessel Dryout Time (s)	94,436	94,762	93,422	91,340
H_2 Release * (kg)	165.3	140.6	139.8	113.2
Xe + Kr * (kg)	0.937	0.955	0.877	0.628
Cs + I * (kg)	0.522	0.532	0.488	0.350

[1] "End of core collapse" is defined as the collapse of all columns except the outermost one.

CD1.

The results showed that the overall event timings are not significantly altered when compared to the reference case. Similar fission products releases and slightly less hydrogen productions are predicted in case CO1 (Table 10). This implies that the current modeling assumptions (i.e. neglecting the bundle slumping effects) does not to appreciably affect accident progression in the core disassembly phase. However, it should be noted that this sensitivity case does not take into account the increase in contact area between fuel elements and the PT inside bottom surface resulting from bundle slumping. Future work will incorporate the modification made by Mladin et al. (2008) to further investigate the effects of bundle slumping and metallic melt relocation inside the fuel channel (possibly for one of the fuel channels).

4.4. Sensitivity to end stub bundle behaviours

The fuel channels fracture at their bundle junctions as the degree of sagging increases. The fuel channel segments between the two junctions where the tears occurred (most likely between third and tenth bundles (Mathew, 2004) will relocate to the suspended debris bed or the calandria vessel bottom depending on whether the lower channel has collapsed. The end stubs remain attached to the calandria vessel tube sheet. The fuel bundles in these end stubs may or may not slide out depending on the degree of sagging and the friction between the fuel bundles and the stubs. While the behaviours of these fuel bundles are somewhat random and difficult to predict, there are three options available in the modified MOD3.6 with option 1 as the default:

- Option 1 (reference case): the bundles in end stubs (i.e. bundle 1, 2, 11, and 12) will not fall out after the fuel channels are torn apart, and will not be relocated to calandria vessel bottom due to core collapse;
- Option 2: same as option 1, but the bundles (i.e. bundle 1, 2, 11, and 12) will be relocated to calandria vessel bottom together with the suspended debris immediately after core collapse.
- Option 3: some bundles in end stubs (i.e. bundle 2 and 11) will fall out and be relocated to the suspended debris after the fuel channels are torn apart. After core collapse, the rest of the end stub bundles (i.e. bundle 1 and 12) if still suspended will be relocated to calandria vessel bottom immediately.

Option 1 is considered the most conservative in term of hydrogen or fission product releases. The fuel bundles in the end stubs will continuously heat up until the supporting PT/CT structures fail (either due to high temperature or due to excessive weight from the above disassembled segments). In reality, the fuel bundles in the end stubs may be relocated much earlier. To investigate the sensitivity to end stub bundle behavior case CE1 and CE2 are simulated with option 2 and 3 respectively (Table 10).

Case CE1 with option 2 differs from the reference case CD1 in that CE1 allows the fuel bundles in the end stubs to fall out immediately after core collapse and be quenched by the remaining moderator. In case CE1 less hydrogen and fission products are released until calandria vessel dryout (Table 10). This is because the relocation of end stub fuel bundles to the calandria vessel bottom terminates the hydrogen generation and arrests fission product releases. Meanwhile, it also causes more water to be expelled out after core collapses and more heat to be deposited into the remaining moderator during the subsequent calandria vessel boil-off phase (Fig. 24). Thus the calandria vessel dryout time is advanced by about 1000 s in case CE1.

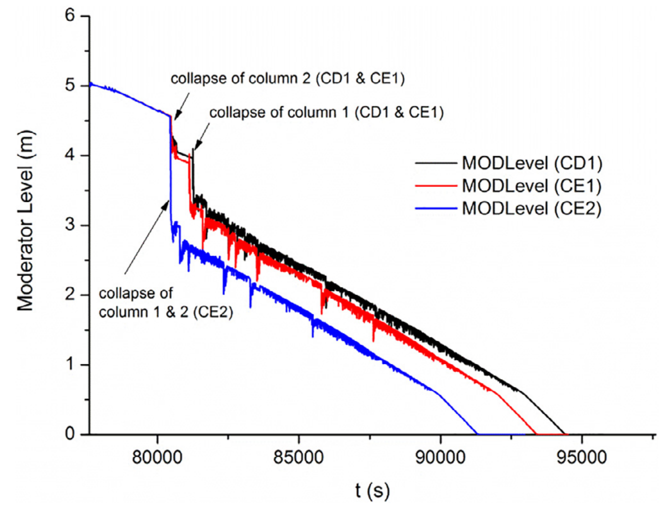

Fig. 24. Collapsed Moderator Level in Case CE1, CE2 and CD1.

Case CE2 with option 3 differs from case CE1 in that CE2 allows end stub fuel bundles to be relocated earlier to the suspended debris bed. It is assumed that the weights of bundle 2 and 11 after sliding out are all transferred to the lower channel at axial nodes corresponding to bundle 3 and 10 respectively. In case CE2, collapsing of the channel columns occurs more rapidly. The elapsed time from the start to the end of core collapsing is significantly reduced (0.8 h in CE2 as opposed to 1.5 h in CE1 and CD1), which again leads to the reduction in hydrogen and fission product releases (Table 10). In case CE2, column 1 and 2 collapse at almost the same time resulting in a more severe moderator expulsion surge than the combined moderator loss due to the collapsing of column 1 and 2 in case CE1 (Fig. 24). The calandria vessel dryout thus occurs even earlier in CE2.

4.5. Sensitivity to severity of moderator expulsion

Following the burst of calandria vessel rupture disks, a significant amount of moderator will be expelled out through the discharge ducts. Different severities of the moderator expulsion surges lead to different numbers of fuel channel rows being uncovered initially prior to core disassembly, which may result in different core disassembly pathway thus different hydrogen and fission product releases. It has been recognized that there are large uncertainties in predicting this moderator expulsion phenomena. Rogers (1989) examined the sensitivity of the transient boiling behavior of the moderator predicted by MODBOIL to its drift-flux parameters. The model was found to be very sensitive to the velocity-void distribution parameter (C_0) and the weighted-mean vapor drift velocity, both of which depend on the geometry of the system and the two phase flow pattern (Rogers, 1989). The appropriate values of these parameters are not yet established due to the lack of relevant experiments on the CANDU calandria vessel geometry (Rogers, 1989).

A sensitivity study is thus carried to investigate the sensitivity to initial moderator level prior to core disassembly (Table 11). Case CM1 and CM2 are both identical to the reference case CD1, but the two-

Table 11
Sensitivity to Number of Initial Uncovered Fuel Channel Rows and Channel Grouping Scheme.

	CD1 (Ref.)	CM1	CM2	CG1
Moderator Level After Rupture Disk Burst	norm.[1]	norm. + 2rows	norm. – 2rows	–
Channel Group	88	–	–	96
Max Historical Core Temp. (°C)	2677.3	2686.5	2588.3	2954.2
Start of Core Collapse (s)	80,475	81,736	79,811	80,476
Calandria Vessel Dryout (s)	94,436	95,193	93,413	96,138
H_2 Release * (kg)	165.3	175.3	164.4	173.3
Xe + Kr * (kg)	0.937	1.029	0.759	1.094
Cs + I * (kg)	0.522	0.573	0.423	0.609

[1] RELAP5 predicted moderator level.

phase moderator level at the beginning of the core disassembly phase is artificially raised by two rows in CM1 or lowered by two rows in CM2 by the addition or reduction of water from the calandria vessel.

With higher initial moderator level, the start of core collapse in case CM1 is delayed by approximately 20 min (Table 11), and the calandria vessel dryout time is also delayed. The decrease in initial water inventory in CM2 has the opposite effects: the first collapse occurs about 10 min earlier. The difference in the moderator inventory at the beginning of core disassembly phase also leads to different core disassembly pathways. In both CM1 and CM2, the first collapse happens in column 1 (i.e. centermost) as opposed to column 2 in the CD1. However, the predicted integral of hydrogen production until calandria vessel dryout is not significantly altered, with a slight increase in case CM1, and nearly no change in case CM2 (when compared to the reference case). Fission product releases show more sensitivity. Increasing initial moderator level leads to an increase in fission product releases (Table 11). The results also show that fission product release is closely tied to fuel temperature, i.e. the higher fuel temperature the larger fission product release.

4.6. Sensitivity to channel grouping scheme

The current channel grouping for the core disassembly phase adopts the 88-group scheme as shown in Fig. 2. In this 88-group scheme, the central three channel columns of the half-core model are grouped together while the columns in the peripheral region are modeled separately. To investigate the sensitivity to channel grouping especially the combination of 12 columns, a sensitivity case CG1 which uses a 96-group scheme is simulated. In the 96-group scheme the central three columns are modeled separately while for the outer columns every two of them are lumped together such that higher resolution is in the central core region (Fig. 3).

In the reference case (CD1), the first core collapse occurs in column group 2 (i.e. 8 and 9 in Fig. 2) followed by the collapse of column group 1 (i.e. 10, 11, and 12). Both collapses cause some moderator to be expelled out of the calandria vessel (Fig. 25). The transient is identical in case CG1 until after the first core collapse (i.e. the collapse of 8 and 9 in Fig. 3). The collapses of the central three columns in CG1 occur separately. This allows them to be quenched by the remaining moderator at different times causing less severe expulsion surges thus less moderator inventory losses (Fig. 25). As a result, the moderator level decreases more smoothly in case CG1 than in CD1, and calandria vessel dryout in CG1 occurs about 28 min later than in CD1 (Table 11). However, slightly higher hydrogen and fission product releases are predicted in case CG1, which is consistent with the above observation (i.e. the longer the core is suspended the greater the hydrogen and fission products releases).

4.7. Sensitivity to creep sag coefficient

The model for predicting the creep sagging of fuel channel assembly considers the entire fuel channel assembly as a beam with two fixed ends (Zhou et al., 2018). The sagging model does not take into account the difference in material properties between PT and CT, and the creep strain rate equation of PT developed by Shewfelt and Lyall (1985) is used. The model also neglects effects such as the stress concentration at the bundle junction, the oxidation of the zircaloy, etc. A study carried out by Mathew et al. (2003) suggested that neglecting the effect of stress concentration could lead to an underestimation of sag by about 25%. To investigate the sensitivity to the potential acceleration (or deceleration) in creep sagging, three cases (CC1 to CC3 in Table 12) are simulated by using a multiplication factor on the sag coefficient in the creep strain rate equation.

A comparison among the reference case and the three sensitivity cases shows that the impact from the change in creep strain rate on the end results is insignificant. The acceleration in creep sag leads to slightly earlier core collapse timing, however, with negligible differences (Table 12). The calandria vessel dryout time also show little or no sensitivity to this sag coefficient multiplier. The predicted hydrogen and fission product releases are not very different, and no clear trend in the relationship between creep sag rate and H_2/fission product releases is observed.

Therefore, neglecting the phenomena which could potentially accelerate or decelerate creep sag (i.e. stress concentration, oxidation etc.) is expected to have small influence on the core disassembly progression. This is attributed to the short time duration in which the sagging of a fuel channel assembly occurs.

4.8. Sensitivity to decay power level

The current fission product and actinide decay modeling are relatively simple (see Section 2.2.1 for details). A more accurate calculation would require the burnup and power history data on every fuel pin. Such a task is difficult to perform for CANDU reactors due to the on-power refueling and the lack of relevant data. A sensitivity study is thus performed to determine the sensitivity to fission product decay. The fission product yield factor is an RELAP5 input factor to allow easy specification of a conservative calculation. The suggested value is 1.0 for best-estimate problems, and a number greater than 1.0 (typically 1.2) for conservative calculations (SCDAP/RELAP5 Development Team, 1997). Two sensitivity cases (CP1 and CP2) are simulated using a fission product yield factor of 1.2 and 0.8, respectively.

Case CP1 with a fission product yield factor of 1.2 results in an

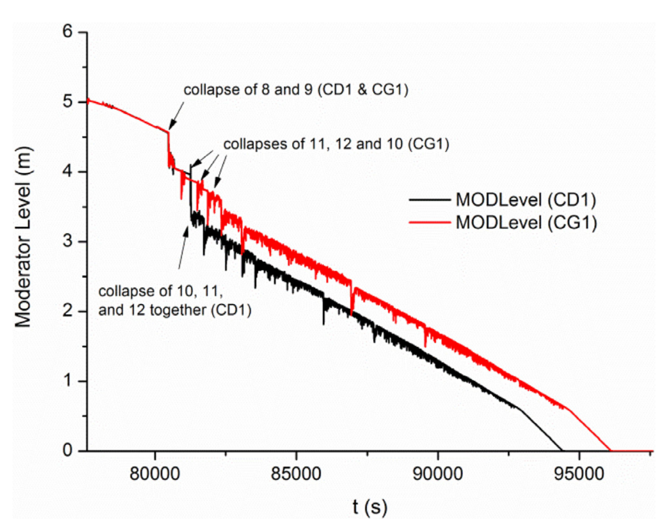

Fig. 25. Collapsed Moderator Level in Case CG1 and CD1.

Table 12
Sensitivity to Creep Sag Coefficient for Channel Sagging Model.

	CD1 (Ref.)	CC1	CC2	CC3
Sag Coefficient Multiplier	1.0	1.5	1.25	0.75
Max Historical Core Temp. (°C)	2677.3	2717.3	2715.9	2765.6
Start of Core Collapse (s)	80,475	80,454	80,477	80,530
Calandria Vessel Dryout (s)	94,436	94,341	94,475	94,599
H_2 Release * (kg)	165.3	158.7	162.4	157.9
Xe + Kr * (kg)	0.937	0.854	0.931	0.838
Cs + I * (kg)	0.522	0.475	0.519	0.467

Table 13
Sensitivity to Fission Product Decay Power Level.

	CD1 (Ref.)	CP1	CP2
Fission Product Yield Factor	1.0	1.2	0.8
SGECS flow begins (s)	1196	1192	1190
Deaerator Flow Begins (s)	1692	1698	1670
IBIF Begins (s)	2020	2088	2046
Steam Generator Dry	16.07 h	13.62 h	20.45 h
Moderator Saturated	11.61 h	8.09 h	17.36 h
Bleed Condenser Relief Valve First Open	18.29 h	14.88 h	23.12 h
Channel Stagnant	18.49 h	15.41 h	23.56 h
RIH/ROH Void	18.65 h	15.58 h	24.07 h
1st PT-to-CT Contact	21.40 h	17.06 h	31.29 h
Calandria Vessel Rupture Disk Open	21.13 h	16.75 h	31.30 h
First Channel Failure	21.41 h	17.07 h	31.30 h
1st CT-to-CT Contact	21.63 h	17.30 h	31.73 h
Start of Core Collapse	22.35 h	17.84 h	32.87 h
End of Core Collapse	23.88 h	18.90 h	34.51 h
Calandria Vessel Dryout Time	26.23 h	21.26 h	38.20 h
Max. Historical Core Temp. (°C)	2677.3	2611.8	2596.7
H_2 Release * (kg)	165.3	169.8	165.1
Xe + Kr Release * (kg)	0.937	0.743	0.745
Cs + I Release * (kg)	0.522	0.414	0.415

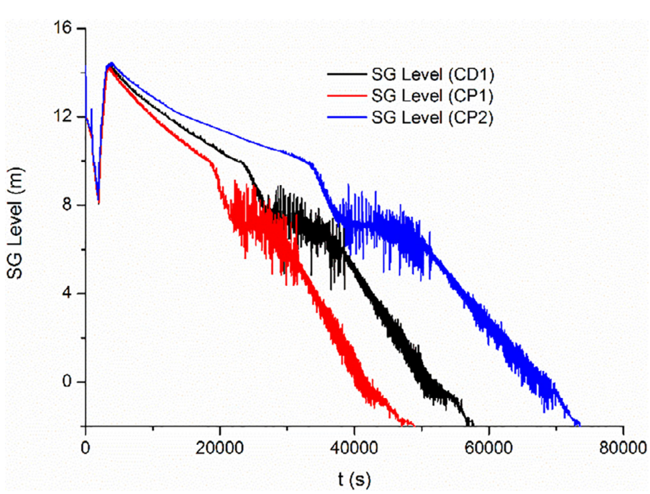

Fig. 26. Steam Generator Water Levels in Case CP1, CP2 and CD1.

increase in fission product decay power by 20% when compared to case CD1. This leads to the increase in heat deposited into all the relevant reactor systems although the timings of events during the first hour such as the beginning of SGECS and deaerator flows are not significantly altered. The subsequent event progression, however, is accelerated (Table 13). The moderator becomes saturated at 8.09 h as opposed to 11.61 h in CD1. The SG dryout occurs 2.45 h earlier than in the reference case (Fig. 26). The start of coolant relief, the first channel failure, and calandria vessel dryout are advanced by 3.41 h, 4.34 h, and 4.97 h, respectively, when compared to case CD1. Other than shifting the events to earlier times, the impacts of higher decay power on the core disassembly phase were considered small with similar peak core

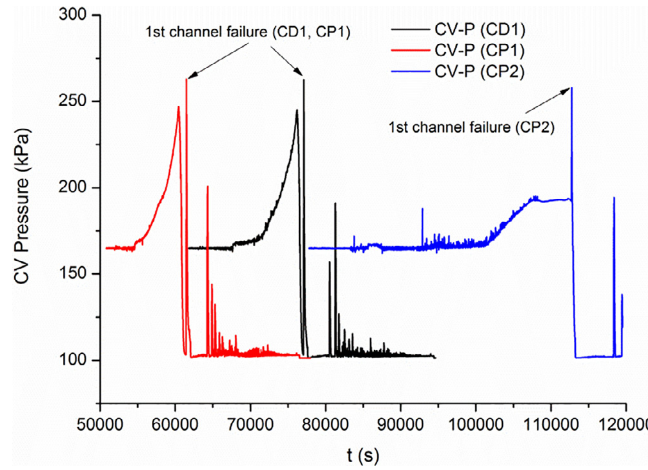

Fig. 27. Calandria Vessel Pressure in Case CP1, CP2 and CD1.

temperature and hydrogen productions being predicted. The fission product releases in case CP1, however, are lower than in case CD1 by appreciable amounts.

The decrease in fission product yield factor in case CP2 has the opposite effects: the moderator saturation and the SG dryout are delayed to 17.36 h and 20.45 h, respectively (Table 13). The subsequent key events are also delayed. One important observation is that in case CP2 the calandria vessel rupture disks do not burst until the first channel failure, while in both CD1 and CP1 the rupture disks burst before fuel channel failure occurs. The difference is attributed to the different decay power level at the time of fuel channel heat-up. In case CD1 and CP1, the rupture disk burst due to the moderator steaming rate exceeding the calandria vessel steam relief valve capacity when the PT ballooning credits the moderator as heat sink. In case CP2, however, the calandria vessel pressure rises above its steam relief valve setpoint (i.e. 165 kPa) without exceeding the rupture disk burst pressure (Fig. 27). Fuel channel failure thus does not occur until the moderator level is boiled down to uncover the first few channel rows, and is thus delayed by almost 10 h if compared to the reference case. Nevertheless, the predicted hydrogen and fission products releases are both similar to case CP1 (Table 13).

5. Conclusions

Three mechanistic models for PT ballooning, PT sagging, and sagging of uncovered channels have been developed and integrated into RELAP/SCDAPSIM/MOD3.6 code. In this paper the modified MOD3.6 is used to simulate postulated SBO accidents for a 900 MW CANDU reactor. Four SBO scenarios with/without operator-initiated crash-cooldown and with different water make-up options are simulated. To maximize the channel resolution during the core disassembly phase, the transient is broken into two phases. The first phase, i.e. from initiating event to channel failure and PHTS depressurization, is simulated using the previously developed and benchmarked full-plant model with 20 characteristic fuel channels. The second phase, i.e. continued from the end of the first phase until calandria vessel dryout, is simulated adopting a new RELAP5 nodalization in which only half of the core is modeled in detail (based on core symmetry) and the channels are grouped into 14 rows and 8 columns. This two-step approach has been proven effective in overcoming the memory constraints of the code and reducing the uncertainty in the modeling of the core disassembly phase.

In the four standard cases, i.e. CD1 to CD4, different operator actions and/or water make-up options result in different duration of natural circulation thus different decay heat levels when the fuel channels start to heat up. However, the subsequent event sequences and the severity of the accident (concerning the hydrogen or fission products releases) are found to be insensitive to decay heat levels. The initial moderator level prior to core disassembly (or the initial number of uncovered fuel channels) plays a more important role in affecting the core disassembly pathways.

A large fraction of the total hydrogen and fission products releases (until calandria vessel dryout) are from the suspended debris bed and occur prior to core collapse. Sensitivity studies showed that the total hydrogen or fission products released (until calandria vessel dryout) are often sensitive to parameters that may influence the duration of the core disassembly phase and/or the temperature of suspended debris bed, e.g. the core collapse criterion and the channel-to-channel contact angle. Regardless of the different disassembly pathways, the end states of all simulations in this study are similar, i.e. a terminal debris bed lay at the bottom of the depleted calandria vessel externally cooled by the shield tank water.

Although the individual deformation models in the modified code were benchmarked against experiments, the code has not been validated against integrated CANDU severe accident experiments. Lacking the relevant experimental evidences, the modeling of some phenomena still relies on "conservative" assumptions (conservative from the perspective of in-core progression). It should be noted that these assumptions are expected to cause greater hydrogen and fission product releases during the core disassembly phase thus less fission product and smaller heat load in the terminal debris bed. Thus they may not be conservative from the perspective of in-vessel retention. The code after all these modifications still has several limitations when applied to CANDU reactors:

1) The molten material relocation and solidification in the suspended debris bed are currently not modeled. The results of the current paper showed that there may be significant amount of molten materials present in the suspended debris bed prior to core collapse. The molten mixtures may relocate downward onto the CT outer surfaces of the lower channels where they may solidify if encountered a cooler surface, or they may flow directly into the moderator and get quenched. In either case there will be a decrease in the oxidation of the reactor core with an associated reduction in hydrogen production during this phase.
2) In the current modeling the steam access to all surfaces of the suspended debris bed is unimpeded, while in reality steam supply to the interior of the debris is expected to decrease considerably once a compact suspended debris bed has formed. Steam supply into the debris may also be affected by the steam circulation pattern in the calandria vessel. All these factors if not taken into account may leads to the overestimation of hydrogen production.
3) Various in-core devices such as the adjuster rods, shutoff rods and control absorbers are currently not modeled. Some structures are made of Zircaloy, e.g. the guide tube, the liquid zone compartment. In MAAP-CANDU, the extra Zircaloy mass is accounted for with an artificial increase in the amount of Zircaloy in the fuel channels. In this study their contributions to hydrogen production are not taken into account, although the amount of oxidation would be limited to the relatively small regions/areas of the core where such assemblies are in direct contact with hot materials (i.e., since the structures contain no fuel and the heat loads are small).
4) Radiation heat transfer from the hot suspended debris bed to the cold calandria vessel wall has not been taken into account. The potential impact on predicted results needs to be investigated since it may tend to limit the extent of molten material in the suspended debris bed.

Acknowledgement

The work is financially supported by the Natural Sciences and Engineering Research Council of Canada (NSERC) and the University Network of Excellence in Nuclear Engineering (UNENE). Technical support from the RELAP/SCDAPSIM development team is greatly acknowleged. The authors also would like to sincerely thank Professor J.C. Luxat, and Professor D. Jackson at McMaster University for their valuable suggestions and assistances.

References

Aydogdu, K., 1998. "Methodology Used to Calculate Moderator-System Heat Load at Full Power and During Reactor Transients." In: 19th CNS Annual Conference.
Jiang, J., 2015. "Electrical System." In: The Essential CANDU, University Network of Excellence in Nuclear Engineering (UNENE). pp. 1–42.
Luxat, J.C., 2008. Thermal-hydraulic aspects of progression to severe accidents in CANDU reactors. Nucl. Technol. 167 (1), 187–210.
Nijhawan, S.M., Wight, A.L., Snell, V.G., 1996. "Addressing Severe Accidents in the CANDU9 Design." In: IAEA Technical Committee meeting on Impact of Severe Accidents on Plant Design and Layout of Advanced Water Cooled Reactors. pp. 167–184.
Rosinger, H.E., Rondeau, R.K., Demoline, K., Ross, K.J., 1985. "Interaction and Dissolution of Sloid UO2 by Molten Zircaloy-4 Cladding in an Inert Atmosphere or Steam." In: CNS 6th Annual Conference.
Akalin, O., Blahnik, C., Phan, B., Rance, F., 1985. "Fuel Temperature Escalation in Severe Accident." In: CNS 6th Annual Conference.
Kohn, E., Hadaller, G.I., 1985. "CANDU Fuel Deformation During Degraded Cooling (Experimental Results)." In: CNS 6th Annual Conference.
Simpson, L.A., Mathew, P.M., Muzumdar, A.P., Sanderson, D.B., Snell, V.G., 1996. "Severe Accident Phenomena and Research for CANDU Reactors." In: 10th Pacific Basin Nuclear Conference, Kobe, JAPAN. pp. 1–12.
Rogers, J.T., 1984. "Thermal and Hydraulic Behaviour of CANDU Cores Under Severe Accident Conditions - Volume 1." AECB Report, vol. 1.
Blahnik, C., Luxat, J.C., Nijhawan, S., 1993. "CANDU response to loss of all heat sinks." In: 9th ANS Meeting on Nuclear Thermalhydraulics.
Meneley, D.A., Blahnik, C., Rogers, J.T., 1996. "Coolability of Severely Degraded CANDU Cores." In: AECL Reports.
Blahnik, C., 1991. "Modular Accident Analysis Program for CANDU Reactors." In: 12th CNS Annual Conference.
Kim, D.H., Jin, Y.H., Park, S.Y., Song, Y.M., 1995. "Development of computer code for level 2 PSA of CANDU plant." In: Korea Atomic Energy Research Institute, KAERI/RR–1573/95.
Kim, I., Cho, Y., Lee, S., 1995. "RELAP5 Simulations of critical break experiments in the RD-14 test facility." In: 16th CNS Annual Conference. pp. 2–4.
International Atomic Energy Agency, 2004. "Intercomparison and Validation of computer codes for thermalhydraulic safety analysis of heavy water reactors.".
SCDAP/RELAP5 Development Team, 1997. "SCDAP/RELAP5/MOD3.3 Code Manual." In: NUREG/CR-6150.
Allison, C.M., Hohorst, J.K., 2010. Role of RELAP/SCDAPSIM in nuclear safety. Sci. Technol. Nucl. Install. 2010, 1–17.
Dupleac, D., Mladin, M., Prisecaru, I., 2009. Generic CANDU 6 plant severe accident analysis employing SCAPSIM/RELAP5 code. Nucl. Eng. Des. 239 (10), 2093–2103.
Tong, L.L., Chen, J.B., Cao, X.W., Deng, J., 2014. Thermal hydraulic behavior under Station Blackout for CANDU6. Prog. Nucl. Energy 74, 176–183.
Bonelli, A., Mazzantini, O., Dupleac, D., Dinca, E., 2015. "RELAP/SCDAPSIM/MOD3.6 – Development of Severe Accident Models for Heavy Water Reactors Including CANDU and ATUCHA-2." In: Proceedings of ICAPP.
Shewfelt, R.S.W., Godin, D.P., Lyall, L.W., 1984. "Verification of High-Temeprature Transverse Creep Model for Zr-2.5 wt.%Nb Pressure Tubes." In: AECL Report 7813.
Shewfelt, R.S.W., Godin, D.P., 1985. "Verification Tests for GRAD, A Computer Program to Predict the Non-uniform Deformation and Failure of Pressure Tubes During a Postulated LOCA." In: AECL Report 8384.
Kundurpi, P., 1986. "Validation of Computer NUBALL for Simulation of Pressure Tube Asymmetric Ballooning Behaviour." In: 2nd International on Simulation Method in Nuclear Engineering.
Luxat, J.C., 2002. "Mechanistic Modeling of Heat Transfer Processes Governing Pressure Tube- To-Calandria Tube Contact and Fuel Channel Failure." In: 23rd CNS annual conference. pp. 1–26.
Cziraky, A., 2009. Pressure tube-calandria tube thermal contact conductance. Master Thesis. McMaster University.
Dion, A., 2016. A mechanistic model to predict fuel channel failure in the event of pressure tube overheating. Master Thesis. McMaster University.
Gillespie, G.E., Moyer, R.G., Hadaller, G.I., 1984. "An Experimental Investigation of the Creep Sag of Pressure Tubes under LOCA Conditions." In: CNS 5th Annual CNS Conference.
Mathew, P.M., White, A.J., Snell, V.G., Bonechi, M., 2003. Severe core damage experiments and analysis for CANDU applications. SMiRT 17, 1–8.
Zhou, F., Novog, D., Siefken, L., Allison, C., 2018. Development and benchmarking of mechanistic channel deformation models in RELAP/SCDAPSIM/MOD3.6 for CANDU severe accident analysis. Nucl. Sci. Eng.
Dupleac, D., Prisecaru, I., Mladin, M., Negut, G., 2008. "SCDAP/RELAP5 Investigation on Coolability of Severely Degraded CANDU 6 Core – Preliminary Results." In: ICAPP.
Mladin, M., Dupleac, D., Prisecaru, I., Mladin, D., 2010. Adapting and applying SCDAP/RELAP5 to CANDU in-vessel retention studies. Ann. Nucl. Energy 37 (6), 845–852.
Dupleac, D., Mladin, M., Prisecaru, I., 2011. "Sensitivity Studies on Uncertainty Parameters and Code Modeling of Calandria Vessel integrity during Late Phase CANDU 6 Severe Accident." In: ICAPP.
Nicolici, S., Dupleac, D., Prisecaru, I., 2013. Numerical analysis of debris melting

phenomena during late phase CANDU 6 severe accident. Nucl. Eng. Des. 254, 272–279.
Zhou, F., Novog, D.R., 2017. RELAP5 simulation of CANDU station blackout accidents with/without water make-up to the steam generators. Nucl. Eng. Des. 318, 35–53.
SCDAP/RELAP5 Development Team, 1997. "SCDAP/RELAP5/MOD3.2 CODE MANUAL VOLUME II: DAMAGE PROGRESSION MODEL THEORY." vol. II.
Hill, R., 1950. The Mathematical Theory of Plasticity. Clarendon Press, Oxford.
Mendelson, A., 1968. Plasticity: Theory and Application.
Hohorst, J., 2013. "RELAP/SCDAPSIM Input Manual." Innovative System Software.
Rest, J., 1983. Evaluation of volatile and gaseous fission product behavior in water reactor fuel under normal and severe core accident conditions 4–4. Nucl. Technol. 61, 33–48.
Kuhlman, M.R., 1985. "CORSOR User's Manual." NUREG/CR-4173, BMI-2122.
Hagen, S., Sepold, L., Hofmann, P., Schanz, G., 1988. "Out-of-Pile Experiments on LWR Severe Fuel Damage Behavior, Tests CORA-C and CORA-2." KfK 4404.
Hagen, S., 1993. "Results of SFD Experiment CORA-13 (OECD International Standard Problem 31)." KfK 5054.
Tayal, M., Gacesa, M., 2014. "The Essential CANDU - Chapter 17 Fuel." UNENE.
Mladin, M., Dupleac, D., Prisecaru, I., 2008. Modifications in SCDAP code for early phase degradation in a CANDU fuel channel. Ann. Nucl. Energy 36 (5), 634–640.
Dupleac, D., Mladin, M., Prisecaru, I., 2009. "Effect of CANDU Fuel Bundle Modelling on Severe Accident Analysis." In: Proceeding of Top Fuel. pp. 367–372.
Aydogdu, K., 2004. "Moderator-system and Shield-cooling System Heat Loads after Reactor Shutdown for CANDU 6 Reactors." In: 25th Annual Conference of CNS. pp. 1–17.
Lewis, B.J., Iglesias, F.C., Dickson, R.S., Williams, A., 2009. Overview of high-temperature fuel behaviour with relevance to CANDU fuel. J. Nucl. Mater. 394 (1), 67–86.
Mathew, P.M., 2004. "Severe Core Damage Accident Progression Within a CANDU Calandria Vessel." In: MASCA Seminar.
Kennedy, J., Maka, P., Chai, M., 2016. "MAAP5-CANDU Development." In: 36th Annual CNS Conference. pp. 1–8.
Whitmarsh, C.L., 1962. "Review of Zircaloy-2 and Zircaloy-4 Properties Relvant to NS Savannah Reactor design." Oak Ridge National Lab. Report ORNL-3281.
Luxat, J.C., 2001. "Analysis of High Pressure Contact Boiling Tests." Ontario Power Generation Report.
Gillespie, G.E., 1981. "An experimental investigation of heat transfer from a reactor fuel channel to surrounding water." In: 2nd Annual CNS Conference.
Nitheanandan, T., 2012. "Proposal for the IAEA International Collaborative Standard Problem on HWR Moderator Subcooling Requirements to Demonstrate Backup Heat Sink Capabilities of Moderator during Accidents." International Atomic Energy Agency. pp. 1–15.
Rogers, J.T., 1989. "Thermohydraulics of Moderator Expulsion From a CANDU Calandria Under Severe Accident Conditions." In: 10th Annual CNS Conference. pp. 27–32.
Canadian Nuclear Safety Commission, 2015. "Severe Accident Progression Without Operator Action," Unclassified Report, no. October.
Shewfelt, R.S.W., Lyall, L.W., 1985. A high-temperature longitudinal strain rate equation For Zr-2.5 wt%-Nb pressure tubes. J. Nucl. Mater. 132, 41–46.

6. Conclusions and Future Work

This thesis provides an alternative and more mechanistic approach to CANDU severe accident modeling through the development and application of best-estimate models/tools. The work was divided into three parts with each part summarized in a Journal article included in Chapter 3, 4 and 5, respectively.

The first part focused on the natural circulation phenomena during an SBO accident, and assessed the effectiveness of several SG water make-up options as an emergency mitigating action in an SBO. A detailed RELAP5 model was created for a 900MWe CANDU including the relevant hydraulic, safety and control systems, in a way that can also be easily adapted to simulate other accident scenarios. The model was first benchmarked against station measurements in a loss of flow event at an operating 900MWe CANDU with good agreement. Then the model was used to simulate several postulated SBO scenarios with/without crash-cooling and with different SG water make-up options. The capability of RELAP5 code for predicting the intermittent natural circulation in a CANDU following crash-cooldown was assessed. The effect of delayed operator actions for crash-cool, the role of the pressurizer, and the sensitivity to channel/U-tube grouping, to CCFL model parameters and other factors were also investigated. A separate study was also carried out by simulating the “standing-start” tests at the Cold Water Injection Test (CWIT) facility in an effort to improve the confidence in the predicted IBIF phenomena by the RELAP5 code, as well as to better understand the limitations of RELAP5.

The second part focused on the model development and model benchmarking to adapt the RELAP/SCDAPSIM/MOD3.6 code to CANDU severe accident modeling. Three mechanistic models based on existing phenomena in literature including PT ballooning, PT sagging, and fuel channel sagging/disassembly, were developed and integrated into MOD3.6. These new models allow a more mechanistic treatment of the deformation processes during CANDU severe accidents, e.g., the PT balloon/sag models track the deformation of PTs, determine PT-to-CT contact, and calculate the contact conductance between PT and CT. The fuel channel sagging /disassembly model possesses significant improvements over the existing ones from most of the integrated CANDU severe accident codes, in that it was developed based on the classical beam theory while taking into account the interactions (i.e. heat and mechanical load transfers) between channels in contact with each other. Benchmarking of the models was performed against the selected PT contact boiling, PT sagging, and PT rupture tests with good agreement.

In the third part the early-phase simulations in the first part were extended to include the fuel channel heat-up phase and the core disassembly phase by using the modified MOD3.6 code. To allow appropriate detail in each stage of the accident progression, the simulations were broken into two stages. The first stage (until the first fuel channel failure and PHTS depressurization) was modeled with extensive nodalizations for the PHTS, the feed and bleed system, and the SG secondary side. Modeling of the core disassembly phase is considered one of the most challenging tasks of this work due to its large uncertainties and the lack of relevant experimental results. The second-stage nodalization therefore used a much more detailed representation of the calandria vessel and the reactor core to allow the physics of moderator heat sink, channel uncovery, channel interactions and core collapsing to be captured. To overcome memory constraints, the irrelevant hydraulic components/systems were removed including the above-core components, the feed and bleed system, and the SG secondary side. The study revealed that a small operator intervention in the early phase (e.g. the credit of crash-cooling to allow water make-up to the boiler) may vastly change (or delay) the subsequent accident progression, and demonstrated that the current CANDU design possesses significant “defense-in-depth”. By maintaining the water level in the boiler, the natural circulation phase can be extended indefinitely. By maintaining the calandria vessel inventory significant core degradation will be prevented.

However, many phenomena are still not mechanistically modeled (Appendix E summarizes the areas needing further improvements). The modeling of some these phenomena still relies on “conservative” assumptions. For example, the suspended debris bed does not limit steam flow into its interior, while in reality a significant reduction in steam supply is expected when a compact debris bed is formed. It is also worth noting that these assumptions are considered “conservative” in this study from the perspective of in-core progression (as they may result in a delayed core collapse or greater oxidation heat load thus larger hydrogen / fission product releases), but may not be conservative from the perspective of subsequent accident progression. For example, most of the fission products released from the suspended debris bed during the core disassembly phase are volatile ones. The fission products after removed from the debris will be transferred out of the calandria vessel to the containment where they will settle over the floor, the containment walls, and other large surfaces which become heat sinks. Meanwhile, when these fission products are removed from the debris their decay heat is also removed. Larger in-core fission product releases thus result in a lower decay heat level in the terminal debris which in turn will lead to a delayed calandria vessel dryout. It will also take longer time to boil down the water level in the shield tank to the surface of terminal molten pool. Therefore, it is not conservative from the perspective of in-vessel retention to remove more fission products from the suspended debris during the core disassembly phase as the calandria vessel failure is expected to be delayed.

In some cases, sensitivity or parametric studies can be performed to look at the envelope behaviors of the processes that are not being modeled with high fidelity. For example, stress concentration at the bundle junctions are not taken into account in the modeling. In order to investigate the potential impacts on the modeling, sensitivity studies have been carried out by multiplying a factor to the creep sag coefficient to mimic the case where fuel channel sagging may be accelerated due to bundle-junction stress concentration. Another example is the modeling of end stub bundles behavior. The bundles in the end stubs may or may not fall out after channel disassembly depending on a number of factors (e.g. the degree of sagging). While there is currently no model to properly quantify such process, several extreme options have been implemented to assist sensitivity studies. However, for many other areas efforts are still needed to develop more mechanistic models in order to further reduce the uncertainty in severe accident modeling.

References

[1] L. Grossi, S. Heim, and M. Waterson, “The impact of the German response to the Fukushima earthquake,” *Energy Econ.*, vol. 66, pp. 450–465, 2017.

[2] CNN Wire Staff, “China Freezes Nuclear Plant Approvals,” *CNN News*, 2011. [Online]. Available: http://www.cnn.com/2011/WORLD/asiapcf/03/16/china.nuclear/index.html. [Accessed: 14-Dec-2017].

[3] Canadian Nuclear Safety Commission, “Canada’s Response to Fukushima,” 2017. [Online]. Available: http://nuclearsafety.gc.ca/eng/resources/fukushima/index.cfm. [Accessed: 20-Jul-2012].

[4] World Nuclear Association, “Nuclear Power in Canada,” 2017. [Online]. Available: http://www.world-nuclear.org/information-library/country-profiles/countries-a-f/canada-nuclear-power.aspx. [Accessed: 14-Dec-2017].

[5] UNENE, *The Essential CANDU, A Textbook on the CANDU Nuclear Power Plant Technology*. University Network of Excellence in Nuclear Engineering (UNENE), 2014.

[6] Wikipedia, “CANDU Reactors.” [Online]. Available: https://en.wikipedia.org/wiki/CANDU_reactor. [Accessed: 17-Dec-2017].

[7] Canadian Nuclear Safety Commission, “CNSC Integrated Action Plan On the Lessons Learned From the Fukushima Daiichi Nuclear Accident,” 2013.

[8] R. Jammal, “Fukushima ’ s Lasting Impacts on the Global Nuclear Industry,” *Presentation*

to the Organization of Canadian Nuclear Industries. 2017.

[9] Ontario Power Generation (OPG), “Darlington NGS Probabilistic Safety Assessment Summary Report,” *Report NK38-REP-03611-10072-R001,*. 2015.

[10] G. Bereznai, “NUCLEAR POWER PLANT SYSTEMS AND OPERATION,” *McMaster Course Material 6P03*. 2005.

[11] P. Sabouri, “LARGE LOCA BEAU ANALYSIS OF A GENERIC 900MW CANDU PLANT,” *McMaster Master Thesis*. 2010.

[12] Training Centre (canteach), “Main Steam Supply and Feedwater System,” *CANDU Trainning Material*. 1993.

[13] C. Blahnik, J. C. Luxat, and S. Nijhawan, “CANDU response to loss of all heat sinks,” in *9th ANS Meeting on Nuclear Thermalhydraulics*, 1993.

[14] CANTEACH, “CANDU Fundamentals,” *CANDU Training Course Material*. 2004.

[15] J. Jiang, “Electrical System,” in *The Essential CANDU*, University Network of Excellence in Nuclear Engineering (UNENE), 2015, pp. 1–42.

[16] J. C. Luxat, “Thermal-Hydraulic Aspects of Progression to Severe Accidents in CANDU Reactors,” *Nucl. Technol.*, vol. 167, no. 1, pp. 187–210, 2008.

[17] Canteach, “CANDU Heat Transport System,” 1996.

[18] AECB, “Fundamentals of Power Reactors Module Two Nuclear Reactor Systems,” 1993.

[19] V. G. Snell, “CANDU Safety #7 - Emergency Core Cooling,” 2001.

[20] E. Wu, “SOPHT USERS MANUAL - DATA Specific to Darlington-A NGS,” 1993.

[21] IAEA, “Analysis of Severe Accidents in Pressurized Heavy Water Reactors,” *TECDOC 1594*. 2008.

[22] U.S. NUCLEAR REGULATORY COMMISSION, “REGULATORY GUIDE 1.155,” *Task SI 5014*. 1988.

[23] G. L. Brooks, “CANDU Origins and Evolution - Emergency Core Cooling System.” 2001.

[24] C. Blahnik, “Modular Accident Analysis Program for CANDU Reactors,” in *12th CNS Annual Conference*, 1991.

[25] C. Blahnik, C. Kim, S. Nijhawan, and R. Thuraisingham, “MODULAR ACCIDENT ANALYSIS PROGRAM FOR CANDU REACTORS,” in *12th CNS Annual Conference*,

1991.

[26] J. Kennedy, P. Maka, and M. Chai, "MAAP5-CANDU Development," in *36th Annual CNS Conference*, 2016, pp. 1–8.

[27] D. Dupleac, M. Mladin, and I. Prisecaru, "Generic CANDU 6 plant severe accident analysis employing SCAPSIM/RELAP5 code," *Nucl. Eng. Des.*, vol. 239, no. 10, pp. 2093–2103, Oct. 2009.

[28] C. M. Allison and J. K. Hohorst, "Role of RELAP/SCDAPSIM in Nuclear Safety," *Sci. Technol. Nucl. Install.*, vol. 2010, pp. 1–17, 2010.

[29] A. Bonelli, O. Mazzantini, D. Dupleac, and E. Dinca, "RELAP/SCDAPSIM/MOD3.6 – Development of Severe Accident Models for Heavy Water Reactors Including CANDU and ATUCHA-2," in *Proceedings of ICAPP*, 2015.

[30] M. Mladin, D. Dupleac, and I. Prisecaru, "Modifications in SCDAP code for early phase degradation in a CANDU fuel channel," *Ann. Nucl. Energy*, vol. 36, no. 5, pp. 634–640, May 2008.

[31] M. Mladin and D. Dupleac, "Verification of Modified SCDAP/RELAP5 Against CANDU Fuel Deformation Experimental Results," in *ICONE17*, 2009, pp. 1–7.

[32] M. Mladin, D. Dupleac, I. Prisecaru, and D. Mladin, "Adapting and applying SCDAP/RELAP5 to CANDU in-vessel retention studies," *Ann. Nucl. Energy*, vol. 37, no. 6, pp. 845–852, 2010.

[33] S. Nicolici, D. Dupleac, and I. Prisecaru, "Numerical analysis of debris melting phenomena during late phase CANDU 6 severe accident," *Nucl. Eng. Des.*, vol. 254, pp. 272–279, 2013.

[34] Information Systems Laboratories, "RELAP5/MOD3.3 CODE MANUAL VOL. 1-8," *NUREG/CR-5535/Rev P4*, 2010.

[35] B. N. Hanna, "CATHENA: a thermal–hydraulic code for CANDU analysis," *Nucl. Eng. Des.*, vol. 180, pp. 113–131, 1998.

[36] D. Naundorf, J. Yin, and A. Petruzzi, "RELAP5 Simulation of Darlington Nuclear Generating Station Loss of Flow Event," *International Agreement Report,*. 2011.

[37] SCDAP/RELAP5 Development Team, "SCDAP/RELAP5/MOD3.2 CODE MANUAL VOLUME II : DAMAGE PROGRESSION MODEL THEORY," vol. II, 1997.

[38] S. M. Petoukhov and P. M. Mathew, "Status of MAAP4-CANDU code development and

simulations of severe core damage accidents for a generic CANDU 6 plant," in *Technical meeting on severe accident and accident management for nuclear power plants*, 2006.

[39] J. T. Rogers, "Thermal and Hydraulic Behavior of CANDU Core Under Severe Accident Conditions - Executive Summary," *AECB Rep.*, 1984.

[40] J. Q. Howieson, H. S. Shapiro, P. J. Allen, J. T. Rogers, P. Mostert, and R. W. van Otterloo, "Probabilistic Risk Assessment Study of a CANDU 600, , March, 1988," in *Proc. Symposium on Severe Accidents in Nuclear Power Plants, IAEA*, 1988, vol. 1, pp. 245–262.

[41] P. J. Allen, J. Q. Howieson, H. S. Shapiro, J. T. Rogers, P. Mostert, and R. W. van Otterloo, "Summary of CANDU 6 Probabilistic Safety Assessment Study Results," *Nucl. Saf.*, vol. 31, no. 2, pp. 202–214, 1990.

[42] D. A. Meneley, C. Blahnik, and J. T. Rogers, "Coolability of Severely Degraded CANDU Cores," *AECL Reports*, 1996.

[43] Canadian Nuclear Safety Commission, "Severe Accident Progression Without Operator Action," *Unclassified Report*, no. October. 2015.

[44] T. Nitheanandan and M. J. Brown, "Backup and Ultimate Heat Sinks in Candu Reactors for Prolonged SBO Accidents," *Nucl. Eng. Technol.*, vol. 45, no. 5, pp. 589–596, Oct. 2013.

[45] S.M. Petoukhov, "MAAP4-CANDU Simulation Results for CANDU6 Accident Management Measure: Steam Generator Secondary Side Water Make-up From Dousing Tank for the Station Blackout Scenario," in *PBNC-2014*, 2014, pp. 1–22.

[46] D. H. Kim, Y. H. Jin, S. Y. Park, and Y. M. Song, "Development of Computer Code for Level 2 PSA of CANDU Plant," in *Korea Atomic Energy Research Institute Report,* 1995.

[47] D. H. Kim, Y. M. Song, S. Y. Park, Y. H. Jin, S. D. Kim, and S. B. Kim, "Validation Report for ISAAC Computer Code," *Korea Atomic Energy Research Institute Report*. 2008.

[48] S. Park and K. Ahn, "COMPARATIVE ANALYSIS OF STATION BLACKOUT ACCIDENT PROGRESSION IN TYPICAL PWR , BWR , AND PHWR," *Nucl. Eng. Technol.*, vol. 44, no. 3, pp. 311–322, 2011.

[49] S. Kim and D. Kim, "Establishment of a Severe Accident Mitigation Strategy for an SBO At Wolsong Unit 1 Nuclear Power Plant," *Nucl. Eng. Technol.*, vol. 45, no. 4, pp. 459–468, Aug. 2013.

[50] World Nuclear News, "Argentina and China sign contract for two reactors," *World Nuclear News, WNN*, 2017. [Online]. Available: http://www.world-nuclear-news.org/NN-Argentina-and-China-sign-contract-for-two-reactors-1805175.html. [Accessed: 31-Jan-2018].

[51] D. Dupleac, I. Prisecaru, M. Mladin, and G. Negut, "SCDAP / RELAP5 Investigation on Coolability of Severely Degraded CANDU 6 Core – Preliminary Results," in *ICAPP*, 2008.

[52] D. Dupleac, M. Mladin, and I. Prisecaru, "Sensitivity Studies on Uncertainty Parameters and Code Modeling of Calandria Vessel integrity during Late Phase CANDU 6 Severe Accident," in *ICAPP*, 2011.

[53] E. Kohn and G. I. Hadaller, "CANDU Fuel Deformation During Degraded Cooling (Experimental Results)," in *CNS 6th Annual Conference*, 1985.

[54] O. Akalin, C. Blahnik, B. Phan, and F. Rance, "Fuel Temperature Escalation in Severe Accident," in *CNS 6th Annual Conference*, 1985.

[55] R. Marcoux, B. Li, G. Arvanitis, A. Etedali-Zadeh, P. Hotari, and R. Dunn, "Mitigation Strategies of Beyond Design Basis Accidents (BDBA) in a CANDU Nuclear Power Plant," in *36th Annual CNS Conference*, 2016, pp. 1–8.

[56] C. Harwood and J. Baschuk, "Assessment of Thermalhydraulic Phenomena for External Water Make-up," in *35th Annual Conference of CNS*, 2015, pp. 1–12.

[57] J. H. Bae, "Severe Accident Code Development for CANDU Reactor," in *CANSAS Presentation Material*, 2017.

[58] S. K. Gupta, S. K. Pradhan, R. S. Rao, and R. Singh, "ANALYSIS OF PROGRESSION OF SEVERE ACCIDENT IN INDIAN PHWRs," *Tech. Meet. Sev. Accid. Accid. Manag.*, 2006.

[59] A. Cziraky, "Pressure Tube-Calandria Tube Thermal Contact Conductance," *McMaster University Master Thesis*. 2009.

[60] J. C. Luxat, "Mechanistic Modeling of Heat Transfer Processes Governing Pressure Tube-To-Calandria Tube Contact and Fuel Channel Failure," in *23rd CNS annual conference*, 2002, pp. 1–26.

[61] M. M. Yovanovich, "Micro and macro hardness measurements, correlations, and contact models," *44th AIAA Aerosp. Sci. Meet. Exhib.*, no. January, pp. 1–28, 2006.

[62] G. E. Gillespie, R. G. Moyer, and G. I. Hadaller, "An Experimental Investigation of the

Creep Sag of Pressure Tubes under LOCA Conditions," in *CNS 5th Annual CNS Conference*, 1984.

[63] F. Zhou and D. R. Novog, "RELAP5 Simulation of CANDU Station Blackout Accidents with/without Water Make-up to the Steam Generators," *Nucl. Eng. Des.*, vol. 318, pp. 35–53, 2017.

[64] J. B. Hedley and T. Chin, "User's Manual GEOFAC," *AECL 153-114160-UM-001*, 2007.

[65] CANTEACH, "Design of CANDU Reactors - Section 2."

[66] Information Systems Laboratories Inc, "RELAP5/MOD3.3 CODE MANUAL VOLUME II: USER'S GUIDE AND INPUT REQUIREMENTS," *U. S. Nuclear Regulatory Commissionn*. 2010.

[67] A. C. Whittier, D. W. Black, and C. R. Boss, "CANDU Channel Decay Power," *AECL-5704*. 1977.

[68] K. Aydogdu, "Moderator-system and Shield-cooling System Heat Loads after Reactor Shutdown for CANDU 6 Reactors," in *25th Annual Conference of CNS*, 2004, pp. 1–17.

[69] IAEA, "Thermophysical properties database of materials for light water reactors and heavy water reactors," *TECDOC-1496*. 2006.

[70] IAEA, "Thermophysical Properties of Materials For Nuclear Engineering: A Tutorial and Collection of Data," *VIENNA*. 2008.

[71] SCDAP/RELAP5 Development Team, "SCDAP/RELAP5/MOD3.2 CODE MANUAL VOLUME IV: MATPRO -- A LIBRARY OF MATERIALS PROPERTIES FOR LIGHT-WATER REACTOR ACCIDENT ANALYSIS," 1997.

[72] P. Majumdar, D. Mukhopadhyay, S. K. Gupta, H. S. Kushwaha, and V. Venkat Raj, "Simulation of pressure tube deformation during high temperature transients," *Int. J. Press. Vessel. Pip.*, vol. 81, no. 7, pp. 575–581, 2004.

[73] R. S. W. Shewfelt and L. W. Lyall, "A High-Temperature Longitudinal Strain Rate Equation For Zr-2.5 wt%-Nb Pressure Tubes," *J. Nucl. Mater.*, vol. 132, pp. 41–46, 1985.

[74] F. Zhou, D. Novog, L. Siefken, and C. Allison, "Development and Benchmarking of Mechanistic Channel Deformation Models in RELAP/SCDAPSIM/MOD3.6 for CANDU Severe Accident Analysis," *Nucl. Sci. Eng.*, 2018.

[75] J. Spencer, "CANDU reactor intermittent buoyancy induced flow analysis," *McMaster University Master Thesis*. 2010.

[76] M. Bayoumi, F. B. P. Tran, K. E. Locke, and A. P. Muzumdar, "Verification of CHAN-II (MOD 6) Against experiments," in *CNS 10th Annual CNS Conference*, 1989.

[77] M. Bayoumi, A. P. Muzumdar, F. B. P. Tran, and K. E. Locke, "CHAN-II (MOD6) - Further Verification Against Single And Seven Element Experiments," in *11th CNS Annual Conference*, 1990.

[78] Q. M. Lei, D. B. Sanderson, K. A. Haugen, and H. E. Rosinger, "Post-test analysis of the 28-element high-temperature thermal-chemical experiment CS28-1," in *4th International conference on simulation methods in nuclear engineering, Montreal, Canada*, 1993.

[79] M. H. Bayoumi and W. C. Muir, "Post-test simulation and analysis of the second full scale CHAN 28-element experiment (validation of CHAN-II (MOD6) against experiments)," in *16th Annual Conf of Canadian Nuclear Society*, 1995.

[80] P. J. Mills, D. B. Sanderson, K. A. Haugen, and G. G. Haacke, "Twenty-Eight-Element Fuel-Channel Thermal-Chemical Experiments," in *17th Annual Canadian Nuclear Society Conference, Fredericton, NB, Canada*, 1996, pp. 1–14.

[81] M. H. Bayoumi, W. C. Muir, and P. S. Kundurpi, "POST-TEST SIMULATION OF THE FIRST CHAN 28-ELEMENT EXPERIMENT (VERIFICATION OF CHAN-II MOD 6 AGAINST EXPERIMENT)," in *4th International conference on simulation methods in nuclear engineering, Montreal, Canada*, 1993.

[82] H. S. Lim, K. M. Lee, M. Y. Ohn, N. H. Lee, and J. H. Choi, "Validation of CATHENA against the CS28-1 high temperature experiment under an impaired cooling condition," *Ann. Nucl. Energy*, vol. 22, no. 9, pp. 593–600, 1995.

[83] B. W. Rhee, H. T. Kim, and J. H. Park, "Validation of a CATHENA fuel channel model for a post-blowdown analysis of the high temperature thermal-chemical experiment CS28-1, I – Steady state," *Ann. Nucl. Energy*, vol. 35, pp. 1373–1379, 2008.

[84] H. S. Kang, "CFD Analysis for the Experimental Investigation of A Single Channel Post-Blowdown," in *Benchmarking of CFD Codes for Application to Nuclear Reactor Safety (CFD4NRS), Munich, Germany*, 2006, pp. 295–305.

[85] H. T. Kim, B. W. Rhee, and J. H. Park, "CFX simulation of a horizontal heater rods test," *Nucl. Eng. Des.*, vol. 238, no. 3, pp. 522–529, 2008.

[86] H. T. Kim, B. W. Rhee, and J. H. Park, "CFX simulation of high temperature thermal-chemical experiment: CS28-2," *Ann. Nucl. Energy*, vol. 35, no. 4, pp. 677–689, 2008.

[87] B. Hamilton, "5 years after Fukushima, Nuclear Industry Alive and Well," *CBC News*,

2016. .

[88] Y. M. Song, S. Y. Park, D. H. Kim, and J. H. Song, “SAMG Supporting Computational Aid Development Using MAAP-ISAAC Code for PHWR,” in *Transactions of the Korean Nuclear Society Spring Meeting*, 2017, pp. 1–3.

Appendices

Appendix A. Descriptions of RELAP5 Model for Early-Phase SBO Simulation

This appendix contains a description of the RELAP5 model used in the early-phase SBO simulation (mostly for things that were not detailed in the first paper [63] in Chapter 3). The model was created using the code US-NRC RELAP5/MOD3.3, including the PHTS, the feed & bleed system, the secondary side, the moderator system, and the shield water cooling system. In addition the model includes the SGECS and deaerator flow path so that the effects of operator initiated crash cool on SBO performance can be assessed. The design geometries, various input parameters and the control systems were mainly taken from the SOPHT input for Darlington NGS [20].

A.1 Primary Heat Transport System

A.1.1Fuel Channel & Grouping

A simplified nodalization of the PHTS is shown in Figure 17. In this nodalization, the 120 fuel channels of each core pass are lumped into an average channel resulting in a total of four characteristic fuel channels. An 8-group model and a 20-group model have also been created with the latter being used as the reference model and the 8-group and 4-group models for channel-grouping sensitivity studies. The three individual models (i.e. 4, 8 and 20-group models) differ only in the number of characteristic fuel channels (and feeder pipes).

The details of the channel grouping scheme and average channel power have already been summarized in the paper [63] in Chapter 3, thus will not be repeated. Table 6 summarized the key input parameters and the desired initial operating conditions of the systems. These initial operating conditions are reached prior to the start of the event by controlling various valves and heaters until a steady state is reached (refer to the Section A.5 for the descriptions of the control systems).

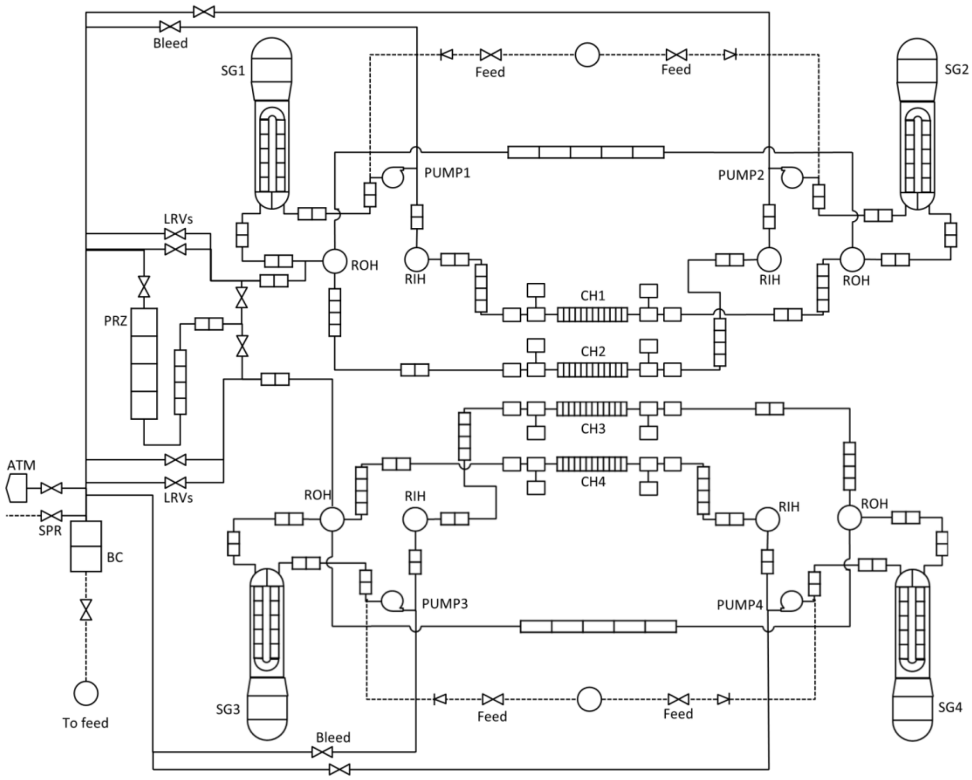

Figure 17 Nodalization of Primary Heat Transport System [63]

Table 6 Key Input Parameters (Normal Operating Condition / Initial Conditions)

Thermal Power (MW)	2651
No. of Fuel Channels in the Core (-)	480
ROH Pressure (kPa)	9921
SG Pressure (kPa)	5050
LRV Set-point (kPa)	10551
Bleed Condenser Pressure (kPa)	1720
Bleed Condenser Relief valve setpoint (kPa)	10270
ROH Coolant Temperature (^oC)	310.6
RIH Coolant Temperature (^oC)	264.5
Feedwater Inlet Temperature (^oC)	178.0
Moderator Temperature (^oC)	59.0
End Shield Water Temperature (^oC)	55.6
Shield Tank Water Temperature (^oC)	60.2
HTS Inventory (without PRZ) (m^3)	213
Pressurizer (PRZ) Inventory (m^3)	64
Moderator Inventory in Calandria Vessel (m^3)	287
No. of Loops, SGs, and Pumps (-)	2, 4, 4
SG Inventory (per SG) (Mg)	91.9
End Shield water inventory (Mg)	23.6
Shield Tank water inventory (Mg)	743
UO_2 Mass in the Core (Mg)	125.3
Zircaloy (Cladding, PT, and CT) Mass in the Core (Mg)	49.8
Pressuriser Level (m)	6.5
SG Level (m)	14.4
Bleed Condenser Level (m)	0.9

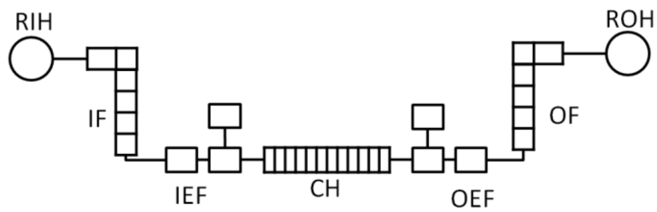

Figure 18 Nodalization of the CANDU fuel channel

Table 7 Input parameters for fuel channel

Pressure Tube material	Zr-2.5%w-Nb
Pressure Tube Diameter (cm)	10.34
Pressure tube thickness (mm)	4.2
Number of fuel bundles per channel	12
Fuel element per bundle	37
fuel bundle length (mm)	495.3
Fuel element diameter (mm)	13.08
Fuel pellet diameter (mm)	12.16
Fuel Cladding Material	Zircaloy-4
Calandria Tube Outer diameter(m)	0.1311
CT Thickness (mm)	1.4
Gap CO2 (mm)	8
Pipe Roughness (m)	8.0e-7
Minor loss at each bundle junction	0.7841

Table 8 Normalized Axial Power Factors

Bundle No.	1^{st} & 12^{th}	2^{nd} & 11^{th}	3^{rd} & 10^{th}	4^{th} & 9^{th}	5^{th} & 8^{th}	6^{th} & 7^{th}
Power Factor	0.017	0.05	0.0795	0.1035	0.1206	0.1294

Table 7 summarizes the key input parameters related to the fuel channels. Each characteristic channel is modeled using one RELAP5 pipe component which is divided into 12 hydraulic nodes corresponding to the 12 fuel bundles (Figure 18). Lumping of the fuel channels is performed by assuming: 1) Area (or volume) of a characteristic channel equals the total area (or total volume) of all fuel channels in the corresponding group; 2) Length (or hydraulic diameter) of the characteristic channel equals that of a single fuel channel. The pipe component of the fuel channel is assumed to have a hydraulic diameter of 7.4e-3m^2 and a roughness of 8.0e-7m. Additional pressure drop at the bundle junctions are accounted for by applying a form loss factor of 0.7841 to each individual junction. The 37-element fuel bundle is modeled as a RELAP5 heat structure of the cylindrical type, and the PT-CO2-CT as another RELAP5 heat structure with three layers of materials, i.e. Zr-2.5%Nb, CO2, and Zr-2 [63]. The heated hydraulic diameter of the fuel heat structure is 9.5e-3m which is estimated by “4 * Flow Area / Heated Perimeter”. The axial power distribution of the channel is assumed to follow the sinusoidal curve with no flux tilt. Table 8 shows the normalized axial power factors for the 12 fuel bundles along the fuel channel.

The cross-section of a typical CANDU fuel channel is shown in Figure 19. Heat is lost from the fuel channel to the moderator through heat conduction via the three layers of materials, and through radiation heat transfer across the annulus gap which is modeled separately with RELAP5 radiation models. The view factor matrix between the PT and CT is shown in Table 9. The 37 fuel elements are lumped into one average element and are represented by one RELAP5 heat structure. In other words, all the 37 elements within a channel are assumed to have the same average temperature at a given axial location. The radiation heat transfer between the 37 fuel sheaths (viewed as a whole) and the inner surface of PT is modelled using RELAP5 radiation models with a view factor matrix as shown in Table 10. The 2×2 view factor matrix is calculated by lumping the individual element view factor matrix 38×38 (i.e. among 37 fuel element surfaces and the PT) calculated by GEOFAC [64]. The emissivity of fuel sheath, pressure tube, and calandria tube used in the current model are 0.25, 0.25, and 0.2 respectively which are for un-oxidized Zircaloy.

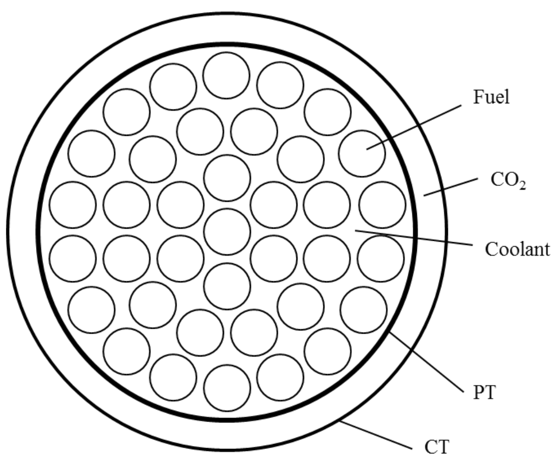

Figure 19 Cross-section of a typical CANDU fuel channel [63]

Table 9 view factor matrix between PT and CT

	PT Outer	CT Inner
PT Outer	0.0	1.0
CT Inner	0.788711	0.211289

Table 10 view factor matrix between the fuel sheaths and PT inner surface

	Fuel Sheaths	PT Inner
Fuel Sheaths	0.79403752	0.20596248
PT Inner	0.964	0.036

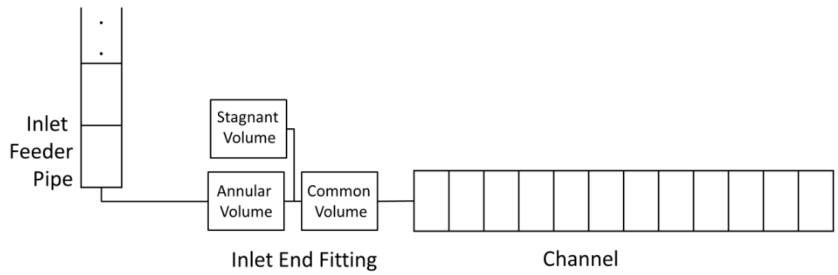

Figure 20 3-component nodalization of the end fitting

The end fitting contains a stagnant volume at the back of the shield plug accounting for approximately 50% of the end fitting total volume. The coolant enters the inlet end fitting via the grayloc, and flows through the concentric annulus which surrounds the stagnant volume to the common volume section where it enters the channel (vice versa for the outlet end fitting). The stagnant volume does not contribute to the overall flow under normal operating conditions. However, under accident conditions the coolant in this section will potentially provide a small amount of water make-up to the fuel channel. The end fitting is thus modeled with three pipe components as shown in Figure 20. The stagnant volume is modeled as a separate pipe component with its one end attached to "Common Volume".

A.1.2 Pressurizer& PHTS Pressure Control

The pressurizer in the system is modeled as a vertical pipe component with six nodes. It connects the two ROHs of the two loops via the surge lines and the two normally-open isolation valves which are modeled using two trip valves. The isolation valves are designed to close when the pressure in either loop is reduced to the ECC activation set-point, i.e. below 5.5MPa. In the event where they are assumed to be unavailable, their response can be easily disabled by inputting a set-point of 0.0 Pa.

The steam bleed valve is modeled as a "servo valve" which connects to the bleed condenser to the top of the pressurizer. The steam bleed valve is key component for controlling the pressurizer and HTS pressure. It responds to the ROH pressure error, i.e. $E_{P\text{-}ROH}$, which is the difference between the maximum of the four ROH pressures and the pressure set-point (P_{set}). The error dead band, E_{db}, is equal to 30kPa. The following control logic is used to actuate the valve (unless otherwise noted, these control logics are all based on the SOPHT input for Darlington NGS.):

$$\text{if } E_{P-ROH} \leq E_{db}, \qquad \text{Valve Demand} = 0$$

$$\text{if } E_{P-ROH} > E_{db}, \qquad \text{Valve Demand} = \text{Gain} \times (E_{P-ROH} - E_{db})$$

where $E_{P-ROH} = P_{ROH} - P_{set}$.

The gain of the steam valve is equal to 0.004 valvelift/kPa. The time lag of the valve is equal to 4 seconds. The pressurizer over-pressure relief valve is not modeled.

The six heaters, i.e. five ON/OFF heaters and one variable heater, are modeled together as one RELAP5 heat structure. The heat input to the heat structure is calculated according to the control logic. Each heater has a maximum power of 250kW. The variable heater is used under normal operating conditions, while the ON/OFF heaters are turned on only if the pressure drops below the range of the variable heater. The total power to the heaters equals to

$$P_{Heater} = 250kW \times (Q_{VH} + 5Q_{ON/OFF})$$

Where Q_{VH} and $Q_{ON/OFF}$ are the power demands of the variable heater and the ON/OFF heater respectively. When the ROH pressure drops below 9801kPa and/or the ROH temperature error ($E_{T-ROH} = T_{Sat-ROH} - T_{ROH}$) is greater than 2.8°C, the ON/OFF heaters are turned on (with the power demand $Q_{ON/OFF}$ set to 1).The variable heater power demand is calculated with the following formula:

$$Q_{VH} = G_1 E_{T-ROH} - G_2 E_{P-ROH}$$

where G1 equals 2.4 $^{o}C^{-1}$ and G2 equals 0.012 kPa^{-1}. Q_{VH} has a range between 0 and 1.

These heaters rely on Class IV power, thus are not available during SBO. In the model, they are only used to achieve the desired steady-state initial condition and the power supplied to the heaters will be overwritten to zero once the SBO trip used to control the heaters becomes true.

The pressurizer also provides a place to monitor the inventory of the PHTS. The inventory of the PHTS is controlled through the adjustment of the feed valves and bleed valves of the "feed and bleed system" (see Section A.3 for details).

A.1.3 PHTS Pumps

The four PHTS pumps are powered by Class IV power. The pumps are tripped after the loss of power in a postulated SBO accident, and will then rundown until the pump inertia is exhausted. These four HTS pumps are modeled using the RELAP5 pump components. The pump properties and the characteristic curves are based on the SOPHT input for Darlington. Table 11 summarizes the input properties for the HTS pumps.

Table 11 HTS Pump Properties

Type of Properties	Value
Rated velocity	188 rad/s
Rated Flow	3.3 m^3/s
Rated Head	220.8m
Rated Density	872 kg/m^3
Rated Torque	649.211 Pa*m^3
Moment of Inertia	27.63 kg*m^2
Constant Frictional Torque	4.22 Pa*m^3

Table 12 HTS Pump Characteristic Curves in Polynomial

		C0	C1	C2	C3	C4	C5
Head Curve	Quadrant I	1.3425	-0.254	0.2373	-0.3245		
	Quadrant II	0.8257	-0.4994	0.5515	-0.1872	0.0958	
	Quadrant III	0.2511	-0.7378	-0.8656	0.6583		
	Quadrant IV	-1.1518	1.4363	0.6479	0.0676		
Torque Curve	Quadrant I	0.6372	0.1117	0.7109	-0.4131	-0.0466	
	Quadrant II	1.0407	-0.5181	-0.1296	-0.0884	0.0851	
	Quadrant III	-0.8050	1.0449	0.1503			
	Quadrant IV	-0.5505	1.2905	0.2005	0.0595		

The pump characteristic curves in SOPHT are in the form of a polynomial with the dimensionless flow or speed as independent parameter and dimensionless head or torque as dependent parameter:

$$Y = C_0 + C_1X^1 + C_2X^2 + C_3X^3 + C_4X^4 + C_5X^5$$

where X is the independent variable, and Y is the dependent variable. The coefficients for the above polynomial are summarized in Table 12.

The pump degradation model for HTS pump in SOPHT is based on the Aerojet Nuclear Company (ANC) two phase correlation models for the head difference and the difference curve multiplier. The same model is used in the current RELAP5 input.

A.1.4 Other Components of PHTS

Liquid Relief Valves (LRVs) are fully instrumented globe valves which are designed to fail open on loss of air supply to the actuators and on loss of control power. The four LRVs are modeled using a RELAP5 motor operated valve, and are assumed available during the postulated SBO, or assumed to fail once available DC power is lost. The valves open when the ROH pressure exceeds 10.551MPa and close when the ROH pressure drops below the same value. The valve opening time is set to 1 second and closing time to 3 seconds. Same as the steam bleed valve of the pressurizer, these valves discharge coolant (vapor or two-phase) to the bleed condenser. The potential loss of DC power will result in the early opening of LRV. However, sensitivity studies where DC power is assumed to be lost at 30mins showed that the event sequences/timings are not significantly affected for both crash-cool and non-crash-cool scenarios.

The inlet/outlet feeder pipes for each fuel channel group are lumped into a single averaged pipe. Due to the lack of design details of the feeder pipes (e.g. length, bends and form losses) the feeder pipes are represented by a number of inclined straight pipes in RELAP5. The elevation change, area and volume of these pipes are calculated and are preserved. The pipe roughness for both the inlet and outlet feeders is set to 4.572e-5m which is the roughness for Carbon Steel. Each pipe is subdivided into a number of cells (typically 5). Form loss factors are applied to the junction elbows and pipe diameter changes based on data from Idelchik, and are adjusted according to the reported channel mass flow map. Similar to the channel power map which is used for channel grouping, the channel mass flow map is also from the input for "NUCIRC II" [11].

The reactor inlet or outlet headers (RIH/ROH) are represented as a RELAP5 pipe with a single volume (similar to the SOHPT input). The details of the feeder connections to the headers (e.g. location) are not considered nor are potential axial header gradients along the headers. Sensitivity studies have been carried out by other researchers to assess the header nodalization on HTS response using RELAP5/MOD3.3, and showed that the difference between single-node and multiple-node nodalizations are negligible [36]. The same wall roughness as the feeder pipe is used for all the headers. The length of the header is the average distance for flow to travel from the inlets (or outlets for the ROH) of the header to the feeder connections. The hydraulic diameter of the inlet header is 0.451m and that of the outlet header is 0.495m.

A.2 Steam Generator

A.2.1 SG Primary Side & Secondary Side

The design parameters related to the primary side SGs are summarized in Table 13. The U-tubes of a SG are lumped into an equivalent averaged pipe using similar parallel averaging method for the fuel channels, i.e. one flow path per SG. Sensitivity cases where the U-tubes of a SG are represented by a number of parallel flow pathways have also been simulated. No significant differences are observed between the "single-flow-path" and the "multiple-flow-path" nodalizations.

The averaged U-tube flow pathway is first divided into three main sections corresponding to the three sections on the secondary side of the SG, i.e. preheater, low-boiler, upper-boiler sections, and is then subdivided into a number of nodes for each section. RELAP5 heat structures of cylindrical type are used to represent the U-tubes. Since the wall thickness of the U-tubes is small, the radial mesh of the heat structure is set to one with its inner wall attached to the primary-side hydraulic volume of the U-tubes and the outer wall attached to the corresponding secondary-side SG volume (Figure 21).

Table 13 Modeling Parameters of the U-tubes

Inner Diameter (m)	0.0136
Thickness (m)	0.00114
Material	Inconel 800
Number of Tubes per SG	4663
Wall roughness (m)	1.5e-6
Conductivity (W/m-K)	15.64
Heat Capacity (J/m^{3}K)	3.652e6

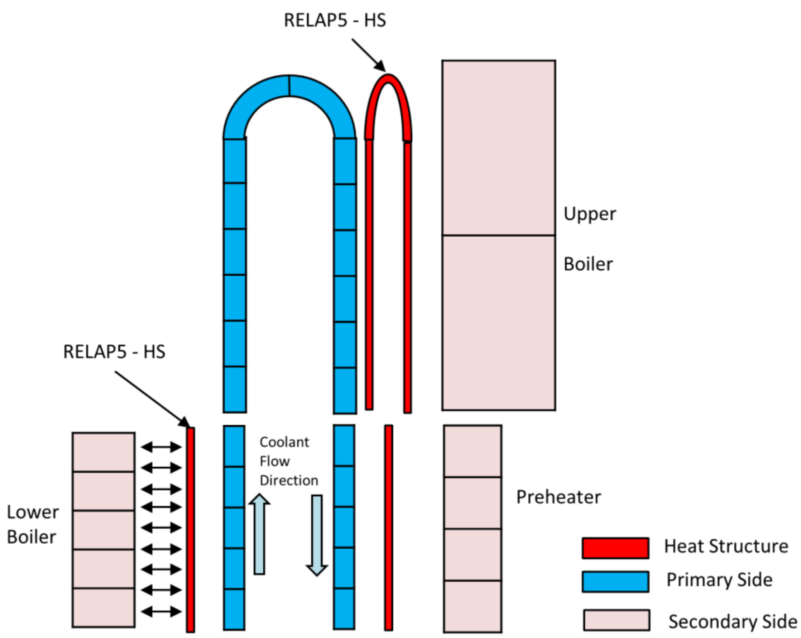

Figure 21 Nodalization of the SG primary side and Heat Structures

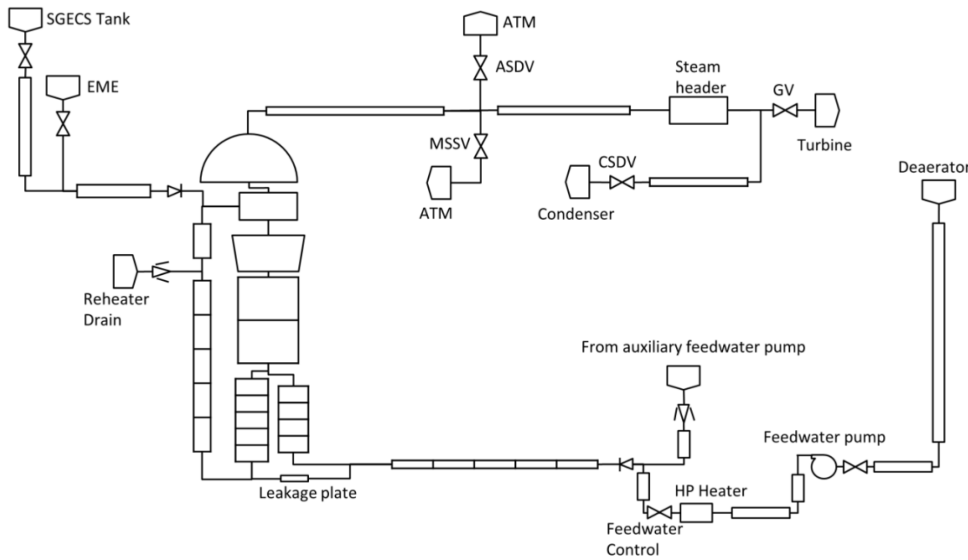

Figure 22 Nodalization of the SG Secondary Side [63]

Table 14 Operating Condition of SGs

<table>
<tr><th colspan="2">Parameters</th><th>Steady State Value</th><th colspan="2">Parameters</th><th>Steady State Value</th></tr>
<tr><th colspan="3">Mass Flow (kg/s)</th><th colspan="3">Level (m)</th></tr>
<tr><td colspan="2">FW Pump</td><td>1239.7</td><td colspan="2">SG1</td><td>14.37</td></tr>
<tr><td colspan="2">SG1 Inlet</td><td>308.4</td><td colspan="2">SG2</td><td>14.37</td></tr>
<tr><td colspan="2">SG2 Inlet</td><td>310.5</td><td colspan="2">SG3</td><td>14.37</td></tr>
<tr><td colspan="2">SG3 Inlet</td><td>310.2</td><td colspan="2">SG4</td><td>14.37</td></tr>
<tr><td colspan="2">SG4 Inlet</td><td>310.6</td><th colspan="3">Power (MW)</th></tr>
<tr><td colspan="2">Re-heater Drain</td><td>15.61</td><td colspan="2">HP FW Heater</td><td>128.9</td></tr>
<tr><th colspan="3">Temperature (K)</th><th colspan="3">Pressure (MPa)</th></tr>
<tr><td colspan="2">Deaerator Tank</td><td>427.9</td><td colspan="2">Deaerator Tank</td><td>0.571</td></tr>
<tr><td colspan="2">FW Pump Out</td><td>427.2</td><td colspan="2">FW Pump Out</td><td>6.308</td></tr>
<tr><td rowspan="5">SG1</td><td>SG Inlet</td><td>451.1</td><td rowspan="5">SG1</td><td>SG Inlet</td><td>5.186</td></tr>
<tr><td>Preheater Outlet</td><td>535.4</td><td>Preheater Outlet</td><td>5.142</td></tr>
<tr><td>Upper Boiler Outlet</td><td>538.7</td><td>Upper Boiler Outlet</td><td>5.129</td></tr>
<tr><td>SG Outlet</td><td>537.7</td><td>SG Outlet</td><td>5.046</td></tr>
<tr><td>Re-heater Drain</td><td>533.0</td><td>Re-heater Drain</td><td>5.140</td></tr>
<tr><td colspan="2"></td><td></td><td colspan="2">Turbine</td><td>4.662</td></tr>
</table>

The nodalization of the SG secondary side is shown in Figure 22, and the steady state conditions of the four SGs are summarized in Table 14. The SG secondary volumes (lower boiler, upper boiler and preheater) are modeled using three vertical pipe components. Heat is deposited into the three sections from the primary side through the U-tube heat structures.

The separators of each SG are modeled using a RELAP5 "separator" component with the "simple separator" model. The downcomer is represented by an annulus component. The key input parameters to the separator model are the VOVER (i.e. the vapor void fraction above which flow out of the vapor outlet is pure vapor) and VUNDER (i.e. the liquid volume fraction above which flow out of the liquid fall back is pure liquid.). They are set to 0.3 and 0.15 respectively in the current model to have the desired recirculation ratio.

A.2.2 Feedwater Supply & SG Inventory Control

The piping from the condenser to the low pressure feed-heater is currently not modeled. The feedwater line starts from the deaerator tank which is simplified as a time-dependent volume with constant (or table) thermodynamic properties. The deaerator tank is placed at a high elevation which provides the necessary hydro-static head for the feedwater pumps to prevent pump cavitation. The piping from the deaerator tank to the feedwater pumps is simplified as a straight and inclined pipe. A trip valve is placed downstream of the deaerator tank (Figure 22). In the case of SBO with operator initiated crash-cool, water from the deaerator tank will flow by gravity into the SGs after the depressurization of SGs. The trip valve will remain open until the integral of the feedwater leaving the deaerator volume reaches the total tank volume.

Under normal operating conditions, the water in the DA tank is assumed to be constant at 571kPa and 427.96K. In the SBO case, after turbine trip the steam/water supply to the DA tank is lost, the pressure and temperature of the DA water is assumed to decrease slowly to 229kPa and 393.15K in 900 seconds (15mins), and remain constant thereafter.

The HP FW heater located downstream of the feedwater pumps uses extraction steam to add heat into the feedwater and raises its temperature to desired value before entering the preheater of the SGs. The HP FW heater is modeled as a RELAP5 heat structure. The heat supplied to the heat structure is a function of the feedwater mass flow rate. In reality, there are no control valves on the extraction steam line, but the heat source of the FW heater has a self-regulating feature, i.e. when the feedwater temperature approaches the saturated steam temperature then condensation of the extraction steam diminishes and therefore the flow of extraction steam to the feedwater heater tends towards zero [12]. In RELAP5, the following "mass flow versus heat addition" table is used to determine the heater power.

Table 15 Feedwater Mass Flow Rate vs. Heat Addition Rate

Mass Flow Rate (kg/s)	**Heat Addition Rate (kW)**
-1.0 *	0.0
0.0	0.0
1294.3	1.34611e5
1.0e8	1.34611e5

*: In an SBO, after turbine trip extraction steam supplied to the heater is lost. The independent variable (i.e. mass flow) supplied to the table for interpolation will be overwritten to "-1.0" which gives 0.0 heat addition rate in RELAP5.

Table 16 HTS Pump Properties

Type of Properties	Value
Rated Flow	1.45 m^3/s
Rated Head	570.0 m
Rated Density	912.5 kg/m^3

Table 17 Pump Characteristic Curve Polynomial Coefficients

		C0	C1	C2	C3	C4	C5
Head Curve	Quadrant I	1.2666	-0.1112	-0.1200	0.1803	-0.02305	-0.1484

The main feedwater pumps (3x50%) are represented in the RELAP5 model using a pump component. Table 16 summarizes the input parameters for the pump. The two-phase multiplier and difference tables are not entered since the operating condition of the pumps is always in single liquid phase. The pump characteristic curve is based on SOPHT input. Because the pumps mainly operate in the first Quadrant, only the coefficients of the head curve polynomial in the first quadrant (refer to Section A.1.3 for the polynomial equation) are provided (see Table 17).

The auxiliary feedwater pump is simplified as a time-dependent junction connected to a time-dependent volume. In cases where the Class III power is available the auxiliary feedwater pump is capable of supplying 3% of full-power feedwater flow. In the RELAP5 model if the auxiliary feedwater pump is started, the mass flow supplied to each SG by the "pump" is fixed at 10kg/s. The water properties in the time-dependent volume attached to the junction are assumed to be constant at 5.40MPa and 450.0K. While lower SG inlet temperatures would be available during emergency auxiliary water supply (from EWS for example) the higher subcooling is not credited in this analysis.

The feedwater control valves are the key components controlling the SG level/inventory. In a CANDU plant, the SG level is controlled using three-element logic control, i.e. the current measured water level, the steam flow and the feedwater flow are all used to determine the gain of the feedwater control valves. In the RELAP5 model, servo valves are used to represent the feedwater control valves. The RELAP5 control variable “feedwater flow controller” (based on proportional and integral control) is used to calculate the valve-lift of these servo valves based on SOPHT inputs.

In SOPHT the SG level is interpolated from “level (m) vs. water volume (m^3)” table. The independent variable is the collapsed water volume in the steam drum node and the downcomer nodes. The same approach as in SOPHT (Table 18) is used in RELAP5 to calculate the actual water level which is then fed to the “feedwater flow controller” together with the “level set-point”, “feedwater mass flow entering the SG”, and “steam mass flow leaving the SG” to control the valve opening.

Table 18 SG water level as a function of water volume

Water Volume (m^3)	Water Level * (m)
0.0	-12.075
7.879	-2.875
16.039	-0.5
18.029	-0.11
106.157	6.02
116.621	6.7
128.2	8.0

*: all the numbers in this column plus 10m yields the actual water level.

The feedwater control valves are designed to fail open, thus in the SBO event these valves will be fully open allowing water to flow by gravity from the deaerator tank to the SG after crash-cooldown. Check valves are used to prevent flow reversal from the SGs and no check valve leakage is assumed since for a majority of the transient the secondary side is at low pressure (i.e., after crash cooling).

A.2.3 Steam Supply & SG Pressure Control

The turbine and the condenser are modeled as time-dependent volumes. In SOPHT the governor is modeled using the “steam valve” with the input “valve position (denoted as frac) vs. reference flow (kg/s)” table (see Table 19). In order to maintain consistency, the five governor valves are modeled as time-dependent junctions with the same “position vs flow” table. The search variable for the table lookup and interpolation is the valve lift calculated by a RELAP5 “steam flow controller”. Similar to the “feedwater flow controller”, the “steam flow controller” responds to the SG pressure error (i.e. difference between the actual SG pressure and the pressure set-point). At full-power steam generator secondary side pressure is controlled at 5050kPa by adjusting the opening of the “Governor Valve”.

In reality, the Emergency Stop Valves will close immediately upon turbine trip. In the RELAP5 model, the Emergency Stop Valves is not modeled explicitly. Turbine isolation is achieved by closing the governor valve after a turbine trip. The valve lifts of these “governor valve” are overwritten to zero (linearly decrease to zero within 0.2s with a delay of 0.08s to mimic the Emergency Stop Valves).

Table 19 Governor Valve position vs. Reference flow in SOPHT

Valve Position (frac.)	Reference flow (kg/s)	Valve Position (frac.)	Reference flow (kg/s)
0.0	0.0	0.4	184.875
0.025	15.406	0.47	246.5
0.05	23.109	0.5	264.988
0.1	36.975	0.55	283.475
0.15	41.597	0.6	295.8
0.2	49.3	0.7	305.044
0.24	52.381	0.75	308.125
0.25	57.003	0.99	311.206
0.3	98.6	1.0	1000.0

Table 20 MSSV Steam Discharge Lookup Table

Pressure (kPa)	Steam Mass flow (kg/s)
5.652e3	0.0
5.653e3	137.4
5.824e3	141.6
5.825e3	283.1
5.996e3	291.4
5.997e3	437.2
6.169e3	449.7
6.170e3	599.7
6.340e3	600.0

The Main Steam Safety Valves (MSSV) are spring loaded pneumatically operable valves designed for overpressure protection of the secondary side. They are also used to initiate auto-depressurization of SGs (often referred to as crash-cooldown). These two functions of MSSVs, i.e. overpressure protection and auto-depressurization, are modeled separately in the RELAP5 model. “Overpressure protection” is modeled using a time-dependent junction similar to the Governor Valve. A table “pressure (kPa) vs. MSSV mass flow (kg/s)” is used in RELAP5 to determine the steam flow through the MSSV in the case of overpressure (see Table 20). “Crash-cooldown” is modeled as a trip valve in the RELAP5 model. The total opening area of MSSVs per SG is assumed to be $0.04m^2$.

In a CANDU plant CSDVs are available they are designed to open after a turbine trip, and ASDVs will only open when the pressure error increases to 270kPa. After the loss of condenser vacuum, CSDVs are no longer available and ASDVs are designed to open when the pressure error is greater than 35kPa (set-point is lowered from 270kPa [12]). Both ASDV and CSDV are controlled by SG Pressure Control (SGPC) if in an AUTO mode. Otherwise they may be manually opened or closed. The valves are designed to close on loss of air supply or loss of both computers or loss of class II control power. In the current modeling, the CDSVs are assumed available only in the first few seconds (to be consistent with [36]), and the ASDVs are available throughout the transient as DC power is assumed available. Sensitivity study on the availability of DC power showed that the results are not significantly altered by the loss of ASDV. If crash-cooldown has been initiated, the loss of ASDV will have no effect on accident progression. However, if crash-cooldown is not credited, the secondary pressure will quickly rise to the MSSV relief set-point following the loss of ASDV and remain nearly constant thereafter.

The same control logic is used in the current RELAP5 model. Both CSDV and ASDV are modeled as time-dependent junctions with lookup tables to determine the steam mass flow through the valves (see Table 21). The ASDV feedback gain on pressure error is 3.33%/kPa and the CSDV feedback gain on pressure error is 0.37%. Thus the CSDV will be fully open when the pressure error reached 270kPa, and ASDV will start to open at pressure error of 270kPa and will be fully open when the error further increases to 300kPa.

Table 21 ASDV and CSDV Steam Discharge Lookup Table

ASDV		**CSDV**	
Valve Position (frac.)	Reference flow (kg/s)	Valve Position (frac.)	Reference flow (kg/s)
0.0	0.0	0.0	0.0
1.0	38.54	1.0	169.87

A.3 Feed & Bleed System

A.3.1 Main Components

The PHTS inventory is maintained by the Feed and Bleed (F&B) system. The system is also used to control the PHTS pressure when the reactor operation is in the solid state (e.g. during warmup or cooldown), or when the pressurizer is out of service. Figure 23 shows a simplified nodalization of the F&B system in the RELAP5 model.

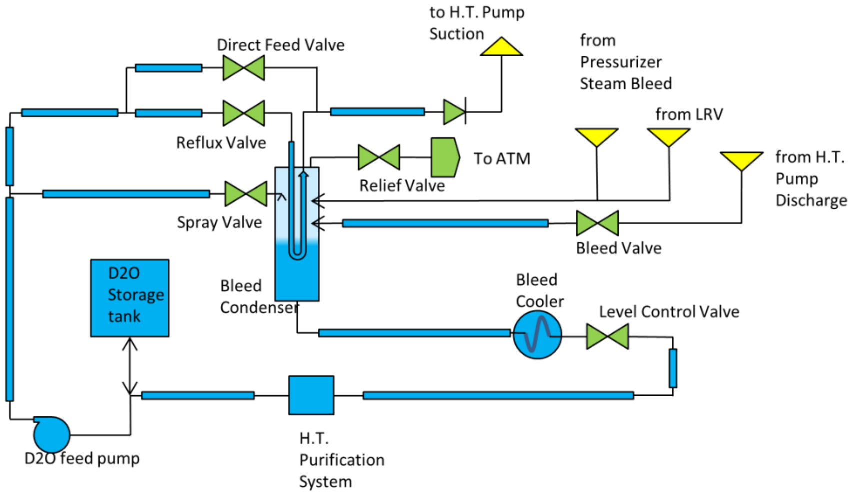

Figure 23 Nodalization of the feed & bleed system

The Bleed Condenser (also called the degasser condenser) accepts coolant discharged from the PHTS via various valves including the LRVs, the pressurizer steam bleed valve, pressurizer relief valve and the bleed valves. The bleed condenser, which has a volume of about 25m^3, is represented by a vertical pipe component with two nodes. Under normal operating conditions, there is constant coolant flow into the bleed condenser from the bleed valves. The coolant leaving the bleed condenser enters the bleed cooler where heat is removed before entering the purification system downstream to prevent damage to the ion exchange column.

The bleed condenser level control valve is modeled as a “servo valve” with a proportional and integral controller that responds the level error in the bleed condenser level (0.9m). The bleed condenser level control valve also has a temperature override which is designed to close the level control valve when the bleed cooler outlet temperature is above a set-point (set to 360K in the current model, SOPHT has a set-point of 71^{o}C). Thus in the case of an SBO where service water to the bleed cooler is lost, the coolant temperature increase very quickly leading to the closure of the level control valve shortly after the initiating event. The bleed condenser level control valve is also designed to fail closed to prevent a potential loss of coolant.

Table 22 Bleed Cooler Heat Removal Rate Lookup Table

Mass flow Rate (kg/s)	Heat Removal Rate (kW)
0.0	0.0
1.0	0.0
10.1	-5680.0
41.25	-2.85e4
1.0e9	-2.85e4

Table 23 Bleed Condenser Tube Design Parameters

Parameters	Value
Number of Tubes (-)	264
Outside Radius (m)	8.0e-3
Inner Radius (m)	5.7e-3
Thermal Conductivity (kW/m-K)	1.659e-2
Specific Heat (kJ/kg-K)	4.438e-1
Density (kg/m^3)	8.43e3

The Bleed Cooler is modeled as a RELAP5 heat structure with heat sink. The heat removed by the bleed cooler is a function of the mass flow rate. Table 22 is the bleed cooler heat removal rate lookup table based on SOPHT. After the loss of power, the heat removal rate of the cooler is overridden to zero.

After leaving the purification system which is represented in the model by normal pipe component, the coolant enters the storage tank located at a high elevation. The D2O feed pump which is located at about 25m below the storage tank then pumps coolant back to the PHTS through the direct feed line and/or the reflux line. The reflux line directs flow through the heat exchanger tubes in the bleed condenser where some heat is taken away by the tube-side reflux flow which is at lower temperature than the coolant in the shell-side bleed condenser. The direct feed line, however, bypasses the bleed condenser to flow back to the PHTS directly. Table 23 summarizes the design parameters of the bleed condenser.

A.3.2 Control Systems

Under normal operating conditions, the bleed condenser pressure is controlled at 1720kPa by varying the bleed valve, feed valve and the reflux valve. Variation of the bleed valve changes the flow rate of the hot coolant entering the bleed condenser, while that of the reflux/feed valve affects the fraction of flow passing through the bleed condenser heat exchanger tubes (thus the heat taken away from the bleed condenser). The bleed, reflux, feed valves are all simulated using the RELAP5 “servo valve” components each with its own proportional and integral controller which responds to the bleed condenser pressure error signal and the pressurizer level signal. In SOPHT similar controllers are used with the following logic:

$$SIG = K_0 + K_1 SIG_1 + K_2 SIG_2$$

Where under narrow range control, "SIG_1" is obtained from bleed condenser pressure error signal, "SIG_2" is determined from pressurizer level error signal; under wide range control (solid mode), "SIG_1" is still the bleed condenser pressure error signal, but "SIG_2" is obtained from H.T. pressure control. Table 24 summarizes the three coefficients for both control modes. With the above controllers, the coolant flow rate bleeding from the HTS and coolant flow rate back to the HTS are varied as such the pressurizer level is maintained at its set-point (currently set to 6.5m in the RELAP5 model).

Table 24 Feed, Bleed and Reflux Valve Control

		K_0	K_1	K_2
Narrow Range Control	Feed	1.8	-0.8	-2.0
	Reflux	1.0	1.0	-2.0
	Bleed	-1.0	0.9	2.0
Wide Range Control	Feed	0.8	-2.0	n/a
	Reflux	1.0	2.0	n/a
	Bleed	-23.6	0.9	-2.0

Table 25 Bleed condenser (BC) relief valve discharge rate lookup table

BC Pressure (kPa)	Volumetric Discharge Rate (m^3/s)
0.0	0.0
10270	0.0
11300	0.17
1.0e9	0.17

In the case of bleed condenser overpressure, additional pressure control is provided by the spray valve and the bleed condenser relief valve. The bleed condenser spray valve has a pressure set-point of 1891kPa, and it cools the bleed condenser by spraying cold fluid into the bleed condenser. The bleed condenser spray valve is modeled as a “servo valve” and is assumed only available during normal operation (i.e. once the SBO trip becomes true the valve gain is overwritten to zero since power supplies to the spray cooling are lost). The bleed condenser relief valve is spring loaded and has a set-point of 10270kPa. After the close of bleed condenser level control valve, the bleed condenser becomes isolated and will be pressurized quickly to the relief valve set-point. The capacity of the bleed condenser relief valve thus determines the maximum pressure of the PHTS. The bleed condenser relief valve is modeled by a RELAP5 “time-dependent junction” similar to the governor valves. A lookup table (Table 25), i.e. “bleed condenser pressure vs. coolant discharge rate”, is used to determine the discharge rate.

A.4 Moderator & Shield Water Cooling Systems

As discussed in the paper [63], the calandria vessel (CV) is modeled as a vertical pipe component with 3, 4, 7 hydraulic cells for the 4, 8, 20-group model respectively. The four large moderator relief ducts are modeled as an average pipe component linked to the top of the calandria vessel.

The volume of relief ducts also accounts for the moderator head tank volume which is important to accommodate the moderator swell during heat-up. The four rupture disks at the ends of the relief ducts are modeled in RELAP5 as a trip valve with a set-point of 239kPa. To be conservative, only one out of four rupture disks is credited, thus the area of the trip valve is set to 0.16417m^2 (i.e. the area of one rupture disk).

The moderator relief valve is designed to prevent the moderator and cover gas pressure from exceeding 165kPa. In the current model, the cover gas system is represented as a pipe component connected to the discharge duct. The relief valve is modelled as a “servo valve”. The relief capacity is determined from the input CSUBV table which contains the forward and reverse flow coefficients as a function of normalized flow area. The flow coefficient when the valve is fully open is estimated to be 270 (gal/min)/(lbf/in^2)$^{0.5}$ which provides about 1.7m^3/s of steam relief capacity at 70kPa(g). The remainder of the moderator and cover gas systems is not modelled since moderator and cover gas circulation is lost as a consequence of the SBO.

The shield tank and the end shields are modeled in a similar way as the calandria vessel (i.e., as a non-uniform diameter vertical pipes). The end shields are connected to the bottom of the topmost node of the shield tank. Thus the water level in the end shields will not change until the water in the shield tank drops to uncover the link between the end shield and shield tank. This will not occur within the scope of this study due to the large water inventory in the shield tank, although such phenomena may become important in the examination of terminal debris-bed cooling. No steam relief is modelled for the shield water cooling system (end shield and shield tank). The rupture disk which is connected to the combined vent line of the shield water cooling system has a burst pressure of 170.2kPa.

Figure 24 shows all the heat transfer pathways in the RELAP5 model. The fuel channel structure consisting of the pressure tube, calandria tube and annulus gap is modeled using the RELAP5 heat structure with its inner surface attached to the fuel channel and the outer surface attached to the corresponding node in the calandria vessel. Similarly, the heat from the end fittings and the lattice tubes to the end shield water is modelled using heat structure with the appropriate linkages. RELAP5 heat structures are also used to represent the tube sheet and the calandria vessel shell so the heat transfer between the end shield and the moderator, and between the moderator and the shield tank are considered. The end shield is filled with light water and steel balls. The steel balls are represented by a heat structure with the heat capacity of Carbon Steel. Table 26 summarizes the design parameters related to these heat structures of the moderator and shield water systems in the current model [65].

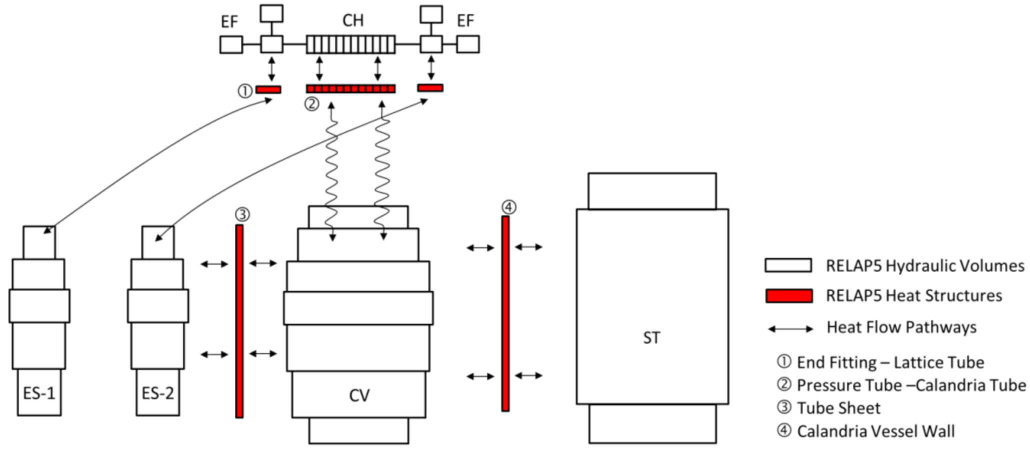

Figure 24 Heat Flow Pathways in the 900MW CANDU Model

Table 26 Moderator and Shield Water System Heat Structures Input Parameters

Parameters	Value	Parameters	Value
End shield diameter (m)	7.741	Subshell length (m)	0.46
End shield thickness (mm)	940	Length of the Core (m)	5.944
Inner tube sheet thick (mm)	76.2	Main/subshell Thick (mm)	29
Outer tube sheet thick (mm)	50.8	CV Main/subshell Material	Stainless Steel
Lattice Tube Number (-)	480	End Fitting Material	Stainless Steel
Lattice Tube Thick (mm)	6.3	End Shield Material	Stainless Steel
Lattice Tube Diameter (mm)	190.5	Steel Ball Material	Carbon Steel
CV Subshell Diameter (m)	7.741	Steel ball diameter (mm)	20
CV Main shell Diameter (m)	8.52		

A.5 Overview of Control Systems

The current RELAP5 input model contains approximately 200 control blocks. Table 27 summarizes the key control systems modeled in the RELAP5 model. The majority of them have been discussed above, thus will not be repeated here. Some of the control systems are used to obtain the steady-state initial conditions of the systems prior to the transient, while some are used to control the valve or heater during the transient.

CANDU reactors have two independent shutdown systems: SDS1 consists of mechanical shutdown rods; SDS2 injects gadolinium nitrate into the moderator. In the current model, only the SDS1 is modeled. The mechanical control absorbers (MCAs) are also modeled and actuated on a turbine trip signal to initiate a reactor step-back. The relevant control logic and safety system set-points used in the model are summarized in Table 28.

Table 27 Control Systems Modeled in RELAP5 model

	through	Target/Set Point	Value
SG Pressure Control	Governor Valve (GV)	Steam Line Pressure	5050kPa
Secondary Side Pressure Relief	MSSV	Steam Line Pressure	5653kPa
	ASDV [1]	Steam Line Pressure	5085 or 5320kPa [2]
	CSDV [1]	Steam Line Pressure	5050kPa
SG Level Control	Feed Water Inlet	SG Level	14.377m
HTS Pressure Control	Pressurizer (Heater & Steam Bleed Valve)	ROH Pressure	9921kPa
HTS Pressure Relief Control	Liquid Relief Valve (LRV)	Control Systems	10551kPa
HTS Loop Isolation	Isolation Valve	ROH Pressure	5.50MPa
HTS Temperature Control	Pressurizer Heater	ROH Temperature	583.5K
HTS Inventory Control	Feed (Reflux) & Bleed	Pressurizer Level	6.5m
Bleed Condenser (BC) Pressure	Feed and Reflux	Bleed Condenser Pressure	1720kPa
	BC Spray valve		1891kPa
	BC Pressure Relief		10270kPa
BC Level	BC Level Control valve	Bleed Condenser Level	0.9m
BC Temperature Override	BC Level Control Valve	Bleed Cooler Outlet T	360K
Calandria Vessel Pressure	Cover Gas Relief Valve	Cover Gas Pressure	165kPa
	Rupture Disks	CV pressure	239kPa
Shield Water System Pressure	Rupture Disks	Shield Tank Pressure	170kPa

1: These set-points for ASDV and CSDV are used in the case of turbine trip

2: If CSDV is available the ASDV open when the pressure error exceeds 270kPa. Otherwise, ASDV open when the pressure error exceeds 35kPa.

Table 28 Reactor Trips Modeled in RELAP5 Model

Reactor Trips	**Target / Set point**	**Value**	**Delay**
SDS1 High Neutron Power	Neutron Power	1.14 frac nom	0.1s
SDS1 High Power Log-Rate	Log Rate	10 %FP/s	0.1s
SDS1 Low HT Flow	Inlet Feeder Flow Rate	0.71 frac nom	0.3s
SDS1 High HT Pressure trip	ROH pressure	10700kPa	0.3s

Table 29 Input Parameters of the RELAP5 Point Kinetic Model

Parameters		Value	Parameters		Value
Total Reactor Power (W)		2.779698e9	Fission Product Yield Factor [2]		1.0
Initial Reactivity		0.0	U-239 Yield Factor [2]		1.0
Beta Over Lambda [1]		6.452328	Fraction of Power by U-235		0.5
Decay Type		ANS-79-3	Fraction of Power by U-238		0.0
Actinide Decay		ON	Fraction of Power by Pu-239		0.5
Delayed Neutron Constants					
GP.	Yield Ratio	Decay Constant	GP.	Yield Ratio	Decay Constant
1	0.050687	6.12e-4	4	0.40378007	0.3175
2	0.20017182	0.03155	5	0.13402062	1.389
3	0.17749141	0.1218	6	0.033848797	3.784

1: Delayed neutron fraction over prompt neutron generation time.

2: 1.0 for best-estimate problems.

A.6 Reactor Power & Heat Load

The reactor power is computed from the RELAP5 point kinetic model which assumes the relative power between each node is preserved, but bulk power changes due to the imposed reactivity. Table 29 summarizes the input parameters for the point kinetic model.

In RELAP5, the decay power model is based on either an ANS Standard proposed in 1973 or on the 1979 ANS Standard for Decay Heat Power in Light Water Reactors. The 1973 proposed standard uses one isotope (U-235) for the fission source and 11 groups for fission product decay [66]. The 1979 standard lists data for three isotopes (U-235, U-238, and Pu-239) and uses 23 groups for each isotope. The ANS79-3, i.e. 1979 ANS Standard data for three isotopes, is used in the current model. Since roughly half the energy output is produced by Pu-239 in CANDU reactors [67], the fractions of power generated in U-235 and Pu-239 are assumed to be 50% and 50% in the RELAP5 model.

Table 30 RELAP5 Calculated Decay and Fission Power

		Normal Operation		10E4 seconds after shutdown	
		Power (W)	Percent of Total	Power (W)	Percent of Total
Decay	Fission Products	1.67586E+08	6.029%	1.33682E+07	76.210%
	Actinides	1.24120E+07	0.447%	4.17301E+06	23.790%
Fission		2.59984E+09	93.525%	4.63233E-20	0.000%
Total		2.77984E+09	100.000%	1.75413E+07	100.000%

Table 31 Heat Load to Moderator and Shield during Normal Operation [68]

		MW	Fission	Decay
To Moderator	Q1-CT	4.3	77.3%	22.7%
	Q2-Guide Tube & Reactivity Mech.	2.7	77.3%	22.7%
	Q3-Moderator	78.6	89%	11%
	Q4-Reflector	5.9	89%	11%
	Q5-Calandria shell to Moderator	0.4	95%	5%
	Q6-Inner Tube Sheet to Moderator	1.4	90%	10%
	Q7-Heat transfer across annulus	3		
	Q8-Heat Loss to Piping	-0.3		
	Q9-Gained From Moderator Pump	0.7		
	Total		82.256MW	11.044MW
		MW	Fission	Decay
To Shield	Q1-Carbon Steel Ball & water in End Shield	0.7	90%	10%
	Q2-Vault water and end shield ring	1	95%	5%
	Q3-Calandria shell to vault water	1.6	95%	5%
	Q4-Inner tube sheet to end shield	0.5	90%	10%
	Q5-Fuel channel to end shield	2.4		
	Total		3.55MW	0.25MW

Table 32 Heat Load Distribution in the 900MW CANDU Model

	Fission	Fission Product Decay	Actinides Decay
To Moderator	4.202%	8.752%	0%
To Shield Water	0.181%	0.198%	0%
To Coolant	95.617%	91.050%	100%
Total	100%	100%	100%

In a CANDU reactor, the actinide decay is mainly from 239U and 239Np. Although, actinide decay amounts to only 0.5% of the power during operation, it accounts for about 20% of the decay power 10E4 seconds after shutdown, and about 30% at 10E5 second [67]. RELAP5 has a built-in actinide decay model which is currently switched on, i.e. power from actinide decay is taken into account. Table 30 shows the RELAP5 calculated powers (fractions) from the three components during normal operation and 10E4 after shutdown.

Aydogdu carried out a heat load calculation for a 2061MW(th) CANDU6 [68], and the results are summarized in Table 31. The relative heat load distributions used in the current model are calculated based on these results and are shown in the Table 32.

A.7 Material Properties

A.7.1 Zircaloy

In CANDU reactors, the pressure tube, calandria tube, and fuel cladding, are made of Zr-2.5%wt-Nb, Zr-2, and Zr-4 respectively. The material properties for these alloy used in the current model are based on references [69] [70] and are summarized in the following sections.

Zr-2 and Zr-4 have similar conductivity. The IAEA recommended thermal-conductivity for these alloys is shown below:

$$k = 12.767 - 5.4348 \times 10^{-4}T + 8.9818 \times 10^{-6}T^2$$

Where k is in W/m-K and T is in K. This equation was obtained from a least squares analysis of the available thermal conductivity data from direct measurements and derived from thermal diffusivity data on Zircaloy-2 and Zircaloy-4 [69]. Figure 25 compares the values of the thermal conductivity obtained from this equation with the Zircaloy-2 and Zircaloy-4 data included in the analysis.

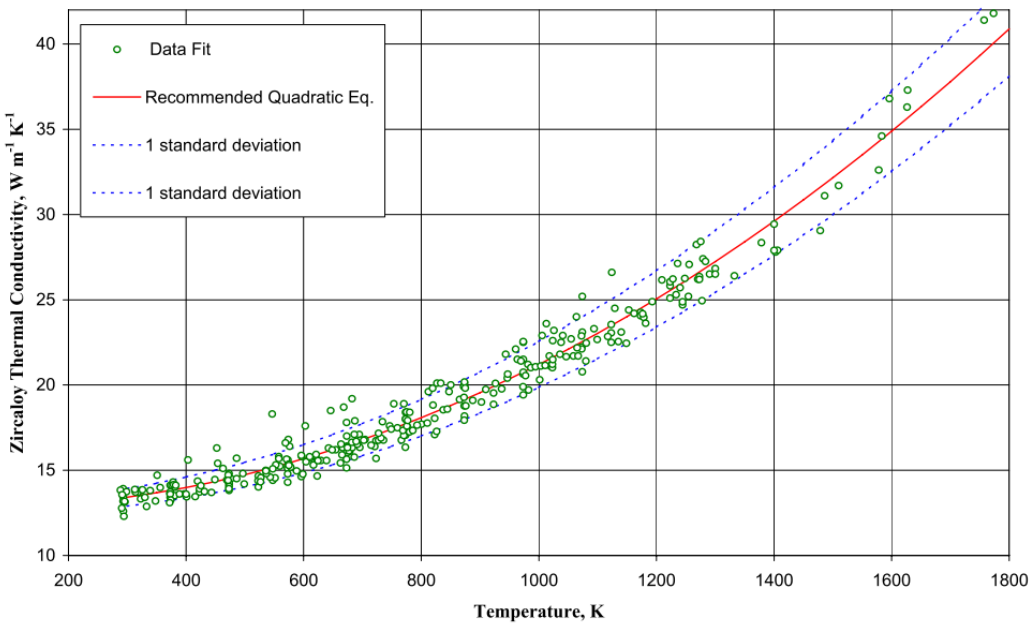

Figure 25 Recommended Equation for Zircaloy thermal-conductivity [69]

For heat capacity of Zircaloy-2, the IAEA recommended equation which is based on least square fits to the available data on the heat capacity of Zircaloy-2 [69] is:

For 273K<T<1100K:

$$C_{p,\alpha} = 255.66 + 0.1024T$$

For 1320K<T<2000K:

$$C_{p,\beta} = 597.1 - 0.4088\,T + 1.565\ \times\ 10^{-4}T^2$$

For phase transition region, i.e. 1100K<T<1320K:

$$C_p = C_{p,\alpha} + f(T) \qquad 1100K \le T \le 1214K$$

$$C_p = C_{p,\beta} + f(T) \qquad 1214K < T \le 1320K$$

$$f(T) = 1058.4 \exp\left[\frac{(T - 1213.8)^2}{719.61}\right]$$

Where temperature is in K and heat capacity is in J/kg-K. Since limited measurements of heat capacity of Zircaloy-4 are available in open literature, the same equations are recommended for Zr-4 in the IAEA report [69].

In the current RELAP5 model, the thermal-conductivity and heat capacity for Zircaloy-2 and Zircaloy-4 are both calculated from the equations in this section.

Zr-2.5%wt-Nb properties are from reference [70]. The recommended equations in the IAEA report are summarized below:

Density (T is in K and ρ is in kg/m^3):

$$\rho = 6657 - 0.2861\,T$$

Heat Capacity (C_p in J/kg-K and T in K):

$$C_p = 221 + 0.172\,T - 5.87 \times 10^{-5} T^2 \qquad 300K \leq T \leq 1100K$$

$$C_p = 380 \qquad 1100K < T \leq 1600K$$

Thermal Conductivity (conductivity in W/m-K, temperature in K):

$$k = 14 + 0.0115\,T$$

The material properties for pressure tube in the RELAP5 model are calculated using the above equations.

A.7.2 UO$_2$

The thermo-physical properties of Solid UO2 that are used in the RELAP5 model are again from reference [70], and are summarized in Table 33.

Table 33 Thermo-Physical Properties of Solid UO2

Temp. (K)	Density (kg/m3)	Conductivity (W/m-K)	Heat Capacity (J/kg-K)	Temp. (K)	Density (kg/m3)	Conductivity (W/m-K)	Heat Capacity (J/kg-K)
300	10.95	7.59	237	1800	10.42	2.12	347
400	10.92	6.58	264	1900	10.37	2.08	359
500	10.89	5.78	281	2000	10.32	2.06	375
600	10.86	5.14	293	2100	10.27	2.07	393
700	10.83	4.61	301	2200	10.21	2.09	415
800	10.79	4.17	306	2300	10.16	2.14	440
900	10.76	3.79	309	2400	10.1	2.2	469
1000	10.73	3.47	311	2500	10.03	2.28	501
1100	10.69	3.19	313	2600	9.96	2.37	538
1200	10.66	2.95	315	2700	9.89	2.48	579
1300	10.62	2.74	317	2800	9.82	2.59	624
1400	10.58	2.56	319	2900	9.74	2.71	673
1500	10.54	2.41	324	3000	9.66	2.84	726
1600	10.5	2.29	329	3100	9.57	2.97	784
1700	10.46	2.19	337	3120	9.56	2.99	796

A.7.3 Other Materials

The conductivity of the annulus gas (CO2) is calculated using the following equation from MATPRO Material Properties Handbook [71]:

$$k = 9.460 \times 10^{-6}\, T^{1.312}$$

The other properties for CO2 used in the model are summarized in the table below:

Table 34 CO2 Thermo-Physical Properties

Temperature (K)	Conductivity (W/mK)	Density (kg/m3)	Heat Capacity (J/kg/K)
300	0.016822	1.8	900
550	0.03726	0.97	1065
700	0.051128	0.76	1139
873	0.068313	0.612	1197
1083	0.090641	0.5	1253
1173	0.100649	0.5	1275
1248	0.109175	0.5	1300
1700	0.163772	0.5	1300
2100	0.216094	0.5	1300
2500	0.271637	0.5	1300

RELAP5 has built-in material properties for Carbon Steel and Stainless Steel. They are used in the current model for corresponding components.

For Inconel 800, constant conductivity and heat capacity are used in the current model, and are 15.64 W/m-K and 3.652e6 J/m^{3}K respectively.

For U-tubes in bleed condenser (material unknown), constant conductivity and heat capacity are assumed. Their properties are from SOPHT input, and are 16.59 W/m-K and 3.741234e6 J/m^{3}K respectively.

Appendix B. Descriptions of Mechanistic Channel Deformation Models in MOD3.6

B.1 Role of New CANDU Models in MOD3.6

A number of mechanistic channel deformation models have been developed and integrated into RELAP/SCDAPSIM/MOD3.6 as new SCDAP subroutines including:

1) Pressure tube ballooning model – BALLON
2) Pressure tube sagging model – SAGPT
3) Fuel channel sagging model - SAGCH

The detailed descriptions of these models and the coupling methods have already been included in the paper in Chapter 4. This appendix mainly presents the information that is not detailed in the paper.

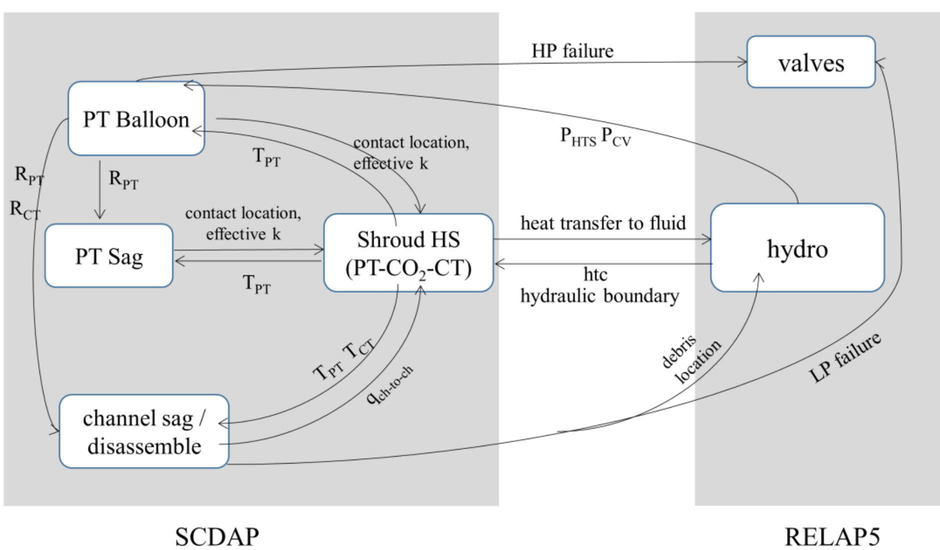

Figure 26 Information Flow Pathways between RELAP5 and SCDAP in the Modified MOD3.6

Figure 26 show the information flow pathways among the new and existing models in MOD3.6. The SCDAP shroud component is commonly used to represent the PT-CT structure in CANDU, thus the new models interact mostly with the existing shroud-related subroutines.

1) "PT Balloon Module (BALLON)" uses the pressures inside and outside the fuel channel (from RELAP5) and the PT temperatures (from SCDAP Shroud) as its input parameters to calculate the hoop strains of the PT, the distances between PT and CT before contact, and the contact conductance after contact. The new gap distance and/or contact conductance at each axial location is converted to the effective conductivity of the annulus gas layer of the shroud component, and is then fed back to "SCDAP Shroud". If the fuel channel is predicted to fail, a channel failure signal is sent to RELAP5 to open a hydraulic valve connecting the fuel channel and the corresponding calandria vessel volume. The pressure tube and calandria radii which are used by the "PT Sag Module" and the "Channel Sag/Disassemble Module" are also updated in this module.
2) "PT Sag Module (SAGPT)" uses the PT temperatures (from SCDAP Shroud) and the PT geometry information (from BALLON) as its main input parameters. It calculates the longitudinal strains of the PT, and determines when and where the pressure tube contacts the calandria tube due to sagging. Similarly, it alters the conductivity of the annulus gas layer at the location of contact to model the contact between PT and CT. Different from BALLON which used a mechanistic method for contact conductance calculation, SAGPT applies a user-input constant contact area and contact conductance to the location of contact.
3) "Channel Sag/Disassemble Module (SAGCH)" uses the PT and CT temperatures (from SCDAP Shroud) and the geometry information (from BALLON) as its input parameters. It tracks the sagging of the entire fuel channel assembly after it is uncovered by the moderator, and predicts when and where the fuel channel sags or disassembles into contact with the lower channel. SAGCH allows both heat and mechanical loads to be transferred between the sagged/disassembled channels and the supporting channels. The mechanical load on the channels are updated every time step which is also used to determine core collapsing. Core collapsing results in the relocation of debris into the calandria vessel bottom, which is modeled in this module by exposing the corresponding heat structure surfaces to the remaining liquid in the calandria vessel. The fuel channel may fail due to excessive sagging, melting, or impingement from the above channel/debris. Similarly, SAGCH will send channel failure signal to RELAP5 to open the valve connecting the channel and the calandria vessel.

B2. Sagging of Fuel Channel Assembly

B.2.1 Governing Equations

The key part of the "Channel Sag/Disassemble Module" is the model used to track the sagging of fuel channel assembly after its uncovery (i.e. SAGCH). In SAGCH, the fuel channel is simplified as a beam with two ends fixed under uniform distributed load "*w*" (Figure 27). The main task of the fuel channel sagging model is to calculate the deflection of the channel due to both elastic and plastic bending.

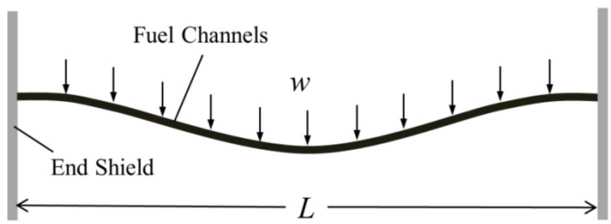

Figure 27 Schematic Diagram for Fuel Channel Sagging Model

<u>*Elastic Component*</u>

Under the given bending moment, $M(x,t)$, the curvature of the beam caused by elastic bending at any location (i.e. *x*) is given by the following equation:

$$K_{el}(x,t) = \frac{M(x,t)}{E(x,t)I(x,t)}$$

in which $I(x, t)$ is the moment of inertia of the pipe, and $E(x,t)$ is the modulus of elasticity which is a function of temperature [72]:

$$E = \begin{cases} 1.088 \times 10^{11} - 5.475 \times 10^{7}T & \text{for } T < 1090K \\ 4.912 \times 10^{10} - 4.827 \times 10^{7}(T - 1090) & \text{for } 1090K \leq T \leq 1240K \\ \max(1 \times 10^{10}, 9.21 \times 10^{10} - 4.05 \times 10^{7}) & \text{for } T > 1240K \end{cases}$$

<u>*Plastic Component*</u>

The longitudinal stress across a section at location *x* where the bending moment is $M(x,t)$ can be expressed as follows:

$$\sigma(x,t) = -\frac{M(x,t)c}{I(x,t)}$$

in which c is the distance to the centroid of the cross-section. The relation between the curvature due to plastic deformation and the plastic strain is:

$$\varepsilon(x,t) = -K_{pl}(x,t)c$$

Thus, the $K_{pl}(x,t)$ can be simplified to:

$$K_{pl}(x,t) = -\frac{\varepsilon(x,t)}{c} = -\frac{\int_0^t \dot{\varepsilon}(x,t)\,dt}{c}$$

In this case, we assume c is the bottom outer fiber of the pipe (i.e. $c = -r_{ct}$). $\dot{\varepsilon}(x,t)$ is the longitudinal creep strain rate given by the following equation (modified from Shewfelt et al. [73] due to the reason explained in Zhou et al. [74]):

$$\dot{\varepsilon} = 8 \times 10^{10}\sigma(t) * \exp\left(-\frac{26670}{T(t)}\right)\left(K_2 - \frac{\varepsilon_c}{\sigma_c}\right)^{2.4}$$

where ε_c is the strain caused by constant stress σ_c under the same temperature transient $T(t)$, i.e.

$$\varepsilon_c = \int_0^t \dot{\varepsilon}_c\,dt = \int_0^t \left[8 \times 10^{10}\sigma_c * \exp\left(-\frac{26670}{T(t)}\right)\left(K_2 - \frac{\varepsilon_c}{\sigma_c}\right)^{2.4}\right]dt$$

The total curvature is then the sum of two components (i.e. elastic curvature and plastic curvature):

$$K_t(x,t) = K_{el}(x,t) + K_{pl}(x,t) = \frac{\frac{d^2y}{dx^2}}{\left[1 + \left(\frac{dy}{dx}\right)^2\right]^{3/2}} \approx \frac{d^2y}{dx^2}$$

Once $K_{el}(x,t)$ and $K_{pl}(x,t)$ are known, deflection y can be calculated by integrating twice the curvatures along *x*.

Bending Moment & Boundary Conditions

The bending moment of a beam with two fixed ends is the sum of moment due to applied loads and the moment due to support. Assuming that the two moments at the left and right ends are M_l *and* M_r, respectively, and the total length is *L*, the bending moment at location *x* is:

$$M(x) = -\frac{wx^2}{2} + \frac{wLx}{2} + M_l + \frac{M_r - M_l}{L}x$$

M_l and M_r may not be the same (due to asymmetrical temperature distribution). Two boundary conditions are used to solve for M_l and M_r: first, the tangents to the curve at both ends are horizontal; second, the deflections at two ends are zero.

The first boundary condition can be interpreted as follows:

$$\Delta\theta = \int_0^L K_{el}(x,t) + K_{pl}(x,t)\,dx = 0$$

i.e. the change of slope from one end to the other is zero. Similarly, the second boundary condition is:

$$\Delta y = \int_0^L \left[K_{el}(x,t) + K_{pl}(x,t)\right](L-x)dx = 0$$

i.e. the change of elevation from one end to the other is zero. M_l and M_r can be determined by solving the above two equations.

B.2.2 Discretization of Governing Equations

To solve the above equations, the beam is first discretized into a total of "N" cells. The curvature due to plastic bending (K_{pl}) is assumed to be uniform within each cell, and is calculated with the creep strain of previous time step as discussed earlier, i.e. $K_{pl,i} = \frac{\varepsilon_i}{r_{ct}}$, in which "$i$" is the cell number. Thus, the two equations $\Delta\theta$ and Δy can be discretized as follows:

$$\Delta\theta = \int_0^L K_{el}(x,t) + K_{pl}(x,t)\,dx = \sum_{i=1}^{N}\left[\int_{x_i}^{x_{i+1}} \frac{M(x,t)}{E_i I_i}dx + K_{pl,i}(x_{i+1} - x_i)\right] = 0$$

$$\Delta y = \int_0^L \left[K_{el}(x,t) + K_{pl}(x,t)\right](L-x)dx$$
$$= \sum_{i=1}^{N}\left[\int_{x_i}^{x_{i+1}} \frac{M(x,t)}{E_i I_i}(L-x)dx + \int_{x_i}^{x_{i+1}} K_{pl,i}(L-x)dx\right] = 0$$

Substitute the equation of $M(x)$ into them and rearrange yields:

$$\begin{cases} a_1 M_l + b_1 M_r = c_1 \\ a_2 M_l + b_2 M_r = c_2 \end{cases}$$

in which $a_1, b_1, c_1, a_2, b_2, c_2$ are constants, and are given by the following equations:

$$a_1 = \sum_{i=1}^{N} \frac{(x_{i+1} - x_i)}{E_i I_i}\left(1 - \frac{x_{i+1} + x_i}{2L}\right)$$

$$b_1 = \sum_{i=1}^{N} \frac{(x_{i+1} - x_i)}{E_i I_i} (\frac{x_{i+1} + x_i}{2L})$$

$$c_1 = \sum_{i=1}^{N} \left[\left(\frac{wx_{i+1}^3}{6} - \frac{wLx_{i+1}^2}{4} \right) \frac{1}{E_i I_i} - \left(\frac{wx_i^3}{6} - \frac{wLx_i^2}{4} \right) \frac{1}{E_i I_i} - K_{pl,i}(x_{i+1} - x_i) \right]$$

$$a_2 = \sum_{i=1}^{N} \frac{1}{E_i I_i} \left[\left(x_{i+1}^2 - \frac{x_{i+1}^3}{3L} - Lx_{i+1} \right) - \left(x_i^2 - \frac{x_i^3}{3L} - Lx_i \right) \right]$$

$$b_2 = \sum_{i=1}^{N} \frac{1}{E_i I_i} \left[\left(\frac{x_{i+1}^3}{3L} - \frac{x_{i+1}^2}{2} \right) - \left(\frac{x_i^3}{3L} - \frac{x_i^2}{2} \right) \right]$$

$$c_2 = \sum_{i=1}^{N} \frac{1}{E_i I_i} \left[\left(-\frac{wLx_{i+1}^3}{3} + \frac{wL^2 x_{i+1}^2}{4} + \frac{wx_{i+1}^4}{8} \right) - \left(-\frac{wLx_i^3}{3} + \frac{wL^2 x_i^2}{4} + \frac{wx_i^4}{8} \right) \right] + \sum_{i=1}^{N} K_{pl,i} \left[\left(Lx_{i+1} - \frac{x_{i+1}^2}{2} \right) - (Lx_i - \frac{x_i^2}{2}) \right]$$

The above two linear algebraic equations are solved for the two unknowns M_l and M_r. The deflection at location x_j (in which *j* is the node number) then can be calculated using the following equation:

$$\Delta y_i = \sum_{i=1}^{j} \frac{x_j}{E_i I_i} \left[\left(-\frac{wx_{i+1}^3}{6} + \frac{wLx_{i+1}^2}{4} + M_l x_{i+1} + \frac{(M_r - M_l)x_{i+1}^2}{2L} \right) - \left(-\frac{wx_i^3}{6} + \frac{wLx_i^2}{4} + M_l x_i + \frac{(M_r - M_l)x_i^2}{2L} \right) \right] - \sum_{i=1}^{j} \frac{1}{E_i I_i} \left[(\frac{wLx_{i+1}^3}{6} - \frac{wx_{i+1}^4}{8} + \frac{M_l x_{i+1}^2}{2} + \frac{(M_r - M_l)x_{i+1}^3}{3L}) - \left(\frac{wLx_i^3}{6} - \frac{wx_i^4}{8} + \frac{M_l x_i^2}{2} + \frac{(M_r - M_l)x_i^3}{3L} \right) \right] + \sum_{i=1}^{j} K_{pl,i} \left[\left(x_j x_{i+1} - \frac{x_{i+1}^2}{2} \right) - \left(x_j x_i - \frac{x_i^2}{2} \right) \right]$$

B3. Sagging of Pressure Tube

Except for the support at the two ends, the pressure tube is also supported at the four garter springs (Figure 28). The same approach is used to model the sagging of the pressure tube. To simplify the model, the two pressure tube ends are assumed to be fixed, i.e. no axial displacement or rotation is allowed, and the supports from garter springs are assumed to be rigid. This results in a total of six unknowns corresponding to six bending moments at the six supporting locations (i.e. the two ends and four garter springs).

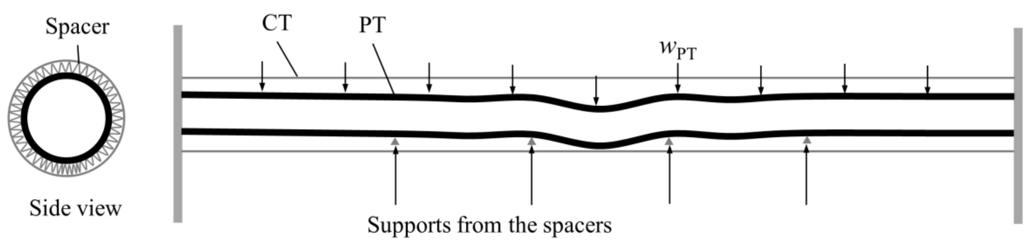

Figure 28 Schematic Diagram for Pressure Tube Sagging Model

To solve for the six unknowns, the following boundary conditions are used:

$$\Delta\theta = \int_0^L K_{el}(x,t) + K_{pl}(x,t)\, dx = 0$$

$$\Delta y_i = \int_0^{L_i} \left[K_{el}(x,t) + K_{pl}(x,t)\right](L_i - x)dx = 0 \qquad i = 1,2,3,4,5$$

$L_{1,2,3,4}$ are the distances from each of the four garter springs to the left end, respectively. L_5 is the distance from the right end to the left end (i.e. $L_5 = L$). The above two equations can be interpolated as follows:

1) Equation of $\Delta\theta$ (one): the change of slope from one end to the other is zero (since the two ends are assumed to be fixed).
2) Equations of Δy_i (five): no vertical displacement is allowed at the garter springs as well as at the two ends (since all supports are assumed to be rigid).

The equations are discretized using the same approach as introduced in the previous section (thus will not be repeated). Again, $K_{pl}(x,t)$ is determined from the PT longitudinal creep strain of previous time step. This results in six linear algebraic equations in the following form:

$$\sum_{j=1}^{6} a_{ij} M_j = c_i \qquad i = 1,2,3,4,5,6$$

in which a_{ij} and c_i are constants, and $M_{1,2,3,4,5,6}$ are the bending moments at the six supporting locations. These linear equations are then solved using the Gauss-Elimination method. Once $M_{1,2,3,4,5,6}$ are known the bending moment $M(x)$, and the deflection at any location can be calculated.

Appendix C. Simulation of Cold Water Injection Test

The above RELAP5 model for the 900MW CANDU was well validated against station data at Darlington NGS. The station data used in the paper, however, do not cover the relevant IBIF conditions. Concerns have been raised that there is a lack of validation of the RELAP5 code on IBIF under CANDU conditions. The purpose of this separate study is thus to further validate RELAP5 by simulating the IBIF phenomena in the two “standing-start” tests from the Cold Water Injection Test (CWIT) facility. In these two selected tests, a single CANDU fuel channel was heated up from stagnant conditions until venting was initiated.

B.1 Description of Test Facility and RELAP5 Model

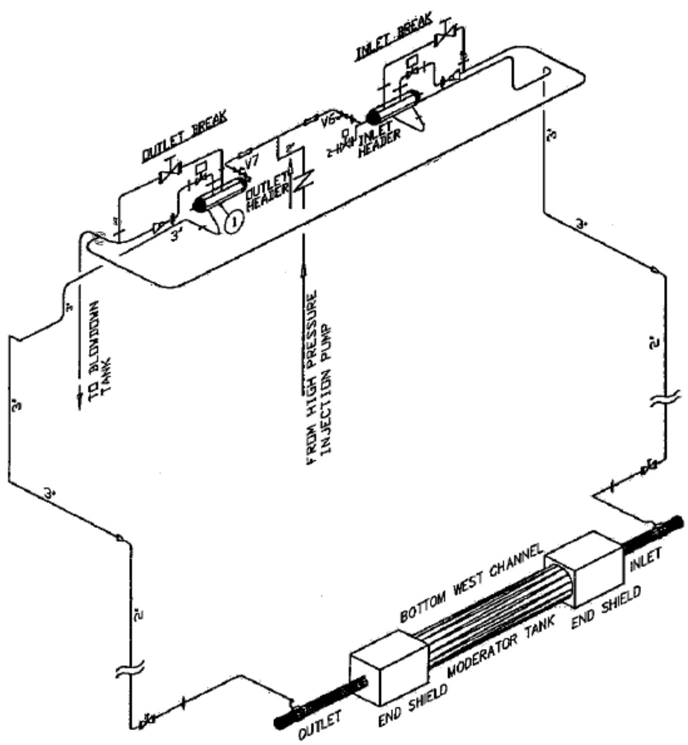

Figure 29 Schematic of the CWIT Facility

A simplified schematic of the experimental loop of the CWIT facility is shown in Figure 29. The loop consists of a fuel channel assembly of identical geometry as a real CANDU fuel channel. The fuel channel includes the electrically heated fuel element simulator (FES), a flow tube (simulating the pressure tube) and the full-scale CANDU end fittings (with modification made to allow the passage of the FES unheated extensions). The inlet and outlet headers are located approximately 10m above the channel.

Table 35 Experimental Conditions of the Selected CWIT Standing-Start Tests

Experiment	Header Pressure (kPa)	Initial Temperature (℃)	Channel Power (kW)	Saturation Temperature (℃)
#1613	2000	30	131	214.9
#1617	7000	30	20 [a]	286.8

a: the channel power in table 6 of reference [75] is 30kW which appears to be a typo and is inconsistent with its context.

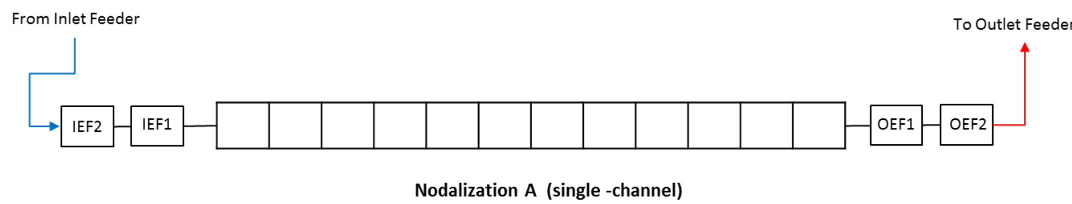

Figure 30 Nodalization of Fuel Channel in RELAP5 (One-Path)

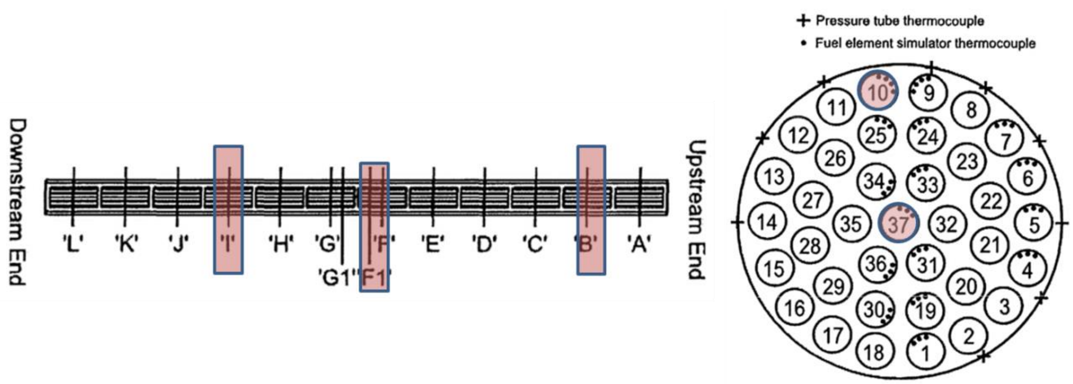

Figure 31 CWIT Thermocouple Location – Planes and Cross-section

Data of the two selected "standing-start" tests were from Spencer's Master thesis [75] in which the tests were simulated using the containment thermal-hydraulic code GOTHIC. The experimental conditions of these two tests are summarized in Table 35. In these two tests, the fuel channel was heated up by the FES from stagnant condition until venting was initiated.

A “One-Path” model (see Figure 30) was first developed using RELAP5/MOD3.3. The geometry, material properties, mass of the test section used in the model are consistent with Spencer’s work [75]. The fuel channel is represented by a horizontal pipe component with 24 nodes, and each end fitting volume by two horizontal pipes with a total of 6 nodes. The center pin and three rings of the FES were modeled each as a RELAP5 heat structure with the radial depression ratio of 1: 0.81: 0.72: 0.68 (from outer to the center pin). The unheated parts, i.e. the pressure tube, the end fitting dead body, the FES extension, and the liner tube, are also included in the model since their presence in the channel is expected to significantly delay the heat-up of fuel channel. They are represented by the RELAP5 heat structures. The feeder pipes are represented in RELAP5 by a combination of vertical and horizontal pipes with the geometry, pipe roughness and minor loss factors taken from Spencer’s thesis (i.e. table 9 and table 35 through 38 in reference [75]). Figure 31 shows the thermocouple location in the CWIT. The comparison between RELAP5 predictions and experimental measurements are made for Pin #10 and #37 on Plane I, F1, and B as marked in maroon (Figure 31).

B.2 Results and Discussion

Test #1613 with a header pressure of 2.0MPa and a channel power of 131kW (Table 35) was first simulated using the “One-Path” model described above. To examine the contributions from the unheated parts (i.e. the pressure tube, the end fitting dead body, the FES extension, and the liner tube) two cases were simulated: in case HP1 the unheated heat structures were removed from the RELAP5 model, while in case HP2 all the unheated heat structures were included. Figure 32 shows the predicted cladding surface temperatures of Pin #10 (Left) and Pin #37 (Right) at Plane F1 in these two cases along with the measured temperatures.

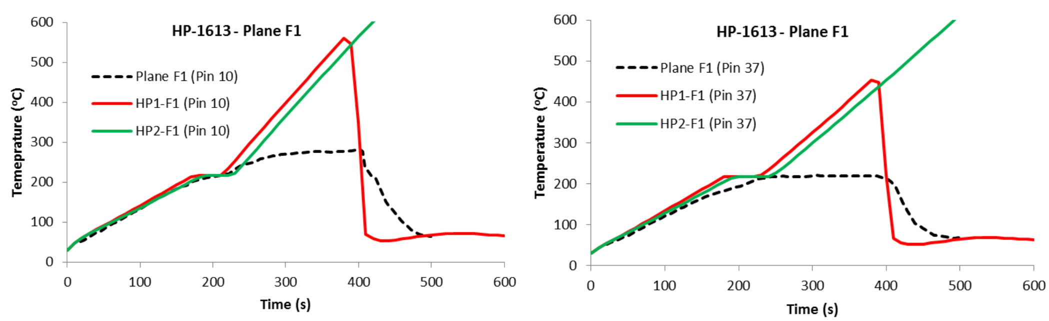

Figure 32 Measured (dash) and Predicted Temperature at Pin #10 (Left) and Pin #37 (Right) of Plane F1 by One-Path Model (HP1: without unheated parts, HP2: with all unheated parts)

In this experiment, the temperatures of fuel pins initially increased linearly until the coolant was heated up to saturation point (214.9^{o}C), and then the temperatures remained nearly constant for a short period of time until the fuel pins were uncovered. Vapor generation first commenced in the middle of the fuel channel. With the accumulation of vapor, a giant bubble or vapor space started to develop along the top of the fuel channel. The top fuel pins (e.g. Pin #10) in the middle of the channel (e.g. Plane F1) soon became uncovered. Subsequently, the increase in fuel temperatures was resumed for these uncovered fuel pins. However, the measured surface temperatures of these pins only exceeded the water saturation temperature by a small amount before venting was initiated, suggesting that some froth or spray was present throughout the steam. At around 400s, venting was initiated quickly cooling down the fuel channel.

The pin temperatures predicted by RELAP5 closely follow the measured temperature curves until pin exposure (Figure 32). After pin exposure the code predicted nearly adiabatic heat-up rate. In case HP2 with the presence of unheated parts, venting was delayed significantly to about 1100s (as opposed to 400s in experiment). As discussed in the paper in Chapter 3, the RELAP5 has limitation in tracking liquid level in horizontal channel. When a node of the horizontal pipe is half-voided, RELAP5 does not discriminate the fuel pins at different elevations, and the same nucleate boiling correlation is utilized for all the fuel pins until the fuel bundle is almost completely uncovered. This limitation, however, is expected to cause the underestimation of venting time (as the heat deposited into the coolant is overestimated). The delayed venting predicted by RELAP5 is thus contrary to the expectation, and suggests that other factors are playing more important roles.

After artificially removing all the unheated heat structures (most of them are in the end fittings), venting in case HP1 occurred much earlier and at almost the same time as in experiment (Figure 32). This implies that the heat-up of the end fittings may be not modeled properly by RELAP5. As described in the paper in Chapter 3, the large vapor space during an IBIF cycle grows from the channel center to the end fittings and eventually reaches one of the vertical oriented feeder pipes. The vertical pipe then provides a flow path for the low density vapor to rise initiating the venting process. In this test (i.e. test #1613), fuel channel was heated up from an initial temperature of 30^{o}C (high subcooled condition). The coolant and all the unheated parts in the end fittings were likely to be significantly subcooled when the vapor first entered the end fittings. Therefore, vapor condensation in the end fitting is expected, and is likely to delay the channel venting. However, the end fitting is a fairly large diameter pipe. The thermocouple measurements suggested that the vapor after migrating from the fuel channel to the end fitting stayed in the top portion of the end fitting due to gravity creating a top-down temperature gradient (i.e. the top portion was at near saturation temperature while bottom was subcooled). The vapor thus was able to enter the feeder to initiate venting before the entire end fitting was heated up to saturation. RELAP5 using volume averaging is not able to capture this effect, and predicts venting when the entire end fitting is heated up to near saturation. This partly explains the overestimation of venting time in case HP2.

Careful examination of the predicted results shows that RELAP5 also has issue in predicting the counter-current flow in the fuel channel during the vapor generation phase of an IBIF cycle. In reality, when the coolant is horizontally stratified the steam being generated will flow in the top portion of the channel towards the end fittings. Liquid in the bottom of the channel but close to the two-phase interface will experience a shear force from this vapour flow and hence may tend to move in the same direction towards the end fittings. However, liquid near the bottom of the channel will be sustained in the opposite direction (towards the center of the channel) through gravitational effects. Therefore, within the liquid there is a velocity gradient which spans both positive and negative values. RELAP5 as a one-dimensional (1-D) code is incapable of predicting such velocity gradient. Figure 7 shows the predicted void fraction distributions along the fuel channel (including end fittings) at different times before venting is initiated in case HP1. It can be seen that RELAP5 predicts “liquid starvation”, i.e. the liquid in the end fitting failed to replenish the centre of the channel where vapor is being generated. The fuel bundles in the centre thus experience prolonged complete dryout and nearly adiabatic heat-up as soon as all the liquid in the corresponding nodes is boiled off. The failure of the code in predicting liquid replenishment leads to the underestimation of vapor generation which in turn contributes to the delay in channel venting.

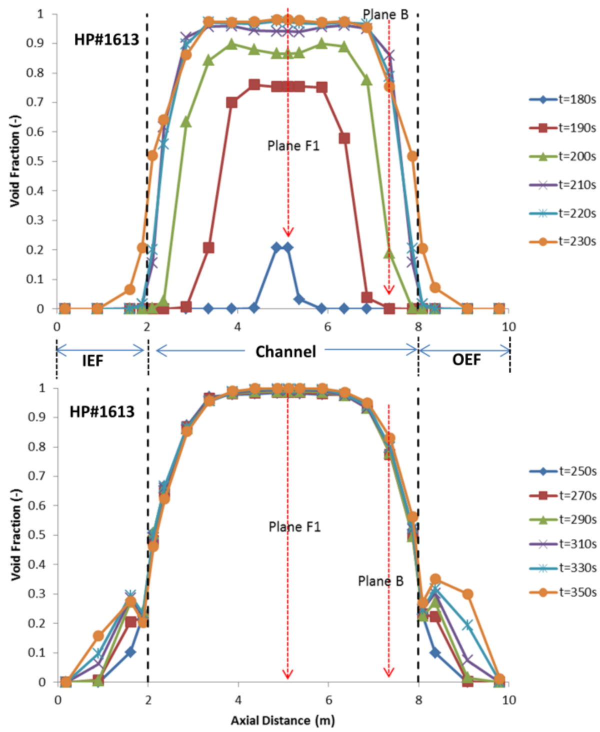

Figure 33 Void Fraction Distributions along Fuel Channel at Different Times Predicted by One-Path Model in Case HP1

B.3 Sensitivity Studies

B.3.1 Sensitivity to Channel Nodalization

The discrepancies between the RELAP5 predictions and the experiments are attributed to 1-D nature of the RELAP5 code. To confirm the proposed explanation and further investigate this issue, a sensitivity study of channel nodalization has been carried out. In this study, two additional RELAP5 models were created in which the fuel channel (including the end fittings) was vertically divided into two and four flow paths respectively (Figure 34).

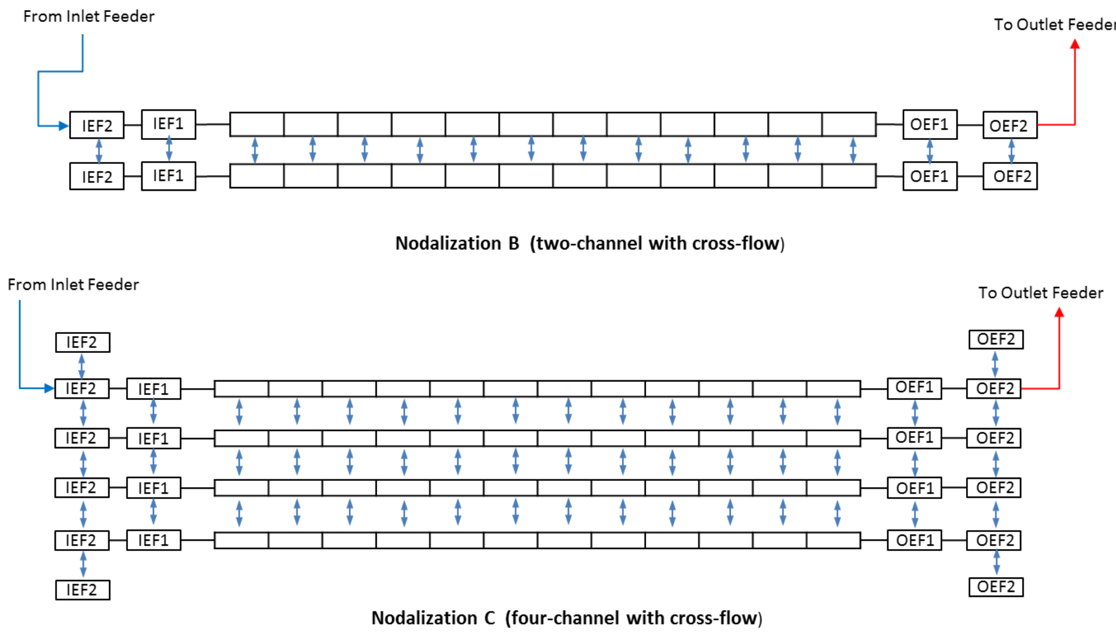

Figure 34 Nodalization of Fuel Channel in RELAP5 (Sensitivity Cases – Multi-Path)

The flow paths were connected via cross-flow junctions at every axial node along the channel. The heat structures (including FES and the unheated parts) were divided carefully according to their fractions in each flow path. Some parts (e.g. pressure tube) were artificially divided into two or more pieces, while the circumferential heat conduction in these parts was not taken into account. The nodalization of the feeder pipes and headers remained unchanged (i.e. identical to "Nodalization A" in Figure 30). Test #1613 and #1617 (Table 35) were then simulated with nodalization B (two flow paths) and nodalization C (four flow paths). Since the following comparisons are made only for pin #10 and #37, it is useful to note that pin #10 is located in the highest flow path in both B and C nodalization, while pin #37 (center) is artificially divided into two halves with the top located path 1 and the bottom in path 2 in the 2-path model (or path 2 and 3 for the 4-path model).

The results are shown in Figure 35 through Figure 38. The two-path and the four-path models show significant improvement over the one-path model. The four-path model appears to be superior to the two-path one with very good agreement between the code predictions and the measured temperatures (Figure 36 and Figure 38).

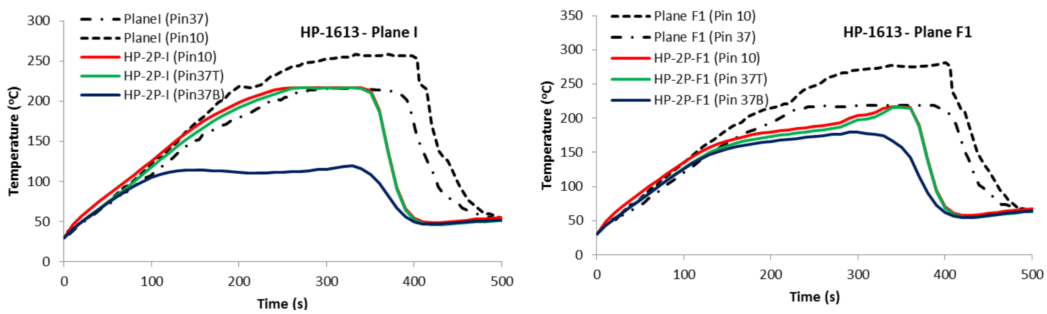

Figure 35 Temperatures Predicted by Two-Path Model at Plane I (Left) and F1 (Right) in Test-1613

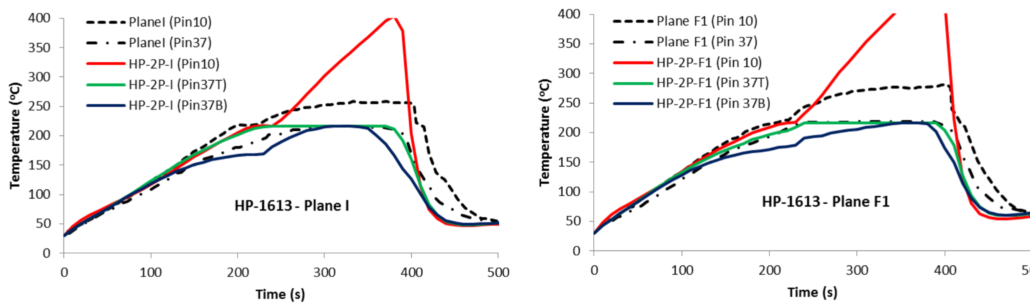

Figure 36 Temperatures Predicted by Four-Path Model at Plane I (Left) and F1 (Right) in Test-1613

In the high-power case (i.e. test #1613), the venting predicted by the two-path model is slightly earlier than observed in experiment. Due to improper flow path division, the two-path model fails to predict the temperature transient for the high-elevation pin (i.e. pin #10) (Figure 35). In the experiments, Pin #10 was already exposed to superheated steam before venting was initiated, thus its surface temperature went about 50^{o}C above the water saturation temperature. In the two-path model, pin #10 is located in the top half of the fuel channel (thus the top flow path in nodalization B), which does not go to complete dryout. In addition, RELAP5 has limitation in tracking liquid level in horizontal channel. Therefore, Pin #10 is never “exposed” to steam throughout the transient. The same nucleate boiling correlation is applied to all the pins at the top half of the channel.

This limitation was overcome by further dividing the channel into four paths (Figure 36). The higher cross-sectional resolution in the vertical direction allows pin #10 to be uncovered during the transient. The corresponding nodes in the highest flow path of nodalization C are completely voided. However, after pin uncovery the four-path model predicts nearly adiabatic heat-up resulting in the overestimation of pin #10 temperature. This implies that RELAP5 still has issue predicting the correct “frothy” heat transfer for those exposed fuel pins (Figure 36). The venting time is correctly predicted by the four-path model.

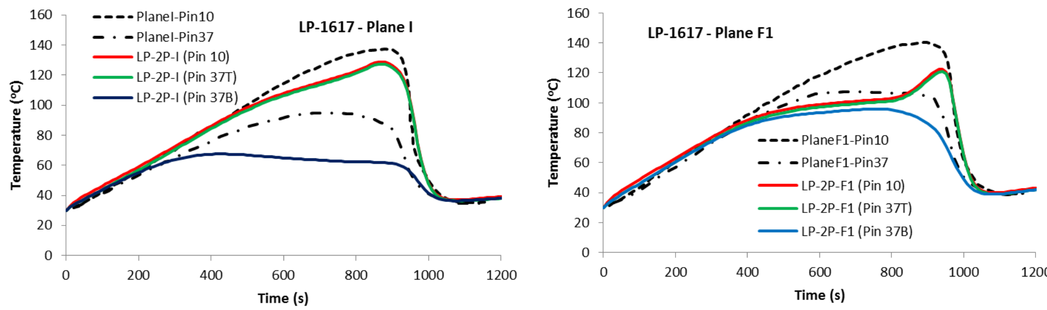

Figure 37 Temperatures Predicted by Two-Path Model at Plane I (Left) and F1 (Right) in Test-1617

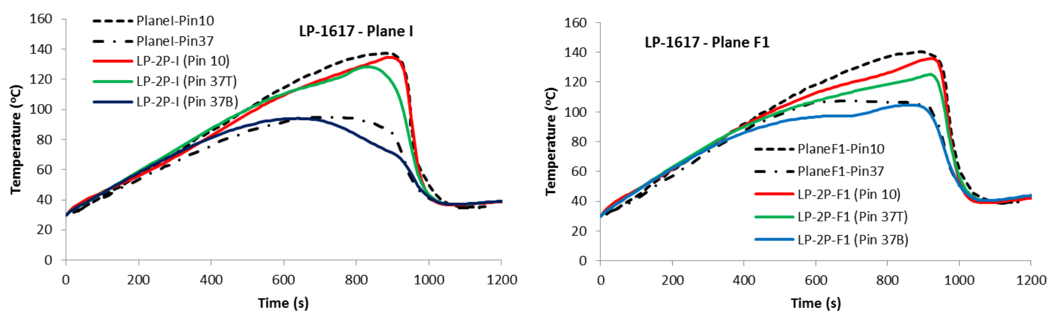

Figure 38 Temperatures Predicted by Four-Path Model at Plane I (Left) and F1 (Right) in Test-1617

In test #1617 the input channel power was lowered to 20kW, and the header pressure was raised to 7.0MPa. In the experiment, venting occurred before the bulk fluid temperature reached saturation (286.8^{o}C). The coolant thus remained single-phase throughout the IBIF cycle. Similar to the two-phase IBIFs that normally occur at higher powers and/or lower pressures, venting in this test was initiated when the hot coolant (lower density liquid) reached one of the two end-fitting-to-feeder connections and rose. Both the two-path and four-path models perform well in reproducing the experiments (Figure 38).

In conclusion, the multi-flow-path approach is successful in overcoming the RELAP5 limitations in predicting multi-dimensional flow phenomena during IBIFs. By vertically dividing the fuel channel and end fittings into parallel flow paths the top-to-bottom temperature gradient and the bi-directional flow (i.e. steam moves from the center towards the end fitting while liquid from the end fitting moves in the opposite direction to replenish the channel) are allowed to occur in the modeling. This sensitivity study thus backs up the discussions in the paper and the above section.

B.3.2 Sensitivity to Initial Coolant Conditions

The above discussion confirmed that vertically dividing the fuel channel into a number of flow paths can significantly improve the performance of RELAP5 in predicting the IBIFs. While such nodalization is possible in the single-channel analysis, it will significantly increase the computational cost in the case of a full-plant simulation. Besides, the fluid conditions after crash-cooldown during SBO are very different from these of the "standing-start" tests. The PHTS pressure is low and the temperature of coolant is at near saturation following crash-cooldown. The length of the IBIF cycle is expected to be much shorter and on the order of 10s (as opposed to 100s in the standing-start tests at CWIT).

To investigate the necessity of splitting the fuel channel in the full-plant simulation, additional sensitivity cases have been simulated with the above one-path, two-path, and four-path models (i.e. nodalization A, B, and C respectively) while employing the post-crash-cool conditions from a selected SBO transient as the initial conditions (Table 36). Unlike the above "standing-start" CWIT tests where the initial coolant temperatures were uniform, the post-crash-cool conditions are taken at the end of an IBIF cycle when the channel has been replenished after venting and the coolant is nearly stagnant. Coolant temperature distribution is axially non-uniform along the fuel channel with slightly higher temperature at the inlet as a result of the previous venting direction, i.e. reversed from outlet to the inlet.

Table 36 Post-Crash-Cool Conditions from a Typical SBO Transient [a]

	RIH	ROH	IEF	OEF	Channel
Pressure (kPa)	305.5	305.5	400.0	400.0	400.0
Temperature (K)	399.8	388.5	398.8	388.2	397.5 – 388.2 [b]

a Input channel power was 69.3kW

b The saturation temperature at 400kPa is 416K.

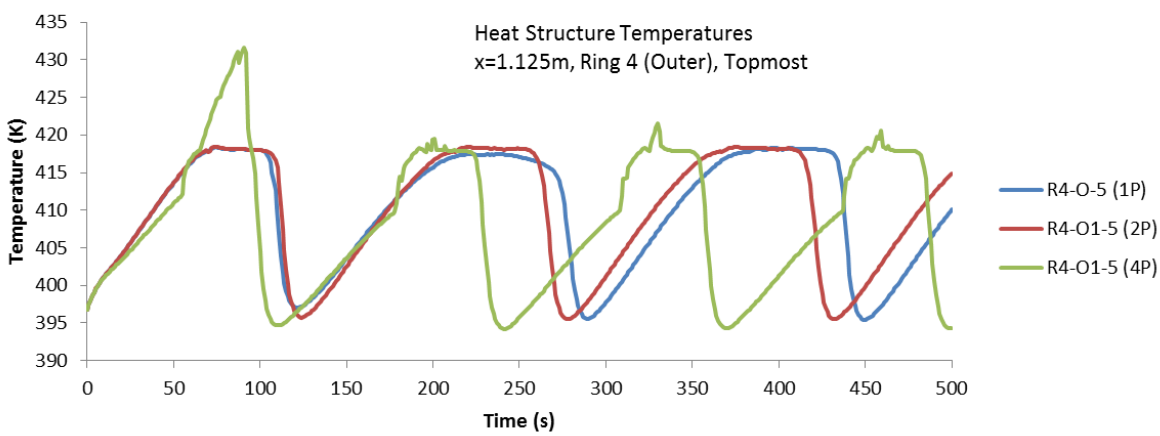

Figure 39 Temperatures of Topmost Pin of Outer Ring at Axial Location x=1.125 Predicted by 1-Path (1P), 2-Path (2P) and 4-Path (4P) Models

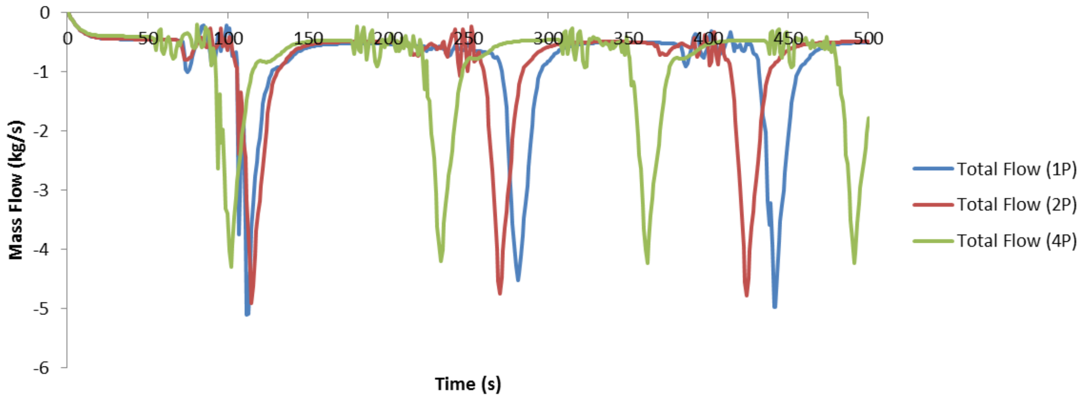

Figure 40 Channel Mass Flow in the Channel Predicted by 1-Path (1P), 2-Path (2P) and 4-Path (4P) Models

The predicted heat structure temperature at selected "preferred dryout" location (i.e. x=1.125m with relatively high power and closer to the channel inlet where temperature is closer to saturation) and the channel mass flow rate are shown in Figure 39 and Figure 40 respectively. At lower pressure and/or lower subcooling the length of IBIF cycle is much shorter. Within the simulated 500s IBIF occurs periodically with more than three cycles observed.

The venting times and the fuel sheath temperature predicted by the three models are not very different under post-crash-cool conditions. Although, RELAP5 has several limitations as discussed above especially with the 1-Path nodalization (e.g. failure to capture the countercurrent flow accurately during the stagnation phase, and failure to predict the correct temperature excursion after pin exposure), the errors are mitigated by the short length of IBIF cycle and the large returning flow at the end of the cycle. As discussed in the paper in Chapter 3, the presence of other channels in parallel connected to the same headers tends to further increase the IBIF frequency. Thus, the sheath temperature deviations in the full-plant simulation with simplified channel nodalization are expected to be small.

Another important observation is that the venting direction is always consistent with the previous venting. This is because the direction of venting is determined by the initial axial temperature gradient (as vapor develops faster at the hotter end) which is in turn determined by the venting direction of the previous IBIF cycle. This also explains why venting tends to occur in the same direction periodically in the full-plant SBO transient in Chapter 3.

Appendix D. Validation of MOD3.6 against CANCHAN Tests

RELAP5/SCDAP code which was originally designed for LWRs has been increasingly used for CANDU reactors. A new version of the code, MOD3.6 is being developed to support the severe accident analysis for PHWRs. A number of mechanistic deformation models for several key severe accident phenomena in CANDU have been developed and integrated into the SCDAP part of MOD3.6 as discussed in Chapter 4. However, the code has not been validated against CANDU specific thermal-chemical experiments. In order to validate MOD3.6 for severe accident conditions where heat is only removed by steam and moderator, the CHAN 28-element series was selected for benchmark. A total of three tests (i.e. CS28-1, CS28-2, and CS28-3) were performed for the 28-element geometry.

C.1 Description of the Experiments

To improve the understanding of CANDU fuel bundle behavior under severe accident conditions and to provide validation data for high-temperature thermal-chemical codes such as CHAN-II and CATHENA, the CHAN thermal-chemical experimental program was carried out at AECL Whiteshell Laboratories. Several series of experiments, progressing from a single fuel element simulator [76], to seven elements [77] and finally to 28 elements [78][79][80], were performed. In those experiments, preheated steam was supplied at constant rate and constant temperature to a test section which typically consists of a pressure tube, fuel element simulator (of single-element, seven-element or 28-element type), and cooling jacket (in some tests a calandria tube and a water tank). Power was supplied to the fuel element simulator (FES) to raise the cladding temperature beyond the zirconium-steam reaction temperature. Power was normally turned off before the surface temperature reaches the zirconium melting temperature (~1765^{o}C). In some tests, the exothermic Zr-steam reaction was self-sustaining and the maximum temperature exceeded the melting temperature until the steam supply was turned off. The surface temperatures at various locations of the FES and pressure tube were measured by thermocouples throughout the tests. Hydrogen generation, steam / cooling water outlet temperature, and pressure were continuously tracked. These tests have been used to validate computer codes, such as CHAN-II [76][77][81][79], CATHENA [82][83], and CFD tools [84][85][86].

Figure 41 shows the experimental apparatus in one of the 28-element tests (CS28-3). Figure 42 shows the cross-sectional view of the test sections in these three tests which only differ in the types of external cooling and the pressure tube used. In the first two experiments (CS28-1 and CS-

28-2), the calandria tube was surrounded by an open tank of water to provide reactor-typical cooling on the external calandria tube surface. In the third test (CS28-3), the water tank was replaced by a cooling water jacket to reduce the uncertainty in determining the radial heat removal by external water. CS28-1 and CS28-3 both used an un-crept pressure tube, while CS28-2 used partially ballooned pressure tube. CS28-1 and CS28-3 were selected for the benchmark of SCDAP code since SCDAP does not solve heat conduction in the circumferential direction, and RELAP5 as a 1-D code is expected to have difficulties in predicting the steam bypass in a ballooned pressure tube. Table 37 summarized the test conditions in CS28-1 and CS28-3.

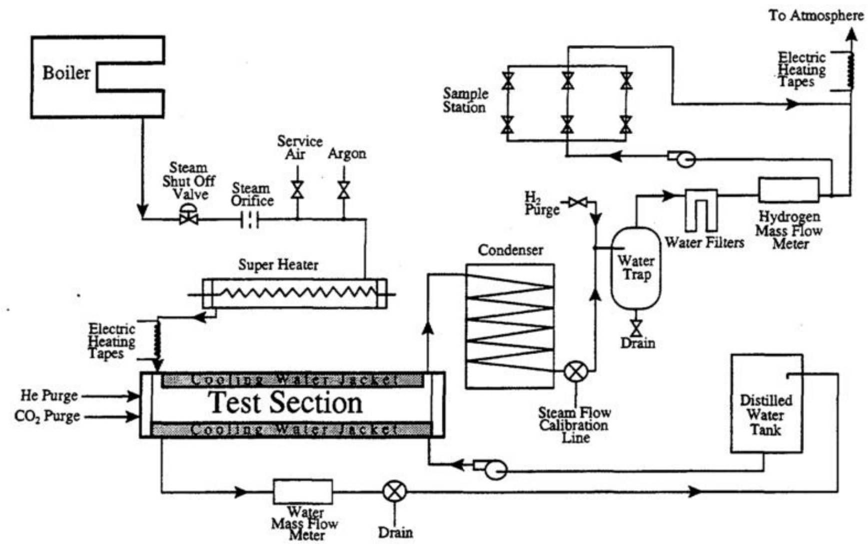

Figure 41 Test Apparatus used for the 28-Element (CS28-3) Experiment [80]

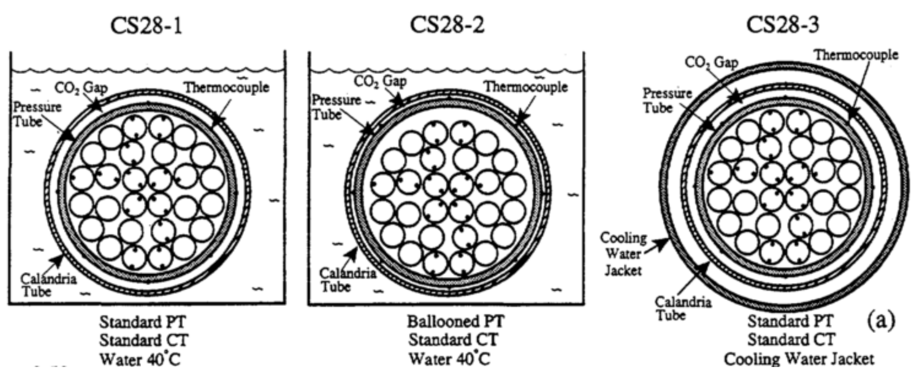

Figure 42 Test Section Cross-Sectional View of the 28-Element Series Test [80]

Table 37 Experimental Condition and Results of CHAN CS28-1 and CS28-3 Tests [80]

		CS28-1	CS28-3
Steam	Pressure (kPa, abs)	100-150	100-175
	Flow (g/s)	10.2	9
	Inlet Temperature (^oC)	700	700
Cooling Water Jacket	Pressure (kPa, abs)	N/A	90-185
	Flow (g/s)	N/A	355
	Inlet Temperature (^oC)	N/A	23
Water Tank (Open)	Water Temperature (^oC)	40 ± 5	N/A
Self-sustaining Zr-steam reaction (time length)		Yes (15s)	Yes (23s)
Total Hydrogen Production (moles)		18	54
Maximum Sheath Temperature (^oC)		1730	1870
Maximum Pressure Tube Temperature (^oC)		1220	1435

C.2 Model Description in MOD3.6

The test section steam volume is represented as a horizontal RELAP5 pipe component with 12 axial nodes. The water tank in CS28-1 and the cooling water jacket in test CS28-3 are also represented by RELAP5 pipe components (Figure 43 a). Only the heated part which has a length of 1.8m is modeled. The 28-element fuel bundle has three rings with 4, 8, and 16 (from inner to outer) elements. The axial power distribution was assumed to be uniform, while the radial power ratios from inner to outer ring are 0.78: 0.87: 1.1. In test CS28-1, one of the four inner ring elements was not powered for instrumentation purposes. Thus the FES was modeled by four SCDAP simulator components (one for each ring, and one for the non-powered pin) (Figure 43 b). The pressure tube was surrounded by CO_2 annulus gas and then by the calandria tube. This PT-CO_2-CT structure was modeled with a SCDAP shroud component with its inner surface heated by the steam via convection and by FES via radiation, with its outer surface cooled by the external cooling water. The emissivity of the fuel cladding, PT inner, PT outer surfaces, and calandria tube inner surface are assumed to be 0.8, 0.8, 0.8 (PT was pre-oxidized), and 0.34 respectively.

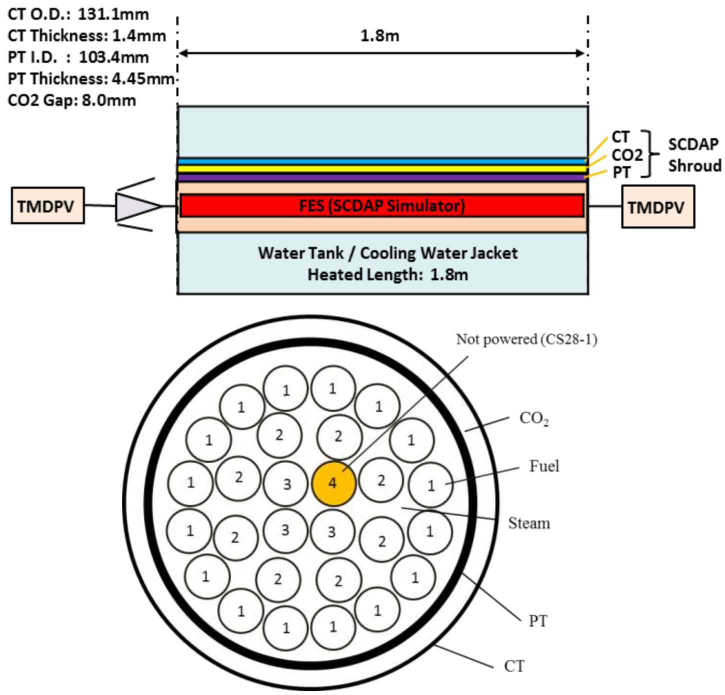

Figure 43 RELAP5/SCDAP Model for CHAN Thermal-chemical Experiments (a) Nodalization of Channel and Water Tank (Left) (b) Heat Structures (Right)

In test CS28-1, the test section was first heated in nitrogen until the minimum PT temperature was above 200^{o}C (stage 1). Steam was then introduced into the test section to start stage 2, while nitrogen supply was stopped. The heater power at stage 2 was at 10kW. This stage lasted for approximately 4800s to ensure a good steady state before starting the next stage. Subsequently, the power of the FES followed the curve in Figure 44, i.e. power was ramped to 20kW to start stage 3, then to 40kW and finally to 135kW at the end of stage 3. Power was turned off at approximately 850s, and 16s later the steam flow was also turned off. The computer simulations were performed in two steps: 1) stage 2 was run for a sufficiently long time until steady state was reached; 2), the steady state conditions (including steam, heat structures, and water temperatures) were used as the initial condition of the transient phase and the simulation was continued from time zero as shown in Figure 44.

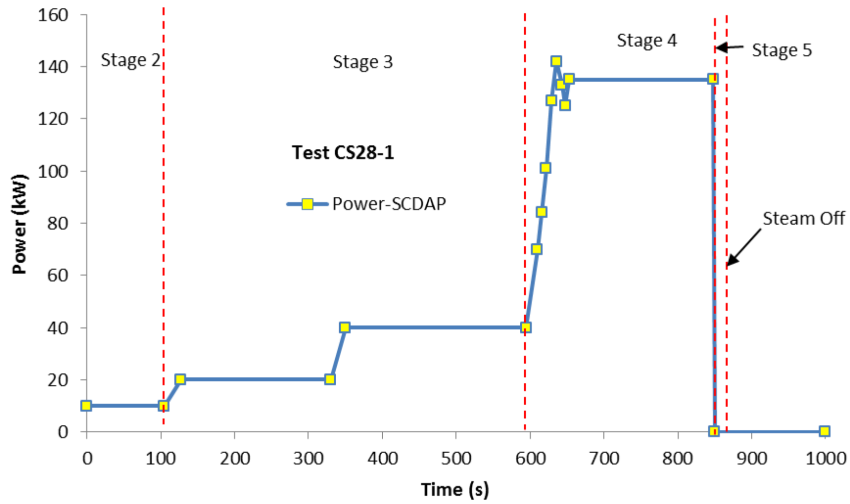

Figure 44 Test Section Power Supply for CS28-1

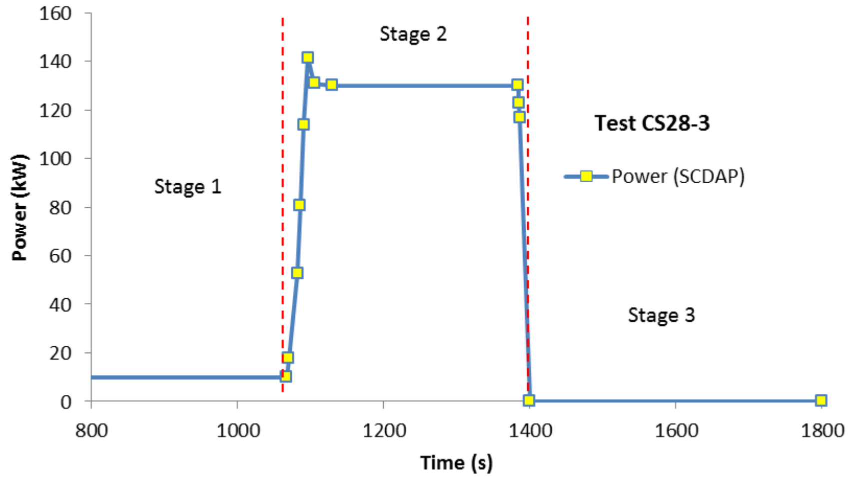

Figure 45 Test Section Power Supply for CS28-1

In test CS28-3, the experiments were divided into three stages. Similar to test CS28-1, stage 1 was designed to establish a good steady state prior to transient. At the beginning of stage 1, the test section was purged with helium. Steam flow was then established and power was raised to 10kW (Figure 45). Stage 1 lasted until a quasi-steady state condition was reached. To start stage 2, power was then ramped up to about 130kW, and was held at this value until the maximum sheath temperature exceeded 1700^{o}C. The power was then turned off at 1385s. Steam flow to the test section was kept at 9g/s and was turned off at 1546s.

C.3 Results and Discussions

C.3.1 CHAN CS28-1 Test

The predicted results for CHAN CS28-1 thermal-chemical test are shown in Figure 46 through Figure 48. The locations of thermocouples selected for comparison are shown in Figure 46 (b). Generally, SCDAP (MOD3.6) showed very good agreement with the experimental data. The important observations are:

1) During the lower power heat-up phase, i.e. Stage 3 in Figure 44, the heat-up rates at various locations agreed well with the experiments. Temperatures of the inner ring and middle ring showed excellent agreement with the experiments, while the outer ring and pressure tube temperature were slightly over-predicted.
2) During the high power stage (stage 4), the heat-up rates of the inner ring surfaces were under-predicted by SCDAP (Figure 47 a and b). The peak temperatures at the inner ring were also under-predicted by approximately 100^{o}C. The temperatures on the outer ring elements showed the opposite behaviors (Figure 47 d). The cross-sectional temperatures distributions predicted by SCDAP are thus more uniform than those measured in experiments. This is attributed to RELAP5's volume averaging effect, i.e. all three rings in the RELAP5 pipe see the same steam conditions while in experiments different sub-channels may experience different steam flow rates.

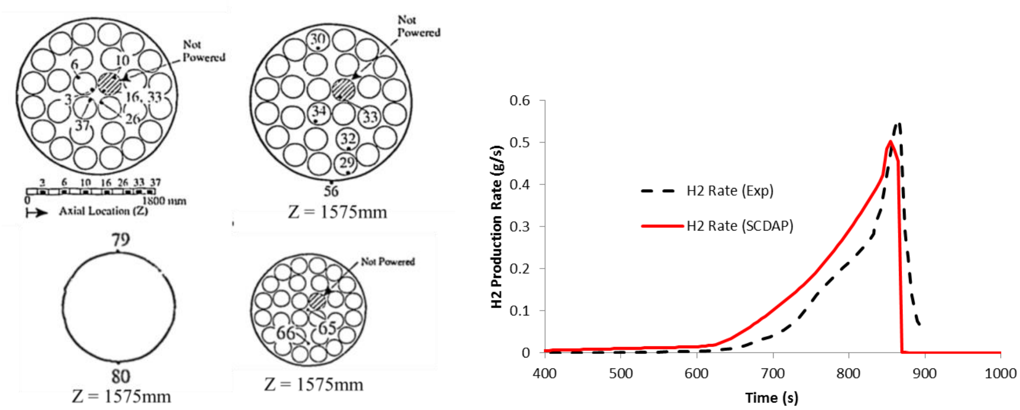

Figure 46 (a) Thermocouple Locations and (b) Measured/Predicted Hydrogen Generation Rate

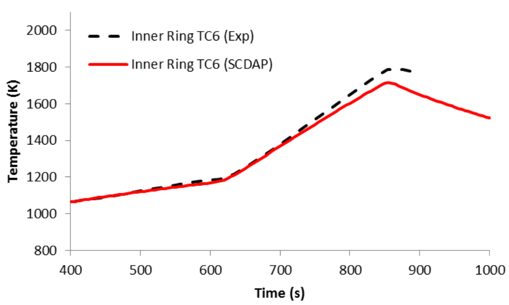

(a) Inner Ring Thermocouple 6

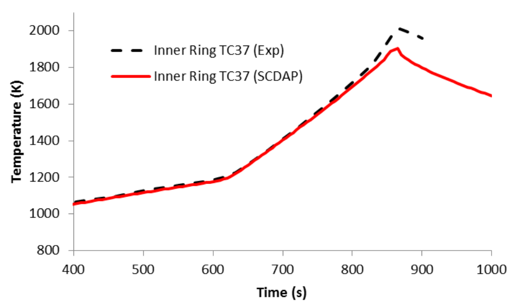

(b) Inner Ring Thermocouple 37

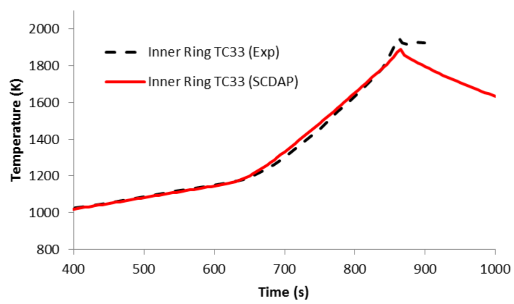

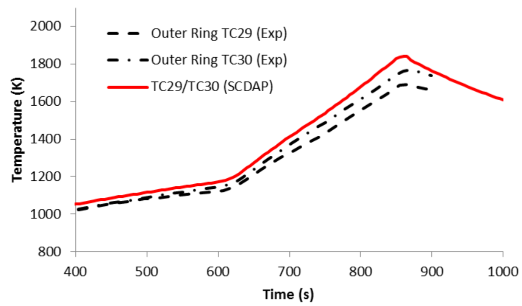

(c) Inner Ring Thermocouple 33 (d) Outer Ring Thermocouple 29/30

Figure 47 Measured and Predicted Inner/Outer Ring Surface Temperatures

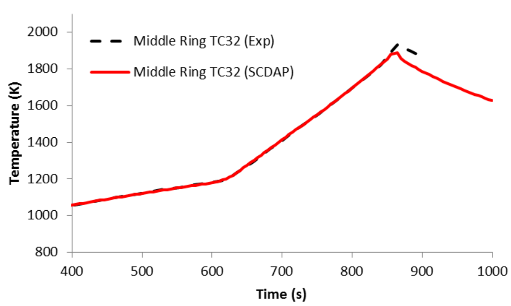

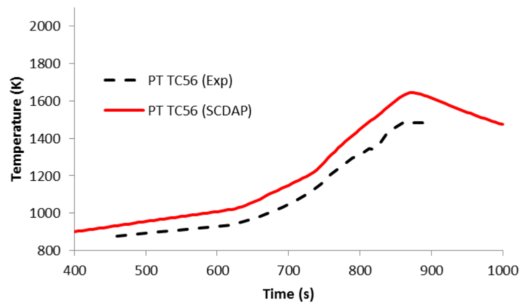

(a) Middle Ring Thermocouple 32 (b) PT Thermocouple 56

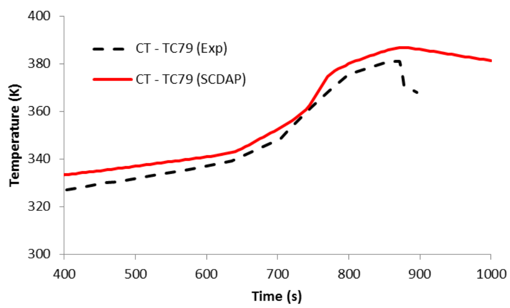

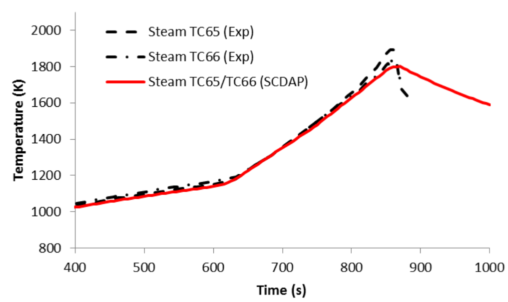

(c) CT Thermocouple 79 (d) Steam Thermocouple 65/66

Figure 48 Measured and Predicted Middle Ring, PT and CT Temperatures and Steam Temperatures

C.3.2 CHAN CS28-3 Test

The only differences in the SCDAP models used for CS28-1 and CS28-3 are that: (1) water tank is replaced with a cooling water jacket in CS28-3 with specified inlet flow; (2) the electrical power and steam flow rate to the test section are different; (3) all elements are powered in CS28-3, and the measured normalized powers for inner, middle, and outer rings are 0.744, 0.880, and 1.123 (as opposed to 0.78, 0.87, and 1.10 in CS28-1). The SCDAP predicted results for the CHAN CS28-3 tests are shown in Figure 49 through Figure 53.

Figure 49 shows the steam and cooling water outlet temperatures, and Figure 50 is the energy removed by steam and the cooling water jacket. In experiments, the heat losses through gap was estimated by calculating the heat conduction and radiation through the annulus gap using the measured PT and CT temperatures and the heat transferred across the gap peaked to 64.6kW at 1465s [80]. The power across the gap predicted by SCDAP followed the same trend and the peak value was almost identical to the experimental value (Figure 50 b), implying that the predicted pressure tube and calandria tube temperatures are close to the experiments (as seen in Figure 53) and the heat transfer across the gap was correctly calculated in SCDAP. The cooling water outlet temperature lagged the calculated gap heat removal rate by an appreciable time in the experiment. This effect, however, was less significant in the SCDAP prediction. Similar phenomena were also observed in steam outlet temperature measurement (see Figure 49 a Figure 50 a, note that the steam power in experiments was calculated based on the average steam outlet temperatures).

The predicted hydrogen production rate closely followed the measured value in the experiments until the turn-off of heater power at about 1385s (Figure 51 a). The rate continues to increase in experiments after the power went zero, and reached as high as 0.8g/s, while the predicted production rate only increased slightly. This suggested that the zirconium-steam reaction in the actual test was more self-sustaining than that in the SCDAP simulation. Some FES temperatures continued to increase for 125 s after electric power to the FES bundle was turned off [80]. The deviation from the experiments was again attributable to the averaging effect of the code and the under-prediction of maximum surface temperature by SCDAP (Figure 52).

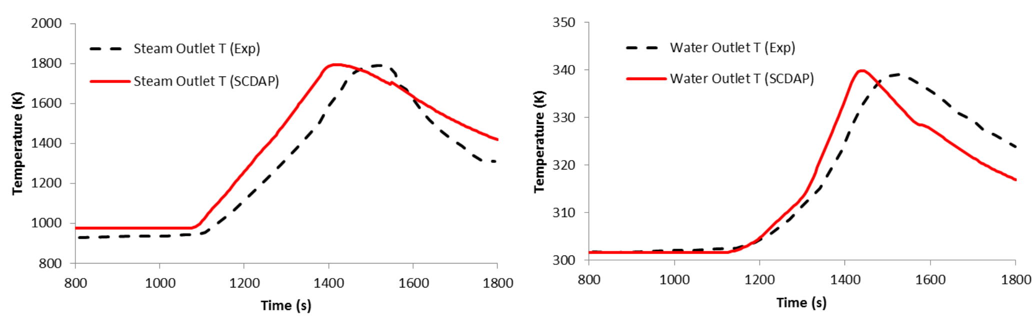

Figure 49 (a) Steam and (b) Cooling Water Outlet Temperatures

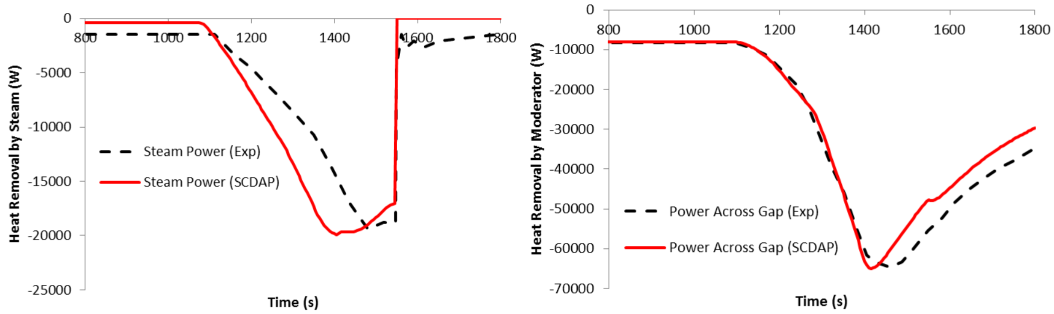

Figure 50 (a) Heat Removal by Steam and (b) Heat Removal by Cooling Water

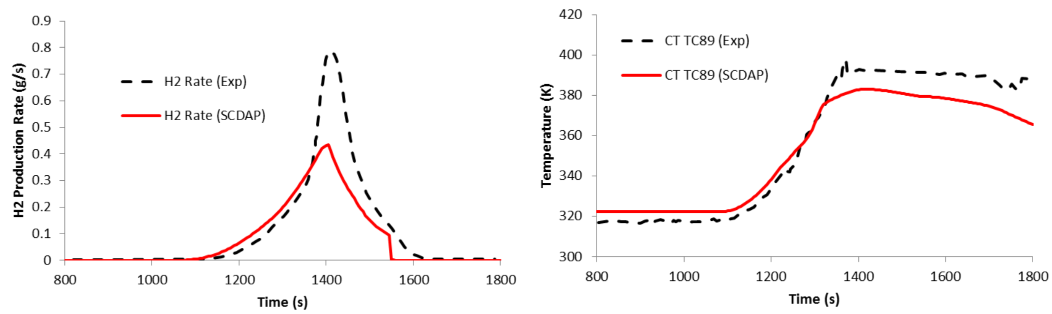

Figure 51 (a) Hydrogen Generation Rate and (b) CT Surface Temperatures Z= 825mm

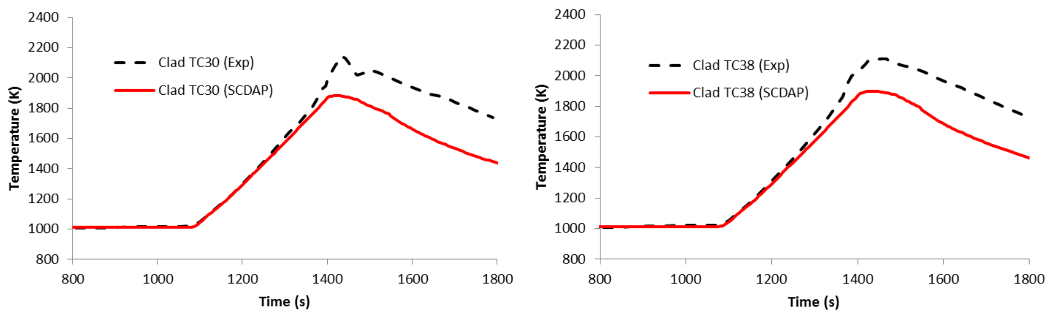

Figure 52 Hottest Fuel Element Simulator Temperature Recorded in CS28-3 and Predicted Temperatures at Same Locations (a) Inner Ring Z=1575mm (b) Inner Ring Z=1725mm

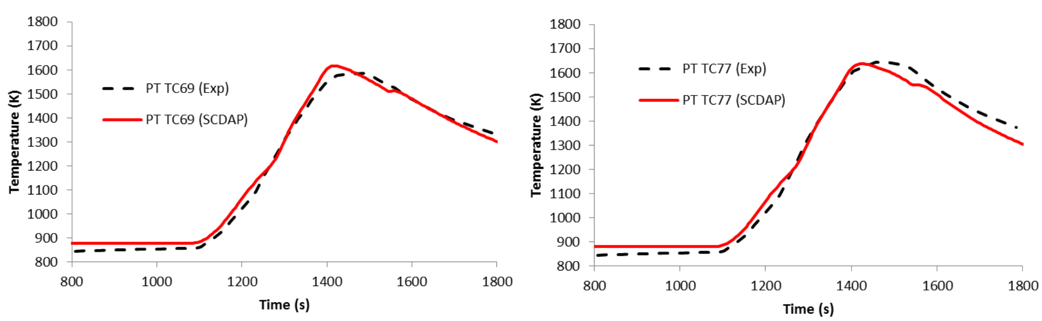

Figure 53 Hottest Pressure Tube Temperature Recorded in CS28-3 and Predicted Temperatures at Same Locations (a) Pressure Tube Bottom Z=1425mm (b) Pressure Tube Side Z=1725mm

Figure 52 is the hottest fuel element temperature recorded, which is located on the inside surface of the inner ring. The heat-up rate of the inner ring during the high-power stage and the maximum temperature were both significantly underestimated by the code. This is consistent with the observation in CS28-1 simulation and is again attributed to the limitation of the current model on volume averaging and circumferential heat conduction.

Appendix E. Potential Future Improvements

Table 38 Potential Improvements for the Current Models in MOD3.6

Areas Need Improvements	Key Phenomena to Consider	Current Study	
		Modeling Assumptions	Potential Consequences
Bundle distortion	Elements contact and fuse with each other to form a close-packed geometry.	Bundle distortion is not modeled; steam access to the bundle interior is not limited	Energy generation due to oxidation and hydrogen production will be over-predicted.
Molten material relocation	Inter-element relocation, Fuel-to-PT relocation, Channel-to-channel relocation, debris-to-moderator relocation.	Do not allow molten material relocation; molten drop slumping velocity set to zero.	Oxidation heat load and hydrogen production will be over-predicted (because otherwise molten material may be transported to cooler locations or to the remaining moderator).
Steam access to debris bed	Steam flow field inside CV; obstructions formed by the suspended debris bed; steam supply into the interior of the suspended debris bed.	CV modeled as a vertical pipe; no steam circulation pattern considered; steam access to the interior of debris bed freely.	Oxidation heat load and hydrogen production will be over-predicted; Fission product releases may also be over-predicted.
Debris bed compaction	The porosity of the debris bed decrease as the weight & temperature increases; its effects on debris heat conduction and steam access to the interior of debris bed	Debris bed heat conduction largely depends on the input channel-to-channel contact angle.	Overestimation of debris temperature and steam supply to the interior of debris bed; as a result, hydrogen production and fission product releases may be over-predicted.
Moderator expulsion	Moderator expelled out of CV due to rupture disks burst; expulsion due to core collapsing	Discharge duct is modeled as a pipe component connected to the CV top, and rupture disk modeled as a trip valve	The severity of moderator expulsion affects the moderator level which in turn affects the core disassembly pathway and the rate of accident progression.
Bundle-junction stress concentration	Strain localization at the bundle junctions along the bottom side of the channel (as observed experimentally)	Effect of stress concentration neglected	Neglecting this phenomenon will result in the underestimation of creep sag; however, sensitivity study showed that its impact on the end results (H_2, Fission Product releases, CV dryout etc.) is small.
Alternative disassembly/ relocation pathway	Disassembled core parts may directly fall to the CV bottom; Zircaloy tubes (cladding, PT, CT) melt and breach the oxide shell leading to molten mixture pouring to the CV bottom;	Channel segments after disassembly are supported by the lower channel of the same column until core collapsing.	Neglecting other relocation pathways the mass accumulation rate of the suspended debris bed will be over predicted leading to earlier core collapsing.
End stubs behavior	After channel disassembly the end stubs are attached to the CV tube sheet, the bundles may or may not fall out	Three options are available in MOD3.6: 1) bundles in end stubs do not fall out until the supporting tubes fail; 2) bundles fall out to CV bottom after core collapse; 3) bundles readily fall out to suspended debris.	Option 1 (default) results in the largest H_2/Fission Products releases and the latest core collapsing, while Option 3 results in the earliest core collapsing thus smallest H_2/Fission Products releases.
Molten pool formation & propagation	Formation and propagation of an in-core molten pool; interaction of molten pool with the supporting crust	Existing molten pool model in MOD3.6 is developed for LWR and is considered unsuitable for CANDU; disabled.	The likelihood of forming an in-core molten pool prior to core collapsing is small, but increases with increasing maximum supportable load or decreasing debris bed heat conduction effectiveness.
Radiation heat transfer	Radiation heat transfer among the uncovered channels, the suspended debris bed, and the cold CV wall; the change in geometry/location, and the feedback on view factors.	Only the radiation heat transfer between fuel and PT, and between PT and CT are modeled;	Neglecting radiation among channels, debris bed, and the cold CV wall may lead to the overestimation of debris bed temperature, and earlier CV dryout.